Modeling and Simulation of Lab-on-a-Chip Systems

Yi Wang

A dissertation submitted to the graduate school
in partial fulfillment of the requirements of the degree of
Doctor of Philosophy
in
Mechanical Engineering

Carnegie Mellon University
Pittsburgh, Pennsylvania 15213

Committee:

Professor Qiao Lin
Professor Tamal Mukherjee
Professor Shelley L. Anna
Professor Shi-Chune Yao

August 12, 2005

To my parents, Changshou and Hongqiu, and brother, Jian
and to my wife, Qian, and daughter, Rebecca

Abstract

This thesis presents a behavioral modeling and schematic simulation methodology for top-down Lab-on-a-Chip (LoC) design. The methodology involves decomposing a complex LoC system into a small set of elements. Each of the elements is associated with a parameterized behavioral model that describes its electric and biofluidic behavior. Key issues addressed include schematic representation, behavioral multi-physics modeling and numerical and experimental validation.

The modeling effort focuses on sample transport in LoC devices. Turn and Joule heating induced dispersion in electrophoretic separation chips are studied using the method of moments. The skew of the species band is effectively represented by a set of Fourier cosine series coefficients that are obtained analytically. These coefficients capture the effect of band skew on separation performance in various complex chip geometries (including multiple turns). Variations of sample concentration profiles in laminar diffusion-based micromixers are also derived using the Fourier cosine series representation. The model holds for arbitrary sample flow ratios and inlet concentration profiles, and accurately considers the overall effects of device topology, size and electric field on mixing performance. In addition, a simplified reaction model is developed and integrated with the separation and mixing models to perform system-level schematic simulations of an integrated LoC system. Simulation results at both element and system levels are validated against numerical and experimental data. Excellent accuracy (generally less than $< 5\%$ in relative error) and tremendous speedup ($> 100\times$) have been achieved when compared with finite element analysis. The mixing model is also adapted to pressure driven flow and used to propose a novel concentration gradient generator design. The resulting modeling and

simulation framework is a significant contribution to balancing the needs for efficiency and accuracy thus enabling iterative design of complex biofluidic LoC systems.

Acknowledgements

There are a number of individuals who have been essential to the accomplishments in this thesis, both technically and personally. First, I would like to thank my advisor, Professor Qiao Lin. During my graduate study, I have benefited from him greatly in many aspects of academic research, communication skills as well as personality. His profound knowledge, both theoretical and experimental, of physical phenomena in lab-on-a-chip systems has been a constant source of information for my research. His encouragement and feedback on publications and presentations have helped me vastly improve my communication skills, making me well prepared for my future career. His patient and dedicated mentoring has been extraordinary, and indispensable to the completion of this thesis.

I would like to thank my co-advisor, Professor Tamal Mukherjee, who has always encouraged me to explore new and unknown research fields in the course of my Ph.D. study. His keen insight and broad knowledge in CAD design and biofluidics have always been the most reliable resources when I run into difficulties. Additionally, I have appreciated his advice on research strategies and high-level research issues, such as significance and practical relevance of research topics. Understanding these questions has helped me put my research in context.

I am also grateful to Professors James Hoburg and Steinar Hauan in our SYNBIOSYS project. Discussion with Professor Hoburg always led me to an in-depth and thorough comprehension of the fundamental physics, and his rigorous scientific attitude to research has been a model for me to follow. Professor Hauan provided numerous insightful questions, shared his experience in preparing presentation slides, and generously granted

me access to the Beowulf computer cluster for numerical simulations. Additionally, I would like to thank my committee members, Professors Shelley Anna and Shi-Chune Yao. They also provided important feedback and suggestions for my research, setting a broad context and a high standard for this thesis.

I also wish to express gratitude to the other graduate students in the SYNBIOSYS project for many years of fruitful interactions: Ryan Magargle for discussions on modeling and numerical simulations, helpful tips on computers and interesting chats on living and shopping; Anton Pfeiffer for discussions on model implementation and optimization; Xiang He for suggestions on reaction modeling, and Bikram Baidya for getting me started on Cadence and Neocircuit. Thanks also go to the other members of the Biofluidic Micro Systems Laboratory in the Mechanical Engineering Department: Hsienchung Lin, Shan Liu, Yonduck Sung, Li Wang, Bozhi Yang and Yongjun Zhao. Interacting with them in research as well as daily life has made my time at CMU truly enjoyable.

Last but not least, I want to thank Chris Zeise in the Mechanical Engineering Department for her help with my questions on courses, defense, graduation and immigration status, and to Mary Moore at the MEMS Laboratory in the Electrical and Computer Engineering Department for her kind assistance on many occasions.

Financial support under grants from the Defense Advanced Research Projects Agency (Grant No. F30602-01-2-0587) and the National Science Foundation ITR program (Award No. CCR-0325344) is gratefully acknowledged.

This thesis is dedicated to my parents, Changshou and Hongqiu. Their endless love and high expectations on me have constantly empowered me to overcome difficulties and frustrations in my career. Whenever I needed them, they were always there to patiently

listen to me and give me encouragement. I also want to thank my brother, Jian, for enabling me to study abroad by taking care of our parents in my absence. Finally, I would like to dedicate this thesis to my wife, Qian and my lovely daughter, Rebecca. Qian’s considerate care and unconditional love for me and for our family has allowed me to maintain a clear focus and pay undistracted attention to research. Rebecca, my little angel, has always brought me enjoyment during my busy school life. Indeed, my family let me know home is the warmest place in the world.

Table of Contents

List of Tables

List of Figures

Chapter 1 Introduction

1.1 Introduction

Lab-on-a-chip (LoC) systems, also called Micro Total Analysis Systems (MicroTAS), have been a major research area over the past decade, due to their potential in a wide spectrum of applications in biology, biomedicine and chemistry. A LoC system can be thought of as a miniaturized chemical or biological workbench that integrates many functions (e.g., sample pretreatment, sample transportation, mixing, reaction, separation and detection) typically performed in an analytical laboratory. Miniaturized LoC systems offer advantages beyond conventional biochemical and clinical laboratories. A distinct benefit of miniaturized LoC systems is the dramatic (thousands of fold) reduction of sample consumption. Multiplex and multi-functional systems for fluidic handling, sample preparation, synthesis and analysis can be integrated for high-throughput assays. A high degree of automation relieves experimentalists from labor- and time-intensive biochemical characterization processes and hence allows more precise and reproducible analysis. Most significantly, miniaturization drastically improves analysis characteristics (e.g., shorter analysis time and higher separation performance) and even achieves innovative applications that are not otherwise attainable.

A variety of state-of-the-art biomedical and biochemical integrated devices have been successfully demonstrated in applications ranging from drug discovery, drug delivery and clinical diagnostics, to DNA and protein analysis, immunoassays and flow cytometry [1]. Indeed, there is enormous commercialization potential for LoC technology. The LoC market has increased from $ 400 million in 2000 [2] to $ 2 billion in 2004 and is projected

to rise to $ 5 billion by 2009 [3]. A host of LoC-based biotech companies such as Affymetrix, Caliper, Cepheid, Fluidigm, Micronics and Nanogen have developed their own LoC systems in the drug discovery, genomic analysis, proteomics and cellomics sectors [4]. Large electronics companies such as Agilent, GE, Hitachi, IBM, Intel and Texas Instruments have also been attracted to LoC technology.

While LoC technology holds enormous potential, its promise in delivering the low-cost, low-volume and application-specific integrated systems has not yet been fulfilled, primarily because of the technical difficulties and extremely long development cycles involved in microsystem design [5, 6]. This issue becomes even more acute for large-scale microfluidic integration and automation, which is considered a major trend for the next generation LoC devices. In the next section, fundamental problems and technical challenges that act as a bottleneck to rapid LoC design will be examined.

1.2 Motivation

1.2.1 Limitations of Existing LoC Design Approaches

Currently two approaches are commonly used in biofluidic chip design: experimental and numerical. The experimental approach starts off with the designer making a rough conceptual schematic of the design and writing basic equations to ensure the design feasibility. After being satisfied with the schematic, the designer proceeds to physical layout, which is then sent to fabrication. As there is no simulation-based verification of the chip prior to fabrication, this approach often results in non-functional chips. Errors (e.g., insufficient mixing and low electrophoretic separation resolution) detected during the characterization of the fabricated chip are used to instruct the chip redesign. Thus, this design methodology is based on a fabrication-design loop, which is extremely expensive

and time-consuming. Typically, customized chip design can take several months to a year, which is prohibitive to medium-size and small biotech companies and academic laboratories.

A new option to verify the physical layout before fabrication through numerical simulation has emerged over the past few years. This process involves translation of the chip layout into a solid model via a process simulator, followed by meshing and then continuum simulation [7-12]. This simulation-based verification leads to a cheaper iterative simulation-design loop. However, a series of issues associated with the numerical approach still preclude it from being employed as an effective tool for biofluidic LoC design. For example, it is difficult for numerical simulations to provide adequate insight into the multi-physical phenomena within LoCs, such as the dispersive skew effects caused by electrophoresis turns, mass transfer regimes of Joule heating induced band-broadening in electrophoresis and slow molecular diffusion-based mixing. Hence, the designer's understanding of the candidate design is based on simulation data rather than on functional behavior of the system, generally leading to a large number of repetitive and poorly-targeted simulations.

The most serious issue of the numerical approach arises from its demanding computational overhead (e.g., CPU time, memory requirements and expertise). As the numerical approach solves the discretized transport equations, fine meshes and time steps, and expert knowledge of numerical algorithms are often required to ensure the solution convergence and accuracy (e.g., minimizing the error of numerical diffusion [9]). When transient and three-dimensional multi-physics problems are involved, numerical analysis can become intractable. For example, a solution of 3D Joule heating dispersion by a Finite

Element Method (FEM) tool can cost 4 days and 4 GB of physical memory [13], and a steady-state flow solution of a 3D low-voltage electroosmotic pump can devour 18 GB of physical memory [14]. Such computational cost is prohibitive for system-level design of complex LoC systems.

An additional issue associated with numerical simulation is that solid models need to be regenerated when layout geometries are modified during iterative design loops, further aggravating the design burden.

1.2.2 LoC Design Trends

Large-scale microfluidic integration (e.g., integrated multiplex and multi-functional LoCs) that enables high-throughput and fully-automated biochemical assays is a major trend for the next generation LoC.

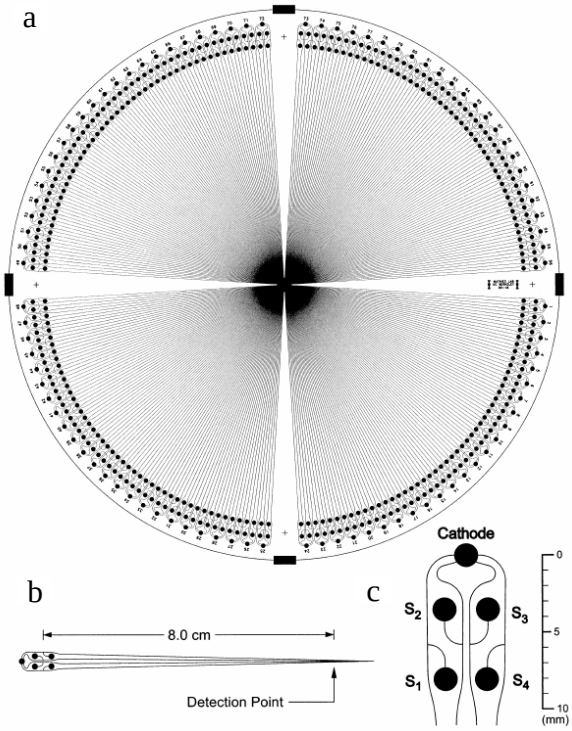

Figure 1-1. (a) Layout of the 384-channel capillary electrophoresis bioanalyzer. (b) Enlarged view of a single channel with injector. (c) Enlarged view of the injector design and sample reservoirs [15].

To illustrate this trend, consider two different design examples: a multiplex and a multi-functional integrated LoC. Figure 1-1 illustrates a multiplex genotyping chip consisting of 384 electrophoresis subsystems operating simultaneously and independently to achieve high throughput. Figure 1-2a depicts an integrated multi-functional (mixing, reaction, injection and separation) immunoassay LoC system. Figure 1-2b illustrates another immunoassay LoC device that has both multiplex and multi-functional system complexity. Numerical analysis of such chips involves repetitive and arduous solutions of multi-physics (e.g., electrostatics, fluidics, sample transport, reaction and heat transfer) and disparate operational phases (e.g., continuous-flow mixing-reaction and transient separation analysis). Given that the existing design methodologies are computationally intractable for today's small designs, there is no potential for their use in answering the types of questions that designers of such complex integrated biochips may have.

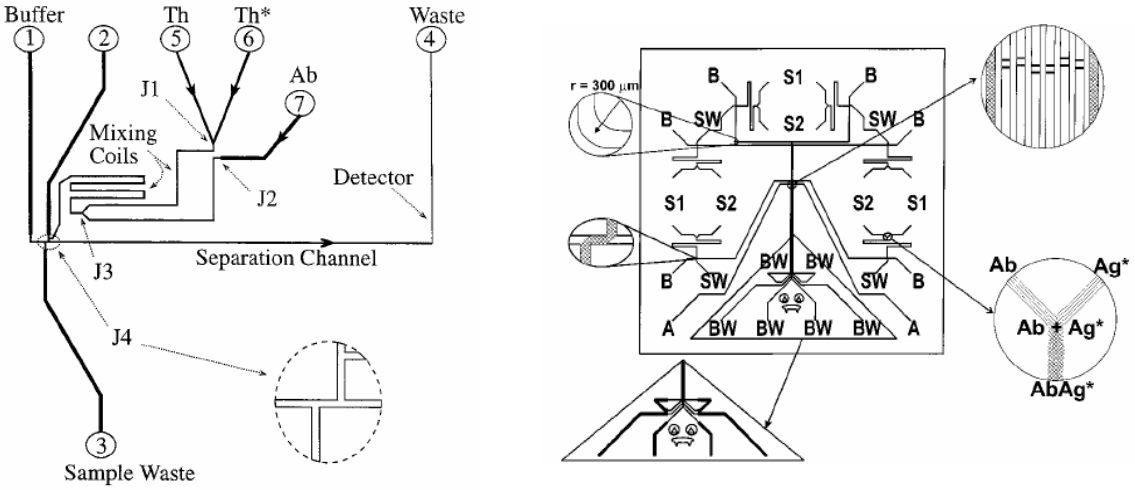

a b

Figure 1-2. (a) An integrated competitive immunoassay microchip, consisting of mixing, reaction, injection and separation subsystems [16]. (b) A multiplex immunoassay microfluidic device consisting of six independent mixing, reaction, injection and separation manifolds operated simultaneously and in parallel [17].

1.2.3 LoC Design Needs

LoC design is typically an iterative process. In each iteration, the designer wishes to assess the quality of the candidate design through performance evaluation. From the above description of biochip design methodologies and trends, we can identify the ideal characteristics of the performance evaluation techniques needed to answer the design questions that a biochip engineer may have:

- **Ability to handle system complexity**

LoC designers are integrating longer channel networks with multiple functions (e.g., separation, mixing and reaction) and arraying such networks onto a single multiplex LoC as shown in Figure 1-1 and Figure 1-2. Therefore, emerging design aids need to handle such types of complexity in LoCs.

- **Ability to handle physical phenomena from multiple domains**

Physical phenomena from multiple domains co-exist and interact within each LoC. In an electrokinetic LoC, for example, there is bulk fluidic transport that can be characterized using electric current and flow rate. Therefore LoC design aids must handle electric and fluidic state during simulation.

- **Ability to handle local non-ideal sample transport**

Performance limitations in biofluidic LoCs tend to be governed by non-ideal sample transport. In LoCs that integrate electrophoretic separation, skew in species band limits separation resolution. Mixing, which is typically diffusion-limited in many LoC designs, often involves non-uniform sample concentration profiles in the channel networks. Therefore, non-ideal sample transport phenomena such as the band skew and non-uniformity in the sample concentration must be accurately captured.

- **Fast evaluation speed**

Design is an iterative process. Therefore, fast simulations are desirable to speed up the entire design flow.

- **Adequate accuracy**

Performance evaluation in the iterative design is used to characterize the impact of changes in candidate design topologies and sizes. Therefore simulation accuracy, in comparison to both detailed numerical analysis and experimental characterization is important.

- **Model reusability**

Design typically involves modifying the channel network, channel geometry, material and operational parameters. Therefore, parameterized models that enable reusability are essential.

1.3 Approach

In this thesis, a behavioral modeling and schematic simulation methodology for top-down design of integrated biofluidic LoC systems that meets all the requirements mentioned above is presented. In contrast to numerical simulation, a hierarchical modeling approach is explored, inspired by the system hierarchy existing in all integrated biofluidic LoCs. A complex system can be functionally and geometrically decomposed into a collection of commonly used elements. This provides a potent means of handling system complexity. Non-ideal sample transport, such as the skewed electrophoretic species band and non-uniform transverse mixing concentration profile in constituent elements, is effectively represented by a set of Fourier cosine series coefficients that are obtained from analytical solutions of the convection-diffusion equation without resorting to any existing

macromodel or analogy between fluidic and sample transport. The models are in closed-form and parameterized by material, geometrical and operational parameters, offering reusability and fast evaluation speed. The use of hierarchical decomposition to develop a network representation for LoCs requires communication between adjacent elements. This is enabled by defining electric and biofluidic pins at element terminals to capture local physical state. Kirchhoff's law and signal flow network theory are employed to respectively calculate the electric, fluidic and sample transport state throughout the network.

1.4 Thesis Scope

This thesis is focused on the modeling and simulation of key sample preconditioning, synthesis and analysis components (e.g., mixers, reactors, separators and detectors) in LoC devices driven by electrokinetic flow, as well as systems that integrate all these functions. The methodology can be readily extended to pressure driven flow with proper modification of the driving velocity fields in the multi-physics models. The analog network abstraction of LoCs is not applicable to microarray and digital microfluidics (see Section 2.1 for categorization of LoC) due to their fundamentally different operational principles.

1.5 Thesis Organization

The thesis is organized as follows. Chapter 2 briefly categorizes LoC devices, introduces electrokinetics fundamentals and surveys the state-of-the-art modeling and simulation efforts for biofluidic LoC devices. Chapter 3 proposes the behavioral modeling and schematic simulation methodology, in which the hierarchical system representation and modeling formulation are discussed in detail. Chapter 4 and Chapter 5 respectively present the models of turn and Joule heating dispersion for system-level simulation of electrophoresis microchips along with numerical and experimental verification. Behavioral

modeling and schematic simulation of electrokinetic laminar diffusion-based micromixers are developed in Chapter 6. In Chapter 7, a simplified model for immunoassay reactor is presented and integrated with the models that have been described (e.g., mixer and separator) for system-level simulation of a competitive immunoassay microchip. Chapter 8 extends the mixer modeling from electrokinetic to pressure driven flow and proposes novel biofluidic devices, concentration gradient generators that are particularly useful to cell analysis. Finally, the thesis concludes with summary and future work in Chapter 9.

Chapter 2 Background

2.1 Lab-on-a-Chip Systems

This section reviews and categorizes existing LoC devices. In general, LoCs can be classified into two main categories: microarray-chips and microfluidics-based chips.

2.1.1 Microarrays

Molecular biology has been one of the most active LoC application areas. Traditional molecular biological methods analyze genes and their products (i.e., RNA and proteins) within an organism in a low-throughput manner limiting their ability to obtain an overview of gene composition and function. DNA microarrays [18-20], have introduced an innovative means to examine the whole genome on a single chip so that researchers can capture the interactions among thousands of genes simultaneously.

DNA microarrays are used to directly compare the amount of each gene among different samples in a miniaturized and high-throughput fashion. The principle is illustrated in Figure 2-1. The labeled cDNA (by fluorescence of different colors) prepared by reverse transcription of the messenger RNA extracted from each cell population is mixed, incubated and hybridized with probes (spots for DNA hybridization reaction) on the microarray. Each probe represents a specific gene. Regardless of their fluorescent labels, the cDNA sequence representing a unique transcript selectively binds with the corresponding gene pair on the array probe. Thus, the relative amount of the transcript from each individual gene of different cells is manifested by the intensity of the labeling fluorescent colors measured at the array probe.

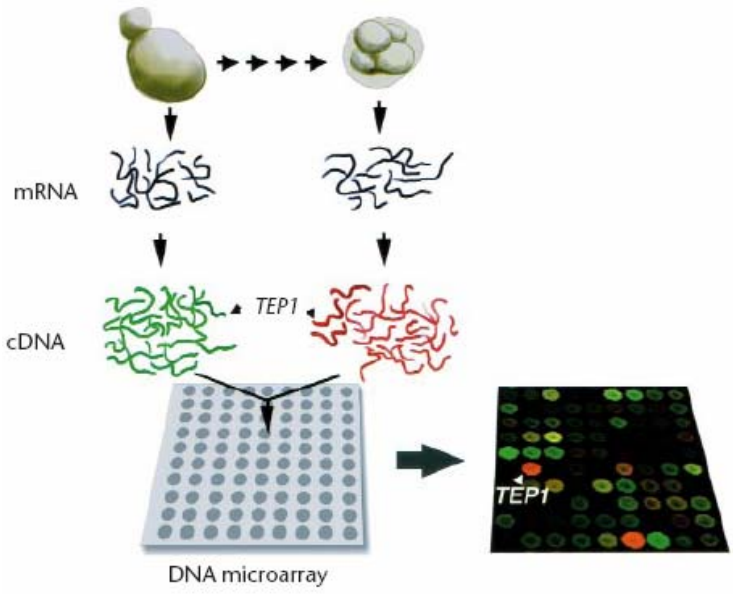

Figure 2-1. Gene expression analysis using a DNA microarray [21], in which mRNA samples from vegetative and sporulating yeast cells are compared.

Therefore, the techniques for fabricating the microarrays and spotting the probes with high selectivity and efficient hybridization reactions, robust and low-noise detection by fluorescence scanning/imaging or mass spectroscopy, and accurate post-processing of the complex data into useful information are desired during the design [22].

Microarray technology later has also been extended to proteomic research [23, 24], specifically for protein identification and quantification (e.g., miniaturized and parallelized immunoassays), protein interaction analysis (e.g., protein-protein interactions, enzyme-substrates assays, protein-DNA interactions), as well as cell analysis in gene activities, protein expression and cell surface molecules [23].

2.1.2 Microfluidic Lab-on-a-Chip Systems

Depending on the sample size and transportation mechanism, microfluidics can be divided into two domains: digital and continuous-flow microfluidics. Here, sample refers to the species of interest or their mixture involved in the preconditioning, synthesis and analysis functions in a LoC. In contrast to microarrays, transport phenomena (e.g.,

electrical, fluidic, thermal and sample) in microfluidic chips are of primary interest and pivotal to system performance.

2.1.2.1 Digital Microfluidics

In digital microfluidics, the sample is transported in terms of a single immiscible gas bubble or a liquid droplet within the bulk fluid (e.g., water droplets immersed in an oil pool, where water is sample-carrying liquid and oil is bulk liquid), or the size of the species particles is comparable to the transverse channel dimensions (e.g., cell in a microchannel). The underlying mechanism for forming and driving the droplets and particles are very diverse [25-27], including capillary effects (e.g., chemically [28] and thermally [29] induced surface tension gradients, or capillary pressure different due to chemically non-uniform surfaces [30, 31], electrowetting on dielectric substrates [32-36] and thermal gradient [37]) and dielectrophoresis [38-40]. Among them, electrowetting on dielectric (EWOD) and dielectrophoresis have found broad LoC applications.

In EWOD, a chemically inert and dielectric layer separates the electrolyte and electrode surface, eliminating the direct electrochemical interaction between the electrolyte and electrode. The inert layer also minimizes the experimental complications due to residuals of oxide layers and contaminants on electrode surfaces from the fabrication process. A voltage is then applied between one end of a droplet and the electrode underneath to reduce the local surface tension, which induces pressure difference between the ends of the droplet and then drives the droplet. Complete bio-processing functions such as droplet creation, transportation, merging and cutting have been successfully demonstrated [36, 41] (Figure 2-2). More recently, peptide and protein analysis [42] and a colorimetric enzymatic glucose assay on serum, plasma, urine, and saliva [43, 44] on EWOD chips have been reported.

Dielectrophoresis (DEP) [38, 40, 45] refers to electromechanical forces exerted on an electrically neutral but polarizable particle due to the induced dipole when subjected to a non-uniform electric field. DEP has been found especially effective in spatially manipulating cells [46-53], separating cells of different types (e.g., mixtures of bacteria, viable and unviable cells, cancerous and normal cells, and red and white blood cells) [39] as well as generating and processing fluid particles [54].

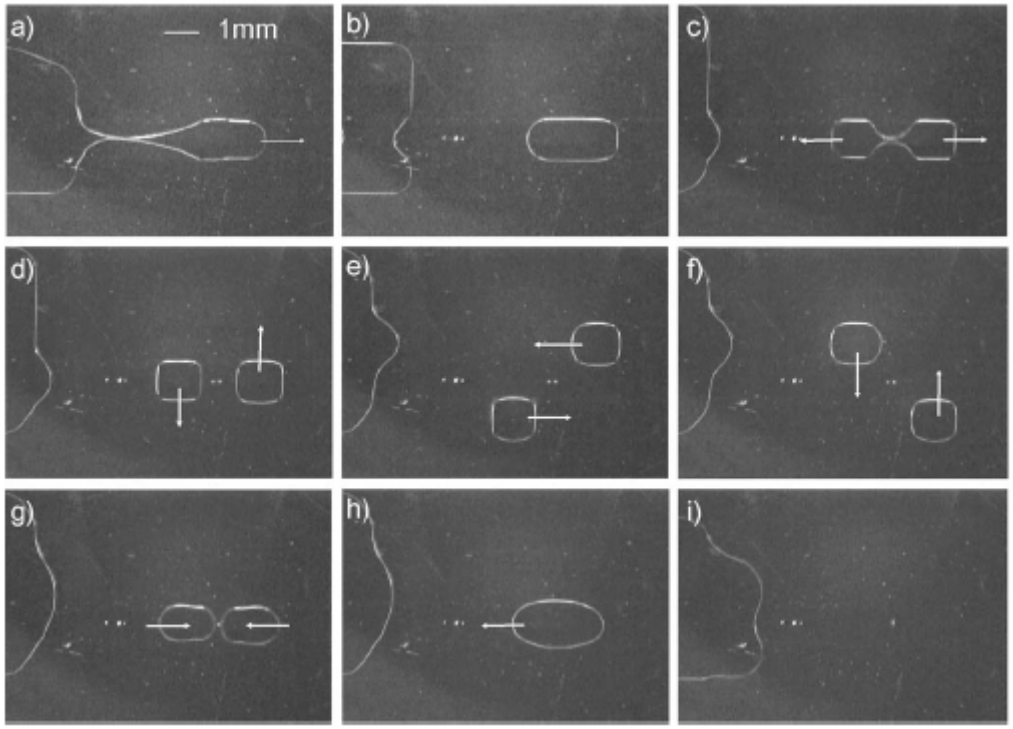

Figure 2-2. Droplet operations in a digital EWOD fluidic circuit [41]. (a) and (b): droplet creation; (c) droplet cutting; (d)-(f): droplet transportation; (g)-(i) droplet merging and collecting.

2.1.2.2 Continuous-Flow Microfluidics

In continuous-flow microfluidics, sample-carrying fluid continuously flows through microchannels (rather than a discretized and immiscible droplet). The sample's spatial distribution within the system can be collectively represented by a scalar value, concentration. Continuous-flow microfluidics-based devices have been actively and

extensively investigated in a variety of fields. In this subsection, continuous-flow microfluidic devices are categorized by their functions.

Fluid handling

Fluid handling refers to pumping and switching fluid within microchannel networks either by external devices (e.g., syringe pumps) or micro-fabricated pumps. Since fluid handling supporting sample transportation is needed in all biofluidic LoC devices, it has been studied most extensively [55-57]. Micropumps can be categorized into valve-type and valveless pumps [55]. Valve-type micropumps count on the reciprocating movement of a flap (e.g., diaphragm-ring mesa, cantilever and tethered plate) [55, 57] to propel the liquid, usually actuated by piezoelectric, thermo-pneumatic, pneumatic and electrostatic forces. Valveless micropumps include electrohydrodynamic (EHD), electroosmotic (EOF) and magnetohydrodynamic (MHD) pumping approaches [55, 57] that do not need moving parts and result in simple fabrication processes. In addition, bioanalytical devices taking advantage of gravity [58], capillary force [59, 60] and centrifugal pumping [60, 61] also have been reported.

Sample preconditioning

A key challenge for biomolecular assay design is to properly precondition the sample before the assay itself [62]. Sample preconditioning includes preconcentration, removing interfering species and increasing the concentration of the species of interest; dilution, diluting the species with buffer solvent to a single or an array of desired concentrations; and gradient generation, generating desired streamwise or widthwise species concentration gradients. Figure 2-3 shows a microfluidic H-filter in which a “receiver” and a sample stream flows side by side. The filter operates on the basis of the different diffusion rate of molecules with disparate molecular weights. Small molecules diffuse from the sample

stream to the “receiver” stream, while almost all large molecules remain in the original sample stream leading to a higher relative concentration.

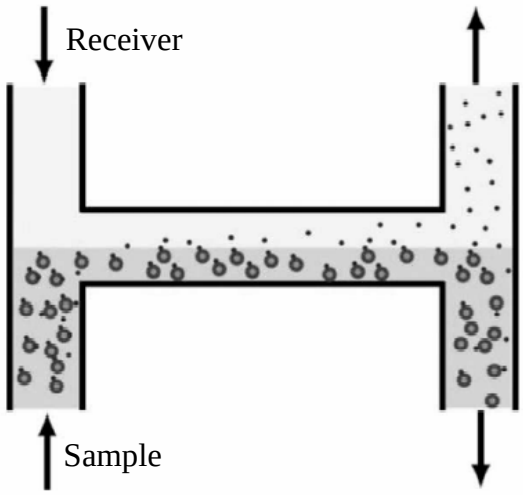

Figure 2-3. H-Filter schematic. Small molecules are removed from the sample stream leading to a higher relative concentration of large particles [63].

Field amplification stacking (FAS) [64] is another very effective approach to magnify the sample signal in both capillary [65-67] and microchip [68, 69] electrophoresis. A high electric field within an injected sample plug is used to rapidly drive and stack charged molecules at the ends of the plug to achieve preconcentration. Recently, an electropherogram signal increase by a factor of 1100 in the electrophoretic separation of fluorescein and Bodipy has been reported [70].

In contrast to preconcentration, complex mixing networks to obtain continuously diluted sample concentrations along flow direction based on repeated mixing units in both electrokinetic [71] and pressure driven flow [72] have also been presented for parallel bio-analysis (e.g., immunoassay [72]). Tree-like microfluidic networks that continuously split, mix and recombine samples [13, 73, 74] using stacked branch channels (Figure 2-4a) have also been proposed to create desired widthwise concentration gradients (e.g., linear and parabolic in Figure 2-4b) for cell chemotaxis [75, 76] and microfabrication [73].

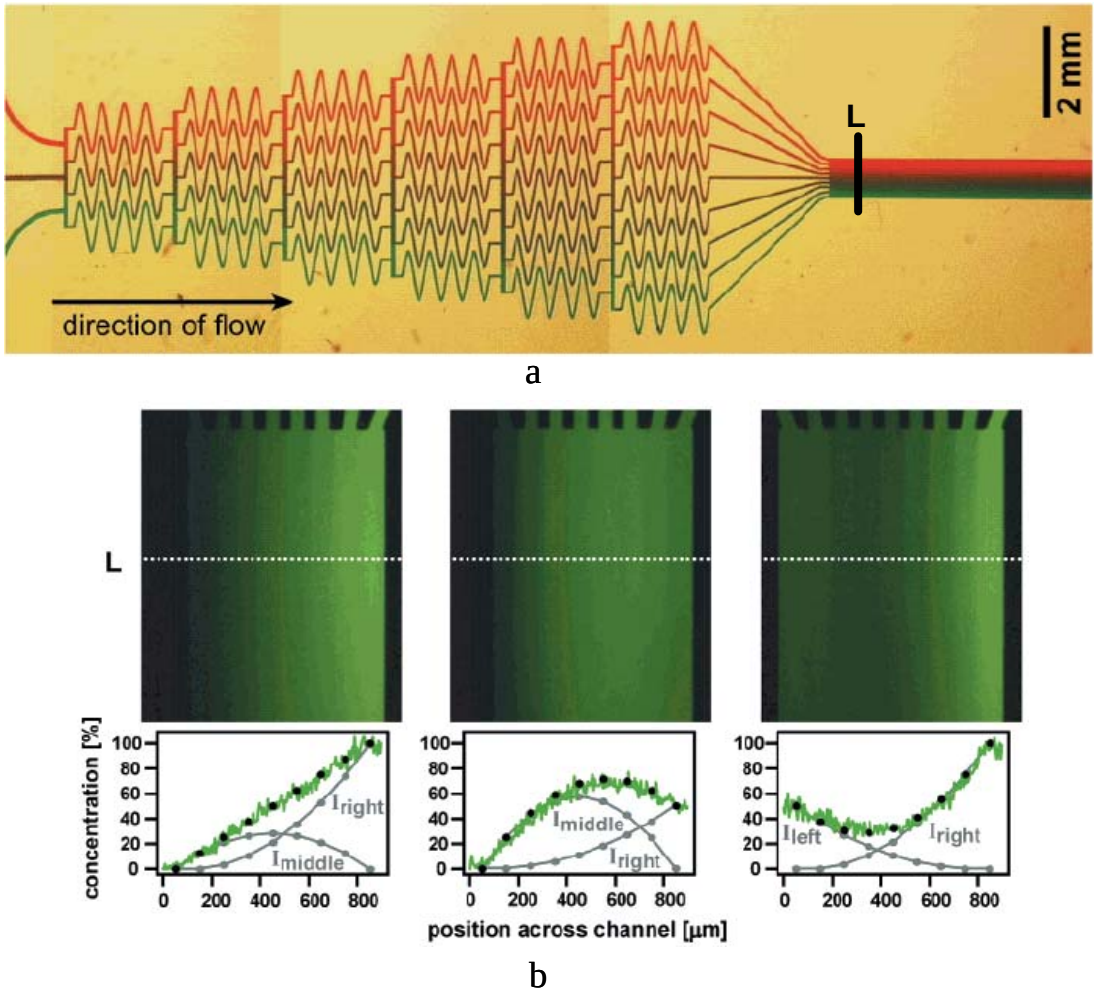

Figure 2-4. (a) A microfluidic device used to generate widthwise concentration gradients of red and green samples. (b) The generated linear and parabolic gradients [74].

Mixing and reaction

Mixers and reactors are the key synthesis components in biofluidic LoCs. They combine and convert samples and reagents into products for further analysis. At the microscale, laminar diffusion is the dominant mixing mechanism, which is not efficient and often impairs the synthesis and analysis quality promised by LoCs. Therefore, numerous mixing-enhancement techniques have been proposed, which are summarized in Figure 2-5. Micromixers can be classified into passive and active micromixers [77, 78]. Passive mixing relies on spontaneous molecular diffusion; hence it can be improved by increasing the

contact surface area and shrinking diffusion distance between different sample streams (e.g., lamination, injection, chaotic advection etc.). Active mixers rely on external energy (e.g., pressure, electrohydrodynamic, dielectrophoretic, magnetohydrodynamic, acoustic, thermal, piecoelectrically vibrating membrane and impellers [77, 78]) to induce stochastic disturbances of sample-carrying buffer to speed up mixing. Although active mixing is faster and more effective, it typically involves more complicated fabrication processes which can be difficult to integrate with the other functions needed for a complete LoC.

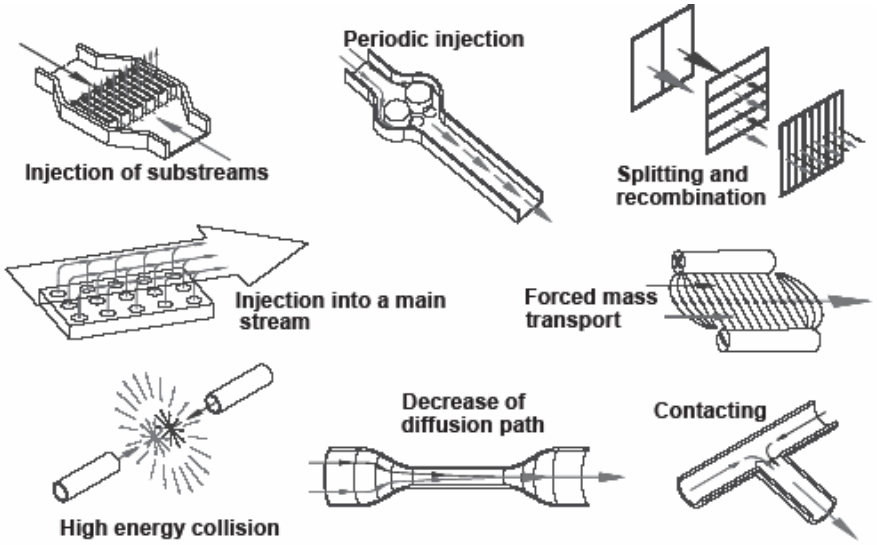

Figure 2-5. Mixing techniques used in microfluidic LoC systems [77].

A variety of microreactors for both inorganic and organic syntheses have been successfully demonstrated in combinatorial chemistry, drug discovery and fundamental gene study. Depending on the synthesis contents and applications, the on-chip reactions most commonly performed are chemical, enzymatic, PCR, immunoassay, post- and before-column labeling reactions [79]. The reactor material, structure and fabrication process are also distinctly different [80, 81]. In some circumstances, appropriate activations, such as catalyst, heat or light can be integrated onto chips or exerted from the outside to initiate or expedite the reaction [79, 80].

Separation-based analysis

Eventually, reaction products need to be separated and analyzed. One of the most effective and prevalent on-chip analysis approaches is electrophoresis. As most biomolecules in aqueous buffer are electrically charged, electrokinetic LoCs integrating electrophoresis can be readily operated by adjusting reservoir voltages. Simply speaking, electrophoresis is the movement of charged species under an electric field. Biomolecules (e.g., different amino acids or DNA) with different charges or sizes move at different speeds and can be separated (Section 2.2.1). As supporting platforms, glass and quartz are the most widely used substrate materials attributed to their stable electroosmotic flow characteristics, favorable transparency for optical detection and reliable electrical insulation. Currently, electrophoresis-based analysis is mostly applied in protein analysis, DNA studies and immunoassay diagnostics, which will be described in detail in the next subsection.

2.1.2.3 Applications of Integrated LoC Systems Based on Continuous-Flow Microfluidics

A total analytical LoC integrates both synthesis and analysis functions to improve its throughput and minimize the manual effort and associated errors. Presently, the dominant application fields of integrated LoC systems based on continuous-flow microfluidics include DNA and protein analysis and immunoassays.

Integrated LoCs for DNA analysis

Since the first electrophoresis microchip was invented [82], DNA analysis (e.g., PCR reaction, DNA sequencing) has attracted significant attention in LoC community and continues to be on the active area [83]. A huge amount of research has been directed towards achieving high-throughput electrophoresis in a single chip [15, 84] or combining

capillary electrophoresis with other functions, such as restriction enzyme reactions [85, 86], electrochemical detections [87, 88], injection [89] and PCR [90-93] to attain a fully integrated and independent device. Figure 1-1 shows the schematic of a 384-channel capillary array electrophoresis bioanalyzer for genotyping [15]. In such a system, all DNA samples can be injected, separated and detected in less than 325 seconds. Ref. [94] also reports a miniature and highly integrated device for genetic assays. The multiple steps of extracting and concentrating nucleic acids, PCR amplification, enzymatic reactions, labeling, dilution and hybridization are all automated.

Integrated LoCs for protein analysis

Relatively speaking, the development of LoCs for protein analysis is less mature than for DNA. Additional technology and effort that integrate the protein analysis processes (e.g., extraction, separation, digestion and mass spectrometry) [95] are needed.

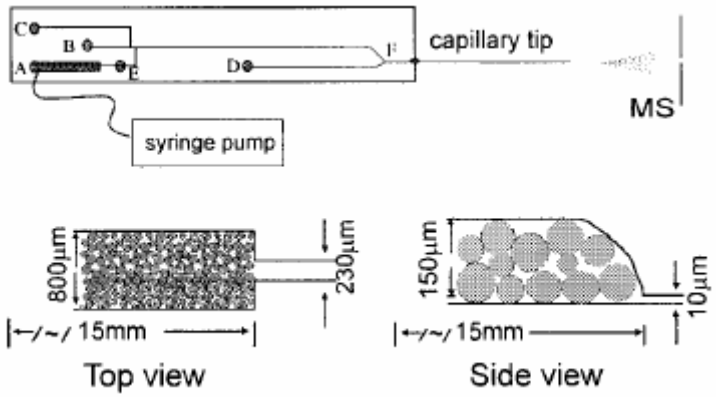

Figure 2-6. Schematic of a protein analysis microchip integrating an enzymatic reaction bed and an electrospray ionization interface to mass spectrometer and electrophoresis [96].

Recently, several highly integrated LoCs have been successfully demonstrated in this area. Ref. [97] reports integrating the microdialysis membrane into a protein analysis chip for desalting and purifying samples. Isoelectric focusing has also been employed in both glass [98, 99] and plastic [100, 101] microfluidic devices for protein purification and

separation. To speed up digestion efficiency, a membrane reactor [102], a porous surface [103] and ensembles of beads [96] with immobilized enzyme have been fabricated and integrated on-chip. Figure 2-6 shows an integrated protein analysis microchip, in which the integrated bead-based enzymatic reaction bed, micro-fabricated electrospray ionization interface (ESI) to mass spectrometer and electrophoresis are all integrated [96].

Integrated LoCs for immunoassay analysis

An important application area for immunoassay microchips is clinical diagnostics, where a large number of repetitive, labor- and time-intensive steps are involved. Therefore, the integrated biofluidic LoCs with a high-degree of automation and fast analysis are particularly suited to this application. Early immunoassay analysis focused on on-chip electrophoretic separation, while time-consuming mixing, incubation and reaction were performed off-chip [104-106]. The first immunoassay microchip combining all steps of mixing, incubation, reaction, injection, separation and detection was achieved by Chiem *et al* [16]. Later, six parallel manifolds of integrated immunoassay LoC systems were fabricated in a microfluidic wafer and operated simultaneously [17]. In addition, an immunoassay microchip with integrated pre-column reactions and electrophoretic separations was also developed [107]. In addition to homogeneous (solution phase) immunoassay reactions, heterogeneous (surface phase) immunoassay reactions have also been realized in Refs. [108-111], in which efficient bead-based reactors precoated with antibody are exploited.

From the survey, it can be found that electroosmotic flow, using electric field and electrokinetic injection to generate and control bulk flow with minimal analyte dispersion, is most preferred in biofluidic LoC systems attributed to its prominent amenability to electrophoretic separation and accurate flow control (~1 % accuracy) in the nanoliters-per-

second domain. Therefore, electrokinetic flow-based fluid handling, sample preconditioning, mixing and reaction, and separation will be the primary modeling focus in this thesis. Specific efforts will be directed toward the electrophoretic separation microchips and laminar diffusion-based micromixers as they are commonly used in LoCs. A preliminary study of competitive immunoassay reaction will also be presented to demonstrate the capability to integrate these models for system-level simulation of an integrated LoC. Finally, the electrokinetic mixing model will be extended to pressure driven flow to propose and design a novel sample preconditioning device, the concentration gradient generator. Figure 2-7 illustrates the categorization of LoC devices and those investigated by this thesis (underlined terms).

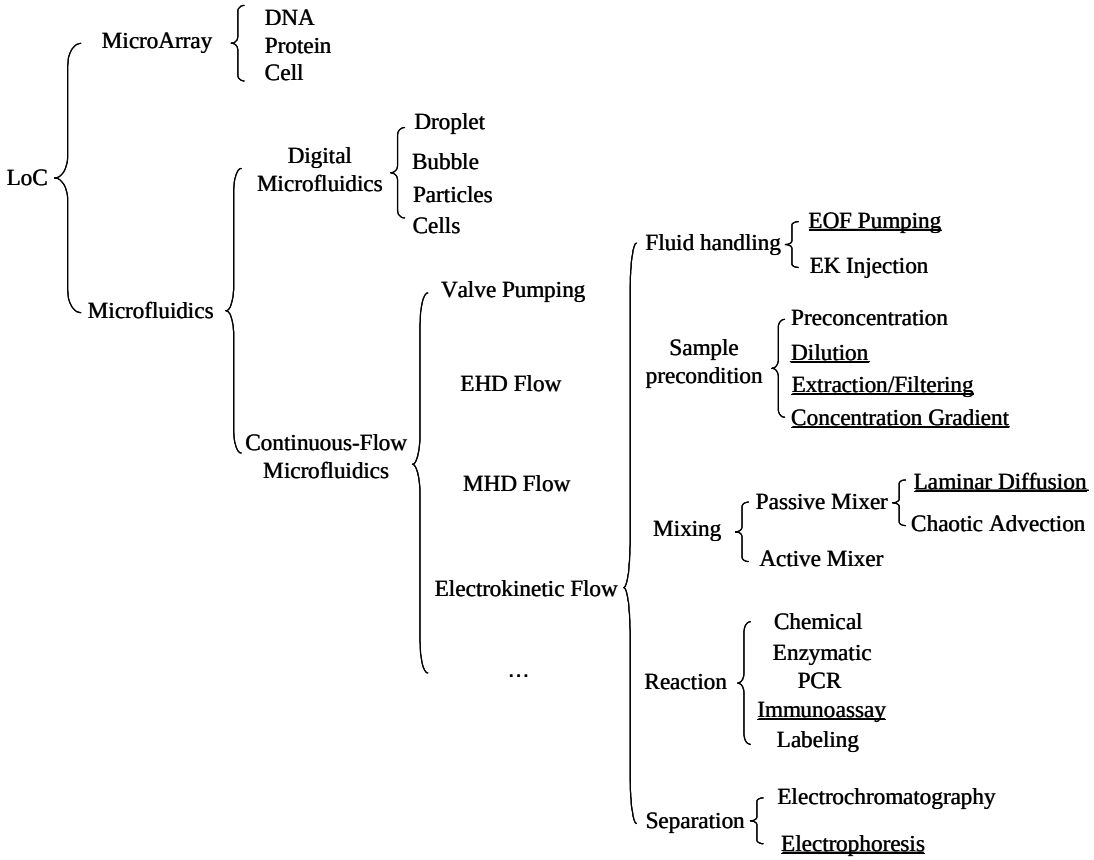

Figure 2-7. Categorization of lab-on-a-chip devices.

2.2 Theoretical Background

This section describes the theoretical fundamentals needed to develop the models and simulation capabilities in the following chapters.

2.2.1 Electrokinetics

Electrokinetic (EK) transport includes four phenomena: electroosmosis, electrophoresis, streaming potential and sedimentation potential [112]. Among them, electroosmosis and electrophoresis have found extensive applications in biofluidic LoC systems. Electroosmosis, or electroosmotic flow (EOF), refers to the bulk movement of liquid past a stationary charged solid surface (e.g. a capillary or a microchannel) driven by an externally applied electric field. Electrophoresis is the movement of a charged particle submerged into stationary liquid under an external electric field. Since both transport mechanisms arise from an electric double layer (EDL) [112, 113], a brief introduction to EDL is given first.

2.2.1.1 Electric Double Layer (EDL)

In general, when a liquid solution comes into contact with a solid surface, the surface may become electrically charged by several mechanisms. Particularly, in the case of aqueous electrolytic solutions interfacing with glass microchannels, the silanol groups on the glass surface deprotonate [56],

$$SiOH \leftrightarrow SiO^{-} + H^{+} \tag{2.1}$$

The extent of deprotonation depends on the local pH value and the ion concentration of the solution. The resulting negatively charged surface attracts positively charged ions (counter-ions) in the solution, but repels the ions of the like-charge (co-ions). In the region close to the wall, ions distribute in two parallel layers: the Stern layer and the Guoy-Chapman layer [112, 113]. The immobile counter-ions adsorbed to the wall form the Stern layer, while the Guoy-Chapman layer is comprised of the diffusive and mobile counter-

and co-ions that can be moved upon the application of an external electric field. The shear plane separating the Stern and Guoy-Chapman layers is the location of the fluid motion's no-slip condition. The potential at the shear plane is called the zeta potential ζ. A sketch of the induced potential in the EDL is shown in Figure 2-8. The magnitude of the potential decays away from the wall, and the bulk liquid far from the wall is assumed net neutral.

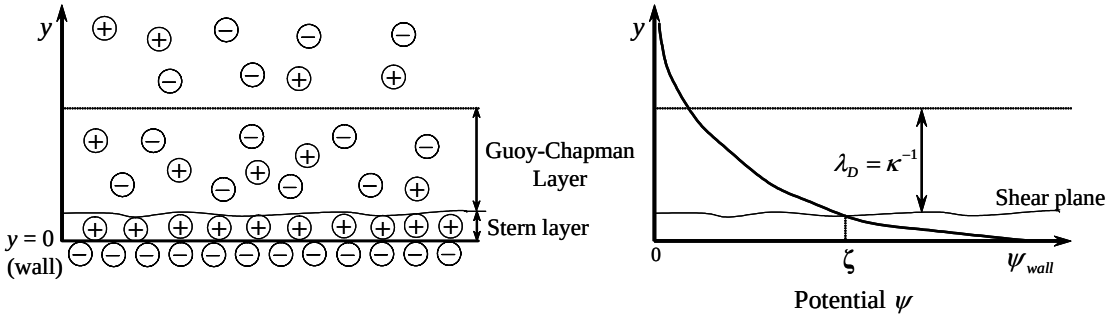

Figure 2-8. Sketch of the Electric Double Layer (EDL) and zeta potential ζ [56].

At equilibrium, the concentrations c_i of both counter-ions and co-ions in the Guoy-Chapman layer are governed by a Boltzmann distribution [112, 113], resulting from the balance between electrostatic force and thermal diffusion, which is shown in Eq. (2.2),

$$c_i = c_{\infty,i} \exp\left[\frac{-Z_i F \psi}{R_g T}\right] \tag{2.2}$$

The electrical charge density ρ in the Guoy-Chapman layer is given by

$$\rho = \sum_i Z_i F c_i \tag{2.3}$$

where Z_i is the valence number of the i^{th} specie, $c_{\infty,i}$ the concentration of the i^{th} species in the bulk solution, F Faraday's constant, R_g the ideal gas constant, T the absolute temperature and ψ the electric potential induced by the EDL and described by Poisson's equation in Eq. (2.4),

$$\nabla^2\psi = -\frac{\rho}{\boldsymbol{\varepsilon}} \tag{2.4}$$

where $\boldsymbol{\varepsilon}$ is the electrical permittivity of the liquid solution within the Guoy-Chapman layer.

Substituting Eqs. (2.2) and (2.3) into (2.4) and assuming an aqueous and symmetric univalent electrolytic solution yields,

$$\nabla^2\psi = \frac{2FZc_\infty}{\boldsymbol{\varepsilon}}\sinh\left(\frac{-ZF\psi}{R_gT}\right) \tag{2.5}$$

The detailed solution to Eq. (2.5) is available [113, 114]. However, to estimate the Guoy-Chapman layer thickness, also known as the Debye length λ_D, the Debye-Hückel approximation is invoked by assuming $\frac{-ZF\psi}{R_gT} \ll 1$ (i.e., $\psi \leq 25$ mV). Hence, $\sinh\left(-ZF\psi/R_gT\right) \approx -ZF\psi/R_gT$ and Eq. (2.5) can be recast as

$$\nabla^2\psi = \frac{1}{\lambda_D^2}\psi \tag{2.6}$$

and

$$\lambda_D = \left(\frac{\boldsymbol{\varepsilon}R_gT}{2F^2Z^2c_\infty}\right)^{\frac{1}{2}} \tag{2.7}$$

λ_D can be treated as an approximate thickness of the entire EDL due to the negligible Stern layer (usually only an ion diameter thick). Because the electrolytic solution (or called buffer solution) in microfluidic systems usually is aqueous, it has the similar properties as water. Given constants: $R_g = 8.314$ J kg^{-1}K^{-1}, $F = 96485$ C mol^{-1}, $\boldsymbol{\varepsilon} = 7.08\times10^{-10}$ CV^{-1}m^{-1} and $T = 298$ K, Table 2-1 shows the typical values of λ_D for several different electrolyte concentrations and valences. It can be seen that the Debye length typically ranges from

0.1~10 nm and is negligible compared with the transverse microchannel dimensions in biofluidic LoC devices (10~100 μm).

Table 2-1. Debye length λ_D for typical electrolytic buffer solutions [113]

	Symmetrical electrolyte		**Asymmetrical electrolyte**	
Molarity	$Z_+ : Z_-$	λ_D (m)	$Z_+ : Z_-$	λ_D (m)
0.001	1:1	9.61×10^{-9}	1:2, 2:1	5.56×10^{-9}
	2:2	4.81×10^{-9}	3:1, 1:3	3.93×10^{-9}
	3:3	3.20×10^{-9}	2:3, 3:2	2.49×10^{-9}
0.01	1:1	3.04×10^{-9}	1:2, 2:1	1.76×10^{-9}
	2:2	1.52×10^{-9}	3:1, 1:3	1.24×10^{-9}
	3:3	1.01×10^{-9}	2:3, 3:2	7.87×10^{-10}
0.1	1:1	9.61×10^{-10}	1:2, 2:1	5.56×10^{-10}
	2:2	4.81×10^{-10}	3:1, 1:3	3.93×10^{-10}
	3:3	3.20×10^{-10}	2:3, 3:2	2.49×10^{-10}

2.2.1.2 Electroosmosis

When an electric field is applied axially along a microchannel filled with a buffer solution, the counter-ions with a high concentration in the double layer feel a force and begin to move, which dominates any opposing drag caused by co-ions. Therefore, the net force drags all the liquid within the channel and quickly forms flow as shown in Figure 2-9, where *y* is the coordinate normal to the channel wall and *E* is the externally applied electric field in the axial *x*-direction.

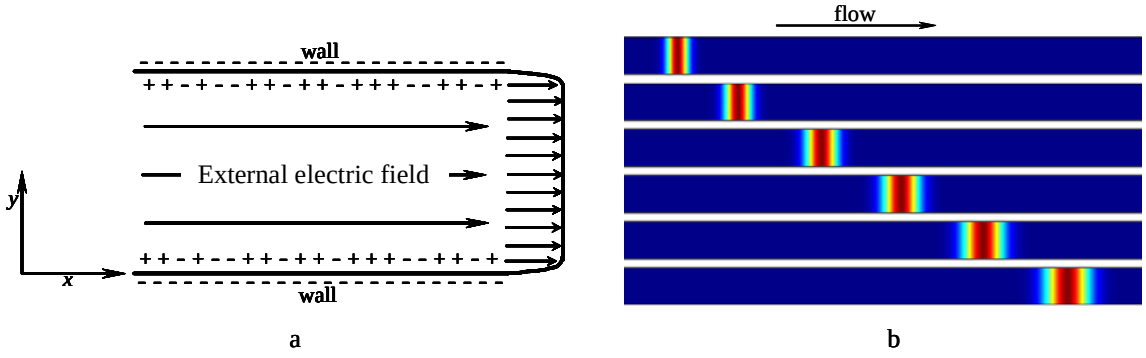

Figure 2-9. (a) A plug velocity profile of EOF. (b) A species band driven by EOF (numerical plots).

The velocity field around the channel wall can be assumed steady state and close to a half-infinite plane. The Navier-Stokes equation governing the electroosmotic flow velocity u (without considering pressure driven flow) is then given by

$$\eta \frac{d^2u}{dy^2} = -\rho E \tag{2.8}$$

where η is the dynamic viscosity of the buffer solution, u is independent of x coordinate if the applied E is axially uniform. As described above, the Debye length λ_D is rather small compared with the transverse microchannel dimensions (10~100 μm), thus boundary conditions used to solve Eq. (2.8) are

$$\begin{matrix} \frac{du}{dy} \to 0 \\ u \to 0 \end{matrix} \text{ and } \begin{matrix} \frac{d\psi}{dy} \to 0 \\ \psi \to \zeta \end{matrix} \text{ as } \begin{matrix} y \to \infty \\ y \to 0 \end{matrix} \tag{2.9}$$

Substituting Eq. (2.4) into Eq. (2.8) and then integrating Eq. (2.8) twice yields,

$$u = \frac{\varepsilon \zeta E}{\eta} = \mu_{eof} E \tag{2.10}$$

Eq. (2.10) is known as Helmholtz-Smoluchowski equation and shows that the velocity profile of EOF is plug-shaped, provided the Debye length λ_D is small. This is confirmed by Figure 2-9b where a transversely uniform concentration profile of a species band driven by electrokinetic flow is observed. An EOF mobility μ_{eof}, the ratio of the buffer flow velocity to the applied electric field, is also defined, which is dictated by the buffer properties (ε and η) as well as the interaction between buffer solutions and channel walls (ζ).

2.2.1.3 Electrophoresis

When charged particles are submerged into an electrolytic buffer solution, they will attract the counter-ions and repel the co-ions in the buffer to form the EDL just like the

electroosmosis description (Section 2.2.1.2). However, different from electroosmosis, in the presence of an applied electric field, a net force is exerted on the suspended particle and causes it to move. In this subsection, the velocity of the electrophoretic motion will be analyzed.

Because of the wide range of particle sizes, two limiting cases are taken into account: $\lambda_D \gg a$ and $\lambda_D \ll a$, where a is the radius of the charged particle.

When $\lambda_D \gg a$, the particle can be treated as a point charge in an unperturbed electric field strength E and the electrostatic and Stokes drag forces are balanced, leading to

$$Q_s E = 6\pi \eta u a \tag{2.11}$$

where Q_s is the total surface charge around the particle and can be found from the conservation of electric charges [113],

$$Q_s = 4\pi a \varepsilon \zeta \tag{2.12}$$

Combining Eqs. (2.11) and (2.12) yields

$$u = \frac{2}{3}\frac{\varepsilon \zeta E}{\eta} = \mu_{ep} E \tag{2.13}$$

Eq. (2.13) is known as Hückel equation, and an electrophoretic mobility μ_{ep}, the ratio of the electrophoretic velocity of the charged particle to the external electric field, is also introduced. Note that ζ in Eq. (2.13) is the zeta potential in the EDL of the charged particle rather than that at the microchannel wall.

When $\lambda_D \ll a$, the particle can be considered as a half-infinite plane relative to the EDL and treated in the same way as EOF,

$$u = \frac{\varepsilon \zeta E}{\eta} = \mu_{ep} E \tag{2.14}$$

When λ_D and a are comparable, μ_{ep} varies between the two limiting cases [115].

2.2.1.4 Similarity between Electric Field and Electrokinetic Flow

It should be pointed out that Eq. (2.10) provides a very convenient means to predict the EOF velocity in straight and uniform cross-sectional microchannels from electric field. To determine EOF velocity in channels with complex geometries and cross-sections, direct solutions of coupled electric, fluidic and species transports are needed. In addition, distinctly different scales in dimensions of the EDL and microchannel lead to difficulties of numerical analysis (e.g., EDL thickness: ~ 10 nm; cross-sectional dimension of microchannel: 10 ~ 100 μm; axial dimension of microchannel: 1 mm ~ 1 cm). To address this issue, Cummings *et al.* [116] have proved that the EOF velocity uniformly parallels to the external electric field, if the following conditions are satisfied,

(1). Uniform zeta potential

(2). Thin EDL compared to microchannel dimensions

(3). Electrically insulated channel walls

(4). Uniform fluid properties

(5). Flow parallel to electric field at inlets and outlets

These conditions are fairly attainable for most EOF applications. Thus, Eq. (2.8) yields,

$$u = \mu_{eof} E\left(x, y, z\right) \tag{2.15}$$

In contrast to Eq. (2.10), Eq. (2.15) is valid for a non-uniform geometry and electric field. Only Laplacian equation governing the external electric field needs to be solved for its spatial distribution, from which the flow velocity can be explicitly obtained by Eq. (2.15). Another useful observation from Eq. (2.15) is that the EOF flow rate q of the buffer solution is linearly proportional to the electric current I through the channel and given by,

$$q = \int_{A_r} u \cdot dA_r = \mu_{eof} \int_{A_r} E \cdot dA_r = \frac{\mu_{eof}}{\sigma} I \tag{2.16}$$

where A_r is the channel's cross-sectional area and σ is the electric conductivity of the buffer solution and treated as a constant within a single chip.

2.2.2 Composition and Operation of Lab-on-a-Chip Systems

As described in Section 2.1.2, a variety of LoCs with diverse chemical and biological applications have been demonstrated to date. A canonical LoC integrating multiple functions (e.g., micromixing, reaction, injection and separation) is shown in Figure 2-10. Its operation involves typical processes from a biochemical lab: synthesis and analysis. In the first phase, electrical voltages are applied at reservoirs 1, 2, 3 and 4 with 5 grounded. The sample is moved by EK flow arising from the electric field, diluted by the buffer solvent and mixed with the reagent or enzyme in the micromixer. The mixture then flows into the bio-chemical reactor where reaction products are produced often with the aid of external activations such as heat, light or catalyst. At the end of the reactor, appropriate voltages could be applied at reservoirs 6 and 7 to pinch and load a narrow stream of the mixture of the reaction products and unreacted samples (or called analyte hereon) into the injector. Usually samples and reagents are continuously supplied from reservoirs; therefore concentrations of all samples, reagents and products in the mixer and reactor at this phase are in steady state. This completes the synthesis operation.

In the second phase, the voltage drop is switched on reservoirs 6 and 7 with the others left floating. Thus, a band of the analyte is injected into the separation channel for further analysis (in addition to the cross injection shown in Figure 2-10, other injection schemes are also available [117]). Because the analyte is comprised of biological species/molecules (e.g., DNA or amino acids) with different electric charges and sizes, they move at different

speeds and eventually can be separated by electrophoresis [118] during their migration through the channel. In this phase, the species bands broaden due to molecular diffusion and other dispersion sources; therefore transient evolution of the band concentration and its impact on separation performance are of prime importance.

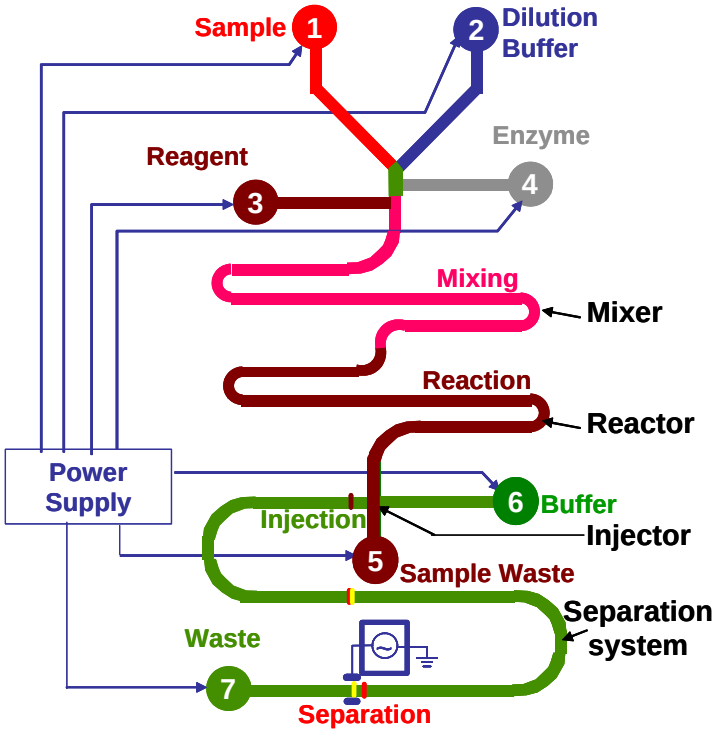

Figure 2-10. Sketch of composition and operation of a canonical lab-on-a-chip system consisting of four subsystems: micromixer, reactor, injector and separator.

2.3 LoC Modeling and Simulation Methodologies

In this section, prevalent modeling and simulation approaches for biofluidic LoC design are reviewed and their individual drawbacks are examined.

2.3.1 Numerical Modeling and Simulation

Prior to the work described in this thesis, the detailed numerical simulation using Finite Volume Method (FVM) or Finite Element Method (FEM) was the only available way to obtain desired modeling accuracy. Commercial FVM and FEM tools commonly used by the LoC design community include Fluent [12], CFX [9], CFD-ACE+ [119, 120],

FLOW3D [11], CoventorWare [45], ANSYS [121] and FEMLAB [122, 123]. Generally, these methods first construct the geometric solid model of the device and mesh the model. Then the system matrices based on the discretization of the continuum multi-physics are solved using iterative or direct approaches with appropriate boundary and initial conditions. Given sufficiently fine grids, accurate simulations on coupled multi-physics can be obtained. However, as discussed in Section 1.2, their demanding CPU times and memory requirements, as well as the inflexibility of geometric variation are prohibitive for system-level design of complex LoCs.

2.3.2 Reduced Order Macromodels

To overcome the disadvantages of conventional FVM and FEM simulations, a reduced-order modeling technique has been proposed to reduce the degrees of freedom of the system matrices and create macromodels for the devices. Reduced order macromodels have to be built from a series of numerical simulations and stitched together for an overall system simulation [120, 124]. The resulting macromodels in this bottom-up approach to design are specific to the geometry that was numerically simulated. Thus the macromodels have to be regenerated whenever the geometry is perturbed for design optimization. This leads to unacceptably long design iterations and hinders the industrial application of this approach to LoC design. More recently, parameterized reduced-modeling techniques have also been studied. Mikulchenko *et al.* [125] and Magargle *et al.* [126] applied neural network (NN) theory and respectively developed a microflow sensor model and an electrokinetic injector model, which are parameterized by geometrical and operational parameters (e.g., electric field and flow velocity) and can be used in design optimization. However, this modeling approach is primarily based on ‘learning’ of data from repetitive

numerical simulations, limiting its usefulness in the case that involves a large number of input and output parameters. For example, as shown in the below, to predict sample concentration profiles propagated within micromixers, the converging intersection at least requires twenty input (for two incoming streams) and ten output Fourier cosine coefficients. Numerical simulations providing sufficient data for network learning becomes intractable.

An additional limitation of the parameterized reduced-order models is that they do not provide adequate and direct insight into the functional behavior of the element and system. For example, within a mixing channel, it can be readily observed that widthwise sample concentration non-uniformity decays at an exponential rate from analytical expression, while the parameterized reduced-order model has to calculate a set of concentration profiles (or mixing residuals) along the channel's axial direction to reach this observation.

2.3.3 Behavioral Modeling and System Simulation

To address these issues, efficient behavioral modeling and system (circuit) level simulation approaches have attracted a lot of attention lately. Qiao *et al.* [127] proposed a compact model to evaluate the flow rate and pressure distribution of both electrokinetic and pressure driven flow within the network and capture the effect of the non-uniform zeta potential at the channel wall. Xuan *et al.* [128] later presented a fully analytical model to capture the effects of the channel size and surface electrokinetic properties on microfluidic characteristics using phenomenological coefficients. Both papers focus on bulk fluid flow in microchannels and ignore the details of sample transport that often become the limiting issues in LoC design. Coventor's circuit level MEMS and microfluidics modeling and simulation environment, ARCHITECT [124, 129], includes an electrokinetic library with simple models for injectors, straight channels and turns that can model sample transport in

electrophoretic separation. But it still requires users to extract dispersion parameters (macromodels) from full numerical simulations and does not allow design of general-shaped electrophoresis channels where the dispersion interaction between turns can be very strong, significantly limiting its usefulness [130]. Zhang *et al.* [131] developed an integrated modeling and simulation environment for microfluidic systems in SystemC, which was used to evaluate and compare the performance of continuous-flow and droplet based microfluidic systems on a polymerase chain reaction (PCR). Like the Coventor solution, the focus is at the system level, with an assumption that reduced order models from detailed numerical simulations or experimental data would become available to populate the system simulation. Most recently, Chatterjee *et al.* [132] combined circuit and device models to analyze fluidic transport, chemical reaction, reagent mixing as well as separation in integrated microfluidic systems. These models exploit an analogy between fluidic and sample transport, effectively reducing the governing partial differential equations into ordinary differential equations or algebraic equations, leading to fast simulation speed. However, this speedup is at the cost of ignoring local geometry induced non-idealities of sample transport.

2.4 Terminology

Table 2-2 lists the commonly used symbols for multi-physics models described in this thesis. Slight local variations are still possible and will be specifically noted where they occur. Since the top-down modeling and simulation methodology of LoCs is analogous to MEMS and SoC designs, the terms from these communities are used. A glossary (Table 2-3) is also included to accommodate readers with different backgrounds (e.g., mechanical, chemical and biomedical engineering).

Table 2-2. Nomenclature

Variables

A	maximum concentration of species band, M
c	concentration of species band, M
c_m	channel width-averaged concentration of species band, M
c_p	the p^{th} moment of the concentration in a longitudinal filament of the species band
d_n	mixing concentration coefficients at outlet
d_m	mixing concentration coefficients at inlet
D	Molecular diffusivity of species, $m^2\ s^{-1}$
E	electric field strength, $V\ cm^{-1}$
F	Faraday's constant, $C\ mol^{-1}$
h	depth of microchannels, μm
I	electric current through buffer, A
K	effective Joule heating dispersion coefficient, $m^2\ s^{-1}$
L	length of microchannels, μm
L_{det}	detector path length, μm
m_p	the p^{th} moment of the widthwise average concentration of species band
M	average relative error, %
N_i	internal node of converging and diverging intersections and injectors
N	plate number of separation
P	pressure, Pa
Pe	Peclet number
q	volumetric flow rate of the buffer, $m^3\ s^{-1}$
$\dot{q}$	volumetric heat generation, $W\ m^{-3}$
Q	index of mixing residual of normalized sample concentration profile
Q_c	index of profile discrepancy
Q_s	total surface charge around the particle, C
r_c	mean radius of turn separation channels, μm
R	resistance of microfluidic elements, ohm
R_g	ideal gas constant, $J\ kg^{-1}\ K^{-1}$
s	flow ratio, combing or splitting position
S_{nm}	skew coefficients of species band
t	separation time, s
T	temperature, K
Δt	residence time of the centroid of species bands within channels, s
u	electrokinetic velocity of species band, $m\ s^{-1}$
U	widthwise average electrokinetic velocity of species band, $m\ s^{-1}$
v	actual electrokinetic velocity of species band (separation), $m\ s^{-1}$
V	voltage at element terminals or reservoirs, V
w	width of microchannels, μm
x	axial coordinate
y	widthwise coordinate
z	depthwise coordinate
Z	valence number of the ion species
α	buffer's temperature coefficient of viscosity, K^{-1}
ε	Joule heating coefficient
$\boldsymbol{\varepsilon}$	electrical permittivity of the solution, $C\ V^{-1}m^{-1}$
ϕ	normalized excess temperature
γ	factor of geometric effect on mixing or shape factor for Joule heating dispersion
φ	included angle of turn channels, rad
λ_D	Debye length of the electrical double layer, m
χ	normalized electrokinetic velocity of species band relative to the average
ρ	electrical charge density, $C\ m^{-3}$
η	normalized widthwise coordinate

η	viscosity of water, Pa s
μ	mobility of sample/species, $m^2\ V^{-1}s^{-1}$
θ	excess temperature, K
σ^2	variance of species band, m^2
σ	electric conductivity of buffer, $S\ m^{-1}$
τ	dimensionless separation time
τ_R	dimensionless residence time
ξ	normalized axial coordinate
ψ	electric potential in electrical double layer, V
ζ	normalized depthwise coordinate
ζ	zeta potential, V

Superscripts and Subscripts

eof	electroosmotic component
ep	electrophoretic component
l	quantities at left inlet or left outlet
r	quantities at right inlet or right outlet
in	quantities at inlet
out	quantities at outlet
det	quantities at detector

Table 2-3. Glossary

Behavioral model	A model that describes the physical behavior in the element by formulating the relation between the variables at the interface connection terminals of the element.
Bus	A collection of signals with same discipline sharing a common base name. A bus is represented by this base name followed with a vector expression.
Discipline	A user-defined binding of potential and flow natures and other attributes of a signal which traverses through the system hierarchy.
Element	The fundamental unit within a system, which encapsulates behavior and structure.
Hardware description language	A language from a class of computer languages for formal description of electronic circuits. It can describe the circuit's operation, its design, and tests to verify its operation by means of simulation.
Hierarchical system	A system in which the components are also systems.
Netlist	A list describes the interconnectivity among elements in a circuit design.
Pin	Represents the connection point for a single signal or multiple signals of the terminal.
Schematic	A representation containing connectivity data and graphics that describe the logical views of a circuit design.
Wire	A line that connects a pin and an instance to represent a net in a schematic. When you draw a wire between a pin and an instance, you create a net.

Chapter 3 Behavioral Modeling and Schematic Simulation Methodology

To address the LoC design's needs mentioned in Section 1.2, this chapter introduces a top-down behavioral modeling and schematic simulation methodology. Several key issues, including system hierarchy, schematic representation and behavioral modeling will be discussed in detail.

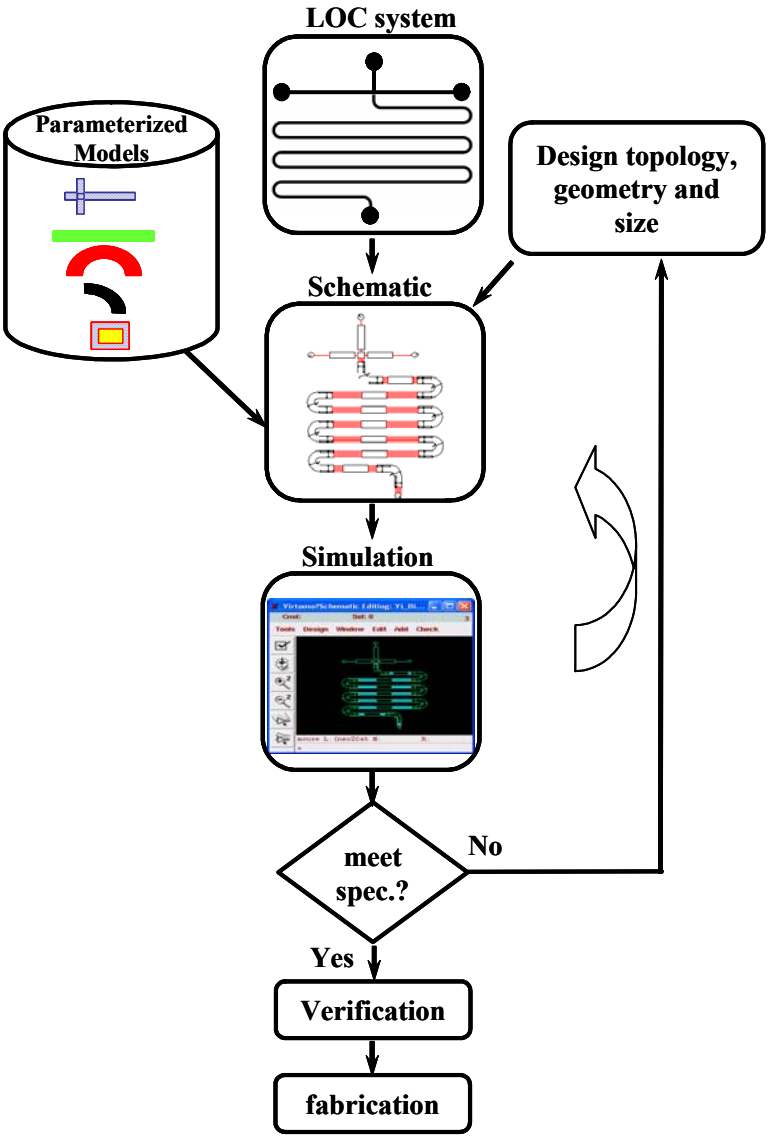

Figure 3-1. Flow chart of the top-down design methodology of biofluidic LoC systems.

Unlike the bottom-up design methodology, where reduced order models are obtained from numerical simulations, the use of parameterized models enables a top-down design methodology similar to SoC [133] and MEMS [134]. The top-down methodology begins with a conceptual schematic representation of the system. The schematic is composed of element instances of behavioral models stored in the library. The element instances are connected according to device topology. A netlist file (a readable text file) that describes this system network is then generated automatically and fed to the simulator for performance evaluation. If the design does not meet the desired performance goals, the designer can either modify the system topology, the element sizes or adjust the operating voltages and re-simulate. An iterative design update and simulation process leads to optimal design. As the schematic simulation uses a model of the actual system, the numerical simulation is employed to verify that the design goals have been reached before the design layout is finally generated and sent to fabrication (Figure 3-1).

In this chapter, the development of the behavioral models and construction of the system-level simulation schematic will be described.

3.1 Schematic Representation

In this section, the LoC geometrical and functional hierarchy, as well as the decomposition of a complex LoC into commonly used biofluidic elements will be introduced first. Then, pins and analog wiring buses that link these elements together will be defined.

3.1.1 System Hierarchy

The schematic representation of the biofluidic LoC is based on its functional and geometrical hierarchy. Functional decomposition breaks down the fully-integrated LoC

(e.g., Figure 2-10) by function into separate subsystems (e.g., mixing and separation in Figure 3-2b and Figure 3-2c). Geometrical decomposition of each subsystem further breaks down the design into a network of elements with simple geometries (e.g., straight and turn channels in Figure 3-2d and Figure 3-2e). The reason for such decomposition is to enable the development of a closed-form and parameterized element model that can be reused in a top-down manner to represent complex chip designs of various topologies, element sizes and material properties.

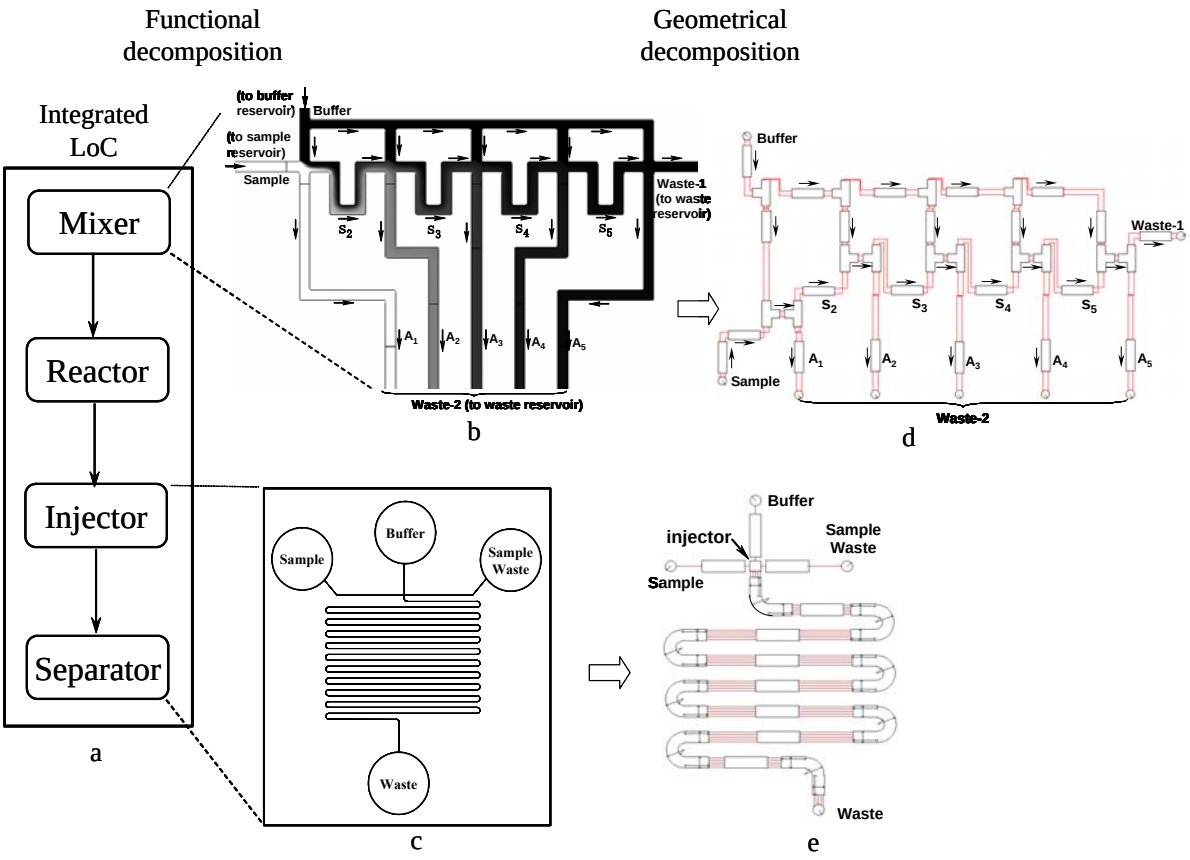

Figure 3-2. (a) Structure of an integrated LoC system (see Figure 2-10). (b) An EK serial mixing network [71]. (c) A serpentine electrophoretic separation microchip [118]. (d) Hierarchical schematic representation of the serial mixer. The network is broken down into reservoirs, mixing channels, converging and diverging intersections. (e) Schematic representation of the serpentine separation microchip. It is decomposed into reservoirs, injector, straight channels, 180° turns and 90° elbows.

Figure 3-2b illustrates a complex EK serial mixing functional subsystem [71]. Its network consists of reservoirs, mixing channels, T- and cross-intersections. The sample is released and collected by the reservoirs at the extreme ends of the network. Within the cross intersection, a portion of the input sample is shunted to channels A1−A5 and the rest continues along the flow direction for further dilution. Repeating this unit cell in series leads to an array of continuously diluted sample concentrations in channels A1−A5 that can be used for parallel bio-chemical analysis and titration tests. Variations of sample concentrations are represented by grey levels from numerical simulation in Figure 3-2b. For the system-level simulation (Figure 3-2d), the serial mixer is represented as a network of mixing elements composed of microchannels, converging intersections and diverging intersections (note that the double-input and double-output cross-intersection is modeled as a combination of the converging and diverging intersections). Figure 3-2c shows a serpentine electrophoretic separation microchip, which is similarly decomposed into a set of elements including reservoirs, injector, straight channels, 180° turns and 90° elbows (Figure 3-2e). The serpentine topology is captured by wiring between the elements. The same elements can be reused to describe alternate LoC topologies as will be discussed later.

3.1.2 Connection Pins

In the schematic, the element connection terminals are represented by groups of pins. Each pin defines the state of electric and biofluidic signal at the element terminals. Pins of the adjacent elements are then linked by wires to enable communication of the state between these elements. Therefore, pin definition affects both schematic composition and behavioral modeling of the elements. There are two types of pins defined in the network. One is the electrical pin at the element terminals. This type of pin is independent of the

function achieved by the LoC and is present in all elements. It describes the voltage at the pin and the electrical current flowing between every pair of the element terminals. The second type of pin captures the biofluidic state of the sample/species at the element terminals. The details of the information that need to be captured for complete definition of the biofluidic state depend on the function of the network. This thesis primarily focuses on two types of biofluidic networks, electrokinetic micromixers and electrophoretic separators (Pins for the injector and reactor behavioral models will be discussed in Chapter 7).

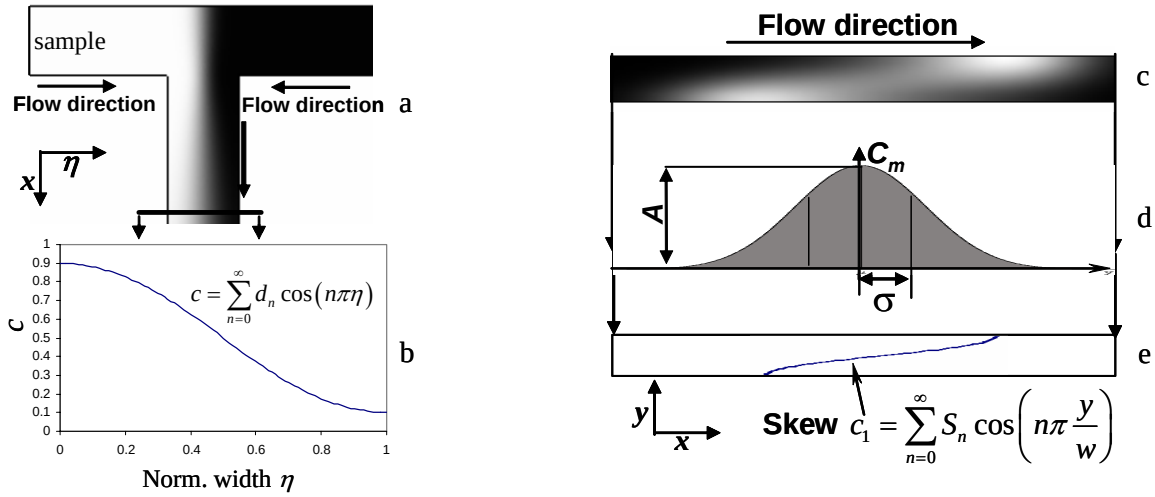

Figure 3-3. (a-b) Biofluidic pin definition for a micromixer. The pin is defined to convey the concentration coefficients-Fourier cosine coefficients (d_n) of a sample concentration profile along the channel width. (c-e) Biofluidic pin definition for an electrophoretic separation microchip, which includes arrival (or separation) time of the band (t), variance (σ^2), skew coefficients (S_n) as well as the amplitude (A).

Within the micromixer, different samples or reagents driven by EK flow mix with each other and their concentrations are in steady-state provided that there is a continuous supply from the inlet reservoirs. The sample concentration profile c as a function of the normalized widthwise position η of the channel describes the biofluidic state at the element terminals and reflects effects of geometry and properties on mixing performance in this network (Figure 3-3a and Figure 3-3b), where $\eta = y/w$ ($0 \le \eta \le 1$), w and y are the width and

widthwise position of the mixing elements respectively. The concentration profile can be captured as a Fourier series. Due to the normalization, only the series coefficients need to be communicated between the elements. Therefore, the biofluidic pin is defined as a vector of the Fourier cosine series coefficients $\{d_n\}$ of the widthwise concentration profile. The reason for such a choice is attributed to the fact that the Fourier cosine series is the eigen-function of the convection-diffusion equation governing the sample transport, given insulation conditions at channel walls and normalized widthwise position from 0 to 1.

For the electrophoretic separator, the injected species bands move through the microchannel accompanied by band-spreading caused by dispersion (e.g., molecular diffusion and turn dispersion [135]). This band spreading adversely affects separation performance by reducing the detectability and separation resolution of the species bands. Therefore, the state associated with the species band shape, such as the width of the band, skew and amplitude (Figure 3-3c), as well as the time at which the band reaches the element terminals. Specifically, the concentration profile c of a skewed band is first cross-sectionally averaged, yielding a distribution of the average concentration c_m in the EK flow direction, as shown in Figure 3-3d. Thus, pins are defined in terms of the variance σ^2, the square of the standard deviation of c_m distribution in the flow direction, representing the width of the band; the Fourier cosine series coefficients $\{S_n\}$ used to reconstruct the skew c_1 (see Figure 3-3e; detailed physical interpretation of this pin definition is given in Chapter 4) caused by the non-uniform electrokinetic velocity and migration distance in turns (the Fourier cosine series is used again for the same reason as the above); the separation time (t), the moment the band's centroid reaches the element terminals; and amplitude (A), the maximum average concentration.

3.1.3 Analog Wires and Wiring Buses

The concentration profile of a sample in micromixers and the skew of a species band in separation channels are defined in terms of a vector of the Fourier cosine coefficients. For most biofluidic applications, ten terms (n = 1, 3,…19 for separation and n = 0…9 for mixing) for each sample/species are found to yield sufficient computational accuracy due to the rapid convergence of the Fourier cosine series. In addition, in practical bio-analysis, multiple species coexist in the buffer and each species requires its own set of pins for the biofluidic state, leading to several pins required at each terminal, although electrical pins are species-independent and can be shared among the species. Thus, wiring pins during schematic assembly consumes a lot of effort and is prone to error.

Table 3-1 Definition of Biofluidic Pins

Micromixing		
Bus	Pins connected	Description
d [0:29]	Concentration coefficients	*d* [0:9]: the 1st species, *d* [10:19]: the 2nd, *d* [20:29]: the 3rd
Electrophoretic Separation		
Bus	Pins connected	Description
t [0:2]	Separation time	*t*[0] for the 1st species, *t*[1] the 2nd, *t*[2] the 3rd
σ^2 [0:2]	Variance	σ^2 [0] for the 1st species, σ^2 [1] the 2nd, σ^2 [2] the 3rd
A [0:2]	Amplitude	*A* [0] for the 1st species, *A* [1] the 2nd, *A* [2] the 3rd
S [0: 30]	Skew coefficients	*S* [0]: the direction of the skew caused by the 1st turn *S* [1:10]: the 1st species *S* [11:20]: the 2nd, *S* [21:30]: the 3rd

To address this issue, analog buses are employed and the wires connecting the pins of the same discipline are grouped, resulting in only one wiring bus (concentration coefficients) and four wiring buses (separation time, variance, skew and amplitude) at the terminals of the mixing and separation elements respectively. This compact terminal

representation reduces wiring effort and lowers the probability of wiring errors. In contrast, the connection of electric pins is quite simple and only a single wire is needed to convey electric information for all species. Table 3-1 summarizes the numbering and discipline of the buses used in both micromixer and separator behavioral models, and describes implementation that supports three species. Extension to accommodate more species is straightforward.

3.2 Behavioral Models

Parameterized behavioral models are the core of system-level LoC simulation. They lump the distributed element behavior within the entire network to a limited number of terminal nodes and hence capture the multi-physical behavior of the element (this is the reason for the term "behavioral model"). The goal of behavioral modeling is to establish the functional relationship between the terminals of each element.

In this section, the Kirchhoff's law and signal flow approach that are respectively used to propagate the electric and biofluidic pin values between the elements in the network will be first described. Then the element model parameters, as well as the modeling and simulation environment will be discussed. Finally, the section concludes with an overview of the behavioral model libraries, paving the path to detailed modeling in the next chapters.

3.2.1 Kirchhoff's Law and Signal Flow Approach

The canonical LoC system (Figure 2-10) involves steady-state electrokinetic flow. Therefore, its fluidic network can be readily treated as resistor-based electric circuitry and governed by Kirchhoff's law [136] (see Section 2.2.1.4 about the similarity between the electric field and electrokinetic flow), in which the "across" and "through" variables are respectively defined as the differential voltage (ΔV) over the element terminals (or nodes)

and current (I) through the element, and related by $I = \Delta V / R$, where R is the electric resistance of the element. Applying this expression to each element yields a set of linear equations that explicitly determine the distribution of the voltage and current in the network given the reservoir voltage settings and the network of the resistance values. Therefore, the fluidic problem essentially is reduced to obtaining a behavioral model of the electrical resistance R associated with each element.

Given a unidirectional background flow, the biofluidic state (e.g., concentration and species band shape) at the downstream do not impact those at the upstream. Hence, they can be determined in terms of a directional signal flow. That is, the biofluidic pin values at an element outlet are calculated from the corresponding values at the inlet and the element's own contribution. Pin values at the outlet are assigned to those at the inlet of the next downstream element. System-level schematic simulation can then serially process each element and propagate the pin values, starting from the most upstream element. For the separation network, this is typically an injector. For the mixing network, the starting element is the sample reservoir.

3.2.2 Element Model Parameters

During iterative simulation-based design, element parameters are indispensable. They can be divided into two classes: material parameters and geometrical parameters.

Material parameters specify the user-input material properties for electro-fluidic (e.g., electric conductivity and electroosmotic mobility), thermal (e.g., thermal conductivity) and sample (e.g., molecular diffusivity and electrophoretic mobility) transport phenomena. Among them, electrokinetic (including both electroosmotic and electrophoretic) mobility and molecular diffusivity are two properties present in all element models as the sample

transport is of primary interest in this thesis. Depending on the primary phenomena being modeled, some other parameters might be needed in the model. For example, modeling of Joule heating dispersion also needs thermal conductivity and temperature coefficient of the viscosity (Chapter 5).

As mentioned previously, the proposed behavioral models are geometrically parameterized, enabling the exploration of geometrical design space in contrast to reduced order macromodels. Therefore, geometrical parameters, such as channel length, width, depth, turn radius and included angle are also involved in the behavioral model.

3.2.3 Model Libraries

Depending on multi-physics phenomena in the individual devices, contents of the behavioral model libraries will be different.

Table 3-2. An overview of model libraries of electrokinetic micromixers, electrophoretic separation microchips and electrokinetic reactors.

Electrokinetic Micromixer Library		**Electrophoretic Separation Library**	
No.	Element Model	No.	Element Model
1	Tapered straight mixing channel	1	Straight separation channel
2	180° clockwise mixing turn	2	180° clockwise separation turn
3	180° counter-clockwise mixing turn	3	180° counter-clockwise separation turn
4	90° clockwise mixing elbow	4	90° clockwise separation elbow
5	90° counter-clockwise mixing elbow	5	90° counter-clockwise separation elbow
6	Converging intersection	6	clockwise separation turn with arbitrary included angle
7	Widthwise diverging intersection	7	Counter-clockwise separation turn with arbitrary included angle
8	Depthwise diverging intersection	8	Injector
9	Sample reservoir	9	Detector
10	Waste reservoir	10	Feed channel
11	Detector	11	Sample reservoir
		12	Waste reservoir
Electrokinetic Reactor Model			
No.	Element Model		
1	Competitive immunoassay reactor		

Model libraries for the micromixers and electrophoretic separation chips are respectively developed in Chapter 4, Chapter 5 and Chapter 6 with particular focus on electrokinetic

flow and sample transport. A simplified model for competitive immunoassay reaction will be formulated as a single-element in Chapter 7. Table 3-2 summarizes the model libraries and their individual element models.

3.2.4 Design Framework

The behavioral models accounting for the multi-physical phenomena are implemented in the Cadence's integrated circuit design framework [137]. Each model has two views: Symbol and Verilog-A. The symbol view is an icon (e.g., a rectangular channel or a semi-circular turn) of the element model used to compose schematics. The governing algebraic equations or O.D.E.s of the element behavioral models are written in the analog hardware description language (aHDL), Verilog-A.

Cadence's schematic editor automatically netlists the complex topology of a biofluidic LoC system into a text file, which is then read and solved by Cadence's simulator Spectre. This integrated design process considerably reduces the design overhead and expedites the development cycles. The implementation in Cadence also enables seamless interface with other widely used commercial layout editing, verification, optimization and synthesis tools, leading to a fully integrated and independent design loop. Additionally, similar tools and solvers that can handle both signal flow and Kirchhoff's networks, such as NanoSim and HSPICE from Synopsys, ADvance MS (ADMS) from Mentor Graphics and SmartSpice from Silvaco can be also used to simulate the Verilog-A models developed in this thesis.

3.3 Summary

Behavioral modeling and schematic simulation of electrokinetic biofluidic LoC systems based on a top-down design methodology have been presented. Complex biofluidic LoCs have been functionally and geometrically decomposed into commonly used elements.

Electric and biofluidic pins, as well as analog wiring buses have been proposed to support the communication between adjacent elements. Parameterized behavioral models have been implemented in the analog hardware description language (Verilog-A), which can accurately capture the functional relationship of both electric and biofluidic state at element terminals in terms of Kirchhoff's law and directional signal flow respectively. Thus, system-level schematics of LoCs can be composed and iteratively simulated by Spectre within Cadence's design framework to evaluate the impacts of the LoC topology, element sizes and material properties on system performance.

Chapter 4 Modeling of Turn-Induced Dispersion in Electrophoretic Separation Microchips

4.1 Introduction

Electrophoretic separation microchips have been actively pursued in the past decade [138-142], and hold great promise for a wide spectrum of applications in biology, medicine and chemistry [79, 80]. By performing separations in microchannels that are integrated with other microfluidic functionalities such as sample preparation, injection, mixing, reaction and detection [79, 80], microchip electrophoresis is a key technology to enable lab-on-a-chip microsystems.

In electrophoresis channels, the molecular diffusion and other dispersion arising from the non-uniform species velocity along channel cross section distorts and broadens the species bands, leading to overlapping of species bands and a decrease in peak concentration (reducing detectability) and eventually limiting separation performance. To characterize the effects of dispersion on the resolving power of the separation chip, quantitative indices need to be defined. In additional to band variance σ^2 [135], other quantitative indices, such as plate height *H*, theoretical plate number *N* and separation resolution *SR*, are extensively used [118, 143, 144],

$$H = \frac{\sigma^2}{L} \tag{4.1}$$

$$N = \frac{L}{H} = \frac{L^2}{\sigma^2} \tag{4.2}$$

$$SR = \frac{\Delta\mu}{\mu_{av}}\sqrt{N} \tag{4.3}$$

where L is the length of the separation channel between injection and detection, $\Delta\mu$ and μ_{av} are the difference in electrokinetic mobility between the species and average electrokinetic mobility respectively. A low value of plate height H and a high value of plate number N and separation resolution SR indicate good resolving power and separation capacity achieved by the chip. From Eqs. (4.2) and (4.3), it can be inferred that electrophoretic separation channels are typically desired to be long for purposes of separating species with small differences in electrophoretic mobility (e.g., DNA) or for obtaining a high separation resolution. As it is not cost- or area-effective to fabricate long straight channels onto microchips, channels are generally folded into compact geometries such as serpentine [118, 135, 145] or spiral [144, 146] shapes. However, such compact channels require the use of circular turn segments (e.g., 90° or 180°), which induce non-uniform electric fields and migration distances and cause skew and band broadening. This is called turn dispersion.

While band broadening in a single turn is well understood and can be modeled efficiently [135, 147, 148], channels containing multiple turns are much more difficult to analyze. This complicates design as different choices of turn geometries and electrophoresis parameters may result in drastically different dispersion behavior [149]. Currently, design of compact electrophoretic separation chips with optimized geometry and performance and that are suitable for specific applications is still an art, requiring long development cycle times. Designers are forced to adopt trial-and-error approaches that involve large numbers of experimental tests and/or numerical simulations as discussed in Chapter 2. This deficiency becomes even more acute when large scale microfluidic integration is needed [6]. Hence, there is a strong need for efficient and accurate models that can be used to efficiently simulate electrophoresis in long, multi-turn compact channels.

Turn dispersion has previously been modeled analytically mainly at the element or component level. Using an empirical model, Culbertson *et al*. [135] analyzed dispersion of both small and large molecules driven by electrokinetic flow in chips containing two complementary turns, and performed a large set of experiments to measure turn-induced dispersion. They also observed that the downstream complementary turn could undo the skew caused by the upstream turn for large molecules with small diffusivities. Griffiths and Nilson [147] used analytical and numerical methods to investigate band spreading in a single constant-radius turn for electrokinetic transport. The analytical approach resulted in rigorous low- and high-Peclet number solutions and a heuristic composite model for the intermediate regime. Molho *et al*. [148] also investigated the convection-diffusion problem and then presented an analytical model of turn dispersion in a single constant-radius turn using the method of moments originally proposed by Aris [150]. The model is valid for all mass transfer regimes and for dispersion of an initially unskewed species band. At the component level, in particular for channels with a pair of complementary turns, Baidya *et al*. [130] considered an analytical formula for band skew and variance growth in inter-turn straight channels, which gives correct predictions along the channel centerline at high convection regime but otherwise exhibits noticeable errors. Molho [151] investigated species dispersion in a pair of complementary turns at the component level. A Green's function formulation was used to describe diffusive band-broadening of an initially skewed band in the inter-turn channel, while transverse diffusion in the turns was ignored. The overall variance was then found numerically. The results are thus limited to the pure-advection limit in the turns and cannot be used for channels involving multiple pairs of complementary turns. While these existing analytical or semi-analytical models provide

appropriate description of single turns, they all assume that the species band is initially uniform and unskewed (i.e., orthogonal to the channel walls), and hence are unsuitable for system-level simulations (turns at the downstream of the first turn are likely to involve non-uniform skewed bands as their input).

This chapter presents analytical models to describe species dispersion behavior in individual separation elements. These element models are based on the same simplified governing equations as previously used [147, 148] and also use the method of moments [150]. In contrast to previous work, these models are valid for species bands of general initial shape. Both electric and biofluidic pins (states) are defined at element terminals to convey the electric and band shape information to the neighboring element. Because of these features, the element models can be composed into a system-level schematic (as shown in Chapter 3) to simulate species dispersion (e.g., skew and band broadening) in the general-shaped channel. The lumped-parameter model offers orders-of-magnitude improvement in computational efficiency over full numerical simulations and allows systematic parametric studies of species dispersion for complex channel geometries (e.g., serpentine, spiral and their combinations). The efficiency and accuracy of the system simulations is validated against the experimental and numerical data of the general-shaped electrophoresis microchips that occur in practice. To our knowledge, this is the first time electrophoretic separation channel networks at this level of complexity have been accurately simulated with lumped-parameter models. Our models therefore represent a significant contribution to addressing the need for efficient and accurate simulation tools for the design of optimal electrophoretic separation microchips.

The chapter is organized as follows. Behavioral models for separation elements will be developed in Section 4.2, with a significant emphasis on straight and turn separation channels (Section 4.2.1). Behavioral models for all elements can then be wired to build a system-level simulation schematic (Section 4.3), which is then applied to practically important electrophoretic separation channels of general shape, including serpentine and spiral channels, with parametric analysis of skew effects between turns (Section 4.4) and verifications by experimental data and numerical simulations (Section 4.5). The paper concludes with a summary of the model and insights gained from the model (Section 4.6).

4.2 Behavioral Model Library

In this section, the behavioral model library for electrophoretic separation microchips will be developed, which includes elements of the straight channel, turn, injector, detector, feed channel, sample and waste reservoirs.

4.2.1 Straight Channel and Turn

In this subsection, governing equations for species dispersion in elemental separation channels are first described and reformulated in terms of spatial moments of the species concentration, and the resulting moment-based equations are solved for arbitrary initial species band's shapes to attain both distributed the behavioral models.

4.2.1.1 Governing Equations

Here, the convection-diffusion equation governing the species transport is formulated for electrophoretic separation channels: a straight channel and a segment of a constant radius microchannel (i.e., a turn). Consider electrophoresis of a charged species band in an element channel. It has uniform rectangular cross sections and its axial axis (the line connecting cross-sectional centers) is either a straight-line segment (a straight channel) or a

segment of a circular arc (a turn) in the chip plane. Let L denote the channel length and w the channel width. In the case of a turn, let the mean radius of the turn be denoted by r_c, and the included angle by φ. Hence, $L = r_c\varphi$ for a turn. It is assumed that the channel is narrow compared with its length, i.e. $w/L \ll 1$, and specifically for a turn, the width-to-radius ratio is small: $b \triangleq w/r_c \ll 1$. As the species transport is independent of the position in the direction perpendicular to the chip plane, a stationary and two-dimensional coordinate frame, which is Cartesian for a straight element and curvilinear for a turn, is chosen in the chip plane: the x-axis is along the arc length on one of the channel's side walls, and the y-axis locally points to the interior of the channel cross section (see Figure 4-1a).

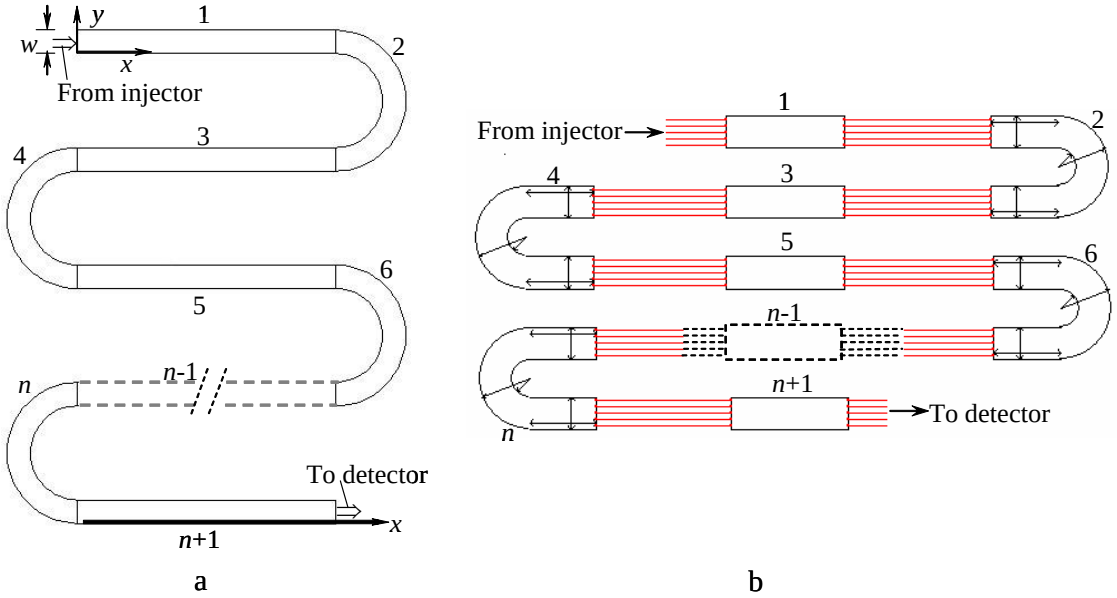

Figure 4-1. Top view of a serpentine channel illustrating the system-level representation of general-shaped microchannels consisting of serially connected straight and turn elements. (a) Geometry, global coordinate frame and element numbering convention. (b) Schematic using elemental models.

The modeling of a given element channel begins with calculations of electric field distributions. As typical cross-sectional dimensions of electrophoresis microchannels are large compared with electric double layer thickness on channel walls, it is accurate to treat

the bulk solution in the channels as electrically neutral [113]. Hence, the electric resistance R of the channel is given by,

$$R = \frac{L}{A_r \boldsymbol{\sigma}} \tag{4.4}$$

where $A_r = wh$ is the cross sectional area, h is the constant channel depth and $\boldsymbol{\sigma}$ is the electric conductivity of the buffer.

Thus, with the assumption of narrow and large-radius channels, the electric potential is linear along the channel length and uniform over any cross section of the channel. Given a potential difference ΔV, across the channel, the electric field is given by [147]

$$(E_x, E_y) = \begin{cases} (E_0, 0) & \text{for a straight channel} \\ (E_0[1 \pm b(1/2 - y/w)], 0) & \text{for a turn} \end{cases} \tag{4.5}$$

where $E_0 = \Delta V / L$, and the plus sign is always assigned to the first turn along x and to any turn in which the species move in the same direction as in the first turn. Minus sign is given to the turn involving species flow in an opposite direction to the first turn. For example, in Figure 4-1a, a plus sign is used for the turns on the right that include clockwise species motion, and minus sign for those on the left (counter-clockwise species flow). The electrophoretic velocity of a charged species band under the electric field is then $(v_x, v_y) = (\mu E_x, \mu E_y)$ [114], where μ is the electrophoretic mobility of the species in the buffer. If the similarity [116, 148] between the electric field and electroosmotic flow exists, the turn dispersion in both electrophoresis and electroosmotic flow can be considered by replacing μ with the algebraic sum of their mobility. Therefore,

$$(v_x, v_y) = \begin{cases} (U, 0) & \text{for a straight channel} \\ (U[1 \pm b(1/2 - y/w)], 0) & \text{for a turn} \end{cases} \tag{4.6}$$

where $U = \mu E_0$. It follows that the migration of species bands is along the axial direction; there is no transverse field-driven migration in either a straight channel or a turn, so long as the channel is narrow compared with the mean radius of the turn. Note that for a turn, E_0 and U are also cross-sectional averages of the electric field and species velocity respectively [135].

The species concentration $c(x, y, t)$ is governed by the convection-diffusion equation [112]

$$\frac{\partial c}{\partial t} + u\frac{\partial c}{\partial x} = D\left(\frac{\partial^2 c}{\partial x^2} + \frac{\partial^2 c}{\partial y^2}\right) \tag{4.7}$$

where t is the migration time from the channel entrance, and D is the diffusivity of the species in the buffer. The apparent velocity u in this equation is given by [147]

$$u = \begin{cases} U & \text{for a straight channel} \\ U\left(1 \pm b(1-2y/w)\right) & \text{for a turn} \end{cases} \tag{4.8}$$

Note that when applied to a turn, terms that are of order b^2 or higher have been neglected in Eq. (4.7). In addition, the apparent velocity u, accounts for both the non-uniform electric field distribution and the "race-track effect" on the species transport [135], i.e., species molecules closer to the smaller-radius side wall move at a higher speed and transmit a short distance.

Eq. (4.7) now is reformulated into a more tractable, reduced-dimension form in terms of spatial moments of the species concentration. Such moments are capable of describing the species band's main characteristics such as mass distribution, skew and variance without solving for detailed concentration distributions. A new coordinate frame is used, which moves at the species band's average velocity U, and normalizes the equation to reduce all

variables into dimensionless forms. Define a dimensionless axial coordinate ξ, transverse coordinate η and time τ by

$$\xi = \left(x - Ut\right)/w, \quad \eta = y/w, \quad \tau = Dt/w^2 \tag{4.9}$$

Note that τ is the ratio of the time for a species molecule to migrate through the channel length to the time for the molecule to diffuse across the channel width. In terms of these dimensionless variables, Eq. (4.7) is reduced to the following form in concentration $c(\xi, \eta, \tau)$:

$$\frac{\partial c}{\partial \tau} = \frac{\partial^2 c}{\partial \xi^2} + \frac{\partial^2 c}{\partial \eta^2} - \mathrm{Pe}\,\chi \frac{\partial c}{\partial \xi} \tag{4.10}$$

where $\mathrm{Pe} = Uw/D$ is the Peclet number representing the ratio of the convective to the diffusive transport rates, and χ is the normalized species velocity relative to the mean:

$$\chi(\eta) = \left(u_x(\eta) - U\right)/U = \begin{cases} 0 & \text{for a straight channel} \\ \pm b\left(1 - 2\eta\right) & \text{for a turn} \end{cases} \tag{4.11}$$

It can be seen that with $\chi = 0$, no convective band-broadening occurs in straight channels as species molecules at different transverse positions migrate at a uniform speed. On the other hand, $\chi \neq 0$ in a turn leads to dispersion. Eq. (4.10) is subjected to the following boundary and initial conditions:

$$\partial c / \partial \eta \big|_{\eta=0,1} = 0, \quad c\big|_{\tau=0} = c\left(\xi, \eta, 0\right) \tag{4.12}$$

Eq. (4.10) now is recast in terms of spatial moments of the species concentration. If the species band is entirely contained in the channel, Eq. (4.10) holds effective over the axial domain $-\infty < \xi < \infty$ (the transverse domain is $0 < \eta < 1$), such that $c \to 0$ as $\xi \to \pm\infty$. Therefore, spatial moments of the species concentration can be defined by

$$c_p(\eta,\tau)=\int_{-\infty}^{\infty}\xi^p c(\xi,\eta,\tau)d\xi,\quad m_p(\tau)=\int_0^1 c_p d\eta \tag{4.13}$$

Here, c_p is the p^{th} moment of the species concentration in the axial filament at η, and m_p is the p^{th} moment of the cross-sectional average concentration of the band, respectively. Note that as a consequence of the coordinate transformation (4.9), all moments are taken with respect to the moving frame (ξ,η). Multiplying Eqs. (4.10) and (4.12) by ξ^p and integrating them with respect to ξ yields

$$\begin{aligned}&\frac{\partial c_p}{\partial\tau}=\frac{\partial^2 c_p}{\partial\eta^2}+p(p-1)c_{p-2}+p\,\mathrm{Pe}\,\chi c_{p-1}\\&\partial c_p/\partial\eta\big|_{\eta=0,1}=0,\quad c_p\big|_{\tau=0}=c_{p0}(\eta)=\int_{-\infty}^{\infty}c(\xi,\eta,0)\xi^p d\xi.\end{aligned} \tag{4.14}$$

In addition, integrating over η further reduces Eq. (4.14) to:

$$\begin{aligned}&\frac{dm_p}{d\tau}=p(p-1)\int_0^1 c_{p-2}d\eta+p\,\mathrm{Pe}\int_0^1\chi c_{p-1}d\eta\\&m_p(0)=m_{p0}=\int_0^1 c_{p0}(\eta)d\eta\end{aligned} \tag{4.15}$$

In both Eqs. (4.14) and (4.15), any term that contains c_i with $i < 0$ should be set to zero. These two equations are valid for both straight and turn elements, with the velocity profile χ given by Eq. (4.11). While these equations in principle can be solved recursively for moments of an arbitrarily large order, for the purpose of capturing species dispersion, it suffices to obtain the moments up to the second order. Specifically, c_0 provides the transverse distribution of the species mass in each axial filament in an element and m_0 the total species mass. Next, c_1 gives the centroid locations of the axial filaments of the species band in the moving coordinate, and hence indicates the skew of the species band. Then, m_1, the transverse average of c_1, is the location of the centroid of the entire species band in the frame (ξ,η). Finally, m_2 can be used to determine the variance of the species band.

4.2.1.2 Distributed Model

Solutions to Eqs. (4.14) and (4.15) now can be presented for a straight channel or a turn, which will provide quantitative information on the evolution of a species band's skew and variance at all times as the band migrates through an element channel. First consider the zero*th*-order moment of the species concentration ($p = 0$). For both straight channels and turns, Eq. (4.15) immediately gives $m_0 = \text{const.}$, which states conservation of mass. $m_0 = 1$ can be chosen without loss of generality. In addition, Eq. (4.14) leads to

$$c_0(\eta, \tau) = \sum_{m=0}^{\infty} d_m e^{-(m\pi)^2 \tau} \cos(m\pi\eta) \tag{4.16}$$

where $d_m = \nu_m \int_0^1 c_{00}(\eta) \cos(m\pi\eta) \cdot d\eta$ with ν_m = 1 if m = 0 and ν_m = 2 if m = 1, 2, 3,…If the initial condition satisfies

$$\int_{-\infty}^{\infty} c(\xi, \eta, 0) d\xi = c_{00}(\eta) = 1 \tag{4.17}$$

then Eq. (4.16) reduces to

$$c_0(\eta, \tau) = \int_{-\infty}^{\infty} c(\xi, \eta, \tau) d\xi = 1 \tag{4.18}$$

Eqs. (4.17) and (4.18) indicate that if all axial filaments of the species band have the same mass initially, then this will be the case at all times. This is typically true in practice. For example, if all axial filaments of an initial band (either in a straight element or a turn) are in the form of a uniformly rectangular plug, they will have identical mass at all times. Alternatively, Eq. (4.17) is also accurate at the exit of a long straight channel with the band injected at its entrance, as diffusion will result in a transversely uniform band. Therefore, the remainder of this chapter will focus on this practically interesting and still sufficiently general case.

Now consider the first-order moment ($p=1$). For both straight and turn elements, Eqs. (4.11) and (4.18) imply that $\overline{\chi c_0}=0$, where overbar means cross-sectional average. Therefore, Eq. (4.15) gives

$$m_1(\tau)=m_{10}=\int_0^1\int_{-\infty}^{\infty}\xi c(\xi,\eta,0)d\xi d\eta=0 \tag{4.19}$$

That is, the centroid of the species band and the origin of the moving frame (ξ,η) coincide at all times if they do so initially. Note that this is always true for straight channels, and is true for turns as long as Eq. (4.17) holds.

Now consider c_1, which represents the skew of the species band. An analytical expression for c_1 that is valid for an arbitrary initial band shape in either straight or turn channels will be obtained. Eq. (4.14) with p = 1 can be solved to yield

$$c_1(\eta,\tau)=\sum_{m=0}^{\infty}S_m(\tau)\cos(m\pi\eta) \tag{4.20}$$

The Fourier coefficients ($m=0,1,2,3,...$) for the band skew $c_1(\eta,\tau)$ at time τ are given by

$$S_m(\tau)=\begin{cases}S_m(0)e^{-(m\pi)^2\tau} & \text{for a straight channel}\\ S_m(0)e^{-(m\pi)^2\tau}+\Gamma_m(\tau) & \text{for a turn}\end{cases} \tag{4.21}$$

$$S_m(0)=\nu_m\int_0^1 c_{10}(\eta)\cos(m\pi\eta)\,d\eta \tag{4.22}$$

where $S_m(0)$ is the Fourier cosine coefficients for the initial skew of the species band. Here, $\Gamma_m(\tau)=0$ for $m=0,2,4,...$ and $\Gamma_m(\tau)=\pm 8\,\mathrm{Pe}\,b(1-e^{-(m\pi)^2\tau})/(m\pi)^4$ for $m=1,3,5,...$ Eq. (4.21) indicates that in a straight channel, all Fourier coefficients associated with the initial skew decay exponentially with the dimensionless time. As a result, an initial skew can be smeared out and the band may eventually become orthogonal to channel walls as it exits

the channel. If the channel is sufficiently long, the location of the axial filament's centroid ultimately moves to the origin (provided the centroid of the entire band is initially at the origin). In the case of a turn, Eq. (4.21) includes the effects of both initial skew and the turn-induced non-uniform velocity profile and migration distance.

Finally, the second-order moment m_2 can be found to obtain the species band's variance. Solving Eq. (4.15) by substituting $p = 2$ and using the relationship [151] $\sigma^2 = w^2\left(m_2/m_0 - m_1^2/m_0^2\right)$ yields

$$\frac{\sigma^2(\tau)}{w^2} = \frac{\sigma^2(0)}{w^2} + \begin{cases} 2\tau & \text{for a straight channel} \\ 2\tau + \Theta(\tau) & \text{for a turn} \end{cases} \tag{4.23}$$

where

$$\Theta(\tau) = \pm 8\,\mathrm{Pe}\,b \sum_{m=1,3,5...}^{\infty} \frac{S_m(0)}{(m\pi)^4}\left(1 - e^{-(m\pi)^2\tau}\right) + 64\,\mathrm{Pe}^2\,b^2 \sum_{m=1,3,5...}^{\infty} \frac{\left(-1 + e^{-(m\pi)^2\tau} + (m\pi)^2\,\tau\right)}{(m\pi)^8} \tag{4.24}$$

Both the straight channel and turn formulas in Eq. (4.23) include band-broadening effects of one-dimensional molecular diffusion (2τ). τ can be related to channel's axial coordinate by $\tau = xD/\left(Uw^2\right)$. Additionally, the turn formula in Eq. (4.24) also contains contributions from initial skew and non-uniform velocity profile and migration distance in the turn.

4.2.1.3 Behavioral Model

Eqs. (4.21) and (4.23) describe the distributed dispersion behavior (skew and variance) of a species band within a straight channel or a turn. With the knowledge of residence time of the species band, the behavioral model that correlates the species dispersion states at element terminals can be attained.

Eq. (4.19) has implied that the centroid of the species band moves at the same speed (U) as the origin of the moving frame (ξ,η); therefore, the dimensional (Δt) and dimensionless (τ_R) residence times of the species band in an element channel are given by,

$$t_{out} - t_{in} = \Delta t = \frac{L}{U} \text{ and } \tau_R = \frac{\Delta t \cdot D}{w^2} \tag{4.25}$$

where indices *in* and *out* represent the quantities at inlet and outlet of the channel.

For the variance and Fourier coefficients of skew, τ_R can be substituted into Eqs. (4.21) and (4.23) respectively, which gives,

$$S_m^{(out)} = \begin{cases} S_m^{(in)} e^{-(m\pi)^2 \tau_R} & \text{for a straight channel} \\ S_m^{(in)} e^{-(m\pi)^2 \tau_R} + \Gamma_m(\tau_R) & \text{for a turn} \end{cases} \tag{4.26}$$

where $m = 0,1,2,3,...$ with the contributions of the non-uniform velocity profile and migration distance given by

$$\Gamma_m(\tau_R) = \begin{cases} 0 \text{ if } m = 0,2,4,... \\ \pm \dfrac{8\varphi}{\tau_R (m\pi)^4} (1 - e^{-(m\pi)^2 \tau_R}), \text{ if } m = 1,3,5,... \end{cases} \tag{4.27}$$

The band variance is given by

$$\frac{\sigma_{out}^2}{w^2} = \frac{\sigma_{in}^2}{w^2} + \begin{cases} 2\tau_R & \text{for a straight channel} \\ 2\tau_R + \Theta(\tau_R) & \text{for a turn} \end{cases} \tag{4.28}$$

and

$$\Theta(\tau_R) = \pm \frac{8\varphi}{\tau_R} \sum_{m=1,3,5...}^{\infty} \frac{S_m^{(in)}}{(m\pi)^4} \left(1 - e^{-(m\pi)^2 \tau_R}\right) + \frac{64\varphi^2}{\tau_R^2} \sum_{m=1,3,5...}^{\infty} \frac{\left(-1 + e^{-(m\pi)^2 \tau_R} + (m\pi)^2 \tau_R\right)}{(m\pi)^8} \tag{4.29}$$

where $\mathrm{Pe}b = \varphi / \tau_R$ is used for a turn.

The solutions given in the preceding section apply if the entire species band lies inside the element. When the band is at the interface between two distinct elements, the band does

not lie entirely inside either element, and an analytical solution in this transition region generally no longer exists. However, the transition region is small compared to the total length of the two neighboring elements so that its contribution to dispersion is generally negligible. It is then reasonable to approximate the transition region by thinking of dispersion in the element as that in an infinitely long channel that otherwise has the same geometry as the element. The relative significance of errors caused by this assumption will be discussed below with respect to the overall variance in the general-shaped channel.

By assuming a Gaussian distribution of the cross-sectional average concentration c_m of the species band at element terminals, the amplitude (A) of the species band can be obtained as

$$A_{out} \Big/ A_{in} = \sqrt{\sigma_{in}^2 / \sigma_{out}^2} \tag{4.30}$$

4.2.2 Detector

To automatically acquire necessary information (e.g., electric field and species velocity) for transient analysis, the detector model is embedded into the detected separation channel, although physically it is placed outside of the channel.

The detector is treated as a point-wise element and its size is assumed negligible compared to separation channels, hence the residence time and variation of skew and amplitude of the band can be neglected, that is,

$$R = 0 \tag{4.31}$$

$$t_{out} - t_{in} = 0 \tag{4.32}$$

$$S_m^{(out)} = S_m^{(in)} \tag{4.33}$$

$$A_{out} = A_{in} \tag{4.34}$$

However, the variance change associated with the detector path length is given by [118],

$$\sigma_{out}^2 - \sigma_{in}^2 = \Delta\sigma^2 = L_{\det}^2 / 12 \tag{4.35}$$

where L_{det} is the window size (or laser spot size) of the detector specified by users.

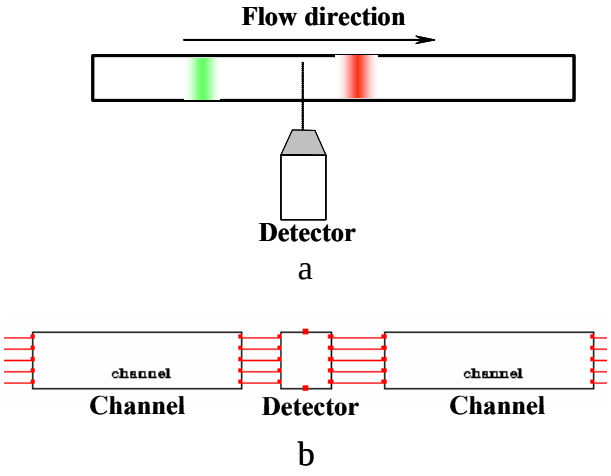

Figure 4-2. (a) Sketch of a single-point detector placed outside of the separation channel. (b) Its modeling representation. The detector model is embedded into the separation channel to extract necessary information for transient analysis.

4.2.3 Injector and Feed Channels

The injector serves as a physical junction among the separation channel, analyte, analyte-waste and buffer feed channels, and initiates the species separation. Electrically, it is modeled as a cross interconnection of four resistors with zero resistance attributed to its negligible size in contrast to other channels,

$$R_a = R_b = R_{aw} = R_{out} = 0 \tag{4.36}$$

where indices *a*, *b*, *aw* and *out* represent the quantities at the injector terminals linking to the analyte, buffer and analyte-waste feed channels and separation channel.

At its interface to the separation channel (*out*), the calculation of separation pin values (states) is initiated and given as,

$$t_{out} = 0 \tag{4.37}$$

$$S_m^{(out)} = 0 \tag{4.38}$$

$$A_{out} = A_{inj} \tag{4.39}$$

$$\sigma_{out}^2 = \sigma_{Gauss}^2 \quad \text{or} \quad \sigma_{out}^2 = \frac{L_{inj}}{16} \tag{4.40}$$

where A_{inj} is the maximum species band concentration (amplitude) at the injector. Calculation of the initial injection variance σ_{out}^2 depends on the injected band profile. For a Gaussian band, $\sigma_{out}^2 = \sigma_{Gauss}^2$, where σ_{Gauss}^2 is the square of the standard deviation of the Gaussian profile. For a plug band, $\sigma_{out}^2 = \frac{L_{inj}}{16}$, where L_{inj} is the injection length. This injector model Eqs. (4.37)-(4.40), needs user inputs of A_{inj}, σ_{inj}^2 or L_{inj} and is only used for simulations of electrophoretic separation microchips. A generalized injector model that can automatically determine the A_{inj} and σ_{inj}^2 will be presented and integrated with reactor models for system-level simulations of integrated LoCs in Chapter 7.

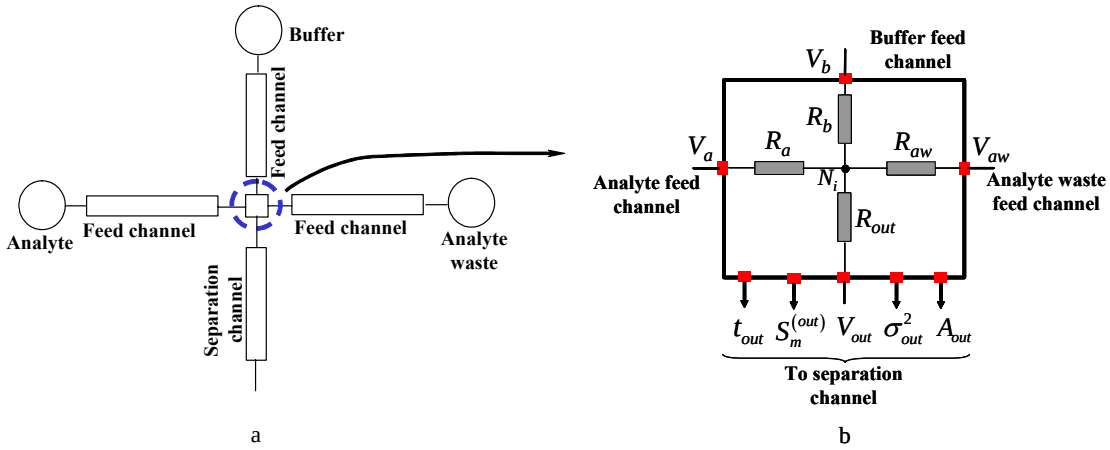

Figure 4-3. (a) Schematic of modeling an electrokinetic injector. (b) Its behavioral model structure.

The feed channels connecting to analyte, buffer and analyte-waste reservoirs are electrically modeled as resistors as the separation channel (Eq. (4.4)) and independent of

the calculation of separation states. Therefore, only electric pins are defined at the interfaces indexed by *a*, *b* and *aw*.

4.2.4 Reservoirs

All reservoirs including analyte, buffer, analyte-waste and waste provide electrical interfaces between the chip and the outside world and work as constant voltage sources. In addition, the waste reservoir at the end of the separation channel also functions as a sink continuously collecting the separation waste.

4.2.5 Model Implementation

An important issue of implementing the separation channel model of the turn geometry (Eqs. (4.27) and (4.29)) is the real-time determination of the turn "sign". Providing this flexibility allows a single turn model to be reused for constructing arbitrary topologies such as a serpentine, spiral or their combination thereof as will be shown later. To address this, two sets of flags are used in the models. One is the system flag F_s, stored as the zero*th* component of the skew coefficients (S [0] in Table 3-1) to record the direction of the skew caused by the first turn or elbow. The other is the intrinsic flag F_i of individual elements. For example, $F_i = 1$ is for turns or elbows involving clockwise flow of species bands; $F_i = 2$ is for counter-clockwise turns or elbows. Since straight channels do not incur any skew, no flag is needed. During simulations, $F_s = 0$ (i.e., S [0] = 0) is first generated by the injector, which is the most upstream element of a separation channel and hence initiates the computation of the separation state. Then as the species band migrates to the first turn (or elbow), F_s is irreversibly set to the intrinsic flag F_i of the first turn (or elbow). Afterwards, the written F_s is compared with F_i of each downstream element as the band moves on. If they are identical, a "+" sign is used for the element, otherwise a "–" sign. Figure 4-4

shows the Verilog-A codes for a 180° turn involving clockwise flow of species bands to implement this logic.

```
`define NUM 10                                  // The number of terms in the Fourier series
...

module Uturn1(...);                             // Module declaration
parameter real sp_D_0 = 500;                    // Diffusivity of the zero-th species; unit: μm²/s
parameter real R2 = 110 ;                       // Outer radius of the U shape turn; unit: um
parameter real R1 = 100 ;                       // Inner radius of the U shape turn; unit: um
...

integer Fs;                                     // System flag
integer Fi;                                     // Intrinsic flag
real dummy1;                                    // Intermediate variable
real W;                                         // Channel width
real delta_t_0;                                 // The residence time of the zero-th species within the turn; unit: s
real pi;                                        // π
...

analog begin                                    // Behavioral description begins

Fi = 1;                                         // The present turn is clockwise
W = abs (R2-R1);
Fs = SKA(sk_in[0]);                             // sk_in is the skew coefficient; sk_in[0] stores the system flag
pi = 3.1415926;
...

if (Fs == 0) begin                              // system flag is not set yet; no turns or elbows upstream
        SKA(sk_out[0])<+(Fi);                   // set the system flag to the intrinsic flag
        generate i (1, `NUM, 1) begin           // this loop is to calculate skew coefficient
                dummy1 = 1- exp(-(2*i-1)*(2*i-1)*pi*pi*delta_t_0*sp_D_0/(W*W));
                Part1_Sk = 8*pi*W*W*dummy1/(pow((2*i-1), 4)*pow(pi, 4)*delta_t_0*sp_D_0); // the 1st part in Eq. (4-29), use "+"
                ...
        end
...

end else if (Fs == 1) begin                     // Species flow in the first turn is clockwise
        SKA(sk_out[0])<+SKA(sk_in[0]);          // Convey the system flag
        generate i (1, `NUM, 1) begin
                dummy1 = 1- exp(-(2*i-1)*(2*i-1)*pi*pi*delta_t_0*sp_D_0/(W*W));
                Part1_Sk = 8*pi*W*W*dummy1/(pow((2*i-1), 4)*pow(pi, 4)*delta_t_0*sp_D_0); // use "+" sign
                ...
        end
...


end else begin                                  // Species flow in the first turn is counter-clockwise
        SKA(sk_out[0])<+SKA(sk_in[0]);          // Convey the system flag
        generate i (1, `NUM, 1) begin
                dummy1 = 1- exp(-(2*i-1)*(2*i-1)*pi*pi*delta_t_0*sp_D_0/(W*W));
                Part1_Sk = - 8*pi*W*W*dummy1/(pow((2*i-1), 4)*pow(pi, 4)*delta_t_0*sp_D_0); // use "-" sign
                ...                             use "-" sign
        end
...

end
...
end                                             // End of behavioral description
endmodule                                       // End of module
```

Figure 4-4. Verilog-A description of a 180° turn involving clockwise flow of the species band. It determines the signs used in Eq. (4.29), as well as the skew canceling and strengthening effects.

4.3 Constructing System-Level Representation

Previous sections built the behavioral models that correlate both electric and biofluidic states at the element inlet and outlet, which can be linked to construct the system level

schematic, that is, $\{V_{out}\}^{(j)} = \{V_{in}\}^{(j+1)}$, $\{t_{out}\}^{(j)} = \{t_{in}\}^{(j+1)}$, $\left\{S_m^{(out)}\right\}^{(j)} = \left\{S_m^{(in)}\right\}^{(j+1)}$, $\left\{\sigma_{out}^2\right\}^{(j)} = \left\{\sigma_{in}^2\right\}^{(j+1)}$ and $\{A_{out}\}^{(j)} = \{A_{in}\}^{(j+1)}$, where index $j = 1, 2...n$ is the numbering of the element downstream of the injector in the flow direction. This protocol enables the transmission of the biofluidic states associated with the band shape within the entire channel network. Figure 4-1b depicts the system-level schematic of the serpentine separation channel shown in Figure 4-1a consisting of straight channels and complementary turns.

4.4 Skew Interactions between Turns

This section will apply the system-level schematic to analyze the skew interactions between turns, which are important to interpret the disparate dispersion behavior of species bands at different flow regimes.

Serpentine channels containing a pair of complementary turns are considered. Such a channel, with a species band of general shape (subject to Eq. (4.18)) introduced at the entrance to element 1 (Figure 4-1), has a uniform width *w*. The turns have identical mean radius r_c and included angle $\varphi = \pi$. The inter-turn straight channel has length *L*. The practical case in which the band at the outlet of element 1 is free of skew will be studied. This can occur if an unskewed species band is injected at the inlet, or the length (L_1) of element 1 is sufficiently long to smear out the skew of an initially skewed band. According to Eqs. (4.26) and (4.28), the skew and variance growth at the other element terminals relative to the inlet of element 2 depends entirely on the dimensionless times of the turn and the inter-turn straight channel, respectively defined as follows:

$$\tau_s = (L/w)/\mathrm{Pe}, \quad \tau_t = \varphi/(\mathrm{Pe}b) \tag{4.41}$$

As they are inversely proportional to the Peclet number Pe, a large dimensionless time generally corresponds to a relatively small Pe (i.e., diffusion is significant in the dispersion process). On the other hand, a small dimensionless time corresponds to a large Pe, indicating that convection is dominant.

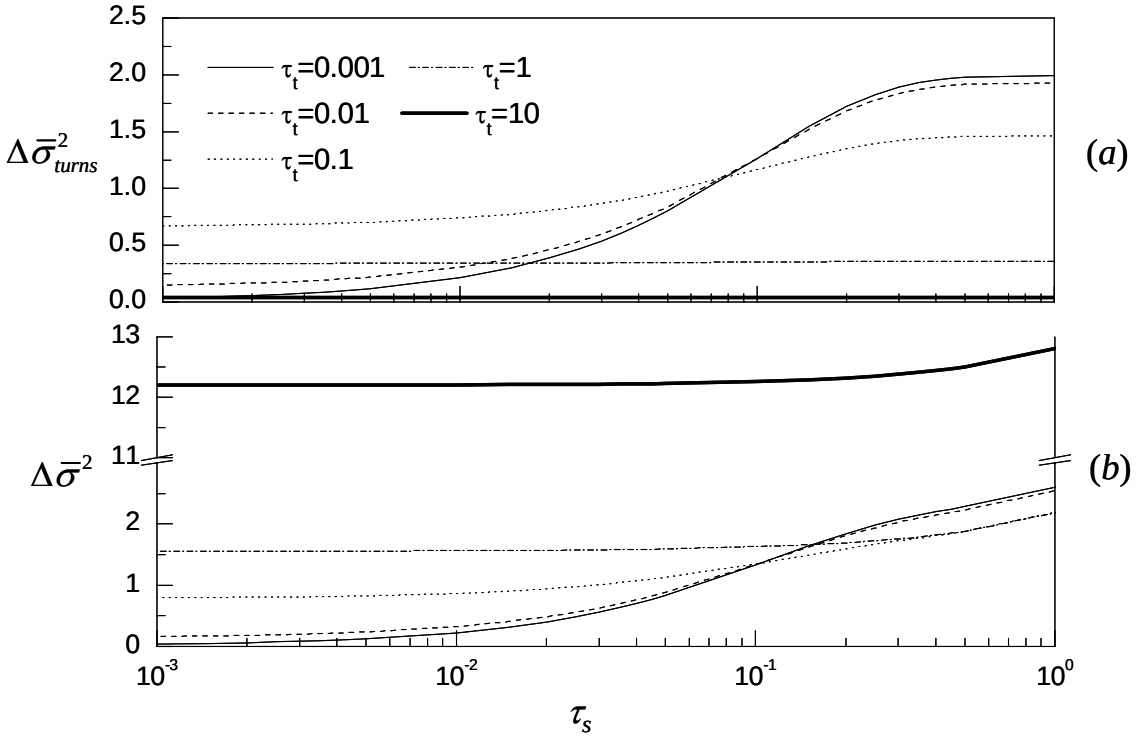

Figure 4-5. The dependence of the total variance and turn-induced variance for two complementary 180°-turns vs. dimensionless times τ_t and τ_s. (a) The turn-induced variance and (b) the total variance. Their difference represents the variance from molecular diffusion.

General effects of τ_s and τ_t on dispersion of a species band are considered, which is assumed to have an initial concentration given by the Dirac δ function at the inlet of the first turn (element 2). Note that there is no need to consider the residence times of the band in the straight elements upstream of the first turn and downstream of the second turn, as they do not affect the skew interactions between the turns. Hence, the total increase in variance is $\Delta\sigma^2 = \left\{\sigma^2_{out}\right\}^{(4)} - \left\{\sigma^2_{in}\right\}^{(2)}$ and $\left\{\sigma^2_{in}\right\}^{(2)} = 0$. $\Delta\sigma^2$ is normalized by defining

$\Delta\bar{\sigma}^2 = \Delta\sigma^2 / \Delta\sigma_\infty^2$, where $\Delta\sigma_\infty^2 = (\varphi w)^2 / 3$ is the variance change in a single turn if diffusion is absent [148] (i.e., $\mathrm{Pe} \to \infty$). In addition to $\Delta\bar{\sigma}^2$, the change in variance that results exclusively from the non-uniform velocity profile and migration distance in the two turns will be also examined: $\Delta\bar{\sigma}_{turns}^2 = \left(\{\Theta\}^{(2)} + \{\Theta\}^{(4)} \right) w^2 / \Delta\sigma_\infty^2$, where $\{\Theta\}^{(2)}$ and $\{\Theta\}^{(4)}$ are given in Eq. (4.29). Note that both $\Delta\bar{\sigma}^2$ and $\Delta\bar{\sigma}_{turns}^2$ depend only on τ_s and τ_t, and this dependence is shown in Figure 4-5.

4.4.1 Case of Large τ_t

Consider first the case of large τ_t. From Figure 4-5a, it can be seen that when τ_t is large ($\tau_t > 1$), $\Delta\bar{\sigma}_{turns}^2$ is independent of τ_s. This is because there is significant transverse diffusion, which immediately smears out the skew generated by turns, yielding a band that is always orthogonal to the channel walls in either turn. For example, at $\tau_t = 10$, the species skew due to a single turn is given by $\left\{ S_1^{(out)} \right\}^{(2)} = 0.026 << 1$ with $\left\{ S_m^{(out)} \right\}^{(2)}$ $(m \geq 3)$ at least two orders of magnitude smaller, indicating the skew effects are indeed very small. As the inter-turn straight channel does not skew the band, the contributions of skew effects in the turns to the variance change are small and do not vary with τ_s. For a sufficiently large τ_t, the non-uniform velocity and migration distance induced variance $\Delta\bar{\sigma}_{turns}^2$ in a single turn is almost zero and the total variance is purely due to diffusion. As shown in Figure 4-5b, the total variance increase is significant ($\Delta\bar{\sigma}^2 > 12.2$ for $\tau_t = 10$) even at low τ_s values, due to contributions of diffusive band-broadening in the turns.

4.4.2 Case of Small τ_t

Next consider the case of small turn dimensionless time τ_t. Figure 4-5 shows that both $\Delta\bar{\sigma}^2_{turns}$ and $\Delta\bar{\sigma}^2$ depend rather strongly on the straight-channel dimensionless time τ_s. This is due to the fact that a low τ_t implies strong convective effects, which result in significant skewing of the band in each turn. For example, with $\tau_t = 0.01$, the skew due to the first turn is given by $\left\{S_1^{(out)}\right\}^{(2)} = 2.4$, which is already significant. When the straight-channel residence time τ_s is also small, the skew emerging from the first turn persists throughout the inter-turn straight channel. For example, $\tau_s = 0.01$ yields $\left\{S_1^{(out)}\right\}^{(3)} = 0.9\left\{S_1^{(out)}\right\}^{(2)}$ according to Eq. (4.26), indicating that the skew is largely unchanged when entering the second turn. This skew will be largely undone by the counter-skew in the second turn, resulting in a small $\Delta\bar{\sigma}^2_{turns}$ (Figure 4-5a), and the total variance change $\Delta\bar{\sigma}^2$ is also small due to small diffusive band-spreading as implied by small τ_t and τ_s (Figure 4-5b). On the other hand, when τ_s is large while τ_t is kept small, significant transverse diffusion in the inter-turn straight channel smears out the skew induced by the first turn. For example, $\left\{S_1^{(out)}\right\}^{(3)} = 0.37\left\{S_1^{(out)}\right\}^{(2)}$ when $\tau_s = 0.1$, meaning that 63% of the skew induced by the first turn has been smeared out. The mostly upright band that results will be reversely skewed, leading to a large $\Delta\bar{\sigma}^2_{turns}$. In particular, $\Delta\bar{\sigma}^2_{turns} \to 2$ is expected for sufficiently small τ_t and large τ_s (Figure 4-5a), indicating that the undesirable skew effects in the two turns and large diffusion in the inter-turn straight channel are all present and add up (Figure 4-5b). To our knowledge, this is the first time the combined effects of τ_s and τ_t have been systematically investigated in the entire (τ_s, τ_t) parameter space, with the special case of an

extremely small τ_t (e.g., τ_t = 0.001) agreeing with the results of Molho [151], where diffusion in the turns is ignored. The effects of τ_s and τ_t on diffusion, skew and variance growth are summarized in Table 4-1.

Table 4-1. Dependence of skew, turn variance and total variance on dimensionless times τ_t and τ_s.

τ_t	τ_s	Skew			Turn Variance		Total Variance
		$\{S^{(out)}\}^{(2)}$	$\{S^{(out)}\}^{(3)}$	$\{S^{(out)}\}^{(4)}$	$\{\Delta\sigma^2_{turn}\}^{(2)}$	$\{\Delta\sigma^2_{turn}\}^{(4)}$	$\{\Delta\sigma^2\}^{(4)}$
>1		No	No	No	0	0	$2\tau_t + \tau_s$
<0.01	>1	Large	No	Large	$\frac{(\varphi w)^2}{3}$	$\frac{2(\varphi w)^2}{3}$	$\tau_s + \frac{2(\varphi w)^2}{3}$
	<0.01	Large	Large	No	$\frac{(\varphi w)^2}{3}$	~0	~0

4.5 Simulation Results and Discussion

In this section, we will first describe the simulation procedure, in which the Kirchhoffian resistor network to predict electric voltage, current and field as well as the signal flow network to evaluate species band shape are solved sequentially, then present results obtained from the system-level schematic simulations of general-shaped electrophoresis separation channels. Serpentine channels containing one and multiple pairs of complementary turns, as well as spiral channels constructed from turns with different radii will be considered. These results will be compared with numerical solutions and experimental data extracted from the literature.

4.5.1 Simulation Description

System simulations for separation chips involve both electric and biofluidic calculations. For DC analysis, given the applied potential at reservoirs, system topology and element dimensions, nodal voltages at element terminals within the entire system are first computed by Ohm's and Kirchhoff's laws using the resistor models presented in Section 4.2.1. The

resulting nodal voltages are in turn used to calculate the electric field strength (E) and its direction within each element. With these results and user-provided sample properties (D and μ), the sample speed is then given by $u = \mu E$. Next, values of biofluidic pins at the outlet of each element (e.g., arrival time, variance, skew and amplitude) are determined. The process starts from the injector, the most upstream element in a separation channel, in terms of the directional signal flow as described in the previous chapter. As such, both electric and fluidic information in the entire system is obtained.

Transient analysis can be also conducted for separation chips that involve the species band's motion and broadening. An electropherogram (average concentration c_m vs. time) can be obtained at the detector, yielding an intuitive picture of separation resolution between species bands. The transient analysis first calculates for the DC operating points of the amplitude A_{det}, separation time t_{det} and variance σ_{det}^2 of the species band at the detector. Based on these points, the actual read-out time is scanned and the average concentration output c_m is calculated. Assuming the species band does not appreciably spread out as it passes through the detector, c_m is given by

$$c_m = A_{\text{det}} \cdot e^{\frac{-(E\mu)^2 (t - t_{\text{det}})^2}{2\left(\sigma_{\text{det}}^2 + \Delta\sigma^2\right)}} \tag{4.42}$$

where t is the actual read-out time and $\Delta\sigma^2$ is the variance growth associated with finite detection window size (or laser spot size) and given in Eq. (4.35).

4.5.2 Dispersion in Double Complementary Turn Serpentine Channels

In this section, the variation of skew and variance as the species band migrates in a pair of complementary turns will be studied by system simulations. The results are compared with numerical simulation and experimental data. Three dimensionless time combinations

as discussed above will be considered. The case of large τ_t and small τ_s is qualitatively similar to that of large τ_t and large τ_s, and will not be considered, as it would imply that $\tau_t / \tau_s = r_c \varphi / L \gg 1$. Such a separation channel consisting of long turns and short straight channels is of little practical interest.

4.5.2.1 Case of Large τ_t and τ_s

For the case of large τ_t and τ_s, consider τ_t = 6.12 and τ_s = 15.6 in a complementary-turn serpentine separation channel. The simulation results are compared with experimental data from Culbertson *et al.*[135] (see microchip electrophoresis of rhodamine B in Appendix).

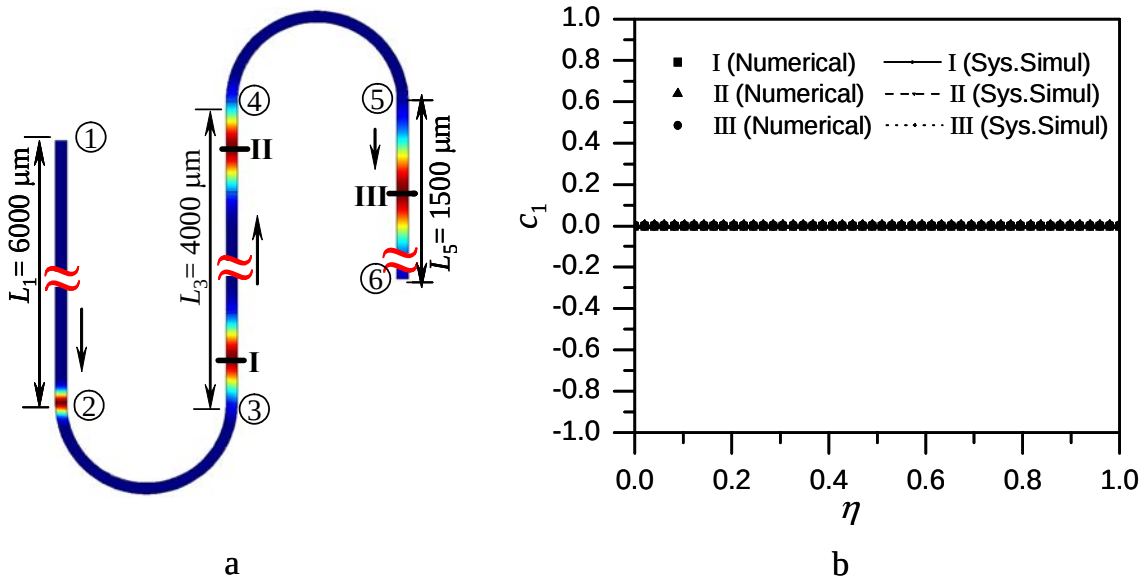

Figure 4-6. Band shapes at different locations in a double complementary-turn serpentine channel for large dimensionless times (τ_t = 6.12 and τ_s = 15.6). (a) Contour plot of concentration (not to scale). (b) Transverse distribution of the first moment c_1.

Shown in Figure 4-6 are contour plots of band shapes and skew at different locations in the channel, determined from numerical and system simulations. The band skew is calculated at three locations just downstream of the first turn, and upstream and downstream of the second turn for convenience of data extraction (Figure 4-6a), as this

allows the band to lie entirely in the straight channel. This method of data extraction [147] is also used for numerical simulation results in the following discussion.

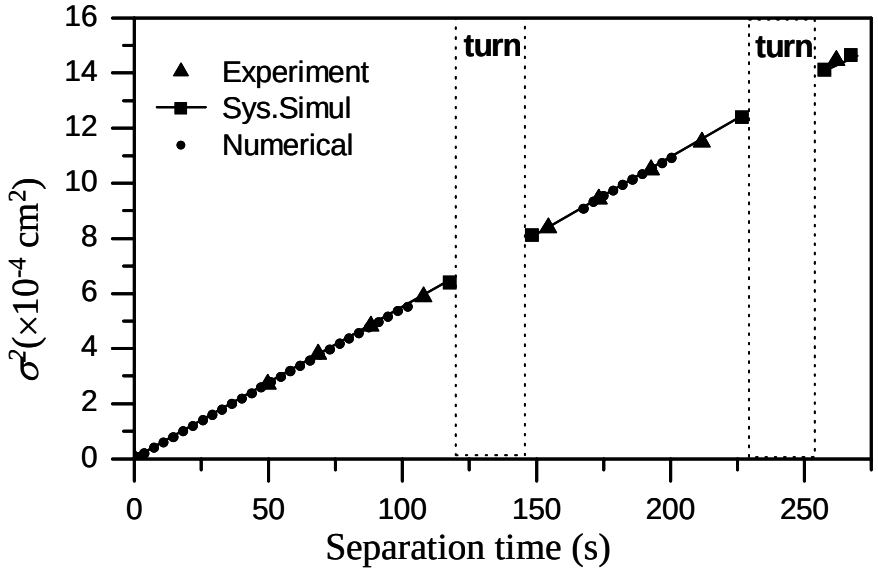

Figure 4-7. Variance vs. migration time in a double complementary-turn serpentine channel in the case of large dimensionless times (τ_t=6.12 and τ_s=15.6). Results from the system simulations are compared with those from numerical analysis and experiments [135].

Figure 4-7 compares variance from the system simulation, numerical simulation and experiments. The numerical simulation is performed over the entire serpentine channel using FEMLAB [152]. The variance calculated by the system simulation is given at the nodes (interfaces 1-6). As τ_t is large, transverse diffusion dominates, suppressing virtually any skew induced by convection in the turn. Therefore, the species band exhibits negligible skew throughout the entire separation channel. Band broadening is almost exclusively caused by diffusion. In this case, Eq. (4.29) correctly predicts that $\Theta(\tau_t) \to 0$, and Eq. (4.28) that the species band's variance increases linearly with the dimensionless time, as shown in Figure 4-7. The results from the system simulation are also compared with numerical and experimental results [135], with an error smaller than 1%. As discussed in the general considerations above, the large τ_t minimizes the band skew and convection term in Eq.

(4.27), hence reducing the error caused by the approximation in the transition regions (between straight channels and turns) and velocity linearization, and yielding the model's excellent accuracy. Second, since τ_s and τ_t are large, the contributions to the overall variance by diffusive band-broadening in the straight channel and in the turn are large, diminishing the relative significance of convective dispersion to the total variance.

4.5.2.2 Case of Small τ_t and Large τ_s

Next consider the case of small turn dimensionless time $\tau_t = 0.068$ and relatively large inter-turn straight channel dimensionless time $\tau_s = 0.696$ and its comparison with experiments [135] (see microchip electrophoresis of TRITC-Arg in Appendix).

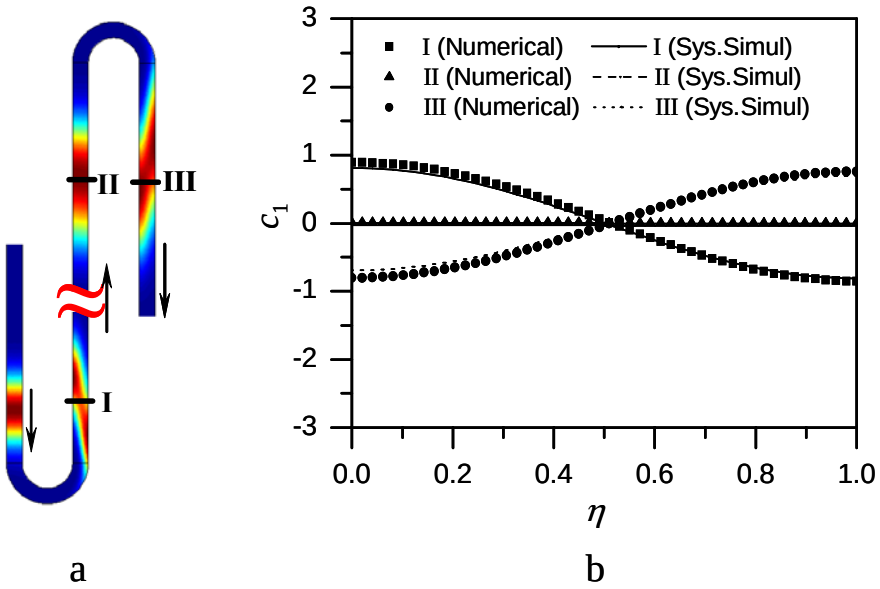

Figure 4-8. Band shapes at different locations in a double complementary-turn serpentine channel for small turn and relatively large inter-turn straight channel dimensionless times ($\tau_t = 0.068$ and $\tau_s = 0.696$). (a) Contour plot from numerical simulation (not to scale). (b) Transverse distribution of the first moment c_1.

The species band shapes at different locations are shown in Figure 4-8. As τ_t is small, species molecules in a turn have little time to diffuse transversely. Hence convection dominates within the turn, resulting in a skewed band shape at the exit of the first turn (station I). In the inter-turn straight channel, transverse diffusion has sufficient time to

smear out this skew (station II), and the resulting upright species band is skewed in the opposite sense to the first skew at the exit of the second turn (station III), leading to a final skewed band shape.

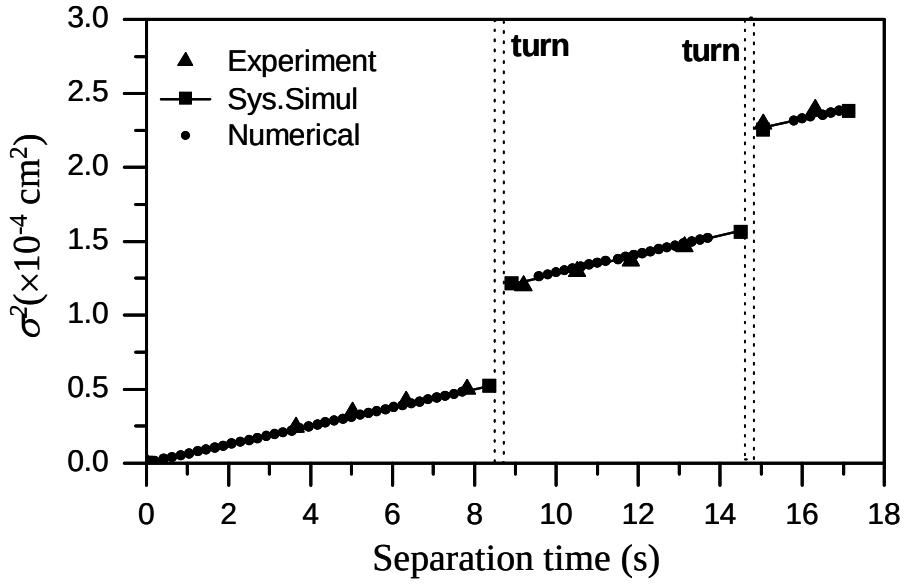

Figure 4-9. Variance vs. migration time in a double complementary-turn serpentine channel in the case of small turn and large inter-turn straight channel dimensionless times (τ_t = 0.068 and τ_s = 0.696). Results from the system simulation are compared to those from numerical simulation and experiments [135].

The variance as a function of time obtained from numerical simulations and experiments is shown in Figure 4-9, and compared with that from system simulations. It can be seen that the variance increases linearly with time in the straight channels, as predicted by Eq. (4.28). However, a significant variance increase occurs after each turn as discussed above. The residual variance after a pair of complementary turns is the sum of the variance from the two single turns and from the straight channel [153]. The excellent accuracy of the system simulation in this case is determined by the accuracy of the elemental model for each single turn. It can be shown that at an extremely small τ_t, the skew length at the interface of a straight element and a single turn computed from the elemental model Eq. (4.26) coincidentally matches the exact solution that exists only in the pure-convection case. The

skew length in the pure-convection case is the axial projection distance between the leading and trailing molecules of the species band at the instant the entire band has just completely moved into the straight channel. This is the reason that the model is accurate even when $w/r_c = 0.4$ is not significantly smaller than unity.

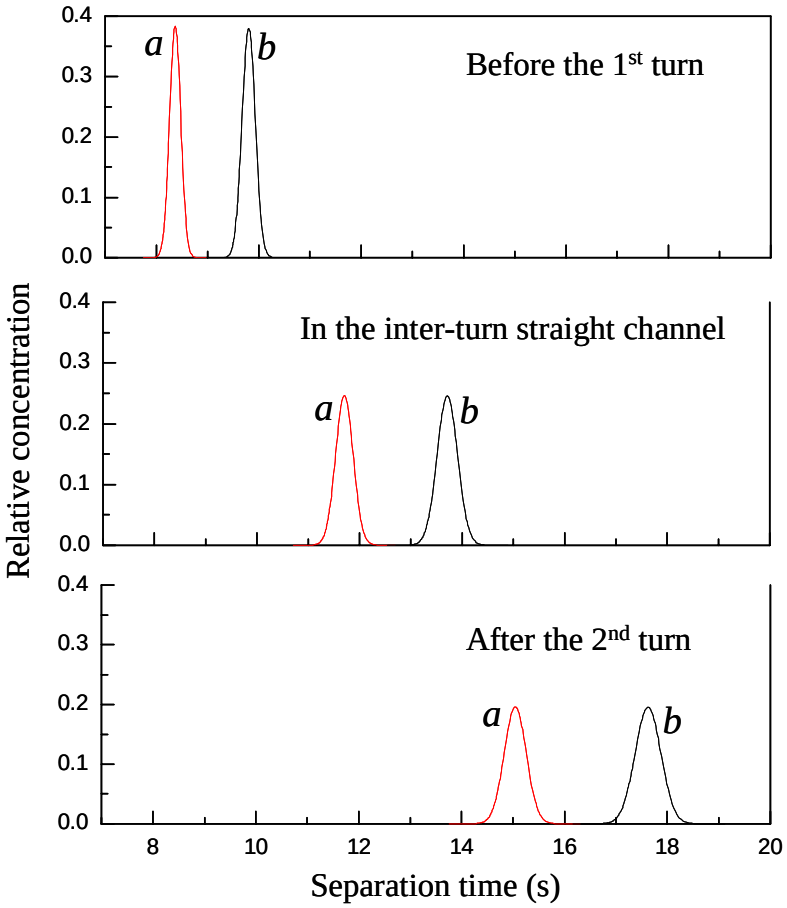

Figure 4-10. Transient analysis simulates the electropherograms output from three detectors, which are respectively arranged before the first turn (top trace), in the middle of the inter-turn straight channel (middle trace) and after the second turn (bottom trace).

Figure 4-10 shows the separation electropherograms of an analyte comprised of two species *a* (TRITC-Arg) and *b* (rhodamine B) at three detectors obtained from the transient analysis. The spacing between concentration peaks of species *a* and *b* increases as they migrate through the channel, but due to the band-broadening effect, the amplitude decreases continuously.

4.5.2.3 Case of Small τ_t and τ_s

Consider the final case where both dimensionless times τ_t and τ_s are small for a double complementary-turn channel. According to Eq. (4.41), the Peclet number Pe is then necessarily large ($L/w > 1$ for practical electrophoresis microchips). The molecules do not have sufficient time to diffuse transversely and convection is the dominant dispersion mechanism in both straight channel and turn elements. High-convective dispersion is practically important for microchip electrophoresis of species with low diffusivities, such as separation of DNA in a gel or sieving matrix [135, 145]. Here a species with a very low diffusivity undergoing electrophoresis with calculated dimensionless times $\tau_t = 8.5\times10^{-4}$ and $\tau_s = 5\times10^{-3}$ (see Appendix) is considered. This geometry has been experimentally investigated by Paegel *et al*. [145]. Since material property information [150] given therein is insufficient for extracting experimental data on band broadening, system simulations are compared with numerical results.

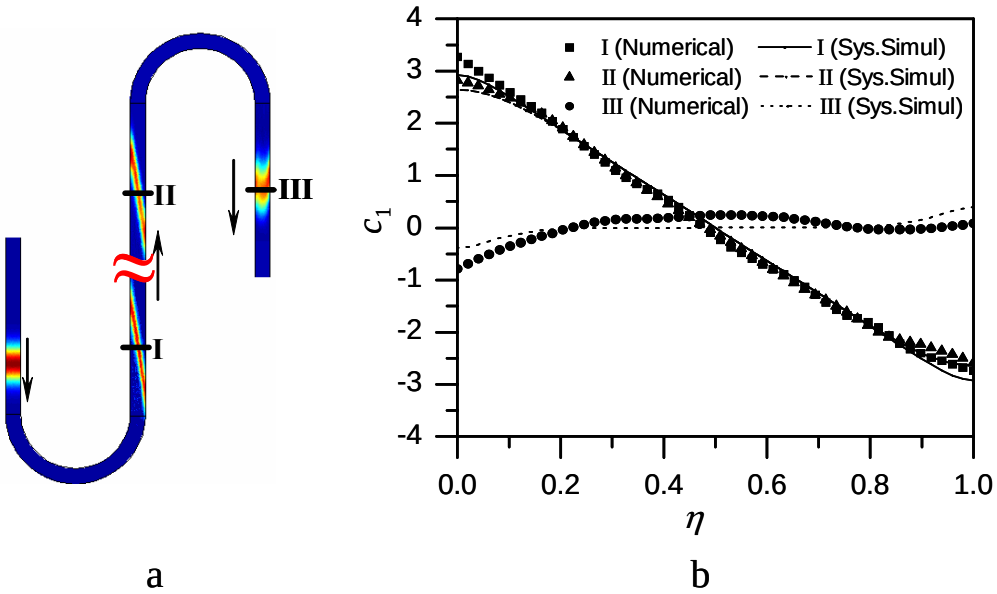

Figure 4-11. Band shapes at different locations in a double complementary-turn serpentine channel when both dimensionless times are small ($\tau_t = 8.5\times10^{-4}$ and $\tau_s = 5\times10^{-3}$). (a) Contour plot from numerical simulation (not to scale). (b) Transverse distribution of the first moment c_1.

Shown in Figure 4-11 are band shapes at different locations in the serpentine channel. A sharp skew forms at the exit of the first turn (at station I) because of the small τ_t. Now, since τ_s is also small, the skew persists through the inter-turn straight channel (station II), and as a result can be significantly cancelled out by the second turn, which causes a counter-skew (station III). Figure 4-12 shows the variance calculated from the system simulation at element interfaces. It can be seen that axial molecular diffusion is negligible, as reflected by the very small change in variance in the straight channels. The variance after each turn changes significantly due to dominant convective effects, and the overall variance is small as a result of skew cancellation.

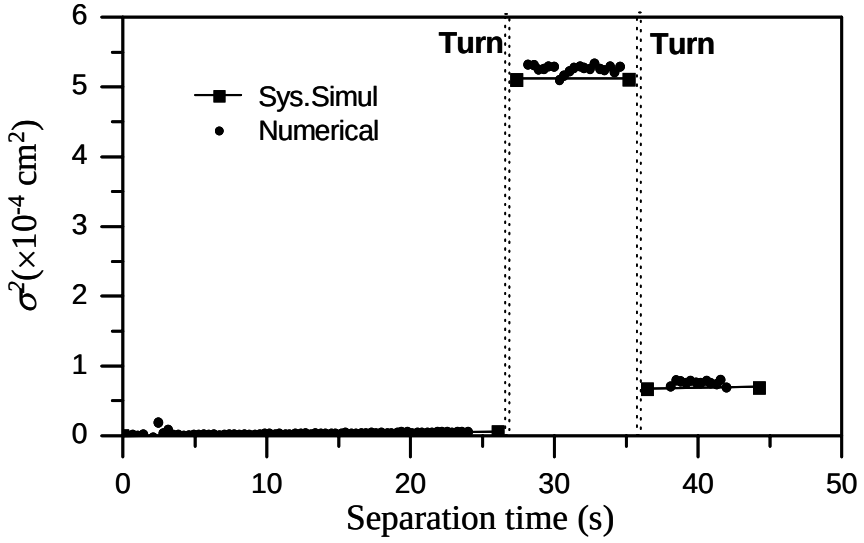

Figure 4-12. Variance vs. migration time in a double complementary-turn serpentine channel in the case of small dimensionless times ($\tau_t = 8.5\times10^{-4}$ and $\tau_s = 5\times10^{-3}$). Results from the system simulation are compared to those from the numerical simulation.

The system simulation results agree with the numerical data. The relative error (< 11%) however, is larger than those in the cases discussed above. This is because, unlike the cases where at least one of the two dimensionless times is large, diffusion plays an insignificant role when both τ_t and τ_s are small, and band-broadening is almost exclusively convective. Thus, errors in convection modeling, which are closely associated with the velocity

linearization and transition region modeling errors in Eq. (4.29), are significant compared to the total variance change, leading to larger overall relative errors.

4.5.3 Dispersion in Multi-Turn Serpentine and Spiral Channels

To illustrate the utility of the model for efficient simulations of complex electrophoretic separation channels, a serpentine channel containing three identical pairs of complementary, 180°-turns are considered.

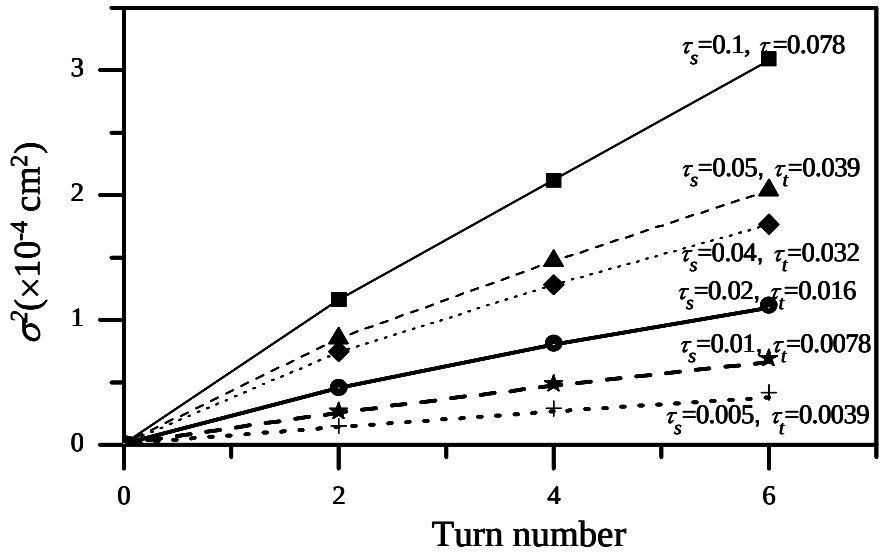

Figure 4-13. Species band's variance at various locations in a serpentine channel consisting of three pairs of complementary turns, as calculated from the system (Lines) and numerical (Symbols) simulations. τ_t and τ_s range from 0.0039 to 0.078 and 0.005 to = 0.1 respectively.

The schematic is again as shown in Figure 4-1 (with $n = 13$). To our knowledge, this is the first time an electrophoretic separation channel of this level of complexity has been accurately simulated with the lumped-parameter model. The channel has dimensions w = 50 μm, r_c = 250 μm (b = 0.2), inter-turn straight channel $L_3 = L_5 = L_7 = L_9 = L_{11}$ = 1000 μm, leading channel L_1 = 200 μm and ending channel L_{13} = 500 μm. With this geometry, the dimensionless times are related by $\tau_t / \tau_s = 0.78$. τ_s ranging from 0.005 to 0.1 by varying the diffusivity of the species is considered. Figure 4-13 shows the variance from system

and numerical simulations extracted in the straight channels (L_5, L_9 and L_{13}) after the 2nd, 4th and 6th turns, when the centroid of the species band is at their midpoints. The variance increases with even-numbered turns in a linear to sublinear manner depending on τ_t and τ_s, as has been reported in the literature [10]. Very good agreement between system and numerical simulation results is found. The best match between them is found to be within 0.3% for τ_t = 0.078 and τ_s = 0.1, when both dimensionless times are relatively large and transverse diffusion plays a more significant role to limit skew effect in the turns. The relative error increases progressively as the dimensionless times are decreased. The largest overall error is found to be 9.5%, when the dimensionless times take on the smallest values considered: τ_t = 0.0039 and τ_s = 0.005. Similar to the case of a single pair of complementary turns, this relatively large error at small dimensionless times can be attributed to the transition region errors due to diminished diffusion effects.

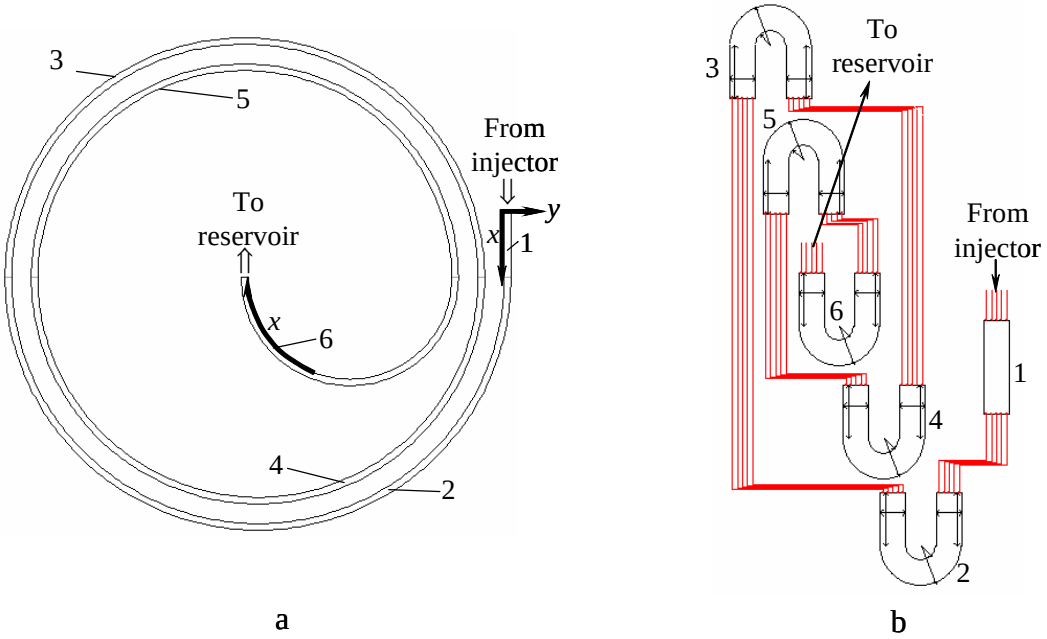

Figure 4-14. A spiral-shaped channel modeled as serially connected turn elements with increasing radii. (a) Geometry and element numbering. (b) Schematic using elemental models.

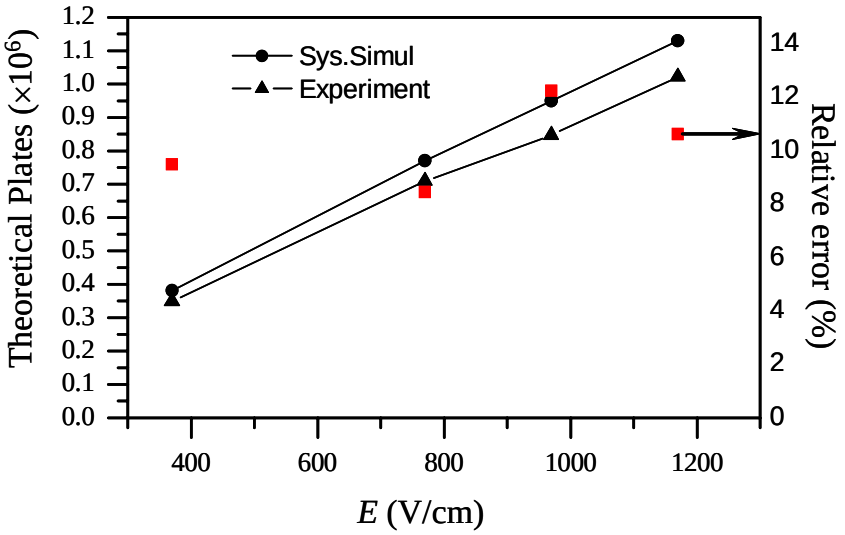

Figure 4-15. Comparison between the system simulation results and experimental data for a spiral shaped channel. Left coordinate: theoretical plate number; and right coordinate: relative plate-number error of the model compared with experimental data [144].

Now the accurate lumped-parameter analysis of a multi-turn spiral-shaped separation channel will be presented, which has also been commonly used in microchip electrophoresis systems [144]. The schematic of this type of complex channel is shown in Figure 4-14. Such channels differ from serpentine channels in that the skew, turn variance and total variance always increase with the turn number since the band skew in all turns has the same sense and does not cancel. A spiral channel consisting of a straight inlet channel and five 180°-turns connected in series ($n = 6$ in Figure 4-14) is considered. The dimensionless times in turns, calculated from Eq. (4.41), range from 1.4 to 10.5 (see Appendix). A channel with this geometry and dimensionless times has been experimentally studied by Culbertson *et al.* [144], who presented band-broadening measurements in terms of the theoretical plate number N [154, 155]. To facilitate comparison with the experimental data, $\{N_{out}\}^{(5)}$, the plate number is considered at the outlet of element 5, where species detection is made. Figure 4-15 shows the plate number from the system

simulation as the species band is electrophoretically driven in the spiral-shaped channel, compared with experimental data [144]. Due to the relatively large dimensionless times, the molecular diffusion dominates and excellent agreement between the system simulation results and experimental data is observed. The overall relative error of 12% is considered acceptably small considering uncertainties in the knowledge of species diffusivity [144].

4.5.4 Dispersion in Hybrid Networks Including Both Serpentine and Spiral Channels

Finally, a more challenging case of hybrid electrophoretic separation microchips [153] including both spiral and serpentine channels will be considered, as shown in Figure 4-16. Due to the difficulty of accounting for the coexisting skew canceling and strengthening effects in such a topology, it has not been effectively investigated since proposed [153].

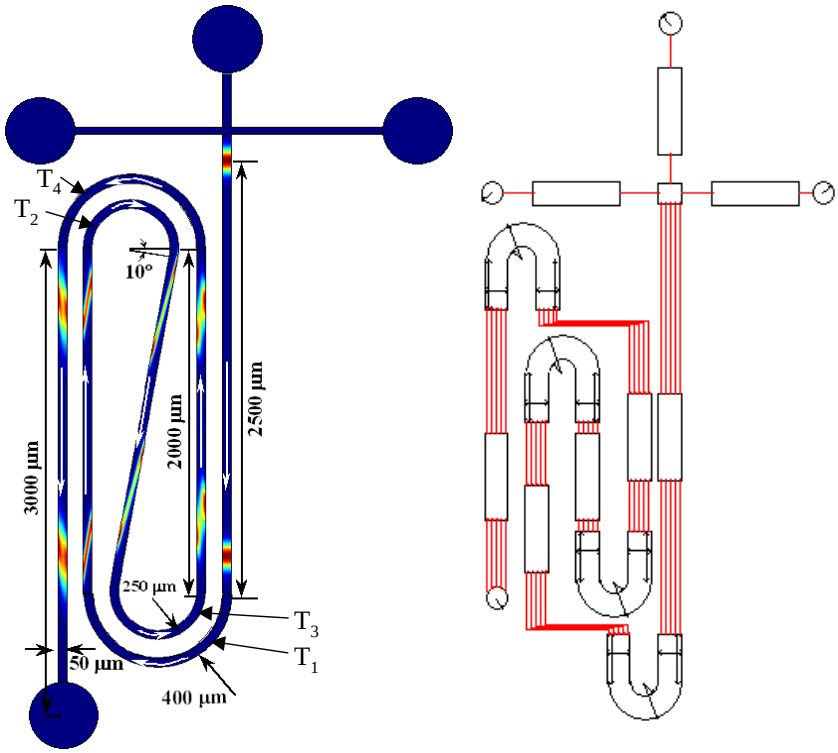

Figure 4-16. A hybrid electrophoretic separation microchip including both spiral and serpentine channels and its simulation schematic.

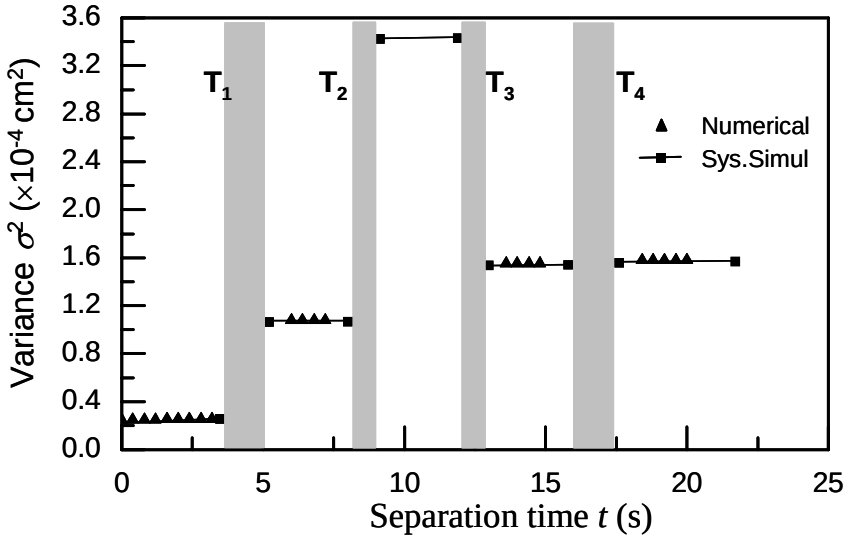

Figure 4-17. Comparison between numerical data and system-level schematic simulation on variance vs. separation time in the hybrid electrophoretic separation microchip.

Figure 4-17 shows system simulation results of the variance of a species band vs. time in this chip using the behavioral models, along with the comparison to numerical data. A low species diffusivity of $D = 1\times10^{-11}$ m^2 s^{-1} is chosen to analyze the high-convective dispersion and the strong skew interaction among elements (other properties and parameters are the same as those of TRITC-Arg in Appendix). It is shown in Figure 4-17 that since species flows in the clockwise direction in both turns T1 and T2 (spiral topology), T2 strengthens the sharp skew generated by T1, leading to a more skewed band and higher variance. Due to the small species diffusivity, the skew almost persists through the inter-turn straight channel between T2 and T3 and is significantly cancelled out by T3, which as a result yields a drastic variance drop in T3 (serpentine topology). However, the skewed band after T3 is overly corrected by T4 and a counter-skew is shown afterward. Excellent agreement between the system and numerical simulation results with 1% relative error and tremendous speedup up to 400,000× have been achieved in Figure 4-17. This is also the

first time that the high convective dispersion in the hybrid electrophoresis microchip at this complexity level has been accurately and efficiently simulated by analytical models.

Computation efficiency. Finally, the drastic improvement in computational efficiency offered by the model over full numerical simulations should be discussed. Based on integration of parameterized and lumped elemental models, the schematic is reusable and allows efficient exploration of design parameter space. A non-expert user can quickly compose a complex design schematic by wiring the blocks representing elemental models and inputting parameters for a fast and reliable top-down iterative system-level design. Modifications of chip topology and dimensions can be readily and robustly evaluated using the model. This is in contrast to full numerical simulations, which are time-consuming for both problem setup and solution. Numerical simulations also involve subtle accuracy versus numerical stability tradeoffs, requiring the user to have expert knowledge in electrophoretic dispersion physics. Finally, the geometrical models used for numerical simulation cannot be reused when designs are modified. The system simulations are run on a multi-user, 10-CPU 360 MHz UltraSPARC II processors with 640MB RAM per CPU node. With these tools, complementary-turn channels are simulated using the behavioral model within 50 seconds with netlisting (necessary for the first of a series of iterative simulations) and less than 1 second without netlisting (for subsequent simulations in the iterative process) with accuracies reported in the examples above. In contrast, numerical simulations of such channels, conducted in FEMLAB 2.3b [152] on a PC with a Pentium IV 1.8 GHz processor and 1 GB of RAM, require 10 minutes (when the dimensionless times are large in Figure 4-6) to 39 hours (when the dimensionless times are small in Figure 4-11, requiring small mesh sizes for accuracy and stability). The numerical

simulation in Figure 4-16 for the hybrid network is performed on a multi-user, 2-CPU 1-GHz Sun Fire 280 processors with 4 GB RAM due to its demanding memory requirement, and costs around 4.5 days to achieve the reported accuracy. The computational advantage of the behavioral model is thus clear, making possible system-level optimal design that may involve hundreds or thousands of iterative simulations. Pfeiffer *et al*. [149] recently presented a synthesis engine in MATLAB [156] employing this model and optimized electrophoresis chip topology in 30 minutes for a two species separation system involving 21 elemental channels. Iterations for optimal microchip design would have taken several days if the numerical simulation had been used.

4.6 Summary

A behavioral model library for analyzing the dispersion of charged species molecules in complex separation microchannels has been presented. A microchannel of general shape has been decomposed into a system of element channels with simple geometries connected in series. Parameterized analytical models for elemental channels have been developed, and a representation of the entire electrophoresis channel has been obtained. The resulting system-level schematic simulation has been verified with experimental data and numerical analysis, and used to perform a systematic analysis of species band-broadening in serpentine and spiral-shaped electrophoresis channels, yielding insights into the effects of key dimensionless parameters. The model has demonstrated drastically improved computational efficiency over numerical simulations, and is thus well suited for optimal microchip design processes that typically involve large numbers of design iterations.

Parameterized behavioral dispersion models for element microchannels are the key components in the model library. Two types of element channels with uniform rectangular

cross sections, straight channels and circular turns have been considered. Such elements are amenable to analytical modeling and are sufficiently general to represent channels commonly used in the microchip electrophoresis community. The models hold for species bands with general initial shape, which allows us to consider the effects of initial skew on species band dispersion and the skew interaction between turns for the first time. This proves a key to modeling a channel system where all elements generally involve skewed species bands as input.

The system-level schematic has been used to perform a parametric study to account for the skew interactions in serpentine channels consisting of a pair of complementary turns. It has been found that when τ_t is relatively large (e.g., $\tau_t > 1$), the turn-induced variance is minimized and is independent of τ_s, while the overall variance arises primarily from contributions of diffusion and grows linearly with the dimensionless times. As a result, high accuracy is obtained and agreement with numerical simulations is within 1%. On the other hand, when τ_t is small (e.g., $\tau_t < 0.01$), there is strong convection in the turns. In this case, the turn-induced and overall variance both depends rather strongly on τ_s. For a large τ_s, the overall turn-induced variance is the sum of contributions from the individual turns, and the system simulation results agree with numerical analysis again within 1%. On the other hand, when τ_s is small, strong convective effects are present in both straight and turn elements, resulting in small turn-induced and overall variance. Errors in transition region modeling and in velocity approximation are more pronounced but are still within 11%.

Finally, the high computational efficiency of the model has allowed accurate system-level simulations of serpentine channels consisting of multiple pairs of complementary turns and multi-turn spiral-shaped channels to be performed for the first time. The model

has been applied to a serpentine channel with three pairs of complementary turns, and reveals trends in the effects of the dimensionless times τ_s and τ_t that are similar to single-pair complementary turns. That is, as τ_s and τ_t vary from small ($\tau_s = 0.0039$ and $\tau_t = 0.005$) to relatively large magnitudes ($\tau_t = 0.078$ and $\tau_s = 0.1$), the accuracy of the model, as compared with full numerical simulations, improves from 9.5% to 0.3%. Spiral-shaped channels differ from serpentine channels in that the skew, turn-induced variance and total variance always increase with the turn number, as the band skew in all turns has the same sense and does not cancel. The system simulation has been successfully applied to a five-turn spiral channel, and the results are within 12% compared with experimental data [144]. The simulation capabilities on hybrid electrophoretic separation networks including both serpentine and spiral topologies and involving coexisting skew strengthening and canceling effects have been eventually confirmed with excellent agreement with numerical simulations (1%).

4.7 Appendix

Extraction of Experimental and Numerical Data from the Literature.

Parameters for serpentine channels. Data are extracted from two experiments reported by Culbertson *et al.*[135]. In the first experiment, the two complementary turns each had mean radius 500 μm, and the inter-turn straight channel had length L_3 = 4000 μm. The most upstream and downstream channels (L_1 and L_5) respectively had lengths of 6000 μm (starting from injection point) and 1500 μm (at experimental detection point). The channel cross section was trapezoidal in shape but approximated by a rectangle of width 37 μm and depth 10 μm [147]. Electrophoresis of rhodamine B was performed in the channel

with a 50/50 (v/v) MeOH/20 mM sodium borate buffer. The average electrokinetic velocity was measured to be U = 0.0051 cm s^{-1} at E = 50 V cm^{-1} in the straight channel, and the diffusivity was found to be $D = 2.72\times10^{-10}$ m^2 s^{-1} by fitting the σ^2 vs. t experimental data to the equation $\sigma^2 = 2Dt$. With these parameters it can be calculated that w/r_c = 0.074, τ_t = 6.12 and τ_s = 15.6.

In the second experiment, the two complementary turns each had mean radius 125 μm, approximate channel width 50 μm [135, 147] and the inter-turn straight channel had length 4000 μm. The most upstream and downstream channels (L_1 and L_5) respectively had lengths 6000 μm (starting from injection point) and 1500 μm (at experimental detection point). The average velocity and diffusivity of the species (TRITC-Arg) were similarly determined to be U = 0.0717 cm s^{-1} at E = 600 V cm^{-1} and $D = 3.12\times10^{-10}$ m^2 s^{-1} respectively. With these parameters it can be calculated that w/r_c = 0.4, τ_t = 0.068 and τ_s = 0.696.

For the case of low τ_t and τ_s, a fabricated microchip of two complementary turns for electrophoresis of a *Hae*III digest of ϕX174 bacteriophage DNA in 1×TAE run buffer and HEC sieving matrix [145] has been modeled. Both turns had a mean radius 500 μm, and the length of the inter-turn straight channel was estimated to be 9330 μm. The most upstream and downstream channels (L_1 and L_5) had length 32000 μm and 9330 μm, respectively. The channel cross section was trapezoidal in shape but approximated by a rectangle of width 124 μm and the average electrokinetic velocity is estimated as 1200 μm s^{-1} at E = 300 V cm^{-1} based on published electropherograms [145, 151]. The molecular

diffusivity is $D = 1\times10^{-11}$ m^2 s^{-1}. Thus, it can be calculated that $w/r_c = 0.248$, $\tau_t = 8.5\times10^{-4}$ and $\tau_s = 5\times10^{-3}$.

Parameters for the spiral-shaped channel. The spiral-shaped electrophoresis microchannel investigated by Culbertson *et al*. [144] consisted of a straight channel and five 180°-turns with radii of 1.9, 1.8, 1.7, 1.6 and 0.8 cm, respectively. The most upstream straight channel L_1 was 2500 μm. Electrophoresis was performed in a 20 mM boric acid/100 mM TRIR buffer at electric field strengths of 370~1170 V cm^{-1}, giving an electrokinetic mobility about 4.14×10^{-8} m^2 s^{-1}V^{-1}, which is calculated from the electropherogram reported therein. A diffusivity of 4.33×10^{-10} m^2 s^{-1} measured at the moderate field in another straight channel using the same buffer and electric field range is assumed for the simulation. Detection was made at 22.2 cm downstream of the injector. The electric field used varied from 370 V cm^{-1} to 1170 V cm^{-1}. From these parameters, the following parameters are calculated: at E = 370 V cm^{-1}, $\tau_1 = 10.5$, $\tau_2 = 10$, $\tau_3 = 9.44$, $\tau_4 = 8.88$, $\tau_5 = 4.44$; at E = 770 V cm^{-1}, $\tau_1 = 5.06$, $\tau_2 = 4.8$, $\tau_3 = 4.53$, $\tau_4 = 4.27$, $\tau_5 = 2.13$; at E = 970 V cm^{-1}, $\tau_1 = 4.02$, $\tau_2 = 3.81$, $\tau_3 = 3.6$, $\tau_4 = 3.39$, $\tau_5 = 1.7$; and at E = 1170 V cm^{-1}, $\tau_1 = 3.33$, $\tau_2 = 3.16$, $\tau_3 = 2.98$, $\tau_4 = 2.8$, $\tau_5 = 1.4$.

Chapter 5 Modeling of Joule Heating Dispersion in Electrophoretic Separation Microchips

5.1 Introduction

For electrophoresis, high electric fields are preferentially used to reduce the separation time and minimize the band-broadening effects arising from molecular diffusion [151, 155] (Eqs. (4.1)~(4.3)). Sub-millisecond microchip electrophoresis has been successfully demonstrated using an extremely high electric field of 53 kV cm^{-1} [155]. This process, however, is accompanied by resistive heating (Joule heating), of the buffer as the electric field also induces a current. Joule heating leads to non-uniformities in the buffer temperature and locally alters species electrophoretic mobility, which contributes to dispersion. Joule heating can also be appreciable in microchannels of relatively large cross-sectional dimensions (larger heat generation and poorer heat dissipation), which are at times used to allow longer detection cells, higher detectability, reduced adsorption of analytes on channel walls, and less stringent requirements on sample injection schemes [157]. It is therefore important to develop models that account for the effects of Joule heating on analyte dispersion that will enable the optimal design of electrophoretic separation microchips.

Closed-form and parameterized models are highly desirable for describing Joule heating dispersion in microchip electrophoresis, as they provide computational efficiency appropriate for use in iterative design processes to explore the parameter space [149]. Taylor [158, 159] and Aris [150] pioneered studies of dispersion phenomena by considering dispersion of a solute in hydrodynamically driven flow in a circular capillary, and developed the classical Taylor-Aris theory in which dispersion at large solute migration

time (i.e., steady state) is represented by a constant dispersion coefficient. This theory has been used extensively in capillary electrophoresis. In particular, Knox *et al*. [160, 161] investigated Joule heating induced Taylor-Aris dispersion of electrophoresis in a circular capillary, while Cifuentes *et al*. [162] studied steady-state Joule heating induced dispersion in a rectangular capillary that is assumed to have an infinitely large aspect ratio. In the context of microchip electrophoresis, Molho [151] presented an analytical steady-state model for Joule heating induced dispersion in rectangular channels that is based on models developed for circular capillaries. For electrophoresis in a constricted turn, he also investigated dispersion effects of Joule heating and turn curvature at specific regimes, which were assumed to be decoupled. Jacobson *et al*. [155] used the results of Knox *et al.* for capillaries to evaluate Joule heating dispersion effects in rectangular microchannels. It is important, however, to note that in microchip-based electrophoretic separations, dispersion is often not in steady state due to short species residence times in the channel. The use of steady-state dispersion models for unsteady dispersion, as well as approximation of rectangular channels by capillaries, in general leads to significant errors. Unsteady dispersion in rectangular channels has been investigated by Doshi *et al*. [163] in the context of gravity-driven hydrodynamic flow. They found that such dispersion involves three stages characterized by diffusion time constants along the two cross-sectional dimensions, and differs distinctly from dispersion in hydrodynamic flow between two parallel plates, as discussed by Dorfman and Brenner [164].

In this chapter, a parameterized analytical model for Joule heating dispersion in electrophoretic separation microchannels is presented. Joule heating-induced variations in temperature and species electrophoretic velocities across the channel are first obtained to

establish the convection-diffusion equation, which is then formulated in terms of spatial moments of species concentration [150] (Section 5.2.1). The equation is then analytically solved to yield a distributed and a behavioral model for Joule heating induced dispersion, which holds for species bands of general initial shape in both straight channels and constant-radius turns (Section 5.2.3) in all mass transfer regimes, including unsteady dispersion processes that commonly occur in microchip electrophoresis. The distributed model is employed to study transient Joule heating dispersion behavior of a species band within a straight channel (Section 5.3), while the behavioral model is integrated into a system-level simulation to investigate the influence of geometrical, operational and material parameters on Joule heating dispersion in both straight channels and turns. The model is also validated with full numerical simulation results; very good agreement and impressive speedup have been demonstrated (Sections 5.3, 5.4 and 5.5). A summary of the chapter is presented in Section 5.6.

5.2 Joule Heating Dispersion Model

In this section, both distributed and behavioral models for Joule heating dispersion in straight channels and turns will be presented. The modeling of other separation elements, such as the injector, detector and reservoirs was discussed in the previous chapter.

5.2.1 Governing Equations

This subsection presents the governing equations for dispersion in the presence of Joule heating during the electrophoretic transport of a charged species in a microchannel. The microchannel is bounded by a pair of planes parallel to the chip surface, and a second pair of planes or a pair of concentric circular cylindrical surfaces perpendicular to the chip surface (Figure 5-1). The channel hence has constant rectangular cross sections with width

w, height *h*, and aspect ratio $\beta = w/h$. The line connecting the cross-sectional centers (the channel axis) is straight with length *L*, or a circular arc with mean radius r_c, included angle φ, and length $L = r_c\varphi$. In the latter case the channel is called a constant-radius turn, and it is assumed that the *width-to-radius ratio is small*: $b \triangleq w/r_c \ll 1$. It is also assumed that *the channel is long*, i.e. $w/L \ll 1$ and $h/L \ll 1$. These straight and constant-radius turn geometries are sufficiently general to be used to represent the majority of general-shaped microchannels that are commonly seen in practice [123].

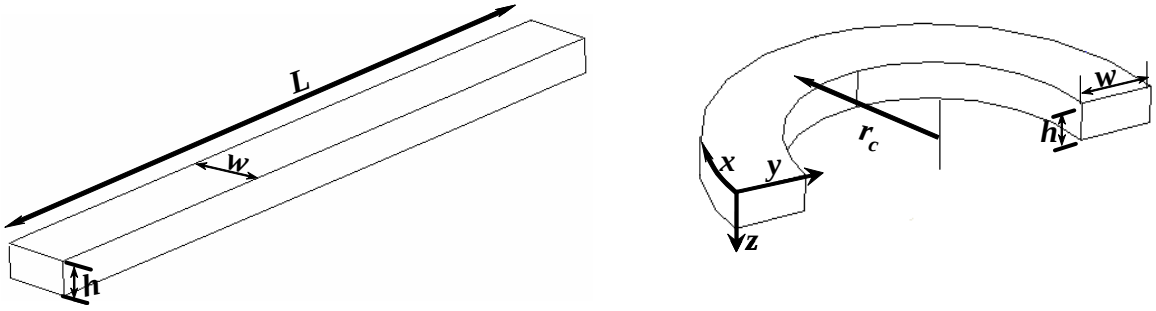

a b

Figure 5-1. Geometry and coordinate frame for (a) a straight channel and (b) a semi-circular turn.

The coordinate frame is shown in Figure 5-1b. The governing equations will be given for a constant radius-turn, which when $b = 0$, reduces to the special case of a straight channel. Given a voltage ΔV applied across the length of the channel, it can be shown that the electric field is approximately given by [123, 147]

$$(E_x, E_y, E_z) = (E_0[1+b(1/2 - y/w)],0,0) \tag{5.1}$$

where $E_0 = \Delta V/L$. That is, the electric field, directed along the channel axis, is constant in a straight channel, and varies linearly across the width of a turn.

The electric field induces a current in the conducting buffer generating heat $\dot{q}$ (Joule heating) [160, 161],

$$\dot{q} = \boldsymbol{\sigma} E^2 \tag{5.2}$$

where $\boldsymbol{\sigma}$ is the buffer's electric conductivity. Joule heating will cause temperature variations along the channel's cross section. Such temperature variations can be assumed in steady state, as the time required for the buffer to reach thermal equilibrium within the channel is generally much smaller than the characteristic diffusion time. For example, for a channel (h = 50 um) filled with an aqueous buffer, its thermal time constant is ~1.8×10^{-3} s, which is 100 fold less than the transverse diffusion time (~2.5×10^{-1} s) of an ionic species (D~1×10^{-9} m^2 s^{-1}). In addition, as the channel length is much larger than the cross-sectional dimensions, the temperature distribution can be assumed to be independent of the axial coordinate x. Thus, by neglecting terms of order b^2 or higher [147], the steady-state heat transfer problem is governed by a two-dimensional equation:

$$\frac{\partial^2 \theta}{\partial y^2} + \frac{\partial^2 \theta}{\partial z^2} = -\frac{\dot{q}}{k} \tag{5.3}$$

where $\theta = T - T_w$, T is the buffer temperature, T_w is the buffer temperature at the channel wall, and k is the buffer's thermal conductivity. Here, to a first approximation, T_w is taken to be uniform everywhere on the channel wall. This approximation is valid especially when the substrate is a good thermal conductor (e.g., silicon) or the microchannel within a thin chip has a large aspect ratio ($\beta \gg 1$), so that the temperature non-uniformity only occupies a small portion of the cross sectional perimeter (around the channel corner). In this case $\theta = 0$ everywhere on the channel wall.

The effect of Joule heating on electrophoretic transport is primarily manifested via the temperature dependence of the buffer viscosity $\boldsymbol{\eta}$. Within temperature ranges relevant to microchip electrophoresis, the viscosity is approximately linear in temperature:

$\boldsymbol{\eta} = \boldsymbol{\eta}_w\left(1-\alpha\theta\right)$, where $\boldsymbol{\eta}_w$ is the buffer viscosity at the channel wall, and α is the buffer's temperature coefficient of viscosity [160, 161]. The electrophoretic mobility of the species is given by $\mu = a\boldsymbol{\varepsilon}\boldsymbol{\zeta}/\boldsymbol{\eta}$, where $\boldsymbol{\varepsilon}$ is the permittivity of the buffer, $\boldsymbol{\zeta}$ the zeta potential and a a constant [161]. It has been experimentally shown that $\boldsymbol{\varepsilon}\boldsymbol{\zeta}$ is independent of temperature [165]**.** Therefore μ depends on temperature only via the temperature dependence of viscosity. When $\alpha\theta \ll 1$, $\mu = \mu_w\left(1+\alpha\theta\right)$ is valid, where $\mu_w = a\boldsymbol{\varepsilon}\boldsymbol{\zeta}/\boldsymbol{\eta}_w$. It follows that the electrophoretic velocity, given by $(v_x, v_y, v_z) = \left(\mu E_x, 0, 0\right)$ [151, 160-162], is non-uniform over the channel's cross section, and causes dispersion of the species band. The combined effect of Joule heating and turn geometry on dispersion is represented by an apparent axial species velocity $u_x = v_x\big/\left(1-b\left(1/2-y/w\right)\right)$ [147]. For convenience, a dimensionless frame $\xi = \left(x-Ut\right)/h$, $\eta = y/h$ and $\zeta = z/h$ moving at the average apparent species velocity $U = u_{w,0}\left(1+\alpha\bar{\theta}\right)$ and a dimensionless time $\tau = Dt/h^2$ are used. Here $u_{w,0} = \mu_w E_0$ and the overbar denotes the cross-sectional average. The three-dimensional convection-diffusion equation, which governs the species transport, then takes the form [123]

$$\begin{aligned} &\frac{\partial c}{\partial \tau} = \frac{\partial^2 c}{\partial \xi^2} + \frac{\partial^2 c}{\partial \eta^2} + \frac{\partial^2 c}{\partial \zeta^2} - \mathrm{Pe}\,\chi\frac{\partial c}{\partial \xi} \\ &\partial c/\partial \eta\big|_{\eta=0,\beta} = 0, \quad \partial c/\partial \zeta\big|_{\zeta=0,1} = 0, \quad c\big|_{\tau=0} = c\left(\xi,\eta,\zeta,0\right) \end{aligned} \tag{5.4}$$

where c is the species concentration and $\mathrm{Pe} = Uh/D$ is the Peclet number. Here, χ is the normalized apparent species velocity with respect to U and is given by

$$\chi(\eta,\zeta) = \frac{u_x(\eta,\zeta)-U}{U} = \begin{cases} \varepsilon\left(\phi\text{-}\bar{\phi}\right)\big/\left(1+\varepsilon\bar{\phi}\right) & \text{for a straight channel} \\ \left[\varepsilon\left(\phi\text{-}\bar{\phi}\right)+b\left(1-2\eta/\beta\right)\right]\big/\left(1+\varepsilon\bar{\phi}\right) & \text{for a turn} \end{cases} \tag{5.5}$$

where $\varepsilon = \alpha(\boldsymbol{\sigma} E_0^2 h^2 / k)$ and $\phi = \theta / (\boldsymbol{\sigma} E_0^2 h^2 / k) = \alpha\theta / \varepsilon$, which can be found from Eqs. (5.1) -(5.3). From these equations, it can be seen that $\boldsymbol{\sigma} E_0^2 h^2 / k$ is a characteristic temperature due to Joule heating. Therefore the dimensionless parameter ε is the characteristic of Joule heating intensity and will be hereafter called the Joule heating coefficient. Also note that $\sqrt{\varepsilon}$ can be thought of as dimensionless electric field strength. The dimensionless variable ϕ, which depends only on the dimensionless curvature *b* and aspect ratio β (Section 5.2.2), can be interpreted as the normalized buffer temperature. Terms of the second or higher order in *b* and α have been neglected for a turn in Eq. (5.5).

Eq. (5.4) can be formulated in a closed form in terms of spatial moments of the species concentration [150, 151] using the method of moments presented in the previous chapter with the difference being that there is non-uniformity in the temperature and species velocity along both η and ζ dimensions. Specifically, if the entire species band is contained in the channel, Eq (5.4) holds effectively for $-\infty < \xi < \infty$ such that $c \to 0$ as $\xi \to \pm\infty$. Define

$$\begin{aligned} c_p(\eta,\zeta,\tau) &= \int_{-\infty}^{\infty} \xi^p c(\xi,\eta,\zeta,\tau) d\xi \qquad \text{and} \\ m_p(\tau) &= \overline{c}_p = \frac{1}{\beta}\int_0^1\int_0^\beta c_p d\eta d\zeta \quad (p = 0,1,2,...) \end{aligned} \tag{5.6}$$

where c_p is the p^{th} moment of the concentration in an axial filament of the species band that intersects the cross sections at η and ζ, and m_p is the p^{th} moment of the cross-sectional average concentration, respectively. Eq. (5.4) can be integrated with respect to ξ to yield

$$\begin{aligned} &\frac{\partial c_p}{\partial \tau} = \frac{\partial^2 c_p}{\partial \eta^2} + \frac{\partial^2 c_p}{\partial \zeta^2} + p(p-1)c_{p-2} + p\,\mathrm{Pe}\,\chi c_{p-1} \\ &\partial c_p / \partial \eta\big|_{\eta=0,\beta} = 0, \quad \partial c_p / \partial \zeta\big|_{\zeta=0,1} = 0, \quad c_p\big|_{\tau=0} = c_{p0}(\eta,\zeta) = \int_{-\infty}^{\infty} c(\xi,\eta,\zeta,0)\xi^p d\xi. \end{aligned} \tag{5.7}$$

which can be further integrated over the cross section to obtain

$$\frac{dm_p}{d\tau} = p\left(p-1\right)\overline{c_{p-2}} + p\,\mathrm{Pe}\,\overline{\chi c_{p-1}}$$
$$m_p\left(0\right) = m_{p0} = \frac{1}{\beta}\int_0^1\int_0^\beta c_{p0}(\eta,\zeta)d\eta d\zeta \tag{5.8}$$

In both Eqs. (5.7) and (5.8), any term that contains c_i with $i < 0$ is set to zero. To determine the broadening of the species band, these equations can be solved to obtain moments up to the second order (Chapter 4).

It should be noted that in addition to the electrophoretic mobility μ, other material properties, such as the buffer's electric conductivity σ, thermal conductivity k, and the species diffusivity D, in general also vary with temperature gradients within the channel. However, the temperature dependence of these parameters influences dispersion less significantly than the temperature dependence of μ. For example, from Eqs. (5.2) and (5.3), the non-uniform component of Joule heating, due to the temperature dependence of σ and k, is generally small compared with the total Joule heating. In addition, from a more general form of the convection-diffusion equation [112], it can be shown that the effect on dispersion resulting from the temperature dependence of D, as opposed to that of μ, is of second order. Therefore, it is reasonable to assume, as in the formulation above, that all material properties except μ are constant [160, 161] and can be evaluated at the average buffer temperature in the channel.

5.2.2 Distributed Model

This section presents a distributed analytical model for dispersion of electrophoretic transport in the presence of Joule heating within a straight channel or a turn. The model is obtained by first solving Eq. (5.3) for cross-sectional temperature distributions. Eq. (5.5)

then provides the electrophoretic velocity profile, which can be used to solve Eqs. (5.7) and (5.8) for the moments of the species concentration and hence the dispersion characteristics of the species band.

The normalized buffer temperature ϕ, introduced with Eq. (5.5), can be found from Eqs. (5.1)-(5.3):

$$\phi = (1+b)\phi_1 + \frac{2b\phi_2}{\beta} \tag{5.9}$$

where

$$\phi_1 = \frac{1}{2}\left\{\frac{1}{4} - \left(\zeta - \frac{1}{2}\right)^2 + \sum_{i=1}^{\infty} \frac{(-1)^i}{\kappa_i^3} \frac{\cosh\left(\kappa_i\left(2\eta - \beta\right)\right)}{\cosh\left(\kappa_i \beta\right)} \cos\left(\kappa_i\left(2\zeta - 1\right)\right)\right\}$$

$$\phi_2 = \sum_{i=1}^{\infty} \frac{2\beta(-1)^{i+1}}{i\pi \cdot \lambda_i}\left(-1 + \frac{e^{(1-\zeta)\sqrt{\lambda_i}} + e^{\zeta\sqrt{\lambda_i}}}{1 + e^{\sqrt{\lambda_i}}}\right) \cdot \sin\left(\frac{i\pi\eta}{\beta}\right)$$

with $\kappa_i = (2i-1)\pi/2$ and $\lambda_i = (i\pi/\beta)^2$ (i=1, 2, 3,…).

The normalized velocity profile χ is then obtained from Eq. (5.5) and substituted into Eqs. (5.7) and (5.8), which can be solved for the moments of the species concentration. The solution procedure has been outlined in the previous chapter; with the difference being that χ here includes a contribution from the Joule heating velocity and varies in both cross-sectional dimensions. First, by conservation of mass, m_0 is constant. $m_0 = 1$ is chosen without loss of generality. In addition,

$$c_0(\eta, \zeta, \tau) = \int_{-\infty}^{\infty} c(\xi, \eta, \zeta, \tau) d\xi = 1 \tag{5.10}$$

provided the initial condition is such that $\int_{-\infty}^{\infty} c(\xi, \eta, \zeta, 0) d\xi = 1$. This indicates that if all infinitesimal axial species band filaments have the same mass initially, then this will be the

case at all times. This is typically true in practice (Chapter 4) and will be assumed in the remainder of this chapter.

For the first moment, it can be found that $m_1(\tau) = 0$ if the origin of the moving frame is chosen such that it initially coincides with the species band's centroid. Thus, the centroid and the moving origin coincide at all times if they do so initially. The first moment c_1, which represents the skew of the species band, is found to be

$$c_1(\eta,\zeta,\tau) = \sum_{m=0}^{\infty}\sum_{n=0}^{\infty} S_{nm}(\tau)\cos(n\pi\zeta)\cos\left(m\pi\frac{\eta}{\beta}\right) \tag{5.11}$$

where $S_{00}(\tau) = S_{00}(0)$ and

$$S_{nm}(\tau) = S_{nm}(0)e^{-\lambda_{nm}\tau} + \frac{\mathrm{Pe}\chi_{nm}\left(1-e^{-\lambda_{nm}\tau}\right)}{\lambda_{nm}} \quad \text{if } n+m \geq 1, \tag{5.12}$$

with $S_{nm}(0) = \nu_{nm}\int_0^1\int_0^\beta c_{10}(\eta,\zeta)\cos(n\pi\zeta)\cos(m\pi\eta/\beta)\,d\eta d\zeta$ and $\lambda_{nm} = (n\pi)^2 + (m\pi/\beta)^2$ ($n \geq 0$ and $m \geq 0$). Here, ν_{nm} is defined as $\nu_{00} = 1/\beta$, $\nu_{0m} = 2/\beta$, $\nu_{n0} = 2/\beta$ and $\nu_{nm} = 4/\beta$ for $n > 1$ and $m > 1$, c_{10} is the initial skew (Eq.(5.7)). The Fourier coefficients for the normalized velocity χ are $\chi_{00} = 0$, $\chi_{0m} = \varepsilon\phi_{0m} + 4b(1-(-1)^m)/\lambda_m$, $\lambda_m = (m\pi)^2$, $\chi_{nm} = \varepsilon\phi_{nm}$, $\phi_{nm} = \nu_{nm}\int_0^1\int_0^\beta \phi\cos(n\pi\zeta)\cos(m\pi\eta/\beta)\,d\eta d\zeta$, $n \geq 0$ and $m \geq 0$. In contrast to the skew c_1 in the previous chapter, here it is a function of both transverse dimensions (η and ζ) and skew coefficients essentially are expressed and conveyed as a matrix.

The second-order moment m_2 can be found by solving Eq. (5.8) with $p = 2$. Then, the relationship $\sigma^2 = h^2\left(m_2/m_0 - m_1^2/m_0^2\right)$ [151] yields the variance of the species band:

$$\frac{\Delta\sigma^2(\tau)}{h^2} = 2\tau + \sum_{\substack{n=0 \\ n+m\geq 1}}^{\infty}\sum_{m=0}^{\infty}\frac{2S_{nm}(0)\,\mathrm{Pe}\chi_{nm}\left(1-e^{-\lambda_{nm}\tau}\right)}{\beta\nu_{nm}\lambda_{nm}} + \sum_{\substack{n=0 \\ n+m\geq 1}}^{\infty}\sum_{m=0}^{\infty}\frac{2\varepsilon^2\mathrm{Pe}^2\phi_{nm}^2\left(e^{-\lambda_{nm}\tau}+\lambda_{nm}\tau-1\right)}{\left(1+\varepsilon\bar{\phi}\right)^2\beta\nu_{nm}\lambda_{nm}^2} + \sum_{m=1,3,5\ldots}^{\infty}\frac{64b^2\mathrm{Pe}^2\left(e^{-\lambda_{0m}\tau}+\lambda_{0m}\tau-1\right)}{\left(1+\varepsilon\bar{\phi}\right)^2\lambda_{0m}^2\lambda_m^2} + \sum_{m=1,3,5\ldots}^{\infty}\frac{16\varepsilon b\mathrm{Pe}^2\phi_{0m}\left(e^{-\lambda_{0m}\tau}+\lambda_{0m}\tau-1\right)}{\left(1+\varepsilon\bar{\phi}\right)^2\lambda_{0m}^2\lambda_m} \tag{5.13}$$

where $\Delta\sigma^2(\tau)=\sigma^2(\tau)-\sigma^2(0)$; $\sigma^2(\tau)$ and $\sigma^2(0)$ are the species band variance at times τ and 0 respectively; τ can be related to the channel's axial coordinate by $\tau = xD/\left(Uh^2\right)$. The right-hand side of this equation shows that the increase in variance consists of contributions from molecular diffusion (the first term), the initial skew (the second term), Joule heating effects alone (the third term), turn curvature alone (the fourth term), and interactions between Joule heating and turn curvature (the last term). To our knowledge this is the first time these interactions are considered in microchip electrophoresis models in all mass regimes and in a coupled manner.

Now several special cases of electrophoretic transport are considered. First, note that if $\varepsilon \ll 1$, Eq. (5.13) indicates that Joule heating can be ignored. Species band broadening will then be exclusively caused by diffusion and turn geometry, which recovers the turn-induced dispersion model (4.23) in the previous chapter. Next, the Joule heating dispersion model can be considerably simplified for straight channels (b = 0). Assuming no initial skew ($S_{nm}(0)$ = 0) for simplicity, Eqs. (5.12) and (5.13) are simplified to

$$S_{nm}(\tau) = \frac{\varepsilon\mathrm{Pe}_w\phi_{nm}\left(1-e^{-\lambda_{nm}\tau}\right)}{\lambda_{nm}}, \quad \text{if } n+m\geq 1 \tag{5.14}$$

$$\frac{\Delta\sigma^2(\tau)}{h^2} = 2\tau + \frac{2\varepsilon^2 \mathrm{Pe}_w^2}{\beta} \sum_{\substack{n=0 \\ n+m\geq 1}}^{\infty} \sum_{m=0}^{\infty} \frac{\phi_{nm}^2 \left(e^{-\lambda_{nm}\tau} + \lambda_{nm}\tau - 1\right)}{\nu_{nm}\lambda_{nm}^2} \tag{5.15}$$

where $\mathrm{Pe}_w = \dfrac{\mathrm{Pe}}{\left(1+\varepsilon\bar{\phi}\right)} = \dfrac{u_{w,0}D}{h}$ is the Peclet number defined using the electrophoretic species velocity at channel walls and independent of aspect ratio β. Define a dispersion coefficient by $K = \frac{1}{2}d(\Delta\sigma^2)/dt$. In the presence of Joule heating, Eq. (5.15) can be used to obtain the dispersion coefficient for a straight channel:

$$K = D\left(1+\gamma\varepsilon^2\mathrm{Pe}_w^2\right), \quad \text{where} \quad \gamma = \frac{1}{\beta}\sum_{n=0}^{\infty}\sum_{m=0}^{\infty}\frac{\phi_{nm}^2}{\nu_{nm}\lambda_{nm}}\left(1-e^{-\lambda_{nm}\tau}\right) \tag{5.16}$$

It can be seen that $K = D$ if Joule heating is absent and band broadening is caused by diffusion only. The dispersion coefficient depends on cross-sectional shape through γ, which is hence called the shape factor. It is important to note that γ is generally time-dependent, and hence Joule heating effects can have different characteristics at different times (regimes). When time is sufficiently large (i.e., $\tau\to\infty$) the shape factor approaches an asymptotic value

$$\gamma_\infty = \frac{1}{\beta}\left(\sum_{n=0}^{\infty}\sum_{m=0}^{\infty}\frac{\phi_{nm}^2}{\nu_{nm}\lambda_{nm}}\right) \tag{5.17}$$

The skew coefficients correspondingly take on asymptotic values $S_{nm}(\infty) = \varepsilon\mathrm{Pe}_w\phi_{nm}/\lambda_{nm}$ ($n+m \geq 1$).

It is interesting to note that the shape factor given by Eq. (5.16) or (5.17) does not approach that for the electrophoretic transport between two parallel plates separated by h. It can be shown that for the parallel-plate case, a dispersion coefficient K can also be defined via the first equation of (5.16), with the shape factor given by

$\gamma = \sum_{n=2,4,6,\ldots}^{\infty} (e^{-\lambda_n \tau} + \lambda_n \tau - 1)/\lambda_n^4$. As $\tau \to \infty$, this expression tends to an asymptotic value γ_∞ = 1/30240, which differs from the limiting value of (5.17) as $\beta \to \infty$.

5.2.3 Behavioral Model

Eq. (5.13) shows the evolution of species band spreading within a channel. With the knowledge of the residence time of the species band, the behavioral model that correlate the species dispersion states at element terminals can be attained in the same manner as that in the previous chapter. The dimensional (Δt) and dimensionless (τ_R) residence times of the centroid of a species band in an element channel are given by,

$$t_{out} - t_{in} = \Delta t = \frac{L}{U} \text{ and } \tau_R = \frac{\Delta t \cdot D}{h^2} \tag{5.18}$$

where indices *in* and *out* represent the quantities at inlet and outlet of the channel.

The variance and Fourier coefficients of skew is respectively given by

$$S_{nm}^{(out)} = S_{nm}^{(in)} e^{-\lambda_{nm}\tau_R} + \frac{\varepsilon \mathrm{Pe_w} \phi_{nm} \left(1 - e^{-\lambda_{nm}\tau_R}\right)}{\lambda_{nm}}, \quad \text{if } n+m \geq 1 \tag{5.19}$$

$$\begin{aligned} \frac{\sigma_{out}^2}{h^2} = \frac{\sigma_{in}^2}{h^2} + 2\tau_R + \sum_{\substack{n=0 \\ n+m\geq 1}}^{\infty} \sum_{m=0}^{\infty} \frac{2 S_{nm}^{(in)} \mathrm{Pe} \chi_{nm} \left(1 - e^{-\lambda_{nm}\tau_R}\right)}{\beta \nu_{nm} \lambda_{nm}} \\ + \sum_{\substack{n=0 \\ n+m\geq 1}}^{\infty} \sum_{m=0}^{\infty} \frac{2\varepsilon^2 \mathrm{Pe}^2 \phi_{nm}^2 \left(e^{-\lambda_{nm}\tau_R} + \lambda_{nm}\tau_R - 1\right)}{\left(1 + \varepsilon\bar{\phi}\right)^2 \beta \nu_{nm} \lambda_{nm}^2} \end{aligned} \tag{5.20}$$

for a straight channel and

$$S_{nm}^{(out)} = S_{nm}^{(in)} e^{-\lambda_{nm}\tau_R} + \frac{\mathrm{Pe} \chi_{nm} \left(1 - e^{-\lambda_{nm}\tau_R}\right)}{\lambda_{nm}} \quad \text{if } n+m \geq 1, \tag{5.21}$$

$$\frac{\sigma_{out}^2}{h^2}=\frac{\sigma_{in}^2}{h^2}+2\tau_R+\sum_{\substack{n=0\\n+m\geq 1}}^{\infty}\sum_{m=0}^{\infty}\frac{2S_{nm}^{(in)}\mathrm{Pe}\chi_{nm}\left(1-e^{-\lambda_{nm}\tau_R}\right)}{\beta\nu_{nm}\lambda_{nm}}$$
$$+\sum_{\substack{n=0\\n+m\geq 1}}^{\infty}\sum_{m=0}^{\infty}\frac{2\varepsilon^2\mathrm{Pe}^2\phi_{nm}^2\left(e^{-\lambda_{nm}\tau_R}+\lambda_{nm}\tau_R-1\right)}{\left(1+\varepsilon\bar{\phi}\right)^2\beta\nu_{nm}\lambda_{nm}^2}$$
$$+\sum_{m=1,3,5...}^{\infty}\frac{64b^2\mathrm{Pe}^2\left(e^{-\lambda_{0m}\tau_R}+\lambda_{0m}\tau_R-1\right)}{\left(1+\varepsilon\bar{\phi}\right)^2\lambda_{0m}^2\lambda_m^2} \tag{5.22}$$
$$+\sum_{m=1,3,5...}^{\infty}\frac{16\varepsilon b\mathrm{Pe}^2\phi_{0m}\left(e^{-\lambda_{0m}\tau_R}+\lambda_{0m}\tau_R-1\right)}{\left(1+\varepsilon\bar{\phi}\right)^2\lambda_{0m}^2\lambda_m}$$

for a turn. By assuming a Gaussian distribution of the average species concentration c_m at element terminals, the amplitude (A) of the species band can be obtained by

$$A_{out}\Big/A_{in}=\sqrt{\sigma_{in}^2/\sigma_{out}^2} \tag{5.23}$$

5.2.4 Model Extensibility to Electroosmotic Flow

Thus, an analytical behavioral model for dispersion due to Joule heating focusing on electrophoresis has been derived. Joule heating dispersion in electroosmotic flow (EOF) is not considered in the model, but may be addressed by conceptually similar approaches. In particular, for the special case of a straight channel, dispersion caused by EOF may actually be negligible if the electric double layer is thin compared with the channel cross-sectional dimensions; if the channel wall temperature T_w is uniform (otherwise, additional dispersion due to the dependence of EOF mobility on temperature would need to be included). Then, the current model will still be valid if the moving frame is given velocity $U+U_{eof}$, where U_{eof} is the EOF velocity (which is uniform over the channel cross section) and the residence time in Eq. (5.25) is defined by $\tau_R=LD\Big/\left(\left(U+U_{eof}\right)h^2\right)$.

5.3 Mass Transfer Regimes of Joule Heating Dispersion

One of the most significant contributions of the present work beyond the previous studies is that the model can accurately capture disparate mass transfer regimes of Joule heating dispersion. In this section, effects of the dimensionless separation time τ on the Joule heating dispersion coefficient K in a straight channel with different aspect ratios β will be considered. Note that K characterizes the time rate of variance growth for the species band. Although obtained in the context of a straight channel, the results are also valid for turns and can be used to qualitatively interpret the simulation results below.

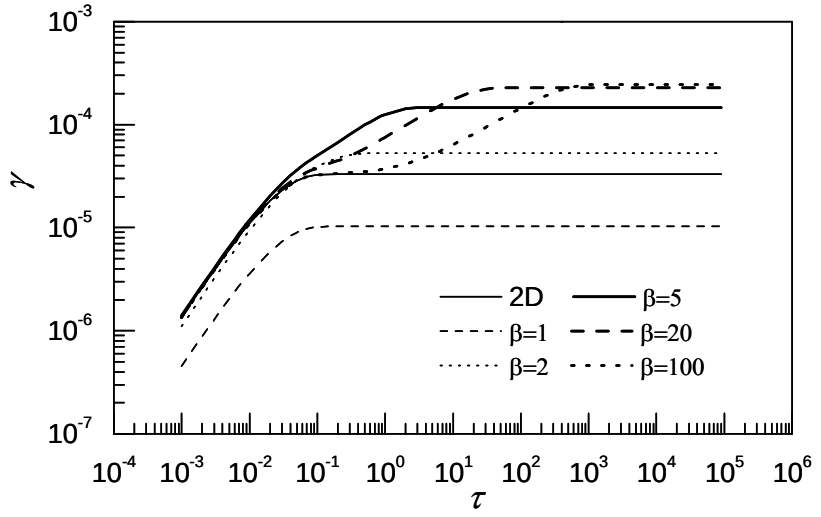

Figure 5-2. Shape factor γ as a function of the dimensionless time τ in a straight channel with different aspect ratios.

In general, K is a function of the species migration time τ. According to Eq. (5.16), the dependence of K on both τ and β is captured by the shape factor γ. A species band that is initially unskewed will be studied. Similar discussions can be made for the case of an initially skewed species band by considering the initial skew effect (the second term in Eq. (4.23)). As shown in Figure 5-2, for all aspect ratios, γ increases with τ and eventually approaches an asymptotic constant value (i.e. the dispersion reaches steady state). This

process is characterized by two diffusion time constants: $t_d = h^2/2D$ for depthwise diffusion and $t_w = w^2/2D$ for widthwise diffusion. Note that $t_w \geq t_d$ as $\beta \geq 1$ (the corresponding dimensionless time constants are $\tau_d = 0.5$ and $\tau_w = 0.5\beta^2$). For relatively large aspect ratios (e.g. $\beta > 5$), these two time constants are distinctly different, and the dependence of γ on τ can be divided into three regimes. The first regime is dominated by depthwise diffusion, which occurs when $\tau < \tau_d$. In this regime, the dimensionless time is small and widthwise diffusion has not started to influence the shape factor. Thus, it is insensitive to the aspect ratio except for $\beta = 1$ (there is a strong interaction between diffusion processes in both cross-sectional dimensions). At the low end of this regime, i.e. $\tau < 0.1\tau_d$, γ increases approximately linearly with τ, and the channel can be reasonably approximated as a pair of parallel plates. On the other hand, in the second regime in which the dimensionless time is sufficiently large (i.e. $\tau > \tau_w$), diffusion in both widthwise and depthwise dimensions is in steady state. The overall dispersion process thus is also in steady state, and the shape factor is approximately a constant asymptotic value γ_∞ (Eq. (5.17)). The overall dispersion can be represented by a constant dispersion coefficient (Taylor-Aris dispersion coefficient). In the third regime, which corresponds to the transition between the first two regimes, diffusion is in steady state in the depthwise dimension, but not the widthwise dimension. In this case, there is a plateau for γ that differs from its steady-state value. Such a plateau is referred to as a pseudo-steady state [163]. It is also interesting to note that in the transition regime, γ is not monotonic in the aspect ratio (i.e. γ is larger for $\beta = 5$ than for $\beta = 20$ and $\beta = 100$). Figure 5-2 also shows the shape factor at aspect ratios that are close to unity. In this case, $t_w \sim t_d$ (i.e. the time constants do not differ significantly). The transition regime accordingly

disappears, and the shape factor increases with time almost linearly until reaching steady state.

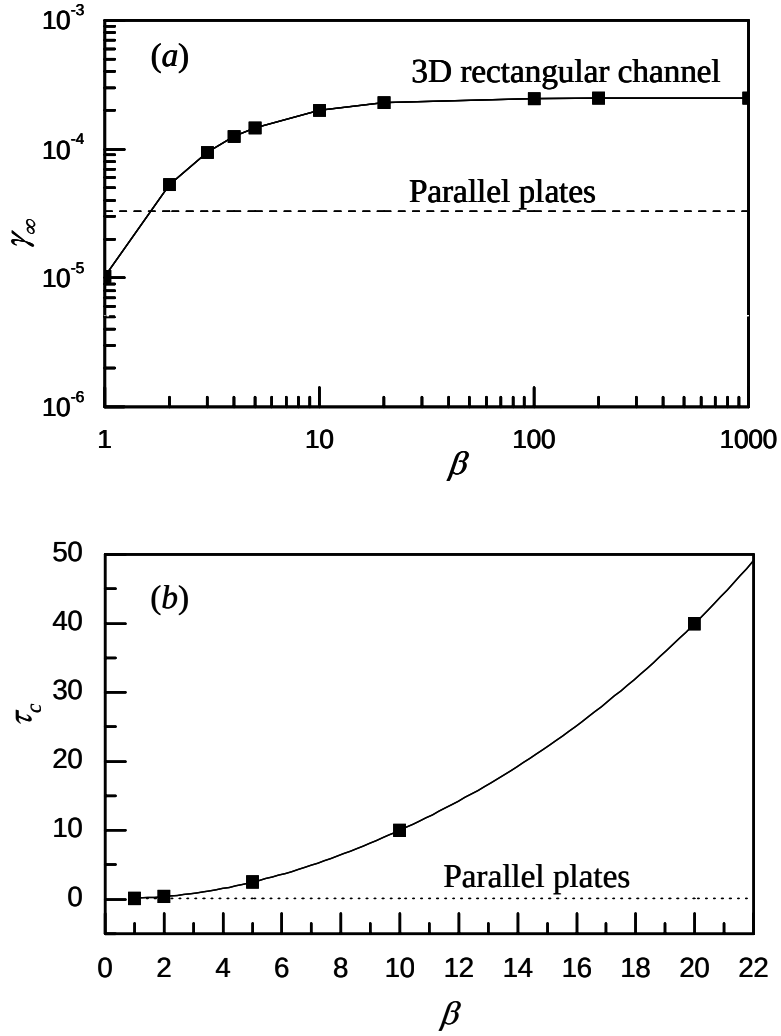

Figure 5-3. (a) The influence of the aspect ratio on the steady-state shape factor (γ_∞) in a straight channel. (b) The dependence of the critical dimensionless time τ_c on the aspect ratio.

Figure 5-3 shows that the influence of the aspect ratio on the steady-state shape factor (γ_∞) and the critical dimensionless time τ_c, defined by $\gamma(\tau_c) = 0.99\gamma_\infty$, which is the time required for dispersion to reach steady state. It can be seen that γ_∞ increases monotonically with β since channels of larger aspect ratios allow less efficient heat dissipation. At sufficiently large aspect ratios (i.e. $\beta \to \infty$), the steady-state shape factor approaches an

asymptotic value: $\gamma \to 2.6\times10^{-4}$. It is important to note that this differs drastically (by a factor of 7.9) from the shape factor for dispersion of an electrophoresis species band between a pair of parallel plates, which is also shown in Figure 5-3a. Therefore, it is inappropriate to describe Joule heating dispersion using the parallel-plate approximation for rectangular channels. As shown in Figure 5-3b, the critical dimensionless time τ_c is nearly proportional to the square of the aspect ratio β, which is consistent with identifying the steady-state regime with the condition $\tau > \tau_w = 0.5\beta^2$. This condition is practically useful to determine the appropriateness of representing Joule heating dispersion by a constant dispersion coefficient (i.e. Taylor-Aris dispersion). For example, in the previously described experiment data [155], the dimensionless time for the band to arrive at the detection point is 0.005, which is much smaller than $\tau_c \approx 1.3$ (for $\beta = 3.7$). Therefore, the constant Taylor-Aris dispersion coefficient does not apply and the regime in which depthwise diffusion dominates should be considered.

5.4 Joule Heating Effects in Straight Channels

In this section, the analytical Joule heating dispersion model for a straight channel is first validated with numerical simulations. Then, a parametric study is performed to explore the design parameter space and investigate the dependence of Joule heating dispersion on the applied electric field, channel length and aspect ratio.

5.4.1 Model Validation

The model-predicted evolution of the variance of a species band in a straight channel is compared with numerical results. In this comparison, the channel is given a fixed width h = 50 μm with an aspect ratio β varying from 1 to 8. The following parameters are used: $\sigma^2(0)$ = 3600 μm^2 and $S_{nm}(0) = 0$ (t = 0 is the time instant when the band's centroid is at the

channel entrance), E = 3.0 kV cm^{-1}, μ_w = 2×10^{-8} m^2 V^{-1}s^{-1}, k = 0.6 W m^{-1} K^{-1}, α = 0.025 K^{-1}, σ = 0.1 S m^{-1}, and D = 3.0×10^{-10} m^2 s^{-1}. These values correspond to Pe = 1072 and ε = 0.94. As shown in Figure 5-4, excellent agreement can be observed between the analytical modeling and numerical results (within 2%). When t is fixed, both analytical and numerical results indicate that band broadening generally increases with β, but not in a monotonic manner. This is attributed to the role of transient dispersion behavior explained in Figure 5-2.

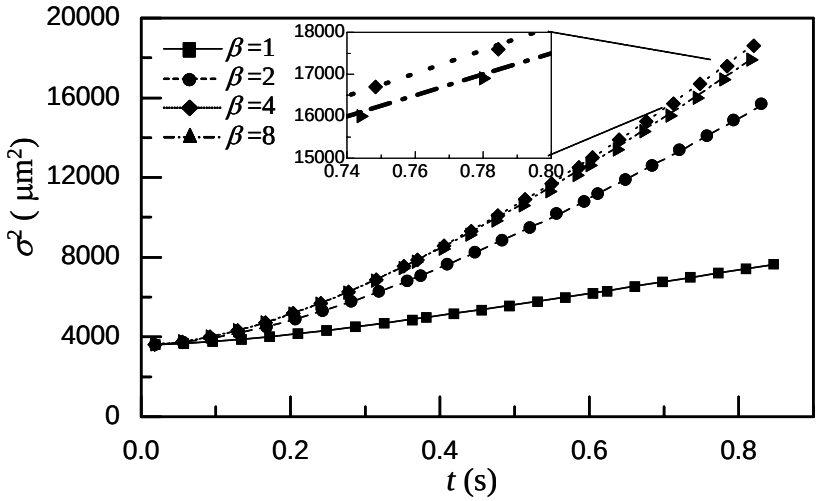

Figure 5-4. Comparison of variances computed from the analytical model (lines) and numerical simulations (symbols) in a straight channel.

5.4.2 Parametric Analysis

This section will demonstrate the utility of the behavioral model by applying it to a parametric analysis of Joule heating dispersion for the design of a straight electrophoresis microchannel. In practice, chip designers are primarily interested in the resolving power at the outlet of the electrophoresis channel. Therefore, the plate number [154, 166] is employed as a measuring index of separation performance (Chapter 4),

$$N = \frac{L^2}{\sigma_{out}^2} \tag{5.24}$$

and the dimensionless residence time is given by,

$$\tau_R = \Delta t \cdot D/h^2 = \left(L/h\right)/\mathrm{Pe} \tag{5.25}$$

where L is the length of the separation channel ($L = \varphi r_c = \varphi\beta h/b$ for a turn), and $\Delta t = L/U$ is the dimensional residence time of the centroid of the species band in the channel.

It can be shown from Eqs. (5.20), (5.24) and (5.25) that the plate number N depends on parameters Pe, ε, L/h and β for an initial uniform ($S_{nm}^{(in)} = 0$) species band in a straight channel. For convenience of analysis and to aid intuition, the effects of these parameters are considered by examining the dependence of N on E_0 as β (Figure 5-5) or L/h (Figure 5-6) is varied. In this parametric analysis, the values of μ_w, k, α, σ and D are the same as those used above in the numerical verification; $\sigma_{in}^2 = 0$ and $0.1 < E_0 < 3$ kV cm^{-1} (correspondingly $0.001 < \varepsilon < 0.94$). As shown in Figure 5-5 (in which L/h=100 is fixed), N initially increases with E_0 until achieving a maximum ($N_{\max}$), and then decreases with E_0. In addition, N is virtually the same at sufficiently low E_0 for all β considered. This is because at low electric fields, Joule heating effects are negligible and N is primarily determined by the effect of axial molecular diffusion that decreases with E_0. As E_0 increases Joule heating effects become increasingly significant and eventually dominate the dispersion causing N to decrease. The value of $N_{\max}$ varies with β and is the largest ($N_{\max} \approx 22800$) for $\beta = 1$. This is not surprising, since of all rectangular cross sections (for same depth h), the square shape allows the most efficient heat dissipation and minimizes Joule heating effects. While $N_{\max}$ generally decreases with β, it is interesting to note that the decrease is not monotonic. For example, $N_{\max}$ for $\beta = 8$ is slightly higher than for $\beta = 4$. This is because as the band

arrives at the channel exit (with the channel length fixed by holding L/h=100 constant), dispersion has reached steady state in both cross-sectional dimensions for β = 4 (see discussion in Figure 5-2), but is still in the transient regime in the widthwise dimension for β = 8, resulting in a shape factor γ and variance that is smaller than those in steady state for a lower aspect ratio [163, 167].

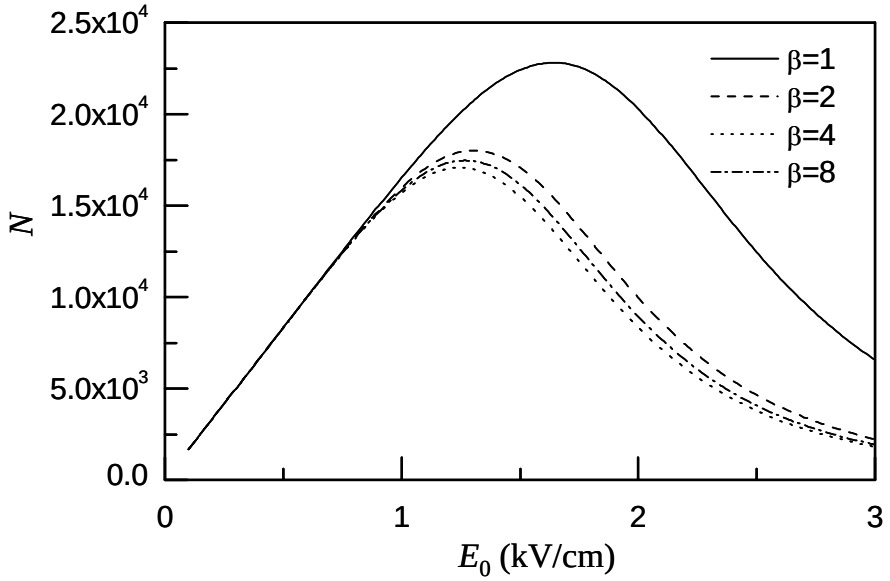

Figure 5-5. Parametric analysis of the dependence of the plate number N on the average electric field E_0 in a straight channel with different aspect ratios.

The effect of the dimensionless channel length L/h on Joule heating dispersion is shown in Figure 5-6 (in which β = 8 is fixed). Here too, the plate number N exhibits a maximum as the electric field E_0 increases for the same reason explained previously. Additionally, N increases with L/h since longer channels lead to a larger separation of the species bands or equivalently shallower channels improve the Joule heating dissipation and hence increase resolving power. However, it is important to note that L/h cannot be infinitely increased to improve the separation performance, since it is not cost-effective to fabricate microchips with straight channels with overly large lengths.

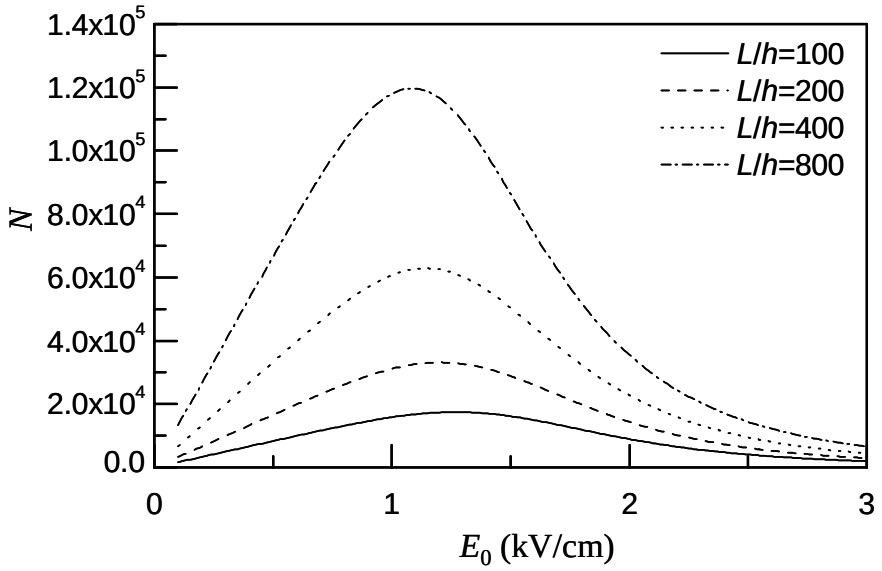

Figure 5-6. Parametric analysis of the dependence of the plate number N on the average electric field E_0 in a straight channel with different length-to-depth ratios.

5.5 Joule Heating Effects in Turns

As indicated above, to improve separation performance long channels with compact topologies, such as the spiral and serpentine are often used in practice. Therefore, in this section, Joule heating dispersion in constant radius-turns will be considered. The Joule heating induced non-uniformity in temperature as well as the significance of Joule heating with respect to diffusion and curvature effects will first be examined. Then a parametric analysis of Joule heating dispersion in turns will be performed and results from the system and numerical simulations will also be compared.

Figure 5-7 shows the comparison between the analytical modeling and numerical simulation results on the normalized temperature variations at half-depth in a cross section of a turn with b = 0.4 and β = 2. The agreement is within 7.7 % even for such a relatively large turn curvature b. The maximum temperature variation does not occur at the centerline of the turn (η = 1), and instead at a location closer to the inner side wall (η = 0.735) attributed to the higher electric field and Joule heating generation intensity at the inside

walls. It is expected that the model accuracy can be improved for turns of smaller b, when the linear electric field approximation (Eq. (5.1)) becomes more accurate.

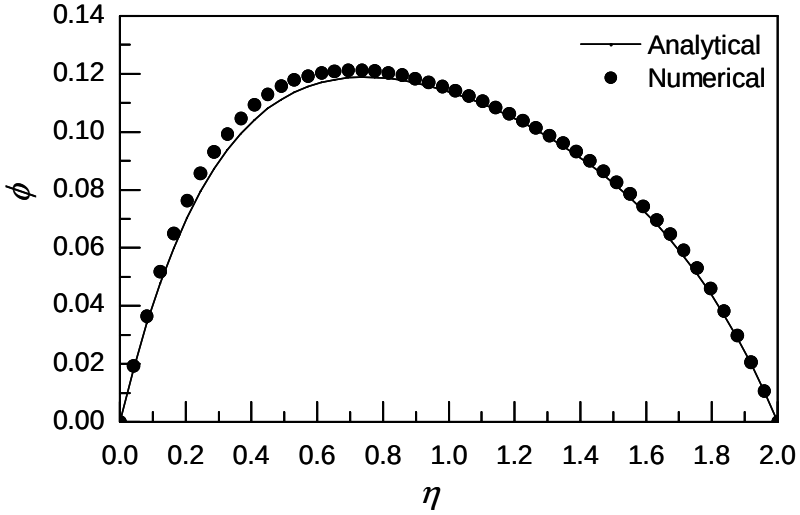

Figure 5-7. Model-predicted and numerically computed cross-sectional temperature variations for a turn (b = 0.4, β = 2 and extracted at the half channel depth).

Next, a parametric analysis of species band broadening due to Joule heating dispersion in a turn will be performed and the plate number N (Eq. (5.24) defined for a single turn) will be used, with the residence time τ_R computed from Eq. (5.25). The system simulations are performed on a separation column consisting of a short leading channel before the turn (containing the initially injected species band), a constant-radius turn and a long ending channel after the turn (containing the strongly distorted species band) as shown in Figure 5-10. The data extraction method is same as that used in Chapter 4, that is, the dispersion contributions from the leading and ending channels are subtracted from the total variance to attain the Joule heating induced band-broadening effects in the turn. Turns with $\varphi = \pi$ and the initial unskewed species band will be studied, although the discussions can be readily extended to initially skewed bands and turns of different included angles. Leading channel L_1 = 1000 μm, ending channel L_3 = 4400 μm, h = 50 μm, r_c = 2000 μm, $D = 1\times10^{-9}$ m^2 s^{-1},

σ = 0.1 S m^{-1}, μ_w = 2×10^{-8} m^2 V^{-1}s^{-1}, k = 0.6 W m^{-1} K^{-1} and α = 0.025 K^{-1} are chosen, and the species band is injected at the middle point of the leading channel L_1 with initial σ^2 (0) = 10000 μm^2.

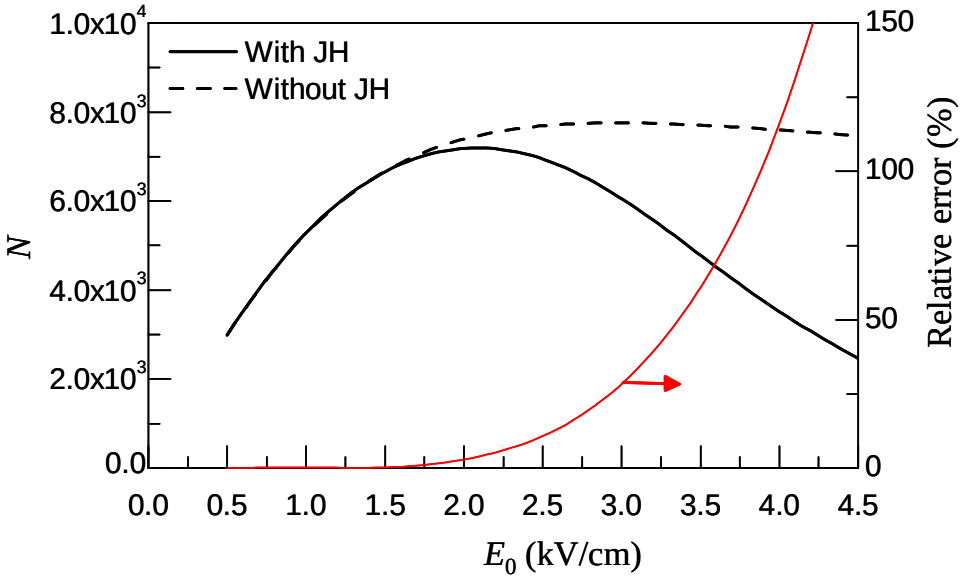

Figure 5-8. Comparison of the plate number N computed with and without consideration of Joule heating, as well as the relative error introduced without considering Joule heating effects on N.

The relative significance of Joule heating dispersion to the overall band broadening is illustrated in Figure 5-8. Here the plate number N, calculated with and without consideration of Joule heating effects is shown as a function of E_0 for β = 1. It can be seen that there exists a critical value of E_0 at which N achieves a maximum (N_{max}) regardless of Joule heating effects. However, in contrast to the turn curvature effect that causes only a slight decrease of N from N_{max}, the presence of significant Joule heating results in a rather pronounced drop in N. Thus, at relatively high electric fields, consideration of Joule heating is crucial for accurate dispersion modeling and electrophoresis microchip design. For example, the prediction of plate number N without accounting for Joule heating dispersion

leads to an error of 30 % at E_0 = 3 kV cm^{-1} (ε = 0.94 and Pe = 322). As E_0 further increases to 4 kV cm^{-1} (ε = 1.67 and Pe = 423), this error is quadrupled, growing to 120%.

The effect of the channel length (or equivalently, the mean radius r_c) is very similar to the straight channel case (Figure 5-6), and will not be repeated here. Hence, with fixed r_c = 2000 μm and h=50 μm, the influence of varying average electric field E_0 and aspect ratio β will be considered. Note that the turn curvature is now uniquely determined by β through $b = w/r_c = \beta (h/r_c)$. A larger aspect ratio β yields a larger turn curvature b. As shown in Figure 5-9, for a given E_0 value, N increases with decreasing β because a more square cross-sectional shape allows more efficient dissipation of Joule heating. Differing from the straight channel case, this increase in N is, in addition to Joule heating effect, also attributable to the reduced turn curvature-induced velocity non-uniformity, as a smaller β means a smaller turn curvature b. Additionally, when E_0 is sufficiently small (e.g., E_0 < 0.03 kV cm^{-1}), N increases virtually linearly with E_0 and almost coincides for all β. This is because at low electric fields, both Joule heating and turn dispersion effects are negligibly small compared with axial diffusion effects, which are independent of β. Thus, Eqs. (5.22), (5.24) and (5.25) indicate that the N is approximately linearly proportional to Pe and hence the electric field E_0. In contrast, N behaves quite differently at higher electric fields (e.g. $0.03 \le E_0 \le 4$ kV cm^{-1}). When β (and hence b) is small (e.g., $\beta \le 4$), N is determined by the coupled effects of diffusion, Joule heating and turn induced dispersion, with the Joule heating effect playing a more significant role than the turn curvature effect at higher electric fields (e.g., E_0 = 3.5~4 kV cm^{-1}), as shown in Figure 5-8. N initially increases with E_0 until reaching a maximum (e.g., N_{max} = 7200 at E_0 = 2.1 kV cm^{-1} for β = 1) and then decreases due to Joule heating and turn induced dispersion. On the other hand, when β (and

hence b) is large (e.g. $\beta \geq 8$), dispersion due to turn curvature is more important (e.g., accounting for 75% of band-broadening for $\beta = 8$ even at $E_0 = 4$ kV cm^{-1}) and more severely reduces N_{max} as well as the electric field at which N_{max} is obtained.

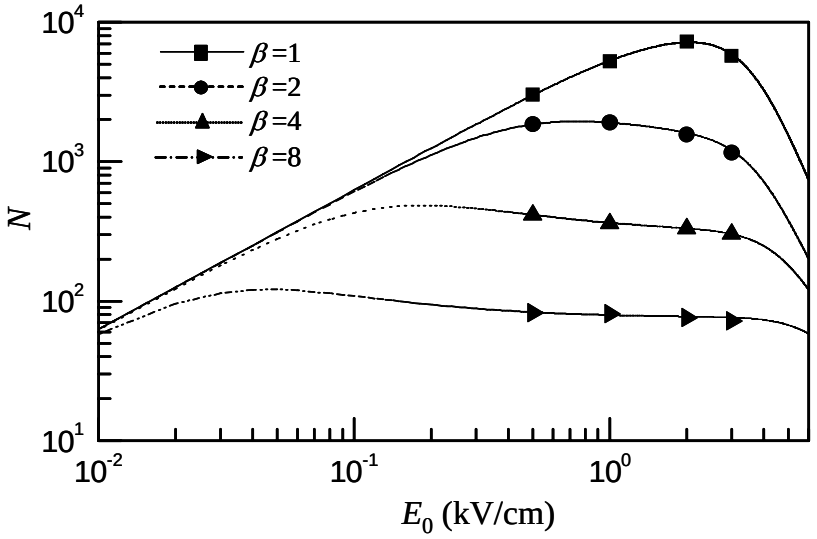

Figure 5-9. The dependence of the plate number N on the average electric field E_0 for different aspect ratios β of a turn, as computed from the system (lines) and numerical (symbols) simulations.

The plate number N obtained from full numerical analysis is compared with the system simulation results in Figure 5-9. When $E_0 < 0.5$ kV cm^{-1} ($\varepsilon < 0.02$), Joule heating dispersion is negligible. In this case, the dispersion model (the 1st, 2nd and 4th terms in Eq. (5.22)) has already been verified in Chapter 4 experimentally and numerically [123]. Here, the numerical simulations are performed for 0.5 kV cm^{-1} < E_0 < 3 kV cm^{-1} (or 0.02 < ε < 0.94), a practical range in which Joule heating effects can be significant. It can be seen that there is good agreement between the system and numerical simulation results. A worst-case error of 5.5 % is observed for $\beta = 8$ and $E = 3$ kV cm^{-1} (Pe = 322 and $\varepsilon = 0.94$), and can be attributed to the relatively large curvature ($b = 0.2$).

In numerical simulations, to address demanding requirements on physical memory and computation time (three-dimensional and transient), a numerical technique of subdomain-

wise simulations is employed. A spatial domain is divided into a set of concatenated subdomains. Only the subdomains that are occupied by the species band are finely meshed while the others left open or very coarsely meshed. The last time-step results at the current subdomain are then stored and serve as the initial condition to the simulation at the next downstream subdomain as shown in Figure 5-10. This approach enables 1/3~1/2 reduction in both memory and computer time compared to the numerical simulations of the entire domain.

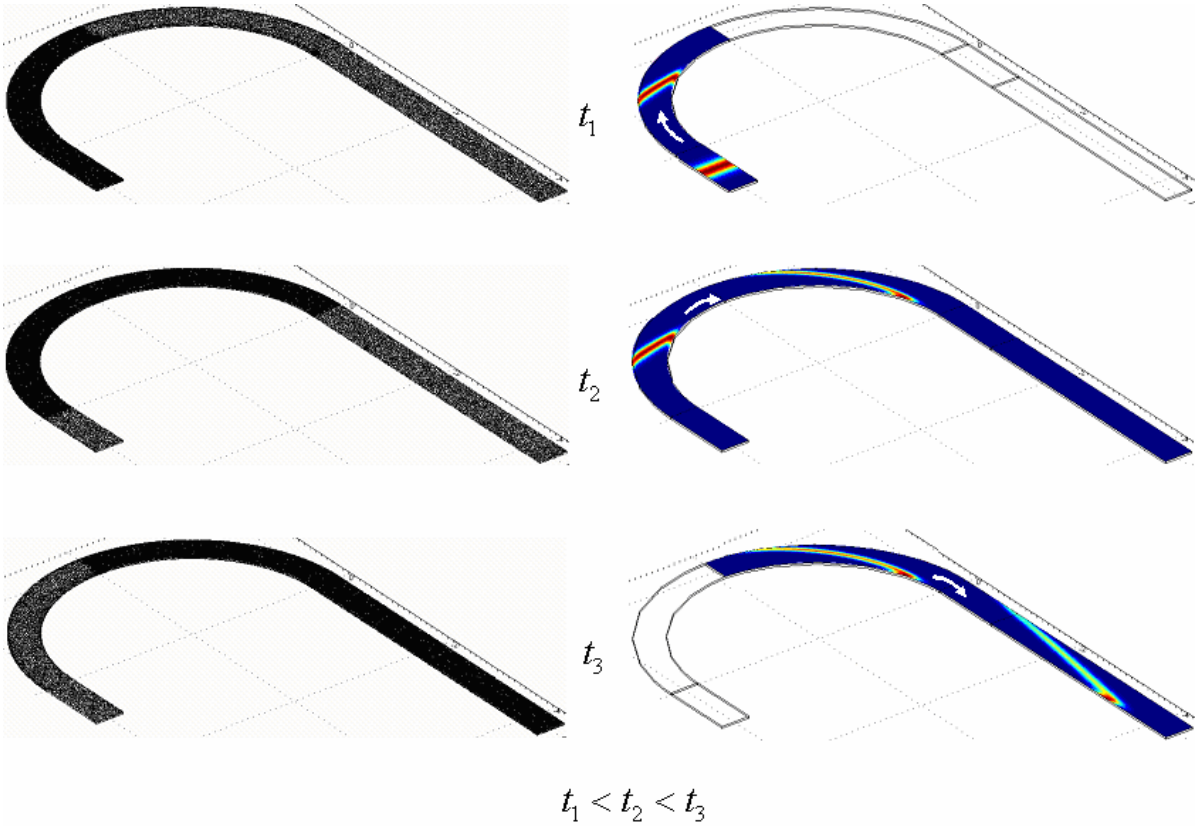

Figure 5-10. Subdomain-wise numerical simulations of Joule heating dispersion in a turn.

Finally, it is interesting to note that the analytical Joule heating dispersion model has led to a drastic improvement in computational efficiency over full numerical simulations. The numerical simulations presented in Figure 5-4 and Figure 5-9 were performed in FEMLAB 3.0a [152] on a multi-user, 2-CPU 1-GHz Sun Fire 280 processors with 4 GB RAM.

Computation of a single plate number value required from 6 hours (for small β and E_0 values) to four days (for the relatively large β and E_0 values). In contrast, the system simulation using the analytical behavioral model required no more than a second of computation time to obtain a plate number value, and is therefore suitable for the simulation of complex electrophoretic separation systems [123].

5.6 Summary

Joule heating-induced species dispersion in electrophoretic separation microchannels has been investigated. Non-uniform electrophoretic velocity distributions caused by Joule heating have been considered, and an analytical behavioral model for species dispersion, valid in all mass transfer regimes has been obtained. In particular, it can be used for unsteady dispersion processes that commonly occur in microchip electrophoresis. The model is given in terms of analytical expressions and fully parameterized with channel dimensions and material properties. It applies to species bands of general initial shape migrating through straight and constant-radius turn channels and hence can be used to investigate JH dispersion in microchannels of more general shape, such as serpentine- or spiral-shaped channels (Chapter 4). The model has been validated with numerical analysis and exhibits compatibility with composable system simulations.

Transient Joule heating dispersion behavior of species bands has been thoroughly examined for the first time. In straight channels, the overall species band broadening consists of contributions from molecular diffusion and Joule heating-induced dispersion and can be represented by a dispersion coefficient K. The dependence of K on the channel's cross-sectional geometry (or specifically the aspect ratio β for rectangular channels) and the dimensionless time τ is captured by a shape factor γ. In general, γ increases with τ and

eventually approaches an asymptotic value. The dispersion can be further divided into three regimes according to two time constants for diffusion in both dimensions of the cross-section. The first regime is dominated by depthwise diffusion and occurs approximately when $\tau < \tau_d$. At the low end of this regime (e.g., $\tau < 0.1\tau_d$) the channel can be reasonably approximated as a pair of parallel plates. In the second regime, τ is sufficiently large ($\tau > \tau_w$), so that diffusion in both dimensions and hence the overall dispersion is in steady state and γ is a constant (γ_∞). A transition regime also lies between the first two regimes, in which depthwise diffusion is in steady state, but widthwise diffusion is not. In this case, there is a plateau (pseudo-steady state) for γ that differs from its steady-state value. The model has in addition confirmed the important fact that γ_∞ (and hence the K at steady-state) in rectangular channels of an infinitely large aspect ratio does not converge to that in a pair of parallel plates. Although presented in the context of straight channels, the analysis can be readily extended to capture the species band-broadening within the turn.

The behavioral model achieves tremendous speedup compared to the numerical analysis and has been broadly used for parametric analysis and chip design. In straight channels, the dependence of the plate number, which characterizes the resolving power of separation, on electric fields for various channel length-to-depth ratios and aspect ratios has been analyzed. It is found that a maximum plate number can be achieved when the combined dispersion due to molecular diffusion and Joule heating dispersion is minimized. A long (or equivalently, shallow) channel is preferred for chip design because it allows larger separation spacing between species or dissipates more heat.

By applying the model to a constant-radius-turn microchannel, the coupled dispersion effects of Joule heating and turn geometry have been considered. In particular, the

influence of the electric field, aspect ratio and turn curvature on such dispersion has been investigated. It is shown that when the curvature is small, both Joule heating and turn curvature effects are important in practically relevant ranges of the electric field. Joule heating dispersion shows a more significant influence on separation performance than the turn curvature at high electric fields, while curvature-effects increase with the turn curvature. Additionally, Joule heating dispersion, coupled with turn induced dispersion, increases with the electric field and eventually causes separation performance to deteriorate.

Chapter 6 Modeling of Laminar Diffusion-Based Complex Electrokinetic Passive Micromixers

6.1 Introduction

Microscale mixing holds great importance in lab-on-a-chip technology. The integration of mixing with sample preparation, reaction, injection, separation and detection [16, 17, 79, 80] makes it generally desirable to have simple mixer designs for minimal fabrication and instrumentation complexity. This enables precise control of flow for efficient mixing and reduced sample consumption, and allows a direct interface with other components and subsystems to create truly integrated systems. Currently, a majority of LoC systems use passive mixers that rely on molecular diffusion. In particular, passive mixers that are based on electrokinetic transport are of great importance as they are amenable to integration within electrokinetic (EK) microsystems [79, 168], which have attracted widespread interest in the LoC community.

Effective mixing in electrokinetically driven micromixers is difficult. The combination of laminar fluid flow in microchannel networks and dominant molecular diffusion in the mixing process generally leads to long channel lengths and mixing times. The time needed to mix sample streams to obtain a uniform sample concentration in the widthwise direction can be estimated by $t \sim w^2/D$, where w is the average diffusion distance between different sample streams (or buffer in the dilution case) and D is the sample diffusivity. For example, consider a microchannel ~1 mm wide ($w = 0.5$ mm), in which two different sample streams with D~1×10^{-10} m^2 s^{-1} flow side by side at a speed of ~1 mm s^{-1}. The channel length has to be 1.25 m to achieve good mixing, which is almost impossible for microfluidic systems. This can be even worse for large molecules with lower diffusivity D

~ 1×10^{-11} m^2 s^{-1}, e.g. DNA. Therefore, a number of diffusion-based mixing-enhancement techniques have explored rapid mixing by reducing diffusion distances between individual sample streams and increasing interfacial areas. For example, the mixing process can be accelerated by narrowing (or focusing) sample streams [169, 170] (Figure 6-7). Instead of diffusing between broad streams (such as the T-mixer), samples can be arranged in the form of alternating thin streams [171-173] (Figure 6-9). Sample concentration profiles in such laminar diffusion-based micromixers are relatively easy to evaluate and reproduce, which also enables other innovative bioanalytical applications by allowing precise handling [174] and dosing [71] of samples, extraction and separation of samples [63, 175], and generation of spatial concentration gradients [13, 73, 74, 76, 176].

However, there are still important issues regarding these passive mixing techniques that need to be addressed. Optimal design of such mixers involving the tradeoffs between mixer performance, mixing time, chip real-estate area and system complexity is still an art. More extensive exploration of the design space to assess the impact of parameters such as the mixer topology, element dimension, voltage control, material property and sample flow ratio has not been pursued. Currently the only approach available to designers is a trial-and-error approach that requires large numbers of experimental tests or numerical simulations. The numerical simulations typically involve unacceptably long computation time and are limited by algorithmic stability. For example, accurate simulations of micromixing at the high Peclet number regime by finite-volume approaches become very difficult due to errors associated with “numerical diffusion” [9], unless extremely fine meshes are used. To address these issues, several parameterized and closed-form models have been developed for mixers. Simplified equations for T-mixers [177, 178] have been extensively used to

provide mixing length estimates that are often overly conservative and do not provide information of the mixing process (e.g., the evolution of the sample concenteration profile along the channel length). Modeling methods using electrical analogy (i.e., resistor-based models) [16, 71, 132] assume complete mixing and generally result in unnecessarily long channels. Branebjerg *et al.* [179] have theoretically studied the diffusion behavior in split-and-recombine (SAR) mixers. An analytical solution for the widthwise sample concentration profile within the last unit was developed by neglecting the effects of its preceding SAR units. As such, the model is valid only for the special case that sample concentration distributions at the channel inlet are saw-tooth (interdigitally) shaped, and even so, still requires a pre-calculation of flow ratios of different samples. Thus, the model is not suitable for system-level simulation and synthesis. Schönfeld *et al.* [180] also derived an analytical formula that accounts for arbitrary sample concentration distributions at channel inlets. However, the formula is limited to symmetric flow ratios (i.e., the flow rates of the buffer streams carrying different samples are the same), and is not applicable to multi-input or multi-output flow intersections that are widely used in focusing and multi-stream mixers.

All the models above are intended for particular instances of micromixers. No general methodology has been proposed to develop a reliable and reusable system-level simulation approach that can accommodate all laminar diffusion-based micromixers and, most importantly, be integrated with simulations of other subsystems (e.g., reactors, injectors and electrophoretic separation channels). This deficiency hinders efficient microfluidic design, which is typically an iterative process, and becomes even more acute for large-scale

microfluidic integration. Therefore, there is a strong need for micromixer design tools that are efficient, accurate and have general applicability.

To address this need, this chapter presents behavioral models compatible to the top-down design approaches to efficiently and accurately simulate laminar diffusion-based passive electrokinetic micromixers of complex geometry. By following the simulation methodology previously described (Chapter 3), analytical and parameterized behavioral models for individual mixing elements are derived to accurately describe the variations of sample concentrations, which hold for arbitrary flow ratios and concentration profiles at the element inlet. With pin and wiring bus connections, the element models are then linked to form a system-level schematic representation of the complex passive micromixer. Simulating this system-level schematic involves simultaneous computation of the electrical network and sample concentration distributions in the entire micromixer. This eliminates the need for input parameters that would have to be determined from user-conducted numerical simulations or experiments, and is thus well suited to computed-aided design (CAD) of complex electrokinetic micromixers. This design methodology and behavioral models offering orders-of-magnitude improvements in computational efficiency over full numerical simulations have been validated against numerical and experimental results with excellent agreement. The efficiency and usefulness of the model is demonstrated by exploring a number of laminar diffusion-based mixers and mixing networks that are of interest to LoC designers. While this chapter focuses on electrokinetic micromixers, the concept and methodology of this top-down approach can be readily extended to pressure-driven micromixers and laminar diffusion-based devices.

This chapter is organized as follows. First, the behavioral model library for mixing elements compatible to the composable system simulation approach will be developed (Section 6.2). Then the process of composing the system-level schematic by wiring the element models will be illustrated (Section 6.3). Finally, the system-level schematic will be applied to several practically important complex micromixers (including that shown in Figure 3-2). The model will be validated by comparing these results to both numerical analysis and experimental data (Section 6.4).

6.2 Behavioral Model Library

As introduced previously, a complex electrokinetic passive micromixer can be represented as a system consisting of interconnected mixing elements that have relatively simple geometry. This section formulates and solves the circuitry and convection-diffusion equation to yield parameterized and analytical behavioral models for the elements, including mixing channels, converging and diverging intersections and reservoirs, which are most commonly seen in EK passive micromixers. The EK motion of the sample consists of two parts: the bulk motion of the carrying buffer due to electroosmosis and the motion of charged sample molecules relative to the buffer due to electrophoresis. The similitude between EK flow and electric field [116] is assumed, which implies that the sample EK velocity can be expressed as $u = \mu E$, where E is the electric field strength and μ is the algebraic sum of the buffer's electroosmotic mobility and sample's electrophoretic mobility in the buffer. The models will be capable of simultaneously simulating multiple dilute samples in the buffer solution if interactions between them can be neglected.

6.2.1 Tapered Mixing Channels with Small Side-Wall Slopes

This subsection formulates the circuitry and convection-diffusion equation for a tapered straight mixing channel with a small side-wall slope. That is, the channel's axial axis (the line connecting cross-sectional centers) is a straight line and its cross sections are rectangular with dimensions varying slowly along the axis. Straight channels with uniform cross sections are included as a special case of zero side-wall slopes. This geometry is employed in micromixers, such as geometric focusing or throttled mixers with the side-wall slope on the order of 10° [172, 181, 182]. The depthwise and widthwise dimensions of the channel are defined as those parallel (along the *z*-axis) and perpendicular (along the *y*-axis) to the sample stream interface, respectively (Figure 6-1). Let L, $h(x)$ and $w(x)$ denote the axial length, depth and width of the mixing channel, respectively, where x is the axial coordinate parallel to the channel axis.

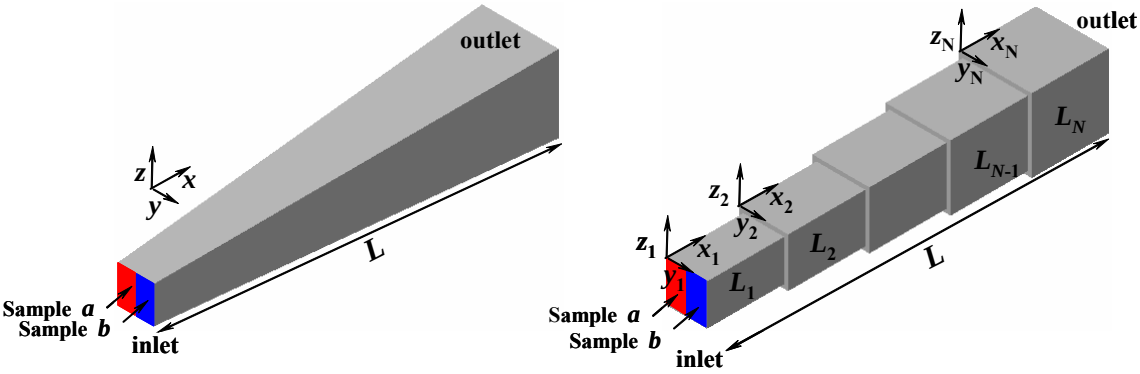

Figure 6-1. (a) Geometry of a tapered mixing channel and (b) its modeling approximation by constant-cross sectional channels.

As the mixing channel is typically narrow ($w/L \ll 1$ and $h/L \ll 1$) and operates in steady state, the axial diffusion of the sample can be neglected and the governing convection-diffusion equation for the sample concentration $c(x, y, z)$ is

$$u_x \frac{\partial c}{\partial x} + u_y \frac{\partial c}{\partial y} + u_z \frac{\partial c}{\partial z} = D\left(\frac{\partial^2 c}{\partial y^2} + \frac{\partial^2 c}{\partial z^2} \right) \tag{6.1}$$

where D is the sample diffusivity, u_x, u_y and u_z are the x-, y- and z-components of the sample velocity. To solve this equation in a channel with slightly sloped side-walls, the channel is approximated as a set of concatenated channel segments, each having a constant rectangular cross section (Figure 6-1b). As a convention, channel segments are numbered $k = 1, 2, ...N$ from the inlet to the outlet. The interface between segments $k-1$ and k is numbered $k-1$, with the channel inlet numbered 0, and the channel outlet numbered N. Likewise, local coordinates (x_k, y_k, z_k) and dimensions (h_k, w_k, L_k) of segment k can be defined, with h_k and w_k independent of z_k. Other variables or quantities in the k^{th} segment channel are also given the index k.

The electric current induced by very dilute sample molecules is negligible compared with the current in carrier buffer, which is typically valid in EK microfluidic systems [71, 183]. Then the electric resistance of the entire channel is given by

$$R = \int_0^L \frac{dx}{w(x) h(x) \boldsymbol{\sigma}} \tag{6.2}$$

where $\boldsymbol{\sigma}$ is the electric conductivity of the buffer solution within the channel. Given a potential difference over the channel length, $\Delta V = V_{in} - V_{out}$ (V_{in} and V_{out} are respectively the voltages at the channel inlet and outlet), Eq. (6.2) yields the electric current $I = I_k = \Delta V / R$ through the entire channel including all constituent segments. As the slope of the channel's side-wall is small, it is reasonable to use the approximation that the electric field in each channel segment is unidirectional, i.e.,

$$\left(E_{x_k}, E_{y_k}, E_{z_k} \right) = \left(I/(w_k h_k \boldsymbol{\sigma}), 0, 0 \right) \tag{6.3}$$

Then EK velocity $\vec{u}_k$ of a charged sample molecule in segment *k* is $(u_{x_k}, u_{y_k}, u_{z_k}) = (\mu E_{x_k}, 0, 0)$. That is, within the segment, sample molecules migrate at a velocity that is uniform over the cross section. It follows from Eq. (6.1) that the sample concentration distribution is two-dimensional and independent of z_k as it is assumed to be so at the channel inlet. This also yields the volumetric flow rate of the buffer stream through a segment: $q_k = u_{eof,x_k} h_k w_k = \mu_{eof} I / \boldsymbol{\sigma}$, where u_{eof,x_k} and μ_{eof} are the electroosmotic parts of u_{x_k} and μ, respectively. That is, q_k is linearly proportional to the current *I*. Then, Eq. (6.1) can be recast in terms of segment coordinates as

$$\frac{w_k^2 u_{x_k}}{D} \frac{\partial c_k}{\partial x_k} = \frac{\partial^2 c_k}{\partial \eta^2} \tag{6.4}$$

where $\eta = y_k / w_k$ $(0 \le \eta \le 1)$ is the normalized coordinate along channel width. With the boundary conditions $\partial c_k / \partial \eta \big|_{\eta=0,1} = 0$ (i.e., no mass transfer across the wall), the solution to Eq. (6.4) at the outlet of segment *k* (interface *k*) is found as $c_k(\eta, L_k) = \sum_{n=0}^{\infty} d_n^{(k)}(L_k) \cos(n\pi\eta) = \sum_{n=0}^{\infty} d_n^{(k)}(0) e^{-\frac{(n\pi)^2 DL_k}{w_k^2 u_{x_k}}} \cos(n\pi\eta)$, where $d_n^{(k)}(L_k)$ and $d_n^{(k)}(0)$ are the Fourier cosine series coefficients of the concentration profile at the inlet and outlet of segment *k*. As the solution is expressed in terms of dimensionless variable η, $d_n^{(k)}(0) = d_n^{(k-1)}(L_{k-1})$ can be obtained. Then a complete solution of Eq. (6.4) is obtained as $d_n^{(k)}(L_k) / d_n^{(k-1)}(L_{k-1}) = e^{-\frac{(n\pi)^2 DL_k}{w_k^2 u_{x_k}}}$. Letting $k = 1, 2, \ldots$ and taking the product of these equations yields

$$d_n^{(out)} = d_n^{(in)} e^{-(n\pi)^2 D \sum_{k=1}^{N\to\infty} \frac{L_k}{w_k^2 u_{x_k}}} = d_n^{(in)} e^{-(n\pi)^2 \gamma\tau} \tag{6.5}$$

where $d_n^{(in)} = d_n^{(1)}(0)$ and $d_n^{(out)} = d_n^{(N)}(L_N)$ represent the coefficients at the channel inlet and outlet, respectively. Here, $\tau = \left(L/w(0)\right)/\mathrm{Pe}$ is the dimensionless mixing time and $\mathrm{Pe} = u(0)w(0)/D$ is the Peclet number defined at the channel inlet, which represents the ratio of convective to diffusive transport rates. The geometry factor γ is given by

$$\gamma = \frac{u(0)w(0)^2}{L}\int_0^L \frac{dx}{w^2(x)u(x)} = \frac{1}{L}\int_0^L \frac{h(x)}{h(0)}\frac{w(0)}{w(x)}dx \tag{6.6}$$

Eqs. (6.5) and (6.6) indicate that the variation of sample concentration coefficients within a tapered mixing channel depends on the dimensionless mixing time and geometry factor γ. Eq. (6.5) provides an excellent approximate solution to Eq. (6.1) when side-wall slopes are small. This will be confirmed with an example in Section 6.4.4.

Now several special cases are considered. First, for constant channel cross sections $h(x)w(x) = A = \text{const.}$, Eqs. (6.2) and (6.6) respectively reduce to $R = L/(A\boldsymbol{\sigma})$ and $\gamma = \frac{w(0)^2}{L}\int_0^L \frac{dx}{w(x)^2}$, and the solution in Ref. [180] is recovered. The second special case concerns a mixing channel with variable width but constant depth, which is widely used in the geometrically focusing mixers [9, 172, 181, 184] or throttled T mixers [182]. If *w* is linear in *x* with $p = \left(w(L) - w(0)\right)/w(0)$, then

$$R = \gamma R(0) \quad \text{and} \quad \gamma = \frac{\ln(1+p)}{p} \tag{6.7}$$

where $R(0) = L/\left(w(0)h(0)\boldsymbol{\sigma}\right)$.

6.2.2 Converging Intersections

The converging intersection has two inlets and one outlet, and acts as a combiner to align and compress upstream sample streams of an arbitrary flow ratio *s* (defined below) and concentration profiles side-by-side at its outlet (Figure 6-2a). As its flow path lengths are negligibly small compared with those of mixing channels, such an element can be assumed to have zero physical size, and electrically represented as three resistors with zero resistance between each terminal and the internal node N_i,

$$R_l = R_r = R_{out} = 0 \tag{6.8}$$

Here, N_i corresponds to the intersection of flow paths and the subscripts *l*, *r* and *out* represent the left and right inlets, and the outlet, respectively. The voltages at the terminals ($V_l = V_r = V_{out}$) are consequently the same.

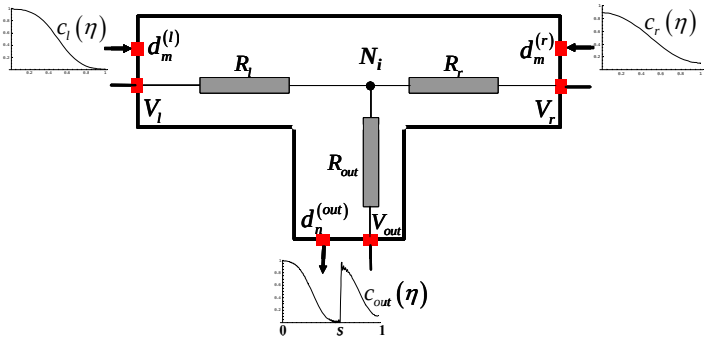

a

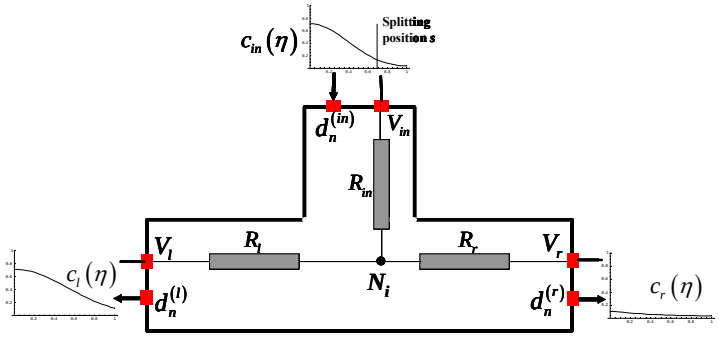

b

Figure 6-2. Behavioral model structures for (a) the converging and (b) the widthwise diverging intersections.

The sample concentration profiles, $c_l(\eta)$ and $c_r(\eta)$, at the left and right inlets respectively, can be expressed as $c_l(\eta)=\sum_0^\infty d_m^{(l)}\cos(m\pi\eta)$ and $c_r(\eta)=\sum_0^\infty d_m^{(r)}\cos(m\pi\eta)$. Then the coefficients $d_n^{(out)}$ ($n=0,1,2...$) of the profile at the outlet ($c_{out}(\eta)$) are related to $d_m^{(l)}$ and $d_m^{(r)}$ by,

$$c_{out}(\eta)=\sum_{n=0}^{\infty} d_n^{(out)}\cos(n\pi\eta)=\begin{cases}\displaystyle\sum_{m=0}^{\infty} d_m^{(l)}\cos\left(\frac{m\pi\eta}{s}\right) & ,\quad 0\le\eta<s\\ \displaystyle\sum_{m=0}^{\infty} d_m^{(r)}\cos\left(\frac{m\pi(\eta-s)}{1-s}\right) & ,\quad s\le\eta<1\end{cases} \tag{6.9}$$

Eq. (6.9) shows that the concentration profile at the outlet can be treated as a superposition of the scaled-down profiles $c_l(\eta)$ and $c_r(\eta)$ in the domains of $0\le\eta\le s$ and $s\le\eta\le 1$, where $s=q_l/(q_l+q_r)=I_l/(I_l+I_r)$ denotes the interface position (or the flow ratio, the ratio of the left-stream flow rate q_l to the total flow rate q_l+q_r) between the incoming streams in the normalized coordinate at the outlet. Note that the flow rates q_l and q_r are respectively linear in the electric currents I_l and I_r as described above, and s can be determined by solving for electric currents within the entire mixer using Kirchhoff's and Ohm's laws. Solving Eq. (6.9) yields,

$$\begin{cases} d_0^{(out)}=d_0^{(l)}s+d_0^{(r)}(1-s)\\ d_{n>0}^{(out)}=s\displaystyle\sum_{m=0}^{m\neq ns} d_m^{(l)}\left(f_1\sin(f_2)+f_2\sin(f_1)\right)/(f_1f_2)+s\sum_{m=0}^{m=ns} d_m^{(l)}+(1-s)\sum_{m=0}^{m=n(1-s)}(-1)^{n-m}d_m^{(r)}\\ \qquad\qquad +2(-1)^n(1-s)\displaystyle\sum_{m=0}^{m\neq n(1-s)} d_m^{(r)}\left(\cos(F_2/2)\sin(F_1/2)/F_1+\cos(F_1/2)\sin(F_2/2)/F_2\right)\end{cases} \tag{6.10}$$

where $f_1=(m\text{-}ns)\pi$, $f_2=(m\text{+}ns)\pi$, $F_1=(m\text{+}n\text{-}ns)\pi$ and $F_2=(m\text{-}n\text{+}ns)\pi$.

6.2.3 Diverging Intersections

A diverging intersection has one inlet and two outlets. A sample stream coming into the inlet is split into two streams exiting the outlets. Similar to converging intersections, it is reasonable to assume that diverging intersections have zero physical size and can be represented by three zero-resistance resistors,

$$R_{in} = R_l = R_r = 0 \tag{6.11}$$

which implies equal voltages at the terminals: $V_{in} = V_l = V_r$. The subscripts *in*, *l* and *r* represent quantities at the inlet, the left and right outlets.

Depending on the orientation of the splitting plane, diverging intersections can be classified into depthwise (normal of the splitting plane parallel to depth *z*) and widthwise (normal of the splitting plane parallel to width *y*) diverging intersection. Let $d_m^{(in)}$, $d_n^{(l)}$ and $d_n^{(r)}$ be the concentration coefficients of the profiles at the inlet, and left and right outlets respectively. For a widthwise diverging concentration, the sample concentration profile is split and stretched out into two parts flowing out of both outlets, which gives

$$\begin{cases} d_0^{(l)} = d_0^{(in)} + \sum_{m=1}^{\infty} d_m^{(in)} \sin(\phi_1)/\phi_1 \\ d_{n>0}^{(l)} = 2\sum_{m=0}^{m\neq n/s} d_m^{(in)} (-1)^{n+1} \phi_1 \sin(\phi_1)/(f_1 f_2) \\ \qquad + \sum_{m=0}^{m=n/s} d_m^{(in)} \left(1+\sin(2\phi_1)/(2\phi_1)\right) \end{cases}$$

and (6.12)

$$\begin{cases} d_0^{(r)} = d_0^{(in)} - \sum_{m=1}^{\infty} d_m^{(in)} \sin(\phi_1)/\phi_2 \\ d_{n>0}^{(r)} = 2\sum_{m=0}^{m\neq n/(1-s)} d_m^{(in)} \phi_2 \sin(\phi_1)/(F_1 F_2) \\ \qquad + \sum_{m=0}^{m=n/(1-s)} d_m^{(in)} \left(\phi_2 \cos(\phi_1) - \sin(\phi_1)\right)/\phi_2 \end{cases}$$

where $f_1 = (n\text{-}ms)\pi$, $f_2 = (n\text{+}ms)\pi$, $F_1 = (n\text{+}m\text{-}ms)\pi$, $F_2 = (n\text{-}m\text{+}ms)\pi$, $\phi_1 = ms\pi$ and $\phi_2 = m(1\text{-}s)\pi$. Similar to converging intersections, $s = q_l/(q_l + q_r) = I_l/(I_l + I_r)$ gives the normalized position of the splitting plane at the inlet and can be determined by electric current distributions within the network.

For a depth-wise diverging intersection, the concentration profile at inlet holds unchanged during splitting, leading to,

$$d_{n=m}^{(l)} = d_m^{(in)} \text{ and } d_{n=m}^{(r)} = d_m^{(in)} \tag{6.13}$$

It should be pointed out that in contrast to the resistor-based mixing models [71, 132] that take advantage of the analogy between fluidic and sample transport and only convey the average concentration values through the entire network, our models (Eqs. (6.14), (6.15), (6.16) and (6.17)) propagate sample concentration profiles characterized by the Fourier series coefficients. This removes the requirement of complete mixing (along channel width) at the end of each channel [71] in the network imposed by the resistor-based models and allows for optimal design of both effective and efficient micromixers. Although a T-type intersection is used to illustrate converging and diverging intersections in Figure 6-2, the developed models are independent of the included angle between branch channels (e.g., T-type or Y-type) as intersections are treated as point-wise entities.

6.2.4 Reservoirs

To enable schematic simulations of a mixer, models for sample and waste reservoirs are also needed. A sample reservoir continuously discharges downstream a sample with a given concentration c_0 while providing an electric potential ϕ_{app} to maintain the EK flow. It can thus be simply represented by

$$V = \phi_{app} \tag{6.18}$$

and $c(\eta) = \sum_0^\infty d_n \cos(n\pi\eta)$ where

$$d_0 = c_0 \text{ and } d_{n>0} = 0 \tag{6.19}$$

A model for a waste reservoir, which provides a fixed electric potential and serves as a sink continuously collecting used samples and reagents, can be given in a similar fashion.

6.2.5 Detectors

To characterize the mixer performance, a detector model that reconstructs widthwise concentration profiles from the Fourier coefficients is also developed and given by

$$c = \sum_{n=0}^{\infty} d_n \cos\left(n\pi \frac{y}{w}\right) \tag{6.20}$$

6.3 Constructing System-Level Representation

A complex mixer can be represented by a system-level schematic using the developed behavioral element models and the composable approach presented in Chapter 3.

Figure 6-3 illustrates the process of composing the system-level schematic of a hypothetical system consisting of a straight channel, a converging and a diverging intersection, in which both electric pins of electric potential $(V_i)^{(j)}$ and biofluidic pins of concentration Fourier coefficients $\left\{d_n^{(i)}\right\}^{(j)}$ are wired, where the index *i* stands for *in*, *out*, *l* or *r*, respectively representing the inlet, outlet, left and right terminals of the element. The index *j* is the element number. This sets the pin values between two neighboring elements equal, i.e., $(V_{out})^j = (V_{in})^{j+1}$ and $\left\{d_n^{(out)}\right\}^j = \left\{d_n^{(in)}\right\}^{j+1}$, hence it enables the simulator to serially process the element models and propagation of the biofluidic states within the network.

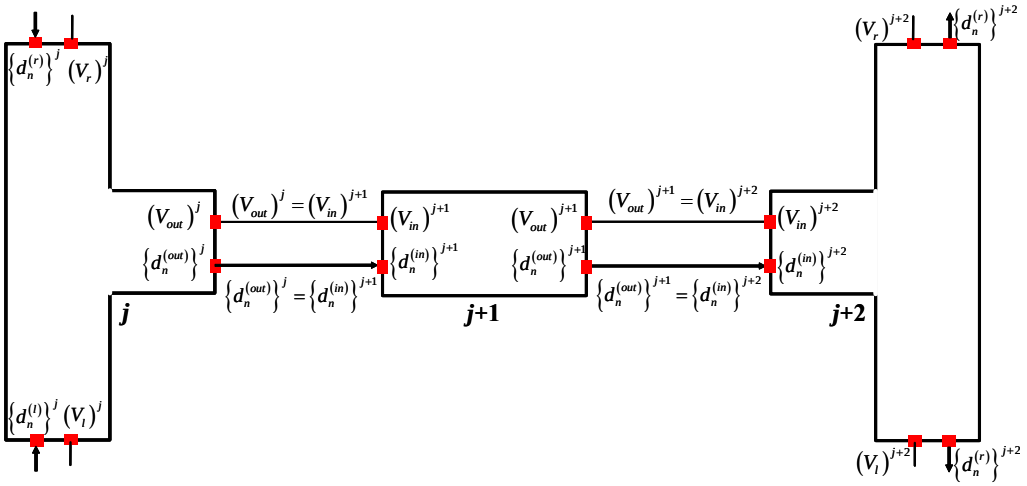

Figure 6-3. Linking behavioral models to form a system-level micromixer schematic.

6.4 Simulation Results and Discussion

To demonstrate its utility in lab-on-a-chip design, the element behavioral models have been implemented, integrated and applied to system-level simulations of several practically important passive electrokinetic mixers. The simulation results, which yield insights into the characteristics of the mixers, will be compared with finite element-based numerical simulations using FEMLAB 3.0a [152] as well as experimental data [71].

6.4.1 Simulation Description

The system-level schematic simulation approach involves both electric and concentration calculations. First, given the applied potential at the reservoir, system topology and element geometry, voltages $(V_i)^{(j)}$ at the element terminals are computed for the entire mixer system by Kirchhoff's and Ohm's laws. The electric field strength (E) and its direction within each element, and flow ratios (splitting ratios) at intersections are then calculated. With these results and user-input sample properties (D and μ), the sample speed is given by $u = \mu E$. Next, the concentration coefficients $\left\{d_n^{(out)}\right\}^{(j)}$ at the outlet of each

element *j* are determined from those at the element inlet using Eqs. (6.5), (6.10) and (6.12), starting from the most upstream sample reservoir (Eq. (6.19)). As such, both electric and concentration distributions in an EK micromixer are obtained. This would enable, in a top-down fashion, efficient and accurate design of complex micromixers. While the model allows for a virtually arbitrary number of different samples coexisting in the buffer, current implementation considered up to three samples, with Eqs. (6.5), (6.10), (6.12) and (6.19) applying to each sample.

To characterize the mixing performance, a scalar index, called the mixing residual *Q* [9, 172, 180], is used to quantify the non-uniformity in concentration distributions:

$$Q = \int_0^1 \left| \overline{c}(\eta) - \overline{c}_{avg} \right| d\eta \tag{6.21}$$

where $\overline{c}(\eta) = c/c_0$ and $\overline{c}_{avg} = c_{avg}/c_0$ are the normalized concentration profile and width-averaged concentration, respectively. $c_0 = 1$ is assumed in the reservoir without loss of generality. Hence, $c(\eta) = \overline{c}(\eta)$ and $c_{avg} = \overline{c}_{avg}$. Note that a small value of *Q* indicates a highly homogeneous sample distribution and good mixing performance. A smaller difference between $\overline{c}(\eta)$ and $\overline{c}_{avg}$, or a smaller width-wise region occupied by this concentration difference, leads to a lower *Q*.

For convenience, the following scalar index will be used to characterize the percentage error of the system-level simulation results compared with numerical analysis,

$$M = \frac{\int_0^1 \left| c_N - c \right| d\eta}{\int_0^1 c_N d\eta} \tag{6.22}$$

where *c* and c_N are the concentration profiles from system-level and numerical simulations, respectively. For all results below, mixing channels have identical width 200 μm. Also,

samples *a* and *b* to be mixed are given $D_a = 1\times10^{-10}$ m^2 s^{-1}, $D_b = 3\times10^{-10}$ m^2 s^{-1} and $\mu_a = \mu_b = 6\times10^{-8}$ m^2 V^{-1}s^{-1} unless otherwise noted.

6.4.2 Electrokinetic T-Mixers

First, the system-level schematic is applied to a T-mixer, which is most widely used in LoC systems. Sample mixing with an arbitrary flow ratio *s* (Figure 6-4a) in the T-mixer, as well as the effect of *s* and sample properties on mixing performance will be investigated. The results will be used as a basis for subsequent discussions of more complex mixers.

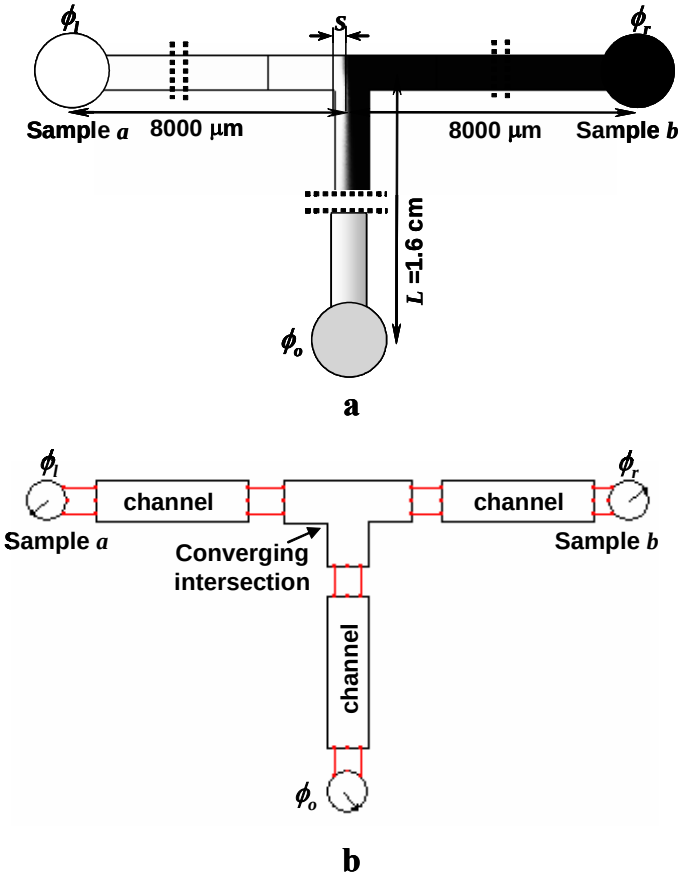

Figure 6-4. (a) An electrokinetic passive T-mixer and (b) its schematic for system-level simulations.

The T-mixer is illustrated and schematically represented in Figure 6-4. Two streams carrying samples *a* (white) and *b* (black) respectively enter from the left and right feed

channels, meet at the converging intersection with a flow ratio *s* and then mix with each other in the downstream mixing channel.

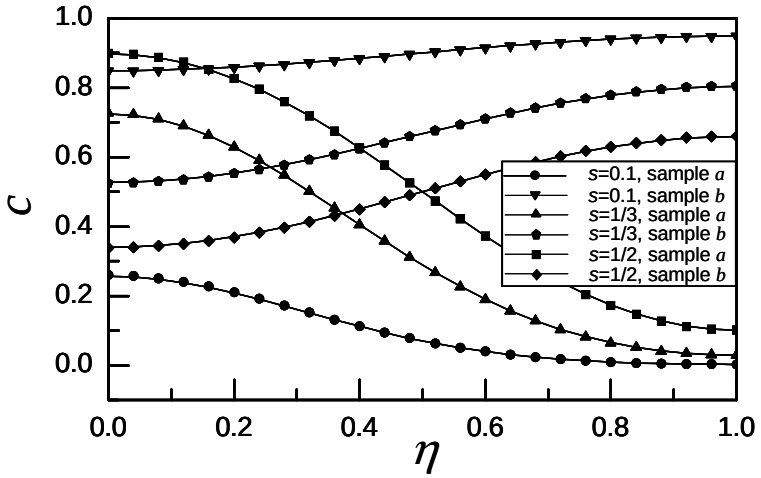

Figure 6-5. System simulation results (lines) compared with numerical data (symbols) on concentration profiles at the channel outlet in the electrokinetic T-mixer.

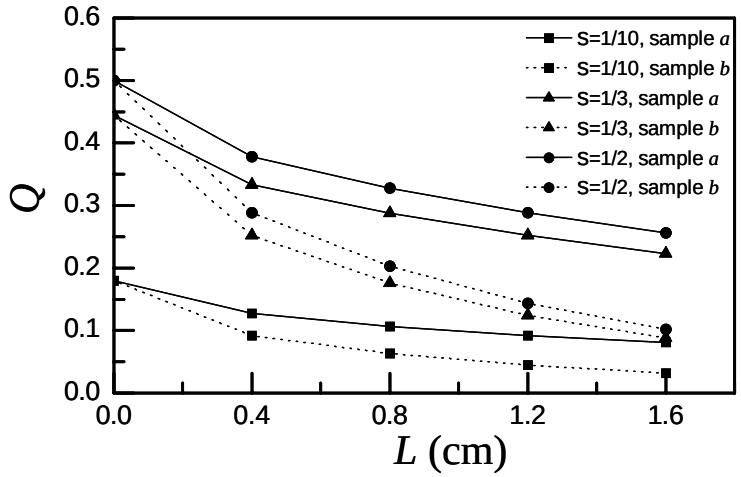

Figure 6-6. System simulation results on variation of mixing residual *Q* along channel length (data points are connected by lines to guide the eye) for the electrokinetic T-mixer.

Figure 6-5 shows the concentration distributions, obtained respectively from the system simulation and numerical analysis, of samples *a* and *b* at the channel outlet for *s* = 1/10, 1/3 and 1/2. During simulations, voltages (ϕ_l, ϕ_r and ϕ_o) are applied at the reservoirs to vary *s* while keeping *E* and sample residence times fixed in the mixing channel. Specifically, ϕ_l = {240, 267, 286} V, ϕ_r = {331, 305, 286} V and ϕ_o = 0 V are chosen to obtain *s* = {1/10, 1/3,

1/2} with E = 143 V cm^{-1}. It can be seen that a smaller flow ratio (e.g., s = 1/10) allows a more uniform concentration profile for both samples than a larger flow ratio (e.g., s = 1/2). Results from the system and numerical simulations are compared and excellent agreement is found, with a worst-case error of $M = 1\%$ at s = 1/10.

To gain insight into the mixer performance, the mixing residual Q along the mixing channel is calculated from the system simulation and shown in Figure 6-6. At the channel inlet (x = 0), Q that is the same for both samples due to their complementary concentration profiles ($c_a(\eta) + c_b(\eta) = 1$), strongly depends on s. When the incoming streams are very asymmetric (e.g., s = 1/10), $c - c_{avg}$ either occupies only a narrow region over the channel width (e.g., sample a) or $c - c_{avg}$ itself is small (e.g., sample b). These two scenarios both lead to low Q values (Q = 0.18 at s = 1/10 compared with Q = 0.5 at s = 1/2) and a more uniform initial profile. Along the channel, Q initially drops rapidly and then becomes saturated because the smaller concentration gradient due to improvement in sample mixing reduces the driving force for further mixing. Given sufficiently long mixing channel length L, concentrations of samples a and b at the outlet will eventually approach their width-wise averages $c_a(\eta) = s$ and $c_b(\eta) = 1 - s$ (i.e., complete mixing). However this may not be efficient from a design standpoint, as a large increase in channel length would only result in minimal decrease in Q. Figure 6-6 also shows that Q decreases faster for samples with higher diffusivity (e.g., sample b), because of larger τ (dimensionless mixing time) values in Eq. (6.5). To summarize, asymmetric streams ($s \neq 1/2$) produce more uniform initial profiles and hence focusing [170, 178] is a very useful technique to enhance the mixer performance, provided accompanying decreases in sample detection is tolerable. Within the mixing channel, Q decays faster for more diffusive (or equivalently less mobile) samples.

6.4.3 Electrokinetic Focusing Mixers

Electrokinetic focusing [169], which first appeared as a sample injection and manipulation technique [71, 118, 143] in EK LoC systems, also can be utilized to speed up mixing, especially in reaction kinetics studies [170, 185]. Such an electrokinetic focusing mixer is illustrated and schematically represented for system simulations in Figure 6-7. In the discussions below, subscripts *i*, *s* and *o* are used to respectively denote the input, side and output mixing channels. The cross intersection where sample *a* (white) from the input channel is pinched by buffer or sample *b* (black) from both side channels, is modeled as two concatenated converging intersections. Therefore, at the mixing channel inlet, two interface positions $s_1 = I_s/(2I_s + I_i)$ and $s_2 = (I_s + I_i)/(2I_s + I_i)$ are obtained if the electric currents from both side channels are identical. Hence, the normalized width occupied by sample *a* is $s = s_2 - s_1 = I_i/(2I_s + I_i)$. Given sufficient mixing channel length, sample concentration profiles will asymptotically approach their averages $c_a(\eta) = I_i/(2I_s + I_i)$ and $c_b(\eta) = 2I_s/(2I_s + I_i)$. Figure 6-8 shows the comparison between system simulation results and numerical data on concentration distributions of sample *a*, which diffuses more slowly than sample *b* with higher diffusivity, at the mixing channel outlet for two flow ratios s = 1/10 and s = 1/3. To allow comparison with results of the T-mixer in the preceding subsection, the voltages applied at the reservoirs are chosen to be ϕ_i = {240, 267} V, ϕ_s = {280, 267} V and ϕ_o = 0 V to obtain s = {1/10, 1/3}, yielding E = 143 V cm^{-1} in the mixing channel. Figure 6-8 shows that the numerical and system simulation results agree well (with a worst-case M = 3% for s = 1/10). Due to its lower initial mixing residual, a smaller stream width yields a more uniform concentration distribution. In addition, it is interesting to note that in contrast to the T-mixer, the focusing mixer greatly improves

sample homogeneity, which can be attributed to the reduced stream width of the sample. That is, as the centerline of the focusing-mixer is effectively an impermeable wall due to symmetry, the diffusion distance is only one-half of that in the T-mixer.

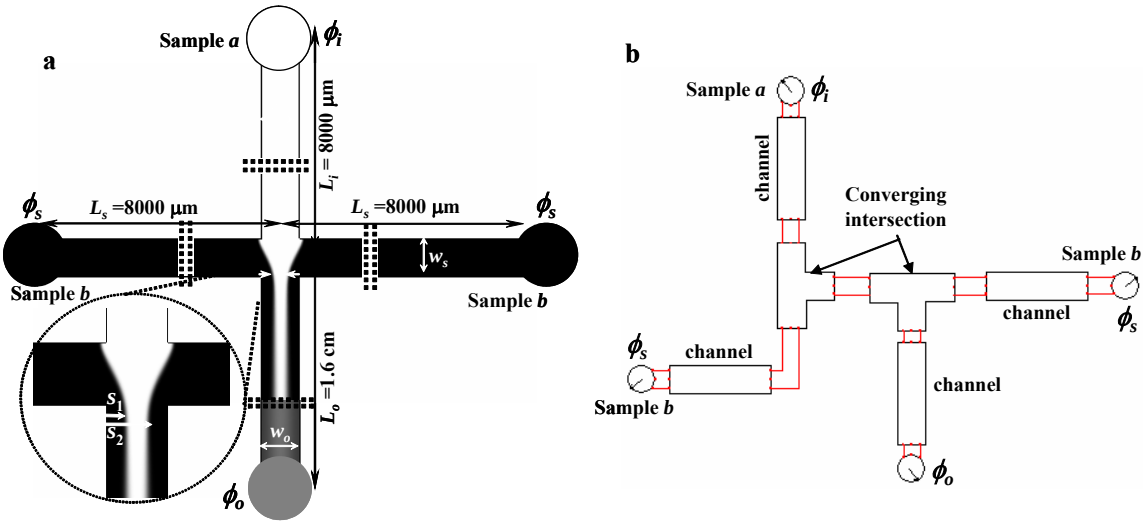

Figure 6-7. (a) An electrokinetic focusing micromixer and (b) its schematic representation for system simulations.

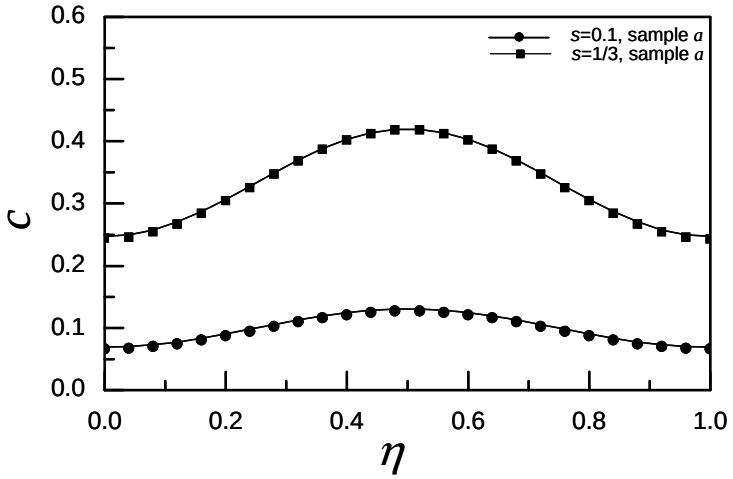

Figure 6-8. System simulation results (lines) compared with numerical data (symbols) on concentration profiles (sample *a*) for the electrokinetic focusing micromixer.

6.4.4 Multi-Stream (Inter-Digital) Micromixers

Now the system-level schematic is applied to electrokinetically driven multi-stream micromixers, which improve mixing by replacing broad sample streams (such as T-mixers) with alternating and thin streams to greatly reduce sample diffusion distances.

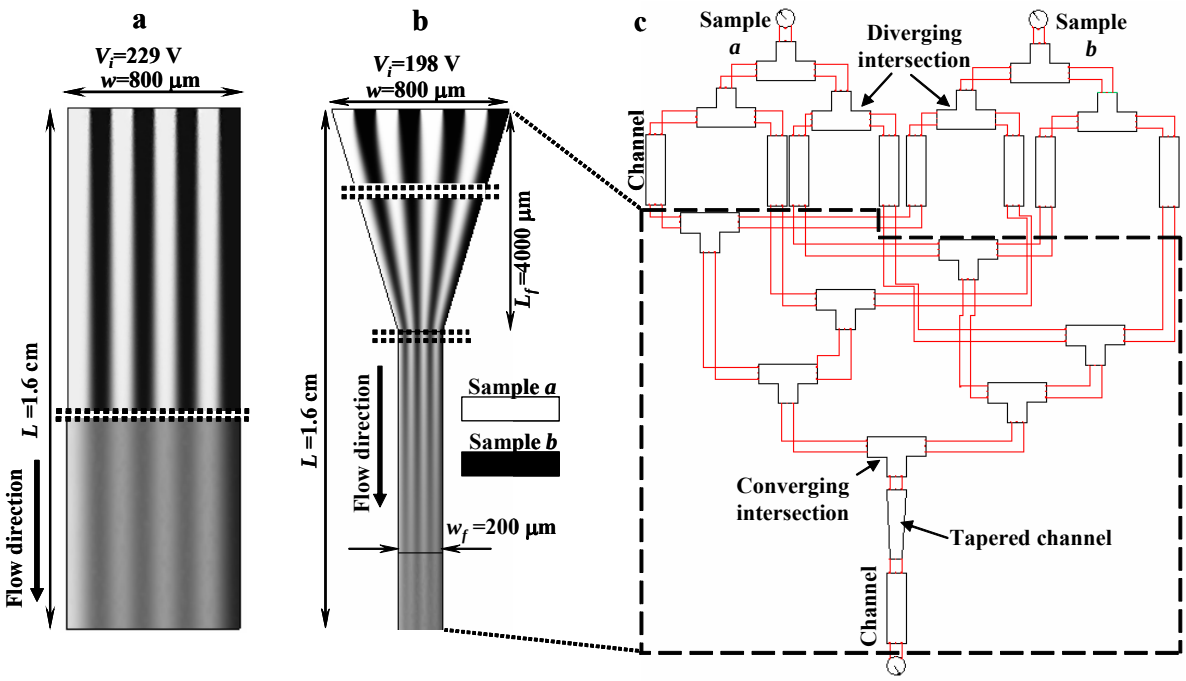

Figure 6-9. Multi-stream micromixers (a) without or (b) with focusing and (c) their schematics for system simulations.

Depending on the geometry of mixing channels, such mixers can be further divided into those without (Figure 6-9a) or with focusing (Figure 6-9b). The schematic representation in Figure 6-9c applies to mixers with focusing, and can also be used for mixers without focusing by removing the tapered channel element. In this schematic, samples *a* (white) and *b* (black) from two reservoirs are branched by successive widthwise diverging intersections into multiple streams. These streams are then arranged to alternate in the sample content using feed channels and converging intersections connected in cascade. An inter-digital concentration profile is obtained at the inlet of the mixing channel, in which the samples are mixed. As the feed channels generally do not influence sample mixing downstream, numerical simulations are focused on the sample diffusion process in the mixing channel, with the voltage at the inlet set to a value calculated from the system

simulation. The mixers with and without focusing are given the voltage ϕ_i = 198 and 229 V so that they both have E = 143 V cm^{-1} in the uniform mixing channel.

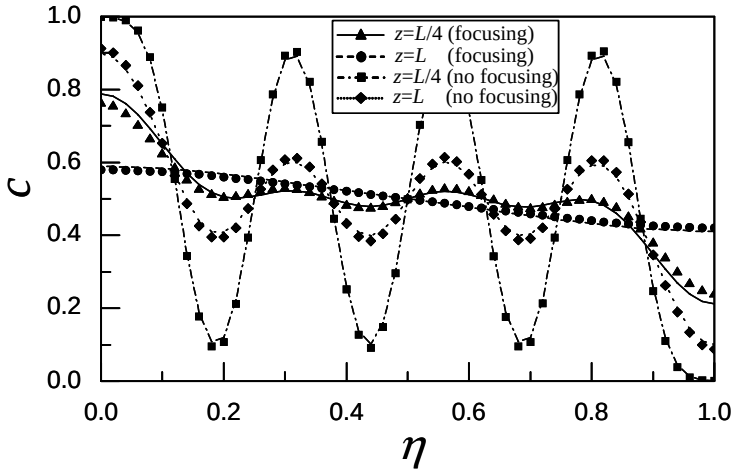

Figure 6-10. System simulation results (lines) compared with numerical data (symbols) on concentration profiles (sample *a*) at $x = L_f$ and $x = L$ in the electrokinetic multi-stream micromixer.

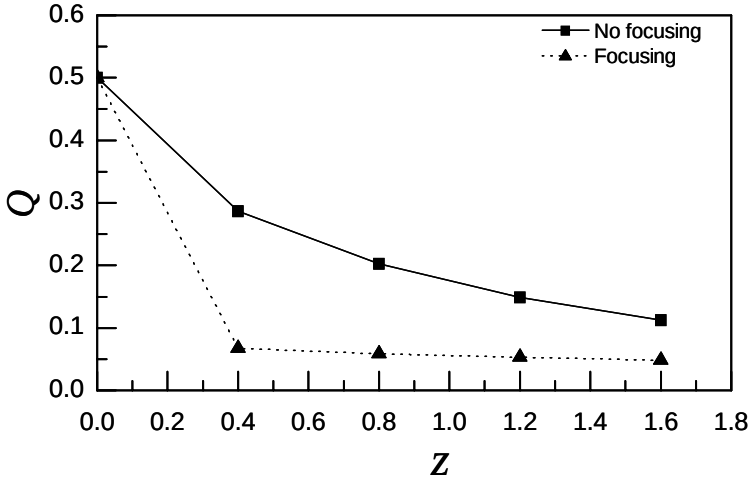

Figure 6-11. System simulation results on the variation of the mixing residual along the channel length (data points are connected by lines to guide the eye) for the electrokinetic multi-stream micromixer.

Figure 6-10 compares concentration profiles of sample *a* for both mixers from the system and numerical simulation results at $x = L_f = L/4$ and $x = L$, where L_f and L are the lengths of the focusing and entire mixing channels. Excellent agreement between the numerical and system simulation results is observed, with M = 3% for the case with

focusing. Sample lamination is clearly seen, and the mixer with focusing facilitates sample diffusion and leads to a highly homogeneous concentration profile (Q = 0.048).

The change of Q along the channel is shown in Figure 6-11. Q drops much faster in the mixing channel with focusing than in that without focusing, as reduced sample diffusion distances improve mixing efficiency. This figure also shows that at $x = L_f = L/4$, a very low mixing residual (Q = 0.067) is already achieved for the mixer with focusing. From $x = L/4$ to $x = L$, a modest decrease in Q (from 0.067 to 0.048) is obtained but accounts for about 75% of the total channel length. This implies the inappropriateness of neglecting the appreciable mixing contribution made by the focusing channel [9, 172]. In addition, this indicates that shorter mixing channel lengths with less complete, yet still sufficient, mixing may be more cost effective for some applications, demonstrating the utility of the behavioral model in optimal choice of mixing channel lengths in mixer design.

6.4.5 Split-and-Recombine (SAR) Micromixers

An alternative to multi-stream mixers (Figure 6-9), the split-and-recombine (SAR) mixer performs multi-lamination of samples within the mixing channel by a number of serially connected mixing units. A SAR unit consists of an inlet channel, a depthwise diverging intersection, a pair of constant cross-section channels, a converging intersection and an outlet channel connected sequentially in such order (Figure 6-12a). Sample flow is first introduced, recombined, mixed and split vertically into two streams. The split streams are then recombined again side by side along the width. Repeating the SAR unit can exponentially ($\sim 2^n$) shrink the inter-stream diffusion distance [179, 180, 186, 187] and promote the sample mixing. Figure 6-12 illustrates the first two SAR units of an electrokinetic SAR mixer and its simulation schematic (the combination of the feed

channels and the first converging intersection is thought of as the first SAR unit). Depending on the requirement of mixing, more SAR units can be integrated.

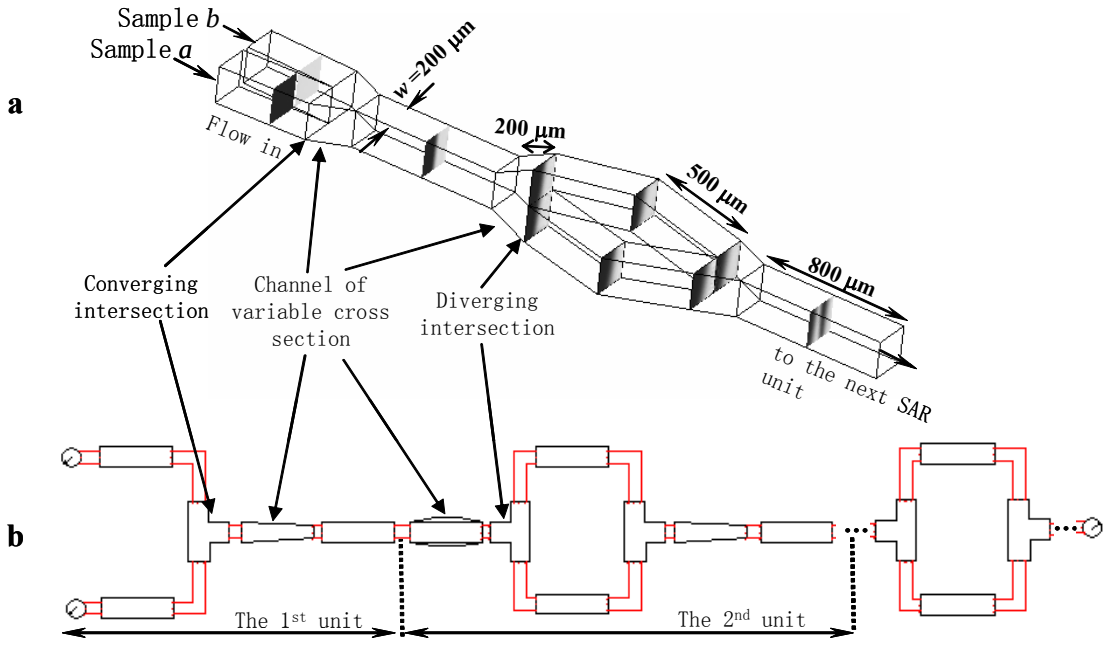

Figure 6-12. (a) Three-dimensional structure of the first two SAR units in an electrokinetic SAR micromixer. (b) Schematic of an electrokinetic SAR micromixer.

Depth-averaged concentration profiles along the normalized width obtained from system and numerical simulations are shown in Figure 6-13a for a six-unit SAR mixer. System simulation and numerical results detected at the midpoint of the straight mixing channel match well with the worst-case M = 5% (due to the demanding requirement on computation resources, only the first two units are numerically simulated). Multiple splitting of sample *a* is clearly observed, which leads to continuously reduced inter-stream diffusion distances. In contrast to a T-mixer with the same channel dimensions (w = h = 200 μm, L = 12145 μm) and operational electric field (E = 143 V cm^{-1}), impressive improvement in mixing performance has been achieved by the SAR mixer. Figure 6-13b shows an inflection point in the dependence of Q on the SAR unit number N_{SAR}, attributed to disparate mixing behavior of different units in the SAR mixer. For the preceding SAR

units (e.g., N_{SAR} = 1 and 2), the sample layer is not sufficiently laminated and the large diffusion distance prevents effective mixing. On the other hand, for the ending SAR units, there is less driving force (concentration gradient) for mixing as sample homogeneity improves, leading to minor or negligible enhancement. Therefore, the most drastic decrease in Q occurs in the middle units (for the example in Figure 6-12, it is N_{SAR} = 3) corresponding to the optimum transport conditions. Therefore, for SAR mixers, the tradeoff among mixing performance, mixer size, mixing time and system complexity also exists, confirming the utility of our models to SAR mixer design.

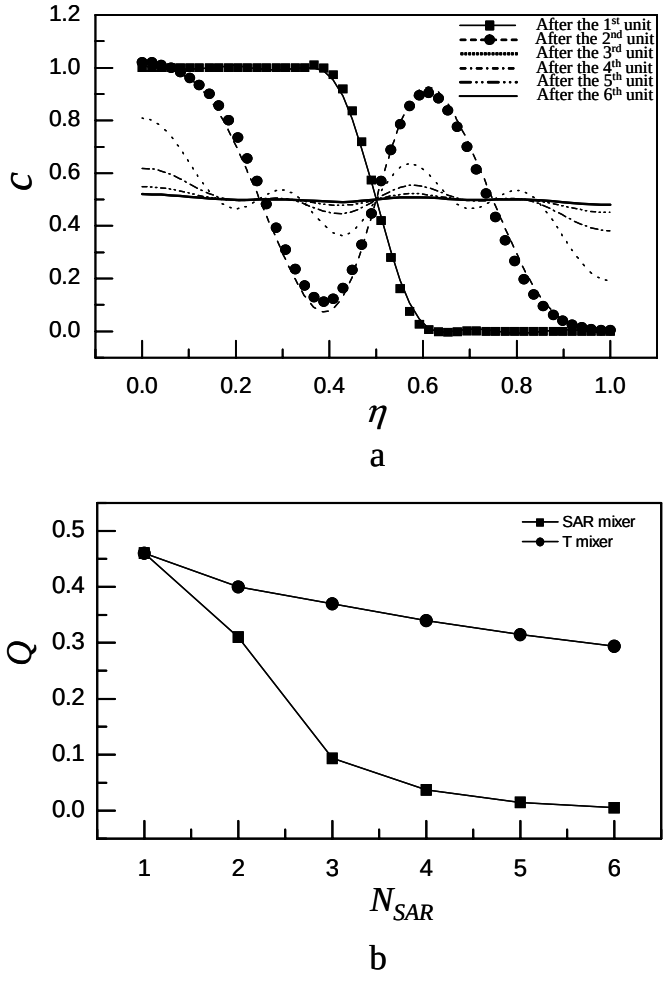

Figure 6-13. Simulation results of the split-and-recombine (SAR) mixer. (a) System simulation results (lines) on concentration profiles (sample *a*) and their comparison to the numerical data (symbols) after the first two units. (b) System simulation results on the variation of the mixing residual along the channel length.

6.4.6 Mixing Networks

Finally, the behavioral model is well suited to the study of complex mixing networks [71], in which different sample concentrations can be obtained at multiple output channels by geometrically repeating units with a single constant voltage applied at sample and buffer reservoirs. Here the model is applied to the serial mixing network (Figure 3-2). The system-level schematic simulation results, along with numerical analysis and experimental data, are presented in Table 6-1, which lists sample (rhodamine B) concentrations in analysis channels A_1–A_5. Both complete and partial mixing situations are analyzed. When a voltage of ϕ_{app}= 0.4 kV is applied to the sample and buffer reservoirs with the waste reservoirs grounded, sample mixing in channels S_2–S_5 is nearly width-wisely complete (with Q = 0.007 at the end of channel S_2). As a result, sample concentrations in channels A_1–A_5 are independent of sample properties and determined *only* by the electric currents in the mixing network. There is excellent agreement between the system simulation and the numerical and experimental data (with an average error smaller than 6%). It is also interesting to note that in contrast to electric resistor-based models [16, 71, 132] that require post-calculations of concentrations from electric current distributions in the network, our models directly yield concentration values.

In addition to complete mixing, partial mixing in which the sample concentrations in channels S_2–S_5 are not width-wisely uniform and hence the resistor-based modeling is not valid, can be readily simulated by the system-level schematic. In this case, sample concentrations in channels A_1–A_5 depend on not only electric currents in the network but also the sample concentration profiles at the exits of channels S_2–S_5. Results from the system simulation are also listed in Table 6-1. While a lack of knowledge of sample

properties does not allow experimental data to be used for comparison, these system simulation results are compared with numerical analysis, assuming a diffusivity of $D = 3\times10^{-10}$ m^2 s^{-1} and an EK mobility of $\mu = 2.0\times10^{-8}$ m^2 V^{-1}s^{-1}. A voltage of $\phi_{app} = 1.6$ kV, as used in experiments in the literature [71], is applied to the sample and buffer reservoirs, with the waste reservoirs grounded. Good agreement can be observed, with an average error of $M = 4\%$. From the table, it can be seen that as a result of high ϕ_{app}, which is four times that used in the complete mixing case above, there is a four-fold increase in EK velocity and decrease in sample residence time in the channels. Therefore, mixing in channels S_2–S_5 is incomplete (with $Q = 0.14$ at the end of channel S_2). At the cross-intersection following channel S_2, the amount of the sample shunted to A_2 is more than that predicted by the complete-mixing based resistor-model due to non-uniform sample distributions at the intersection's inlet. Consequently, concentrations in channels A_3–A_5 have lower values, agreeing with experimental observations [71].

Parallel mixing networks [71] can be represented and simulated in a similar fashion. In such a network, all the channels are designed with similar cross-sectional area. Thus, at the T-intersections (T_2–T_6) the currents from the sample and buffer reservoirs are inversely proportional to the length (Ohm's law) of their feed channels (B_1–B_6 and S_2–S_7) with a single constant voltage (1 kV) applied to all sample and buffer reservoirs (Figure 6-14a). Therefore, through proper choice of the lengths of those feed channels, an array of different sample concentrations can be eventually obtained in the output channels (A_1–A_7). Figure 6-14b illustrates the schematic representation of the parallel mixing network. Comparison between the system simulation results and the experimental and numerical data is shown in Table 6-1. An average error of 3.6 % relative to experiments is found.

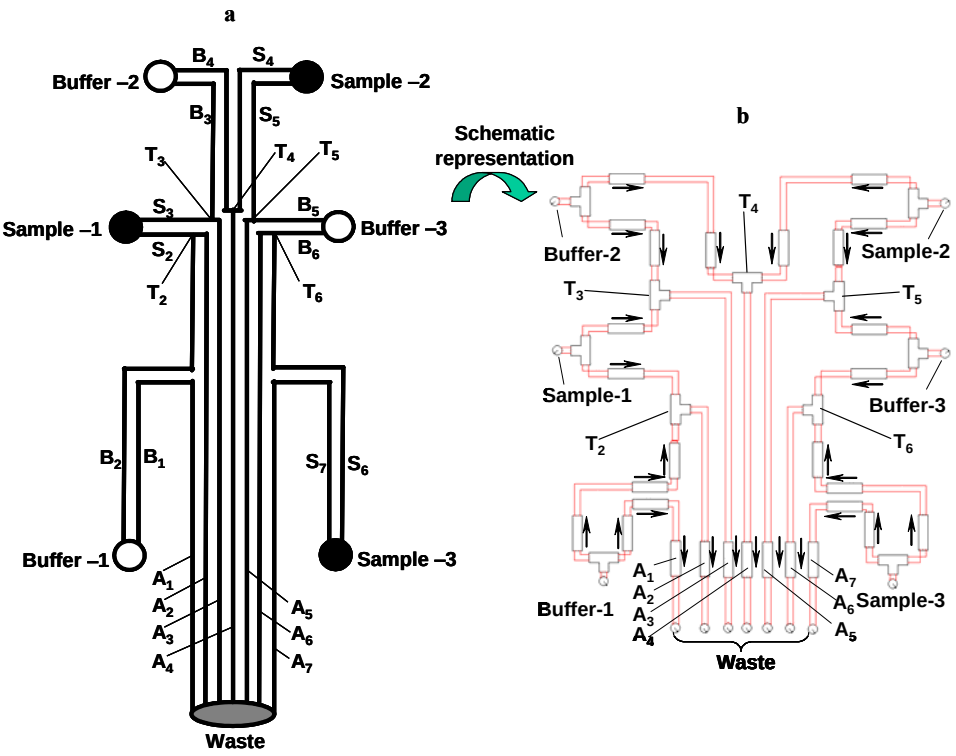

Figure 6-14. A complex electrokinetic parallel mixing network [71] and its schematic representation for system-level simulations.

Table 6-1. Comparison between the system simulation results (sys) and numerical (num) and experimental (exp) data on sample concentrations in analysis channels of serial and parallel mixing networks

Serial Mixing Network						**Parallel Mixing Network**			
	Complete Mixing			Partial Mixing			Complete Mixing		
channel	*c* (sys)	*c* (exp)	*c* (num)	*c* (sys)	*c* (num)	channel	*c* (sys)	*c*(exp)	*c* (num)
A_1	1	1	1	1	1	A_1	0	0	0
A_2	0.37	0.36	0.378	0.48	0.496	A_2	0.83	0.84	0.832
A_3	0.22	0.21	0.224	0.187	0.187	A_3	0.68	0.67	0.674
A_4	0.125	0.13	0.133	0.081	0.0815	A_4	0.52	0.51	0.523
A_5	0.052	0.059	0.0628	0.029	0.0315	A_5	0.35	0.36	0.354
						A_6	0.17	0.19	0.168
						A_7	1	1	1

Finally, it is interesting to note that the system simulations have demonstrated drastic improvement in computational efficiency over the full numerical simulations. For example, on a multi-user 2-CPU 1-GHz Sun Fire 280 processors with 4 GB RAM, system simulations of the serial mixing network above was completed within 20 seconds with

netlisting and less than 1 second without netlisting. In contrast, using the same platform, 6 hours was needed to complete the computation of a numerical model in FEMLAB 3.0a [152], which was not reusable when chip topologies and dimensions were modified. The computational advantage of the system simulation is thus clear, making possible system-level micromixer design that may involve hundreds or thousands of iterative simulations.

6.5 Summary

Analytical and parameterized behavioral models for micromixing elements have been presented for efficient and accurate modeling of laminar diffusion-based electrokinetic passive mixers and mixing networks. Complex micromixers have been decomposed into a system of elements with relatively simple geometry. Behavioral models for elements have been developed and linked to form a system-level schematic representing the entire micromixer. The system simulation has been verified with numerical and experimental data, and used to perform systematic analysis and comparison of sample mixing in T-type, focusing, multi-stream, SAR and complex mixing network devices, yielding insights into the effects of such parameters as system topology, geometry, properties and operational parameters on mixing performance. The model affords drastically improved computational efficiency over numerical simulations, and is thus well suited for optimal micromixer design processes that typically involve large numbers of design iterations.

Parameterized and analytical behavioral models for mixing elements are the building blocks of the system level simulations. Four types of basic elements, mixing channels, diverging and converging intersections and reservoirs have been considered. Such elements are amenable to analytical modeling and are sufficiently general to represent electrokinetic passive micromixers commonly used in lab-on-a-chip systems. The models developed for

these elements are valid for general input concentration profiles and arbitrary flow ratios, and enable us to consider the overall effects of the mixer topology, geometry, operational parameters and material properties at the system level for the first time.

The system-level schematic has been used to perform studies of electrokinetic passive micromixers that employ diffusion-based mixing-enhancing techniques such as focusing, multi-lamination and splitting-and-recombining. These techniques are effective in improving mixing performance but lead to complex mixer geometries, extensive and sensitive design-parameter space and complicated design processes. Generally, system-level simulations have demonstrated that asymmetric sample flow rates should be used for improved mixing efficiency as long as the sample concentrations remain at a detectable level. Sample homogeneity improves rapidly at the early stage of mixing but then tends to saturate eventually, with the region in which this transition occurs determined by the mixer topology and geometry, operational parameters (e.g., flow ratios) and material properties. Therefore, the tradeoff among the chip real-estate area, mixing size and system complexity should be considered. A salient advantage offered by the behavioral model over the resistor-based model is its capability of computing the complex mixing network that involves partial mixing. Therefore, the behavioral model can be a useful tool to design more compact mixer topologies (see Chapter 8). It is worth noting that while the system simulation focuses on electrokinetic micromixers, the conceptual approach can be generalized to micromixers that use pressure-driven flow (see Chapter 8).

Chapter 7 Modeling and Simulation of Integrated Lab-on-a-chip Systems

This chapter demonstrates the integration of the behavioral models for subsystems (e.g., separation microchips in Chapter 4 and Chapter 5; and mixers in Chapter 6) into a system-level schematic of integrated LoCs. Such a schematic can be iteratively simulated to capture the overall effects of subsystem-level parameters (e.g., separator and mixer topologies and types; operational electric fields and injection schemes etc.) and element-level parameters (e.g., length and width of mixing and separation channels etc.) on system performance, as well as the tradeoffs among them, leading to a system-level optimal design achieved by "negotiation" among each subsystem and element.

Integrated LoC design is difficult because of the need to,

(1). Accurately interpret the fundamental multi-physics phenomena (such as electric, fluidic, heat transfer and sample transport) at element or component levels.

(2). Properly classify, decouple and reduce the multi-physics phenomena to tractable mathematical models, while still maintaining their essential physical characteristics.

(3). Efficiently integrate low-level mathematical models to obtain a system-level representation for iterative simulation-based design.

Most of the previous approaches to LoC modeling are not amenable to accurate simulation-based iterative design of integrated systems due to various limitations (Section 2.3), such as difficulties in system-level representation, inaccurate physical descriptions and inflexibilities with respect to geometrical perturbations. Currently, the only general and accurate approach is the classical method of numerical simulation, which however suffers

from unacceptable computational cost. Therefore, a methodology that simultaneously takes into account of balancing accuracy and efficiency without sacrificing generality is needed.

To demonstrate the ability of the methodology developed in this thesis to meet these goals, this chapter describes how it can be used to design a competitive immunoassay microchip consisting of mixing, reaction, injection and separation subsystems. Following a short introduction (Section 7.1), a simplified competitive immunoassay reactor model and connection pins (I/O parameters) of an injector model are proposed (Section 7.2). These models are then integrated with previously developed separator and mixer models (Section 7.3) to compose a system-level schematic of the immunoassay chip. The schematic is then simulated by both DC and transient analysis to capture the influence of topologies, element sizes, material properties and operational parameters on chip performance. The modeling results as well as the design methodology are validated against experimental and numerical data (Section 7.4). Finally, the original LoC device is redesigned using the simulation framework to improve bio-analysis efficiency and minimize chip-area (Section 7.5).

7.1 Integrated Competitive Immunoassay Microchip

Figure 7-1a illustrates an integrated competitive immunoassay microchip proposed by Harrison *et al.* [16], which consists of four subsystems (mixing, reaction, injection and separation). Its operation involves both synthesis and analysis, which are typical functions performed in a biochemical lab. In the first phase, a negative electrical voltage is applied at reservoir 3 with reservoir 5, 6 and 7 grounded and the other reservoirs left floating. Theophylline (Th, from reservoir 5) and fluorescein-labeled theophylline tracer (Th^*, from 6), driven by the electric field, first mix with each other within channel J1-J3. Then Th and Th^* in the mixture compete for a limited number of antibody (Ab, from reservoir 7) binding

sites in the mixing and reaction channel J3-J4. The mixture (hereafter called analyte) of reaction products Ab-Th* and Ab-Th, as well as unreacted Th* and Th are loaded into the double-T injector. Th, Th* and Ab are continuously supplied by the reservoirs; therefore concentrations of all the samples, reagents and products in the mixer and reactor at this phase are in steady-state. This completes the synthesis operation.

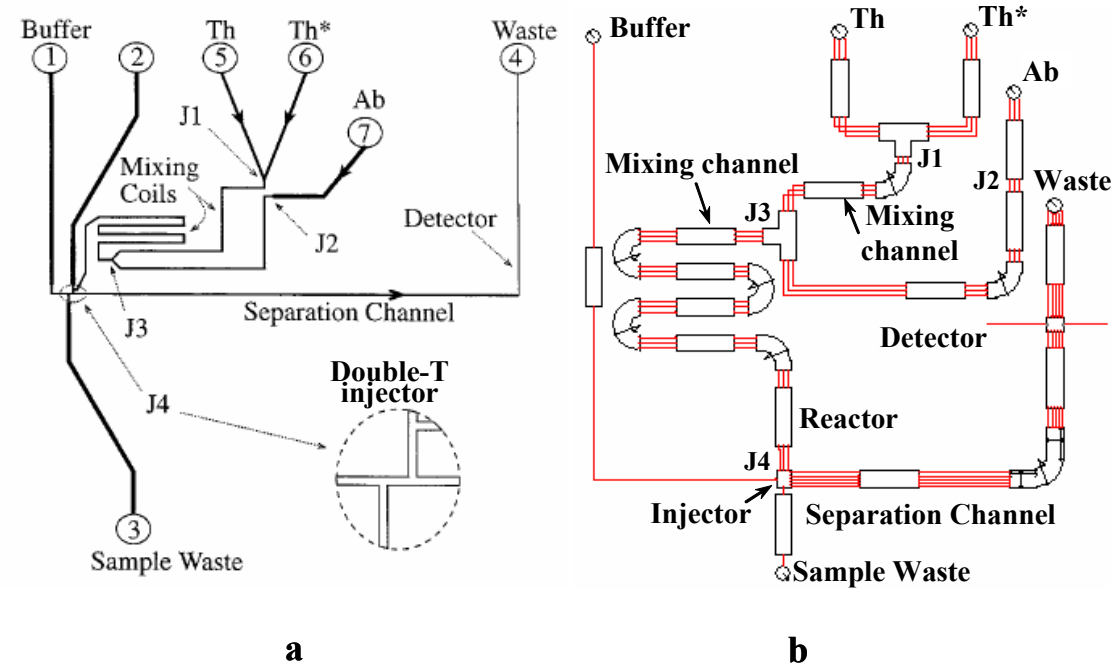

Figure 7-1. (a) Sketch of a competitive immunoassay microchip consisting of four subsystems (mixing, reaction, injection and separation) [16]. (b) Its system-level schematic.

In the second phase (analysis), the voltages are switched on reservoirs 1 and 4 with the others left floating. Thus the loaded analyte is injected as a band into the separation channel J4-reservoir 4. Because the analyte includes tagged Ab-Th* and Th* molecules that have different charges and sizes, they move at different speeds and eventually can be separated by electrophoresis [118]. The amount of Ab-Th* and Th*, represented by the areas under the electropherogram, for a wide range of Th concentration, can be obtained to generate a calibration curve to determine unknown concentrations of Th in the sample at reservoir 5 for clinical analysis. As the Ab-Th complex and Th are not tagged with fluorescent tracers,

they are invisible to detection and not considered in the remaining operation. In this phase, Ab-Th* and Th* bands broaden due to molecular diffusion and other dispersion sources; therefore the transient evolution of their band shapes, directly impacting the analysis quality is of prime importance.

To simulate such a LoC, a system-level schematic that assembles behavioral element models based on the LoC geometric and functional hierarchy needs to be built. Figure 7-1b illustrates the hierarchical decomposition of the LoC. It is decomposed into four functional subsystems and further broken down into commonly used elements, such as the straight mixing channel, injector, reactor and turn separation channel. Therefore, models for reactors and injectors are still needed for integration with previously described models.

7.2 Behavioral Models for Reactors and Injectors

In this section, behavioral models of competitive immunoassay reactors and connection pins (I/O parameters) of double-T injectors that are integral to the schematic in Figure 7-1b will be presented.

7.2.1 Competitive Immunoassay Reactors

The biofluidic pins for a general purpose reactor will be defined to enable the extension of our system-level simulation approach beyond a competitive immunoassay design. The behavioral model for the reactor that will be developed is specific to the competitive immunoassay. General purpose reactor model is being described elsewhere at Carnegie Mellon [188].

7.2.1.1 Pin Definition

In practical integrated LoCs, the reactor fulfills two functions, bridging the mixer and injector, as well as converting samples and reagents into reaction products (synthesis).

Therefore, the biofluidic pins at its input and output terminals are different. Figure 7-2 shows the behavioral model structure for the electrokinetic reactor. In additional to electric pins (V_{in} and V_{out}), biofluidic pins are also proposed with arrows indicating the direction of signal flow for calculating pin values. At the reactor inlet, the Fourier coefficients ($d_m^{(in)}$) of the widthwise concentration profiles of the samples and reagents input from upstream mixers characterize their premixing degree. At the outlet, biofluidic pins are defined as the average concentrations ($c_{avg}^{(out)}$) of the reaction products and unreacted samples that can be used by the downstream injector to determine the band shape of the injected species. Here, indices *in* and *out* represent the quantities at the inlet and outlet respectively. Analog wiring buses carrying vector-type pin values (concentration coefficients or multiple samples and reagents) similar to those used in mixers and separators are also employed.

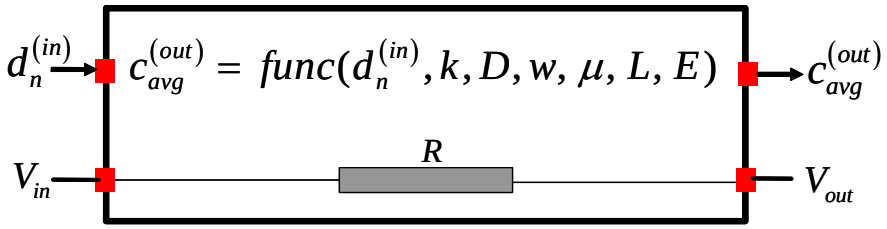

Figure 7-2. Behavioral model structure for the electrokinetic reactor. At the inlet, the Fourier coefficients ($d_n^{(in)}$) of widthwise concentration profiles of samples and reagents conveyed from upstream mixers characterize their premixing degree. At the outlet, biofluidic pins quantify the average concentrations ($c_{avg}^{(out)}$) of the reaction products and unreacted samples.

7.2.1.2 Behavioral Model

Figure 7-3 depicts the process of competitive immunoassay reactions between Th, Th* and Ab, as well as the model we use. The uniformly mixed theophylline Th and fluorescein-labeled theophylline Th* compete for a limited number of antibody Ab binding sites in the main mixing and reaction channel that corresponds to channel J3-J4 in Figure 7-1a. The binding kinetics are governed by the equations in Figure 7-3a, where k_1 and k_2

are the forward and backward kinetic constants for the binding reaction between Th and Ab and k_3 and k_4 are those between Th^* and Ab respectively.

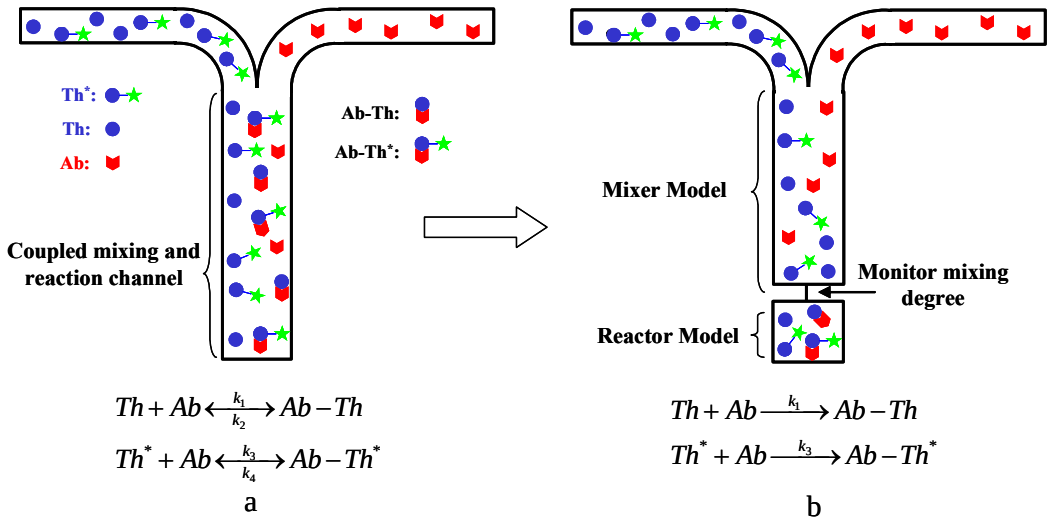

Figure 7-3. (a) Sketch of the competitive immunoassay reaction between Th, Th^* and Ab. (b) Sketch of the competitive immunoassay reaction model.

The concentrations c of Th, Th^*, Ab, Ab-Th and Ab-Th^* in this simultaneous mixing and binding-reaction are spatial-position dependent and governed by a set of convection-diffusion equations with reactive source terms [189]:

$$
\begin{aligned}
u_{Th}\frac{dc_{Th}}{dx} &= D_{Th}\left(\frac{\partial^2 c_{Th}}{\partial x^2}+\frac{\partial^2 c_{Th}}{\partial y^2}\right)-k_1 c_{Th}c_{Ab}+k_2 c_{Ab-Th}\\
u_{Th^*}\frac{dc_{Th^*}}{dx} &= D_{Th^*}\left(\frac{\partial^2 c_{Th^*}}{\partial x^2}+\frac{\partial^2 c_{Th^*}}{\partial y^2}\right)-k_3 c_{Th^*}c_{Ab}+k_4 c_{Ab-Th^*}\\
u_{Ab}\frac{dc_{Ab}}{dx} &= D_{Ab}\left(\frac{\partial^2 c_{Ab}}{\partial x^2}+\frac{\partial^2 c_{Ab}}{\partial y^2}\right)-\left(k_1 c_{Th}+k_3 c_{Th^*}\right)c_{Ab}+\left(k_2 c_{Ab-Th}+k_4 c_{Ab-Th^*}\right) \quad (7.1)\\
u_{Ab-Th}\frac{dc_{Ab-Th}}{dx} &= D_{Ab-Th}\left(\frac{\partial^2 c_{Ab-Th}}{\partial x^2}+\frac{\partial^2 c_{Ab-Th}}{\partial y^2}\right)+k_1 c_{Th}c_{Ab}-k_2 c_{Ab-Th}\\
u_{Ab-Th^*}\frac{dc_{Ab-Th^*}}{dx} &= D_{Ab-Th^*}\left(\frac{\partial^2 c_{Ab-Th^*}}{\partial x^2}+\frac{\partial^2 c_{Ab-Th^*}}{\partial y^2}\right)+k_3 c_{Th^*}c_{Ab}-k_4 c_{Ab-Th^*}
\end{aligned}
$$

where D is the sample diffusivity, u is the sample velocity and subscripts *Th*, *Th**, *Ab*, *Ab-Th* and *Ab-Th** refer to the quantities associated with the corresponding samples. Eq. (7.1)

is non-linear and does not admit analytical solutions. Ref. [16] suggests several simplifying assumptions:

(1). The fluorescein has negligible effects on the binding affinity of Th to Ab (namely $k_1 \approx k_3$ and $k_2 \approx k_4$), and on the material properties of Th and Ab-Th (namely $u_{Th} \approx u_{Th^*}$ and $D_{Th} \approx D_{Th^*}$, $u_{Ab-Th} \approx u_{Ab-Th^*}$ and $D_{Ab-Th} \approx D_{Ab-Th^*}$).

(2). The reaction is essentially irreversible, $k_1 >> k_2$ and $k_3 >> k_4$, such that the forward binding is dominant and the analyte exiting mixing-reaction channel does not contain noticeable Ab (the amount of Ab is limited). This can be inferred from the electropherogram (Figure 6) in Ref. [16] (if the reverse reaction was significant, another concentration peak of Th^* disassociated from Ab-Th^* complex would be observed in the separation channel).

(3). Both mixing and reaction are complete, which are implied by Figures 5 and 7 in Ref. [16] (Figure 5 shows that 99 % mixing has been reached. In Figure 7, except at Th concentration of 10 mg/L, the stop-flow case does not appreciably enhance the reaction, indicating that the reaction is almost complete for the continuous-flow case).

Based on these assumptions, Eq. (7.1) can be reduced to

$$\begin{aligned}
u_{Th}\frac{dc_{Th}}{dx} &= D_{Th}\left(\frac{\partial^2 c_{Th}}{\partial x^2}+\frac{\partial^2 c_{Th}}{\partial y^2}\right)-k_1 c_{Th}c_{Ab}\\
u_{Th^*}\frac{dc_{Th^*}}{dx} &= D_{Th^*}\left(\frac{\partial^2 c_{Th^*}}{\partial x^2}+\frac{\partial^2 c_{Th^*}}{\partial y^2}\right)-k_1 c_{Th^*}c_{Ab}\\
u_{Ab}\frac{dc_{Ab}}{dx} &= D_{Ab}\left(\frac{\partial^2 c_{Ab}}{\partial x^2}+\frac{\partial^2 c_{Ab}}{\partial y^2}\right)-k_1\left(c_{Th}+c_{Th^*}\right)c_{Ab}\\
u_{Ab-Th}\frac{dc_{Ab-Th}}{dx} &= D_{Ab-Th}\left(\frac{\partial^2 c_{Ab-Th}}{\partial x^2}+\frac{\partial^2 c_{Ab-Th}}{\partial y^2}\right)+k_1 c_{Th}c_{Ab}\\
u_{Ab-Th^*}\frac{dc_{Ab-Th^*}}{dx} &= D_{Ab-Th^*}\left(\frac{\partial^2 c_{Ab-Th^*}}{\partial x^2}+\frac{\partial^2 c_{Ab-Th^*}}{\partial y^2}\right)+k_1 c_{Th^*}c_{Ab}
\end{aligned} \tag{7.2}$$

The first two equations in Eq. (7.2) differ from each other by a scaling constant *CR*, the concentration ratio of c_{Th} to c_{Th*}, implying that the amount of Ab bound to Th and Th* (namely, the $c_{Ab\text{-}Th}$ and $c_{Ab\text{-}Th*}$) is proportional to the concentrations of Th and Th* and *CR* holds unchanged from the inlet to the outlet of the mixing-reaction channel. Additionally, the assumption of complete mixing and binding-reaction enables the calculation of the concentrations of reaction products and unreacted samples at the end of the mixing-reaction channel (intersection J4) based on the mass-balance principle. In the model implementation, the main mixing-reaction channel in Figure 7-3a is modeled as a serial connection of a mixing channel having the same dimensions as the original channel and a reactor with negligible physical size (R = 0) in which the binding reaction completes instantaneously (Figure 7-3b). This treatment allows the designer to monitor the mixing degree (or mixing residual) before samples and reagents enter the reactor model and examine if the complete mixing assumption is satisfied during design optimizations.

The mixing model is described in the previous chapter and will not be repeated here. The modeling effort hence focuses on the reactor in Figure 7-3b. As the amount of Ab is limited (eventually completely consumed), the binding reaction in the reactor model can be quantitatively described by,

$$\underbrace{Th}_{M_{Ab}^{(in)}\left(\frac{CR}{CR+1}\right)} + \underbrace{Ab}_{M_{Ab}^{(in)}\left(\frac{CR}{CR+1}\right)} \xrightarrow{k_1} \underbrace{Ab-Th}_{M_{Ab}^{(in)}\left(\frac{CR}{CR+1}\right)} \tag{7.3}$$

$$\underbrace{Th^*}_{M_{Ab}^{(in)}\cdot\left(\frac{1}{CR+1}\right)} + \underbrace{Ab}_{M_{Ab}^{(in)}\cdot\left(\frac{1}{CR+1}\right)} \xrightarrow{k_3} \underbrace{Ab-Th^*}_{M_{Ab}^{(in)}\cdot\left(\frac{1}{CR+1}\right)} \tag{7.4}$$

where $M_{Ab}^{(in)} = u_{Ab} \cdot c_{Ab}^{(in)} \cdot A_r$, A_r is the constant cross-sectional area of the mixing-reaction channel, *M* stands for the molar mass flow rates of samples and indices *in* and *out* represent

the quantities at the inlet and outlet of the reactor model. Similarly, those of Th* and Th are expressed as $M_{Th}^{(in)} = u_{Th} \cdot c_{Th}^{(in)} \cdot A_r$, $M_{Th^*}^{(in)} = u_{Th^*} \cdot c_{Th^*}^{(in)} \cdot A_r$. The contribution of the axial diffusive mass flux is not counted due to the long mixing-reaction channel (L = 81 mm and w = 52 μm). Then, from mass balance, the molar mass flow rates of the reaction product Ab-Th* and unreacted Th* exiting the reactor model are respectively given by,

$$M_{Ab-Th^*}^{(out)} = u_{Ab} c_{Ab}^{(in)} A_r \left(\frac{1}{CR+1} \right) \tag{7.5}$$

$$M_{Th^*}^{(out)} = u_{Th^*} c_{Th^*}^{(in)} A_r - u_{Ab} c_{Ab}^{(in)} A_r \left(\frac{1}{CR+1} \right) \tag{7.6}$$

Table 7-1 summarizes the molar mass flow rates of samples and reaction products flowing in and out of the reactor.

Table 7-1 Molar mass flow rates of samples and reaction products at the inlet and outlet of the reaction model.

	inlet	**outlet**
Th	$M_{Th}^{(in)} = u_{Th} c_{Th}^{(in)} A_r$	$M_{Th}^{(out)} = u_{Th} c_{Th}^{(in)} A_r - u_{Ab} c_{Ab}^{(in)} A_r \left(\frac{CR}{CR+1} \right)$
Th*	$M_{Th^*}^{(in)} = u_{Th^*} c_{Th^*}^{(in)} A_r$	$M_{Th^*}^{(out)} = u_{Th^*} c_{Th^*}^{(in)} A_r - u_{Ab} c_{Ab}^{(in)} A_r \left(\frac{1}{CR+1} \right)$
Ab	$M_{Ab}^{(in)} = u_{Ab} \cdot c_{Ab}^{(in)} \cdot A_r$	~ 0
Ab-Th	0	$M_{Ab-Th}^{(out)} = u_{Ab} c_{Ab}^{(in)} A_r \left(\frac{CR}{CR+1} \right)$
Ab-Th*	0	$M_{Ab-Th^*}^{(out)} = u_{Ab} c_{Ab}^{(in)} A_r \left(\frac{1}{CR+1} \right)$

Denote $M_{Ab-Th^*}^{(out)} = u_{Ab-Th^*} \cdot c_{Ab-Th^*}^{(out)} \cdot A_r$ and $M_{Th^*}^{(out)} = u_{Th^*} \cdot c_{Th^*}^{(out)} \cdot A_r$. The average molar species concentrations of the analytes entering the injector are,

$$c_{avg,Ab-Th^*}^{(out)} = c_{Ab}^{(in)} \left(\frac{1}{CR+1} \right) = d_{0,Ab}^{(in)} \left(\frac{1}{CR+1} \right) \tag{7.7}$$

$$c_{avg,Th^*}^{(out)} = c_{Th^*}^{(in)} - \frac{u_{Ab}}{u_{Th^*}} c_{Ab}^{(in)} \left(\frac{1}{CR+1} \right) = d_{0,Th^*}^{(in)} - \frac{u_{Ab}}{u_{Th^*}} d_{0,Ab}^{(in)} \left(\frac{1}{CR+1} \right) \tag{7.8}$$

where $u_{Ab} \approx u_{Ab\text{-}Th^*}$ is used [16]. The uniform species concentrations (namely the average concentration attributed to complete mixing) $c_{Ab}^{(in)}$, $c_{Th^*}^{(in)}$ and $c_{Th}^{(in)}$ at the inlet of the reactor model can be extracted from the zero*th* component of $d_n^{(in)}$. Eqs. (7.7) and (7.8) establish the signal flow relationship between the species concentrations at the inlet and outlet of the reactor model.

Obviously, this model does not provide reaction kinetics and requires sufficiently long channels to ensure both complete mixing and reaction (this assumption is valid for the integrated LoC in Figure 7-1), leading to conservative assessment of the mixing-reaction channel length for LoC design.

7.2.2 Double-T Injectors

The double-T injector [16] serves as a physical junction between the reactor, separator, sample (analyte)-waste and buffer feed channels. It operates at both loading and dispensing phases and introduces analytes from the continuous-flow reactor into the separation channel that involves transient evolution of species bands. Therefore, it is indispensable in transitioning the LoC from the synthesis to analysis phases. In contrast to the injector model used for separation modeling (Chapter 4), this new model is capable of automatically determining the shape of the injected species band based on the electric fields at both phases and analyte concentrations from the adjacent reactor model.

7.2.2.1 Pin Definition

Figure 7-4 shows the pins at the injector terminals. Since the injector is modeled as a single element, the symbol view does not reflect its real physical geometry, e.g., double-T

or cross [117]. The terminals connecting to the reactor and separation channel are respectively defined as the inlet and outlet, indicating the direction of signal flow for calculating the band shape of the injected species. At the inlet, the information of the average species concentrations ($c_{avg}^{(in)}$) is acquired from the upstream reactor model. At the outlet, the initial species band shape, such as skew coefficients ($S_n^{(out)}$), variance (σ_{out}^2) and amplitude (A_{out}), as well as the starting separation time ($t_{out} = 0$) is set and propagated to the downstream separation channel for separation computation. In addition, four electric pins V_{in}, V_{out}, V_b and V_{aw} are also defined, where indices *in*, *out*, *aw* and *b* represent the quantities at the terminals linking respectively to the reactor, separation channel, sample (analyte)-waste feed channel and buffer feed channel.

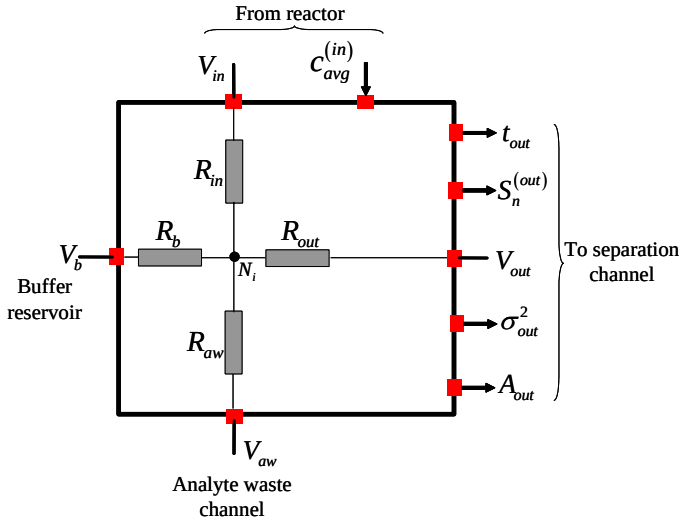

Figure 7-4. Pins for the electrokinetic injector. Indices *in*, *out*, *b*, *aw* refer to the quantities at the terminals respectively linking to the reactor, separation channel, buffer reservoir and sample (analyte)-waste reservoir.

7.2.2.2 Behavioral Model

As its flow path lengths are negligibly small compared with those of feed, mixing-reaction and separation channels, injector can be assumed as a point-wise entity and

electrically represented as four resistors with zero resistance between each terminal and the internal node N_i,

$$R_{aw} = R_b = R_{in} = R_{out} = 0 \tag{7.9}$$

Here, N_i corresponds to the intersection of flow paths. Thus, the voltages at the terminals are consequently the same ($V_{aw} = V_b = V_{in} = V_{out}$). The functional relationship of the biofluidic states between the inlet and outlet of the injector is determined by electric fields in the adjacent channels and quantitatively described by a parameterized reduced-order model developed with the neural network approach [126].

7.3 Connection of Pins

With all behavioral models available, the next step is to link pins at element terminals by wires (electric) and wiring buses (biofluidic) according to the spatial chip layout and compatibility of the physics to accomplish the simulation schematic.

Table 7-2 Biofluidic wiring buses used in the integrated LoC simulations

Connection Type	Subsystem Type	Bus	Pin Name
Intra-subsystem	Mixing	d [0:29]	Concentration coefficients
	Separation	t [0:2]	Separation times
		σ^2 [0:2]	Variance
		A [0:2]	Amplitude
		S [0: 30]	Skew coefficients
	Reaction	N/A	N/A
	Injection	N/A	N/A
Inter-subsystem	Mixing-Reaction	d [0:29]	Concentration coefficients
	Reaction-Injection	c_{avg}[0:2]	Average analyte concentrations
	Injection-Separation	t [0:2]	Separation times
		σ^2 [0:2]	Variance
		A [0:2]	Amplitude
		S [0: 30]	Skew coefficients

In Table 7-2, the biofluidic wiring buses are classified into the intra-subsystem (connecting the element within a subsystem, e.g., mixing or separation) and inter-

subsystem (linking the subsystems involving different functions) buses. The detailed description of the bus allocation is similar to that given in Table 3-1. Since the reactor and injector are modeled in terms of a single element, there is no intra-subsystem pin definition.

7.4 System Simulation of Integrated LoC Systems

In this section, the system-level schematic simulation procedure will be first described. Then, the simulation results of the integrated competitive immunoassay microchip will be discussed and validated against numerical and experimental data.

7.4.1 Simulation Description

The immunoassay schematic is simulated in two consecutive steps arising from the two operational phases (described in Section 7.1). For each step, both electric and biofluidic simulations are conducted.

(1). Mixing-reaction-loading (synthesis) phase. In this phase, voltage is applied at reservoir 3 with reservoirs 5, 6 and 7 grounded and the others left floating (potential setting is inactivated in the schematic). Given system topology and element dimensions, nodal voltages at element terminals within the entire system are first computed by Ohm's and Kirchhoff's laws using the resistor models. The resulting nodal voltage and current through the element are in turn used to calculate the electric field strength (E) and its direction within the mixer, reactor and analyte-waste feed channel, as well as the flow ratios at intersections J1 and J3. With these results and user-input sample properties (D and μ), the biofluidic pin values are computed sequentially starting from the most upstream sample reservoirs (5, 6 and 7) to the injector. The sample (Th, Th^* and Ab) concentrations after mixing are determined and then fed to the reactor model to calculate the concentrations of detectable species, e.g., the reaction product (Th^*-Ab) and the unreacted Th^*. At the

double-T injector, the concentration information along with the electric fields in the adjacent channels is saved.

(2). Dispensing-separation-detection (analysis) phase. In this phase, the voltage is switched to reservoirs 1 and 4 with the others left floating. As the synthesis phase, the nodal voltage in the network is first computed. Then, the computation of separation state (e.g., the arrival time, variance, skew and amplitude) is initiated at the injector outlet using the stored information from phase (1), and subsequently propagated to downstream separation channels using signal flow until the waste reservoir is reached.

7.4.2 Simulation Results and Discussion

In this section, the system simulation results and their comparison to experimental and numerical data will be presented to validate the modeling methodology.

Table 7-3 Comparison between system-level simulation results and experimental data on normalized concentrations of Th^* at channels J1-J3 and J3-J4.

Channel	System Simulation	Experiment
J1-J3	0.5	0.534
J3-J4	0.25	0.257

Table 7-3 shows the comparison between the system simulation results and experimental data on the normalized concentrations of Th^* (by the initial reservoir sample concentration) at channels J1-J3 and J3-J4. Since channels J1-reservoir 5 and J1-reservoir 6 have exactly same dimensions (that is same electric resistance), flow rates through them are also identical with a single constant potential applied at reservoirs 5 and 6. This leads to a two-fold dilution of Th^* at channel J1-J3. Likewise, channel J3-J2-reservoir 7 is fabricated with the same resistance as the combined resistance of channels J3-J1-reservoir 5 and J3-J1-reservoir 6, eventually yielding a four-fold dilution of Th^* at channel J3-J4. The simulation results agree with the experimental data excellently with the worst error of 7 %.

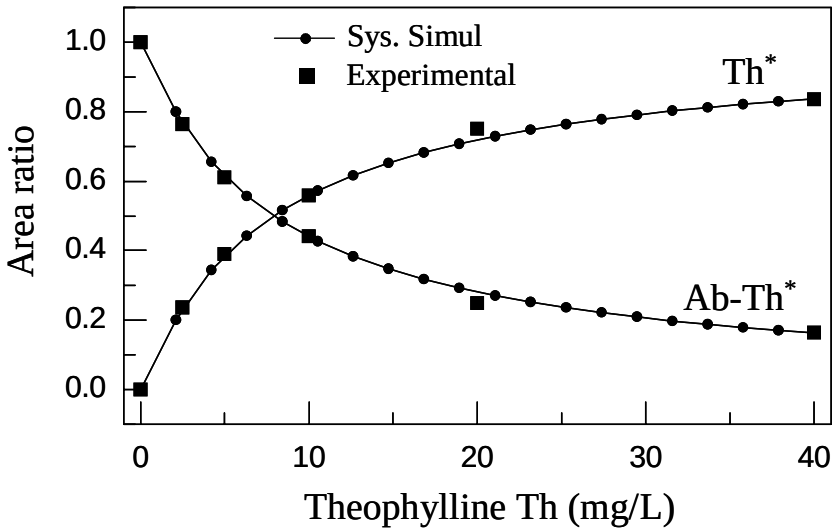

Figure 7-5. Comparison between the system-level simulation results and experimental data [16] on the area ratio of unreacted Th* and Ab-Th* complex. Abscissa shows the initial concentration of Th before the 50-fold off-chip dilution. Actual concentrations of Th* and Ab are not available. Their values were extracted from the results in Ref. [16].

In Figure 7-5, calibration curves of the area ratio for unreacted Th* and Ab-Th* complex are obtained from system simulation results by varying the concentration of Th (Th* concentration is fixed). Area ratios of Th* and Ab-Th* are respectively defined as $\mathrm{Ar}_{Th^*} \big/ \left(\mathrm{Ar}_{Th^*} + \mathrm{Ar}_{Ab-Th^*} \right)$ and $\mathrm{Ar}_{Ab-Th^*} \big/ \left(\mathrm{Ar}_{Th^*} + \mathrm{Ar}_{Ab-Th^*} \right)$, where Ar is the species amount, represented by its area under the electropherogram (Figure 7-6). The simulation results match the experimental data very well with a relative error less than 5 %. As the concentration of Th increases, the amount of Th begins to predominate in the mixture of Th and Th* in mixing-reaction channel J3-J4. Therefore, Ab exhibits a higher probability of colliding and binding to Th than to Th*, leading to more unreacted Th* and the growth of Th* area ratio.

Figure 7-6 shows the simulated electropherograms of separating Th* and Ab-Th* at three detection spots in the separation subsystem. It is seen that species bands of Th* and Ab-Th* gradually separate during their migration through the separation channel but with a

considerable decrease in band's amplitude and spreading in band's width due to the dispersion. The area ratio of the species bands are extracted at the third detector (bottom trace) and compared with numerical simulation [190] in Table 7-4. Very good agreement with the worst-case error less than 10 % and impressive speedup >100× over the numerical simulations have been achieved.

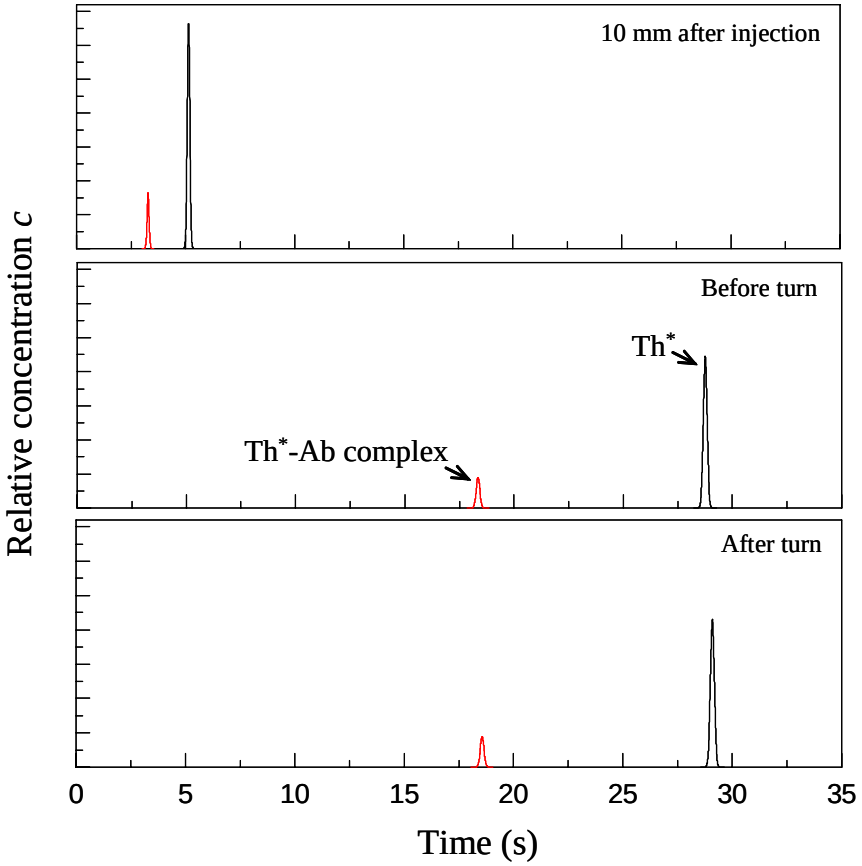

Figure 7-6. Electropherograms of unreacted Th* and Ab-Th* complex from system simulations at three detection spots: 10 mm after injection (top trace), before the 90° elbow (middle trace) and after the 90° elbow (bottom trace). Th concentration used in experiments and simulations is 40 mg/L before the 50-fold off-chip dilution (800 μg/L after the dilution).

Table 7-4. Comparison between numerical analysis [190] and system simulations on the area ratio

	Numerical	**Sys. Simul**
Area ratio Th*	0.845	0.84
Area ratio Ab-Th*	0.155	0.16

7.5 An Improved Design

Finally, the system-level simulation is employed to redesign the original chip and improve its bio-analysis efficiency and minimize its chip-area. Here, the original constraints on the channel size and power supply are kept. Specifically, the mixing, reaction, injection and separation channels are fabricated with channel width 52 μm and those feed channels leading to buffer and sample (analyte)-waste reservoirs are 236 μm wide. The same power supply with a single output of 6 kV is used. Due to the practical fabrication limit, I/O reservoirs are required to be spaced at least 5 mm apart. In addition, the immunoassay reaction is also assumed to be mixing-limited, thus complete mixing also signifies complete reaction (otherwise a period of incubation needs to be added at the end of the synthesis phase from the design, in which all reservoirs are left floating).

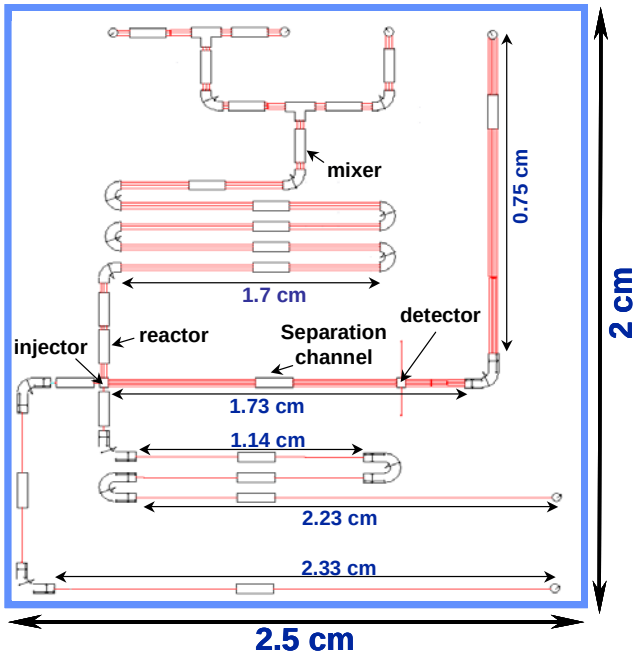

Figure 7-7. Schematic (not to scale) of the improved design of Figure 7-1 using the system-level simulation.

Figure 7-7 shows the redesign by reducing the excessive mixing length and arranging it into a compact serpentine geometry. The original mixing channel J1-J3 and J3-J4 are

shrunk from 26.5 and 81.63 mm to 9.3 and 77.33 mm respectively, while keeping almost the same mixing degree. Additionally, the overly long separation channel is shortened from 81.11 to 25.5 mm, which hence increases the electric field (from 600 V/cm to 1.8 kV/cm) and minimizes the band spreading due to diffusion (Joule heating dispersion is still negligible in this case). Furthermore, the detector is moved to the front of the 90° elbow separation channel to avoid the turn dispersion at the high electric field in the new design.

Table 7-5. Comparison of the channel dimension, separation time, variance, peak height and chip area between the original design and the improved design.

Parameters	**Original**		**Improved**	
J1-J3	26.5 mm		9.3 mm	
J3-J4	81.6 mm		77.33 mm	
Mixing degree	99 %		99 %	
J4-reservoir 4	81.11 mm		25.5 mm	
	Ab-Th*	Th*	Ab-Th*	Th*
Separation Time (s)	18.6	29.1	2.12	3.32
Variance (μm^2)	66607	30091	15926	11400
Amplitude (norm.)	1	4.9	2.4	8
Resolution	24		15	
Chip area	7.6 cm × 7.6 cm		2.5 cm × 2 cm	

Table 7-5 shows the modified mixing and separation channel length, as well as the system performance between the original and improved designs. Although the separation resolution drops to 15, it is still high enough to resolve the species bands. Most importantly, an impressive 1.6-fold increase in concentration amplitude and nearly 3-fold and 10-fold decreases in variance and chip area have been achieved. In other words, an assay chip that is easier to detect has been designed in less area.

7.6 Summary

This chapter describes the system-level schematic simulation of an electrokinetic competitive immunoassay LoC. In contrast to the separation and mixing models from the previous chapters, pins involving different physics have been defined at the terminals of

reactor and injector models, which enable the interconnection among different subsystems and transition between the operational phases of the chip. A simplified reactor model valid for forward immunoassay reactions has been developed, implemented in an analog hardware description language (Verilog-A) and linked to behavioral models of mixers, separation channels and injectors [126] to form a complete simulation schematic. An overview of the pin connections within and between subsystems has been provided to interpret the biofluidic signal transmission within the entire LoC network.

The constructed schematic then has been used to simulate the LoC in both synthesis and analysis phases, each requiring sequential solutions of the electric network by Kirchhoff's law and biofluidic states by signal flow. The simulation results of on-chip mixing, reaction, injection and separation have been verified by numerical and experimental data. A speedup (>100×) is achieved over the numerical FEM simulations, while still maintaining high accuracy (relative error less than 10 %). The system-level simulation captures the overall effects of chip topology, element size and operational parameters on chip performance and is used to redesign the original chip to improve analysis quality but occupy less chip-area. This application of the modeling and simulation framework developed in this thesis demonstrates its effectiveness in system-level design of integrated LoCs.

Chapter 8 Generation of Concentration Gradients of Complex Shapes Using Microfluidic Networks

8.1 Introduction

Concentration gradients (or concentration arrays) of diffusible chemicals or stimulating samples play important roles in the study of cell biology (e.g., chemotaxis [75, 76]), biochemistry [72], surface patterning and microfabrication [191, 192]. Conventionally, the Boyden chamber [193], pipette [194], gel [195] or their derivations [196, 197] are used to release the sample and to investigate cell behavior in a sample concentration gradient. However, these techniques are inefficient in providing spatially stable gradients of complex shapes due to the unbalanced sample flux into and from the region of interest [74]. Therefore, a technique to generate and maintain predictable complex sample concentration gradients over a long period of time is strongly desired to examine the correlation between the gradient and cell behavior, and quantitatively compare the significance of competing gradients by superimposing gradients of different samples [74, 198]. In addition, the development of sample concentration arrays also enables the high-throughout assays (e.g., immunoassay) and efficient multi-dimensional screens for combinational chemistry.

Recently, the laminar diffusion-based microfluidic networks that allow an accurate and reproducible control over the position and quantities of the sample released into the system [74] have been extensively studied for the concentration-related analysis. In general, they can be classified into two categories: complete mixing and partial mixing.

Complete mixing devices generally involve serial recombining, mixing and splitting of the sample solution and buffer (or differently concentrated sample). Sample mixing before each splitting needs to be complete (uniform concentration along the channel width) to

allow the use of resistor-based models. Jacobson *et al.* [71] proposed a serial mixing network driven by electrokinetic flow to achieve an array of continuously diluted sample concentrations for parallel bioanalysis. This approach later was also realized in pressure driven flow [72] to study fluorescent immunoassay and quantitatively analyze multiple antibodies in parallel. Jeon *et al.* [73, 74] proposed a tree-like microfluidic network to generate concentration gradients of complex shapes (e.g., linear, parabolic and periodic) along the channel width. Sample solution with different concentrations was supplied at multiple inlets, then mixed, split and recombined in branched channels, which eventually converged to a wide main channel, yielding a complex widthwise profile. This device was later improved by Lin *et al.* [199], who integrated a simple "mixer module" with the gradient generating network to enable the on-chip dilution of initial samples and obtain dynamically controlled temporal and spatial gradients. More recently, Walker *et al.* [200] studied the effects of flow and diffusion on chemotaxis in such devices using a simplified numerical model and experiments. It has been found that as the flow rate varies, the cell trajectories along the streamwise direction and the transverse concentration profiles of chemokine are significantly affected. Nevertheless, to ensure transversely complete sample mixing before each splitting, such gradient generators [73, 74, 199, 200] often use either bulky and complicated network structures that are prone to leak and clog or use chaotic advective mixers [192] that need complicated layout and fabrication. Additionally, the profiles produced at the output channel are also discretized (non-smooth).

Gradient or array generators fully relying on diffusion-based partial mixing were also proposed and demonstrated. Holden *et al.* [176] built a Y-shape laminar microfluidic diffusion diluter (mDD) that allowed side-by-side mixing of different samples to generate

widthwise concentration gradients. With appropriate simplifications of the convection-diffusion equation, an analytical model was also developed to accurately predict the output profiles. Walker *et al.* [58] designed a cross-mixing microfluidic device that created a widthwise bell-shape concentration profile of virus to study the cell infection within a microscale environment. In addition to the concentration gradient generation along the channel width, Yang *et al.* [201, 202] proposed a microfluidic network that generated continuous gradients across the stream and discontinuous gradients along the stream by manipulating fluid distribution at each intersection of the network and subsequent diffusion between laminas in the mixing microchannels. While these devices are effective in generating simple gradients (e.g., approximately linear or bell-shape), approaches to create complex profiles (such as the periodic and composite gradients in Ref. [74, 75]) as well as the associated models to evaluate the network design have not been adequately explored.

To address this issue, this chapter presents novel and compact microfluidic networks to generate complex concentration profiles along the channel width by integrating constituent profiles (e.g., approximately linear and bell-shape) created by simple T- or cross-mixers. To investigate the design space, the system-level simulation approach developed in this thesis will be used: the generator will be geometrically decomposed into a set of mixing elements. Analytical behavioral models for individual elements are derived to accurately capture the sample transport within the pressure-driven flow network as well as its dependence on the generator topology, element size, material property and initial reservoir sample concentration. The model is validated with FVM numerical analysis of various generators. Finally, a design approach for the proposed device based on iterative evaluation

of the behavioral model is presented and the strategy of achieving desired gradients is also briefly discussed.

In contrast to the previous studies, the proposed generator and behavioral model exhibit two notable novelties. First, we superimpose simple constituent profiles (e.g., linear and bell-shape) arising from partial mixing [58, 176] to construct complex and composite gradients. Therefore, the measures taken to ensure complete mixing, such as long zig-zag mixing channels or chaotic advective mixers, as well as the complicated tree-like network structures [13, 73, 74, 192] are no longer needed. Second, different from the resistor-based mixing model [71, 74] that takes advantage of the analogy between fluidic and sample transport and hence imposes the constraint of complete mixing, our behavioral model evaluates the propagation of concentration profiles (rather than a single average concentration value) within the entire network. Therefore, it not only recovers the resistor-based model, but also captures dynamic evolution of the sample concentration profile and its dependence on design parameters.

This chapter is organized as follows. First, the principle of the generator will be introduced (Section 8.2), followed by analytical and numerical modeling of the transport phenomena (Section 8.3). Then case studies of diverse concentration profiles (e.g., linear, bell-shape, periodic and hybrid) will be demonstrated, along with the comparison between the numerical and system simulation results (Section 8.4). Finally, an optimization and design method based on the iterative system simulation will be proposed and illustrated by design paradigms (Section 8.5).

8.2 Principle of Concentration Gradient Generation

The proposed approach of generating concentration gradients is to superimpose simple constituent profiles (arising from T- or cross-focusing mixers in Figure 8-1) side-by-side along channel width to obtain complex and composite profiles.

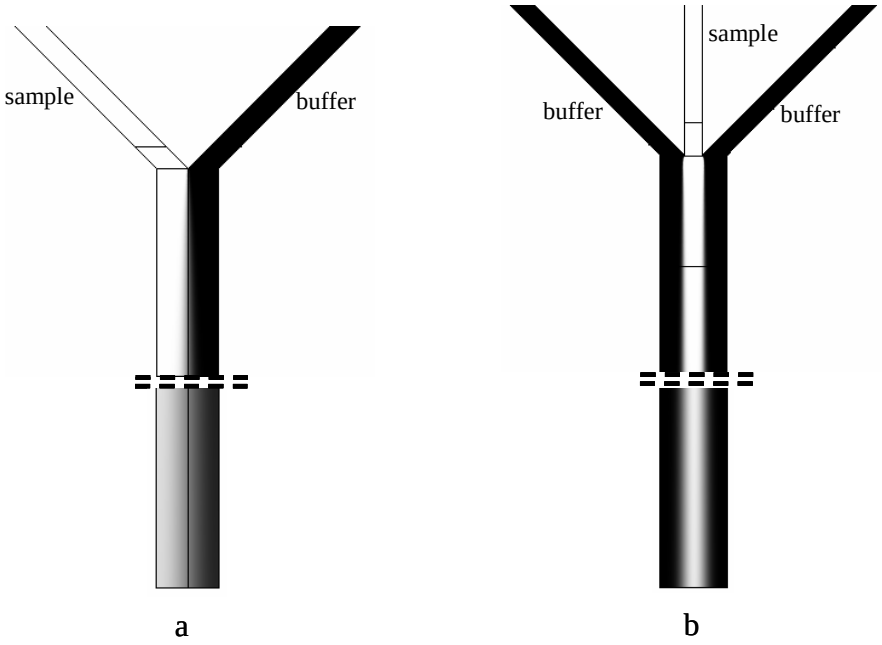

Figure 8-1. Numerical contour plots of concentration distributions in (a) a T-mixer and (b) a cross-focusing mixer, arising from laminar diffusion-based mixing.

Figure 8-1a depicts a simple T-mixer, in which the diffusible sample and buffer solvent are transported to the mixing channel respectively via the left and right branch channels by pressure driven flow. At the intersection, both streams merge into a laminar flow and then mix with each other due to diffusion in the main mixing channel. Figure 8-2a shows that immediately after the T-intersection, an abrupt step-shape sample profile results due to negligible diffusion at the junction region. The location of the concentration discontinuity is determined by the sample and buffer flow rates through both branch channels. On the other hand, at the far downstream of the intersection, an approximately linear concentration gradient can be attained. The profile exhibits an excellent linearity in the middle portion of

the channel. The gradient is slightly nonlinear at both sides due to the mass insulation at channel walls.

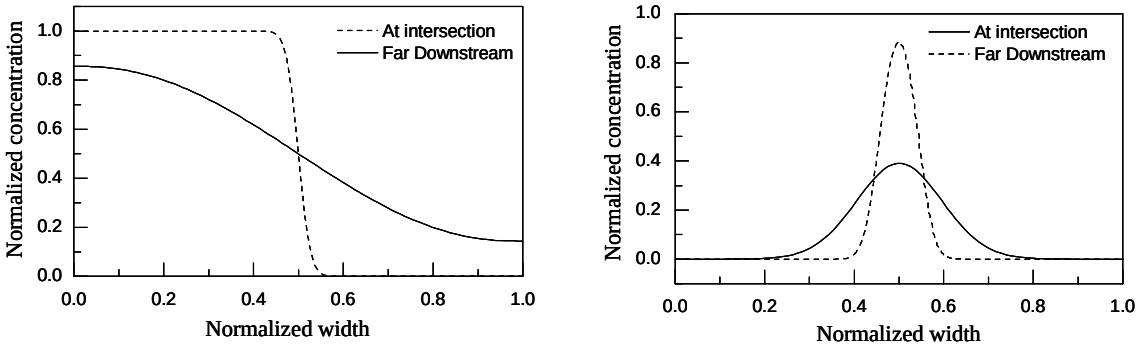

Figure 8-2. (a) A step and an approximately linear concentration profile generated at the intersection and far downstream in a T-mixer (from numerical simulations). (b) A smooth and wide bell-shape concentration profile generated at the far downstream of the intersection in a cross-focusing mixer. Intensifying the focus effect and taking detection immediately after the intersection yields a Dirac δ profile (from numerical simulations).

Similarly, a bell-shape profile can be created by a cross-focusing mixer (Figure 8-1b). The sample is injected from the middle channel and sandwiched by buffer solvent from side channels. By modulating flow rates through these branch channels or changing the detector location, the height, width and position of the bell shape in the mixing channel can be manipulated. For example, at the far downstream of the cross intersection, a smooth bell-shape profile can be generated. Nevertheless, intensifying the focusing effect and taking detection immediately after the intersection can achieve an abrupt Dirac δ profile (Figure 8-2b).

Therefore, by aligning these constituent profiles side-by-side, temporally and spatially stable gradients of complex shapes (periodic and hybrid) can be achieved, due to the balanced mass flux. As the constituent profiles are independent from each other, their shapes (e.g., the width, slope, peak and mean concentration value) can be individually adjusted through branch flow rates, channel sizes and reservoir sample concentrations.

8.3 Analytical Models and Numerical Analysis

Similar to other generator designs, our approach requires a high degree of control over the sample quantity released from individual sources and concentration variations within the network. Therefore, efficient and accurate models to capture the influence of design parameters (e.g., the geometry, flow rate and initial reservoir sample concentration) on individual constituent profiles as well as their superimposed profile are indispensable to the design of the proposed device.

In this section, the hierarchical simulation approach presented in Chapter 3 and Chapter 6 will be used. The analytical behavioral models for mixing elements will be first extended to pressure driven flow and then integrated into a system-level representation (Section 8.3.1). Then numerical analysis will be briefly described (Section 8.3.2) and used as a benchmark to validating the proposed approach and analytical models.

8.3.1 Analytical Models

In this subsection, the Navier-Stokes and convection-diffusion equations respectively governing the fluidic and sample transport in mixing channels and converging intersections will be analytically formulated and solved to attain a parameterized behavioral model.

8.3.1.1 Flat Straight Mixing Channels

Fluidic and sample transport in a flat (the width-to-depth ratio β is large, e.g., $\beta > 5$) straight mixing channel is considered. The Navier-Stokes equation for steady-state and fully-developed (entry effect at the intersection is neglected) flow is given by,

$$\frac{\partial^2 u}{\partial y^2} + \frac{\partial^2 u}{\partial z^2} = -\frac{1}{\boldsymbol{\eta}} \frac{\partial P}{\partial x} \tag{8.1}$$

where $\boldsymbol{\eta}$ is the dynamic viscosity of the buffer, u is the axial pressure-driven flow velocity; x, y and z are axial, widthwise and depth-wise coordinates respectively, with $x \in [0, L]$, $y \in [0,$

w] and $z \in [0, h]$; L, w and h are the channel's length, width and depth respectively; P is the pressure, which is a linear function of the axial coordinate x for fully developed flow. Hence $\frac{dP}{dx} = \frac{\Delta P}{L} = \text{const.}$, where ΔP is the differential pressure applied across the channel length L. The analytical solution to the flow velocity profile in Eq. (8.1) is given by [203]

$$u(y,z) = \frac{4w^2}{\eta \pi^3}\left(-\frac{\Delta P}{L}\right) \sum_{i=1,3,5...}^{\infty} (-1)^{(i-1)/2} \left[1 - \frac{\cosh\left(i\pi\left(z-\frac{1}{2}\right)\Big/\beta\right)}{\cosh\left(i\pi/2\beta\right)}\right] \cdot \frac{\cos\left(i\pi\left(\frac{y}{\beta}-\frac{1}{2}\right)\right)}{i^3} \quad (8.2)$$

Integrating Eq. (8.2) along the channel cross section yields the volumetric flow rate as

$$q = \frac{w^4}{12\beta\eta}\left(-\frac{\Delta P}{L}\right)\left[1 - \frac{192\beta}{\pi^5}\sum_{i=1,3,5...}^{\infty}\frac{\tanh\left(i\pi/2\beta\right)}{i^5}\right] \quad (8.3)$$

Eq. (8.3) indicates that the steady-state pressure driven flow network can be treated as a resistor network with the pressure and volumetric flow rate analogous to the voltage and current (if the flow entry effect is negligible). The associated fluidic resistance can be defined in a similar fashion to the electric resistance by

$$R = \frac{\Delta P}{q} = \frac{12\beta L\eta}{w^4\left[1 - \frac{192\beta}{\pi^5}\sum_{i=1,3,5...}^{\infty}\frac{\tanh\left(i\pi/2\beta\right)}{i^5}\right]} \quad (8.4)$$

Thus, a Kirchhoffian network of pressure driven flow can be solved to determine the pressure at element terminals and the flow rate through the element.

The convection-diffusion equation governing the sample transport within an axially fully developed flow is governed by

$$u\frac{\partial c}{\partial x} = D\left(\frac{\partial^2 c}{\partial x^2} + \frac{\partial^2 c}{\partial y^2} + \frac{\partial^2 c}{\partial z^2}\right) \quad (8.5)$$

Direct analytical solution to Eq. (8.5) is unavailable due to the transversely non-uniform velocity profile *u*. Two assumptions are made to simplify Eq. (8.5). First, Refs [176, 204-206] have shown that for flat channels, the sample transport is not affected by the local velocity distribution. Therefore, the axial velocity *u* in Eq. (8.5) can be replaced with the cross-sectional average velocity (*U*) and the concentration distribution in the depthwise direction is relaxed (i.e., $\frac{\partial^2 c}{\partial z^2} \approx 0$). Second, as the mixing channel is typically narrow (*h* << *L* and *w* << *L*), axial diffusion is also negligible (i.e., $\frac{\partial^2 c}{\partial x^2} \ll \frac{\partial^2 c}{\partial y^2}$). Thus, Eq. (8.5) is reduced to

$$U\frac{\partial c}{\partial x} = D\frac{\partial^2 c}{\partial y^2} \tag{8.6}$$

Eq. (8.6) is exactly the same as Eq. (6.4) with the cross-sectional average velocity *U* analogous to the electrokinetic velocity u_{x_k} . The solution to Eq. (8.6) can be found as

$$d_n^{(out)} = d_n^{(in)} e^{-(n\pi)^2 \tau} \tag{8.7}$$

where $\tau = L/(w\,\mathrm{Pe})$ is the dimensionless sample residence time within the channel, d_n are the Fourier cosine series coefficients of sample concentration profiles and indices *in* and *out* represent the quantities at the inlet and outlet. In contrast to the results obtained in Ref. [176], our model (Eq. (8.7)) holds for arbitrary concentration profiles at the inlet.

As the Reynold number considered in the proposed generators is rather low (Re < 1), the Dean number De, a relative measure of the magnitude of the secondary flow, in general is on the order of 0.01. No noticeable advective sample mixing due to secondary flow in a circular turn with the rectangular cross section was observed in the numerical simulation.

Thus, with L in τ replaced by $r_c\varphi$, Eq. (8.7) is also valid for the circular mixing turn, where r_c and φ are the average radius and included angle of the turn.

8.3.1.2 Converging Intersections

The converging intersection in pressure driven flow is identical to that in EK flow, acting as a combiner to align and compress upstream sample streams with an arbitrary flow ratio s and concentration profiles side-by-side at its outlet. As described previously, the complex multi-input intersection that merges multiple branch flow can be treated as a cascade connection of the converging intersections.

8.3.1.3 Constructing System-Level Representation

A system-level representation of the proposed concentration gradient generator can be obtained by connecting the developed element models using the same approach described in Chapter 6. The only difference is that the electric pin in electrokinetic flow is now replaced with a flow pin including the hydrodynamic pressure difference as the "across" quantity and the flow rate as the "through" quantity. Therefore, the system-level simulation can be conducted in a similar manner to the EK flow. In addition, the system simulation allows multiple dilute samples coexisting in buffer solution with negligible interactions. Hence, it enables quantitating and comparing the role of competing gradients. The analytical behavioral model and system simulation currently are implemented in Mathematica 5.0.

8.3.2 Numerical Models

Numerical analysis is performed within the commercial Finite Volume Method package CFD-ACE+ (ESI CFD, Inc). A three dimensional geometric solid model of the proposed gradient generator with flat channels (h = 60 μm and β = 5~20 in channels) is constructed in CFD-GEOM and then imported to CFD-ACE+ for computational settings and FVM

solution. Two physics modules of incompressible fluid flow (Navier-Stokes equation) and bio-chemistry (convection-diffusion equation without reaction) are invoked to sequentially solve for the flow velocity and sample concentration in the network. A volumetric flow rate of 5.18 μl min^{-1} at the main output channel is fixed during all simulations, with an exception of 1.296 μl min^{-1} used for the cross-focusing generator due to its smaller channel width (see Figure 8-4). Typical sample diffusivity of 1×10^{-10} m^2 s^{-1} and normalized reservoir sample concentrations c = 0~1 are used, unless otherwise noted.

To capture the steep concentration gradient generated at junction regions and diminish the error of "numerical diffusion" [9], very fine meshes in the widthwise direction are used. In addition, a polynomial-type mesh in the axial direction is also selected to accumulate more grids at the junction and resolve flow entry effects on sample transport (globally fine meshes are not computationally affordable). The channel depth is resolved with 10 cells. Depending on the network topology, structured mesh with 480,000 ~ 820,000 cells in total was used for a generator model. A typical mesh plot of a cross intersection is depicted in Figure 8-3.

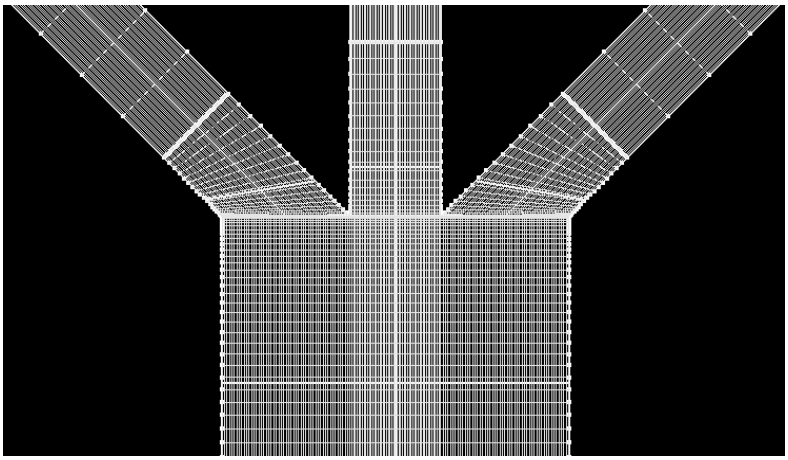

Figure 8-3. Mesh plot of a cross intersection. 156 cells in the widthwise direction of the main channel is used to resolve the steep gradient along the width. Axially, more grids are used at the junction region to capture the flow entry effects on the sample transport.

8.4 Case Studies

In this section, system simulations will be conducted to explore various microfluidic networks that are capable of generating complex concentration profiles. The proposed approach and simulation results will be validated by the numerical analysis.

8.4.1 Bell-Shape Concentration Profiles

There are two ways to generate bell-shape concentration profiles. One is to combine two mirrored approximately linear profiles, each evolving from a T-mixer (Figure 8-1a). However, it would be more convenient to use a single cross-focusing mixer (Figure 8-1b). Figure 8-4 illustrates the network topology and dimensions of such a generator. Sample solution with different sample concentrations *c* is continuously supplied to inlets 1~3 and then mixes with each other in the main mixing channel. Thus, a smooth bell-shape profile can be generated in the mixing channel.

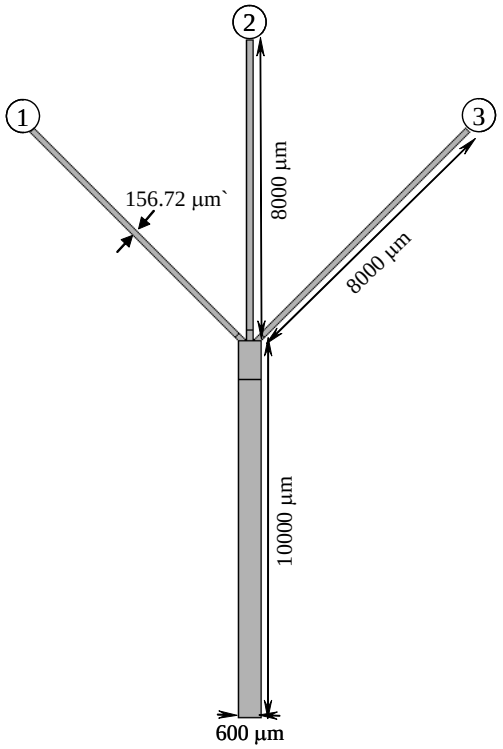

Figure 8-4. Network topology and dimensions of a cross-focusing generator. Solution with different sample concentrations is introduced at inlets 1~3.

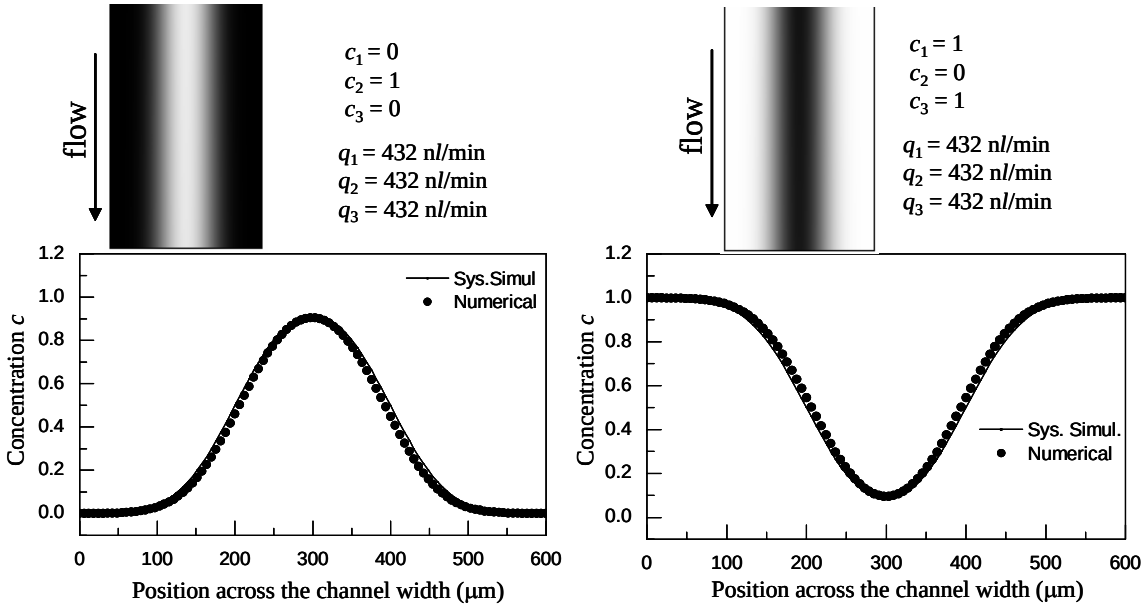

Figure 8-5. (a) A bell-shape profile: a numerical contour plot (top view) of the sample concentration. The comparison between numerical and system simulation on the concentration profile across the channel width (extracted at the end of the main mixing channel). Lines and symbols represent the values from system and numerical simulations respectively. Flow rates ($q_1 = q_2 = q_3$) in branch channels are 432 nl min^{-1}. (b) An inversed bell-shape profile.

Figure 8-5 shows the numerical contour plots (top view) of the sample concentration as well as the comparison between numerical and system simulation results on the widthwise profiles extracted at the end of the main mixing channel. In Figure 8-5a, the sample and buffer are supplied from the middle and side branch channels respectively ($c_1 = 0$, $c_2 = 1$ and $c_3 = 0$ with flow rate $q_1 = q_2 = q_3 = 432$ nl min^{-1}). The appreciable diffusion effect smears out the interface between the sample and buffer stream, yielding a smooth bell-shape profile with the highest concentration value occurring at the axial centerline. By switching the supply of the sample and buffer ($c_1 = 1$, $c_2 = 0$ and $c_3 = 1$) to inlets 1~3, an inversed bell-shape profile results with the lowest concentration value at the axial centerline. Excellent agreement between numerical and system simulation results has been found with M = 6.7 % (Chapter 6).

8.4.2 Periodic Bell-Shape Concentration Profiles

To create a periodic bell-shape concentration profile, multiple cross-focusing generators can be arranged side-by-side.

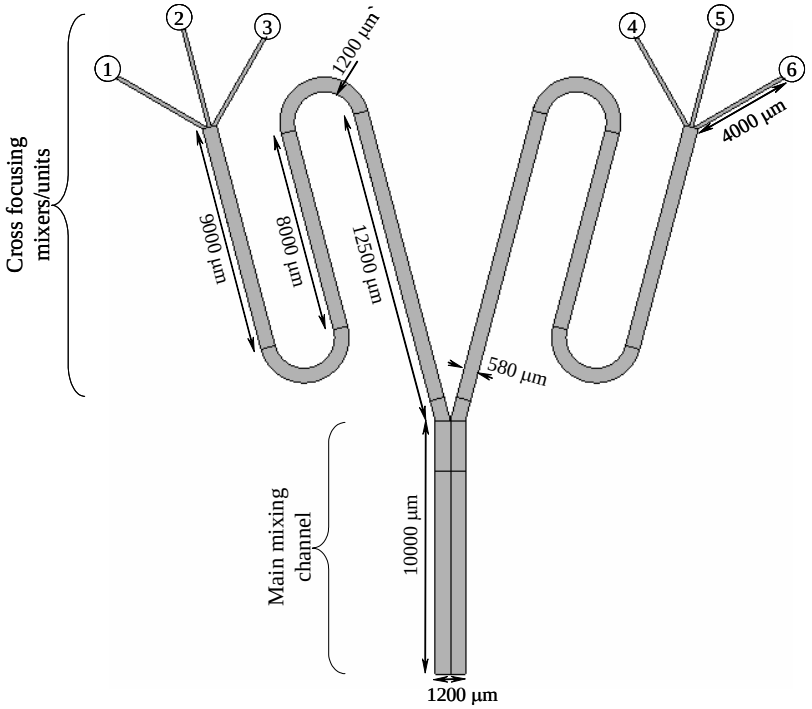

Figure 8-6. Network topology and dimensions of a periodic bell-shape concentration generator. A periodic profile is produced by combining two constituent bell-shape profiles, each evolving from a single cross-focusing mixing unit.

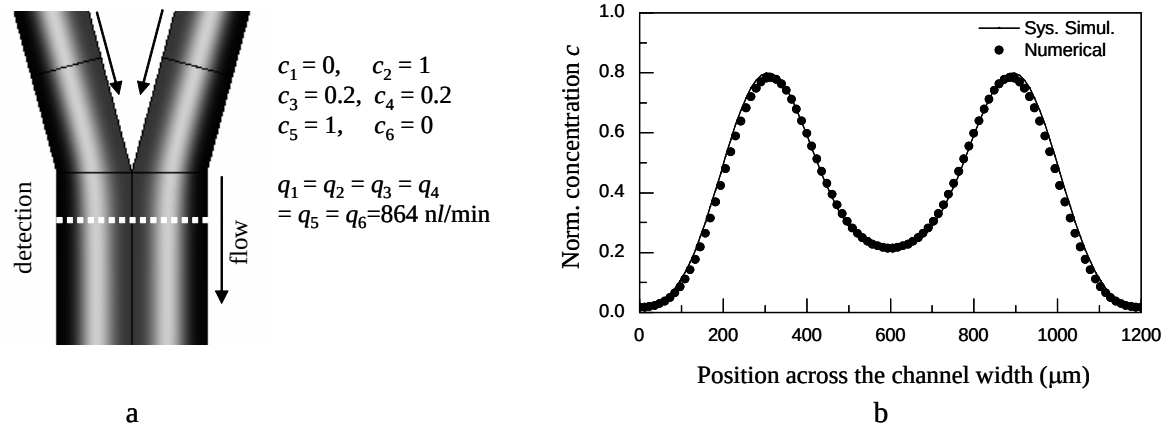

a b

Figure 8-7. (a) Numerical contour plot (top view) of the sample concentration in a periodic bell-shape profile generator. (b) Comparison between numerical and system simulation results on the concentration profile across the channel width, extracted at 400 μm downstream of the intersection in the main mixing channel. Flow rates in branch channels 1~6 are 864 nl min^{-1}.

Figure 8-6 shows the network topology and dimensions of such a generator including two cross-focusing units. Sample solution with different concentrations is first fed to the inlets of cross-focusing units, in which single bell-shape profiles form as described above. The bell-shape constituent profiles then merge in the main mixing channel to create a periodic profile (a). Figure 8-7 shows the numerical contour plot of the sample concentration as well as the comparison between numerical and system simulation results on the widthwise profile extracted at 400 μm downstream of the intersection. In contrast to that in Figure 8-5a, asymmetric constituent bell-shape profiles are generated in the cross-mixing units enabled by the asymmetric arrangement of sample concentrations at reservoirs 1, 3 and 4, 6 (i.e., $c_1 \neq c_3$ and $c_4 \neq c_6$, see Figure 8-7). Thus, a higher concentration value is found at the centerline of the main mixing channel than at the walls. Excellent agreement between numerical and system simulation results has been found with the relative average error $M = 4$ %.

8.4.3 Periodic Linear Concentration Profiles

Linear concentration profiles can be also generated periodically in the widthwise direction by aligning multiple T-mixing units side by side as shown in Figure 8-8.

Sample solutions with disparate concentrations are released from two adjacent reservoirs in a T-mixing unit (e.g., reservoirs 1 and 2), and then mix with each other in the serpentine mixing channel to generate approximately linear profile. The peak and mean concentration values and the slope of the constituent profile are determined by the overall effects of reservoir concentrations, serpentine channel sizes and sample flow rates, which can be effectively captured by the analytical model presented in Section 8.3.1. Eventually,

the approximately linear profiles from serpentine mixing channels are combined to achieve a periodical distribution in the main mixing channel.

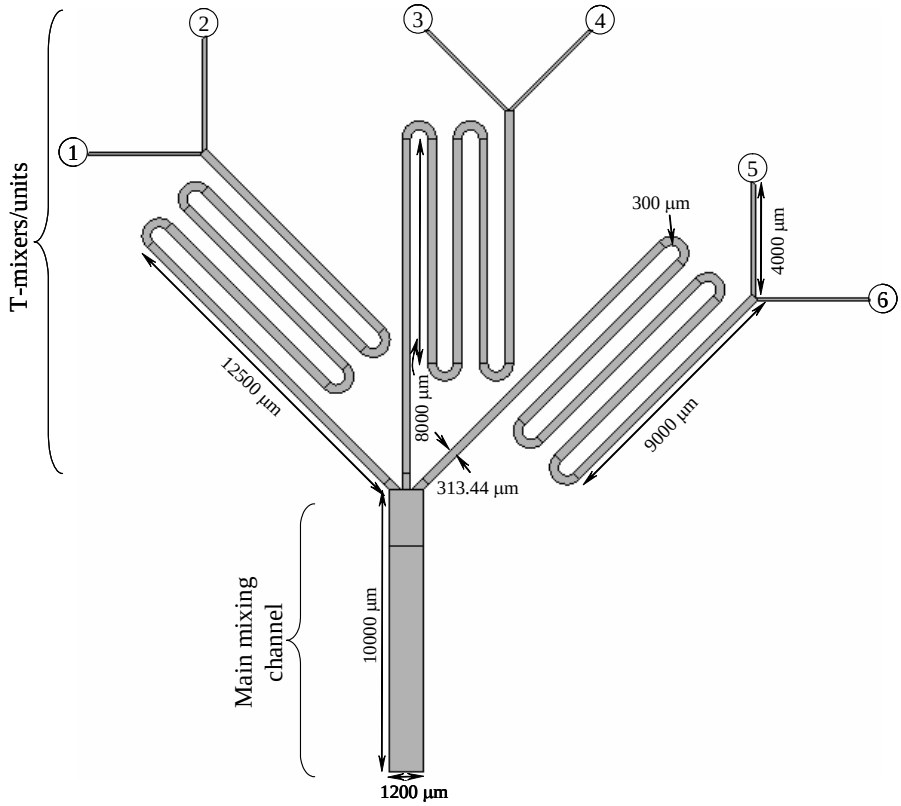

Figure 8-8. Network topology and dimensions of a periodic linear concentration generator. A periodic linear profile is produced by combining three constituent linear profiles, each evolving from a single T-mixing unit.

Figure 8-9 shows various periodic (triple) approximately linear profiles from triple-T generators. Since each constituent profile is generated independently, its slope, mean and peak values can be varied by modulating its corresponding reservoir sample concentrations. In Figure 8-9a, exactly the same linear profiles are replicated along the channel width. Figure 8-9b demonstrates a profile consisting of three constituent profiles, each having the same slope but different peak and mean concentration values. In Figure 8-9c, the constituent profiles with the same mean values but different peak values and slopes are

produced. Figure 9d exhibits a gradient whose constituent profiles have distinctly different slopes, mean and peak concentration values.

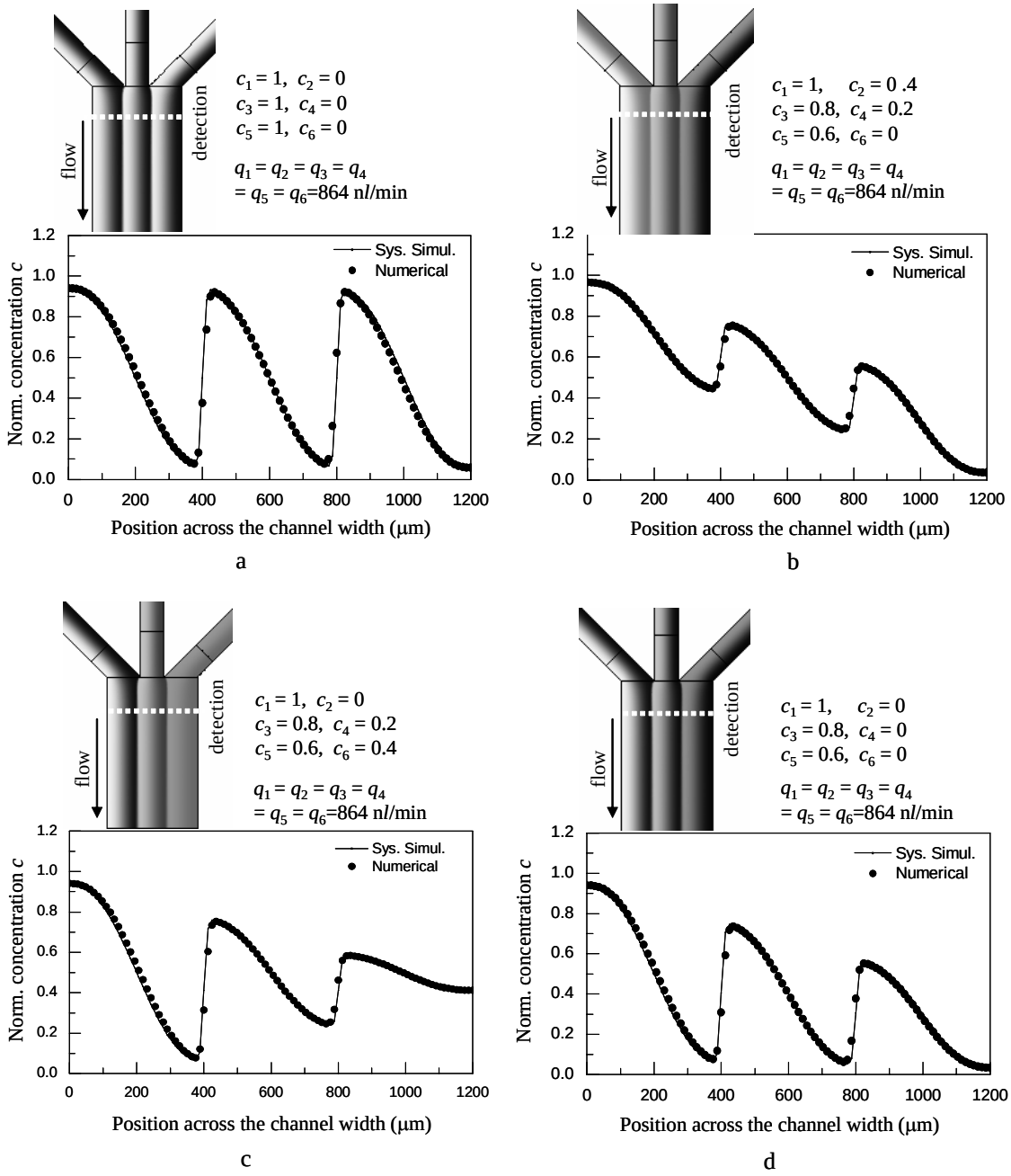

Figure 8-9. Numerical contour plots of the sample concentration and comparison between numerical and system simulations on concentration profiles across the channel width (extracted 400 μm downstream of the intersection). The flow rate in all branch channels 1~6 is 864 nl min^{-1}. Triple approximately linear profiles with (a) the same peak and mean concentration values and slope, (b) the same slope but different peak and mean values, (c) the same mean values but different slopes and peak values and (d) the different slope, peak and mean concentration values.

As an extreme case, given a sufficiently fast flow velocity or a short serpentine mixing channel, sample mixing in T-mixers is negligible, leading to a profile comprised of three square waves. For all periodic profiles in Figure 8-9, steep concentration discontinuities are created at the merging interface between streams, which are very useful for studying the cell behavior subjected to abrupt gradients [75]. Excellent agreement between numerical and system simulation results indicates that the analytical model is able to accurately predict discontinuous profiles as well as their decay along the stream direction.

8.4.4 Hybrid Concentration Profiles

Finally, this section will demonstrate that a hybrid concentration profile consisting of both linear and bell-shape constituent profiles can be generated by combing cross- and T-mixing units as shown in Figure 8-10.

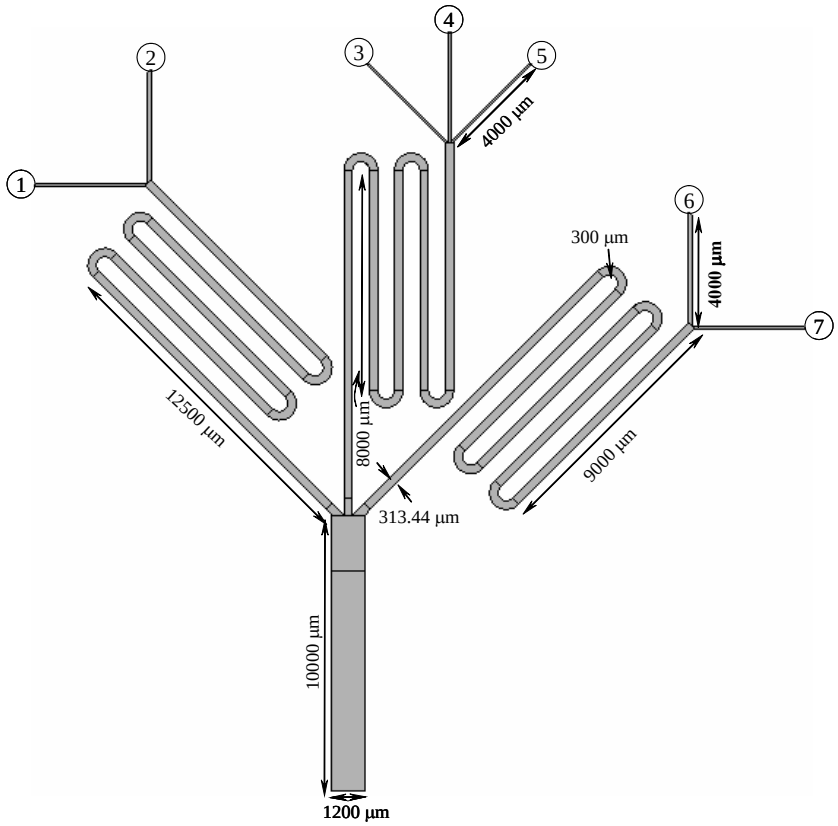

Figure 8-10. Network topology and dimensions of a hybrid concentration generator. A composite profile of both linear and bell-shape profiles could be generated.

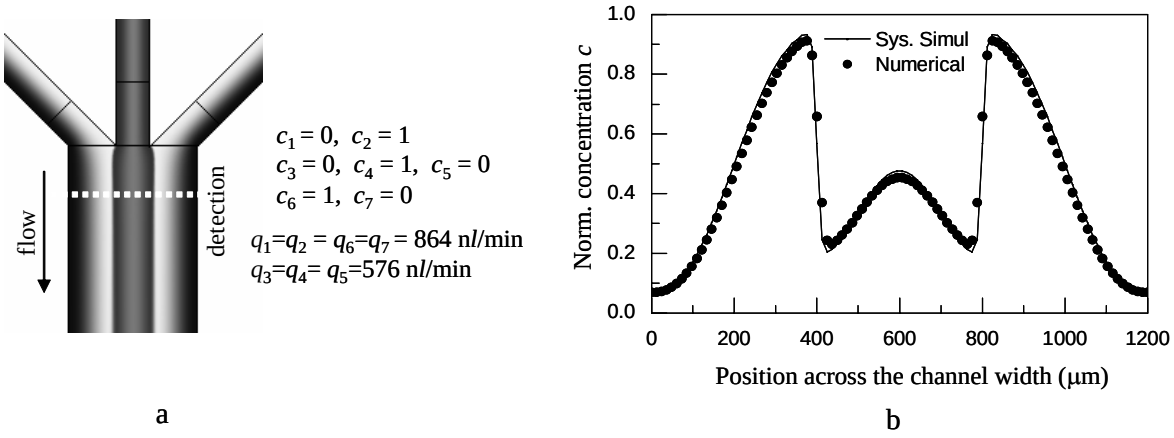

Figure 8-11. (a) Numerical contour plots (top view) of the sample concentration in a hybrid profile generator. (b) Comparison between numerical and system simulation on the concentration profile across the channel width, extracted at 400 μm downstream of the intersection in the main mixing channel.

Figure 8-11 exhibits a composite profile produced by such a device, in which the bell-shape profile from the cross-mixing unit is sandwiched by the linear profiles from T-mixing units. While sample solution in the cross- and T-mixing units is supplied with the same total flow rate (1728 nl min^{-1}) and initial concentration ($c_2 = c_4 = c_6 = 1$), good mixing in the cross-mixer implied by the quicker decay of the peak concentration value has been found, which is attributed to its smaller inter-stream diffusion distance (Section 6.4.3). A higher peak value at the centerline of the main mixing channel can be reached by discharging more concentrated sample solution at inlet 4.

In summary, the class of the achievable concentration profiles (e.g., linear, bell-shape, periodic and hybrid) is basically determined by the type of the mixers (e.g., cross-focusing or T mixers) and their spatial configurations. However, the details of each constituent profile (e.g., slope, mean and peak concentration values, position and width) are captured by the overall effects of initial reservoir concentrations, flow rates, sample properties as well as the channel dimensions. This insight is helpful for designers to select appropriate

parameters to obtain desired concentration profiles using the analytical models and iterative system simulations, which will be discussed in the next section.

8.5 Design Approach

After validating the proposed approach and behavioral models, next we need to determine a strategy to design the generators with appropriate geometries and operational protocols that can meet prescribed profiles. In this section, the optimization formulation will be described, and the design process of three kinds of gradient generators: the linear (Figure 8-1a), bell-shape (Figure 8-1b) and periodic linear (Figure 8-9a) will be demonstrated.

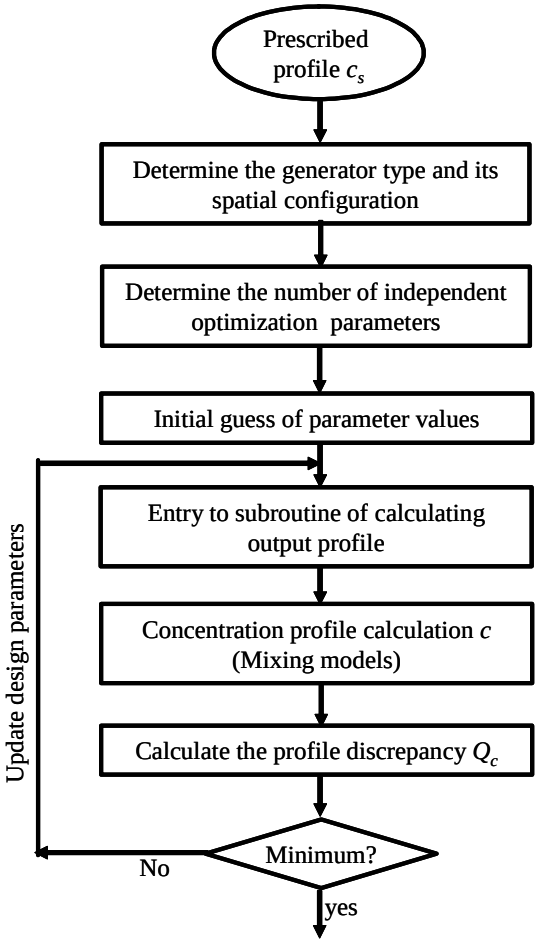

Figure 8-12. Flow chart of the optimization and design of concentration gradient generators.

To begin with the formulation, an optimization objective is needed. An index of profile discrepancy Q_c characterizing the discrepancy between the prescribed (desired) and candidate profiles is defined by

$$Q_c = \int_0^1 |c - c_s| \cdot d\eta \tag{8.8}$$

where c_s is the prescribed (desired) profile and c is the candidate profile. Essentially, the optimization process is to explore the design space and locate the parameters yielding minimal Q_c.

Flow chart in Figure 8-12 illustrates the optimization and design process. First, given the prescribed (desired) profile, designers need to determine the mixer types (e.g., T- or cross-focusing), spatial configuration (e.g., double cross or triple T) as well as the independent design variables that enter the optimization. Given initial guess values, the modeling subroutine calculates the output concentration profile as well as its discrepancy from c_s at the detection spot. This step progresses iteratively to find out the optimal parameter values yielding minimal Q_c. Currently, a simple optimization scheme is used, in which the parameter space is meshed and the modeling subroutine is iteratively evaluated at all grid nodes to locate the optimal combination of the parameters.

8.5.1 Linear Profile Generators

In this section, the process of designing an approximately linear profile generator with the prescribed profile $c = B_1 + B_2\eta$ will be demonstrated, where B_1 and B_2 are its interception and slope.

Clearly a simple T-mixer is needed. The two flow rates through branch channels (Figure 8-13a) are chosen as optimization variables, which in practice can be easily adjusted by external pumps. Other parameters, such as the channel sizes and initial sample

concentrations hold unchanged and are given in Figure 8-13a. Figure 8-13b shows the prescribed and optimized concentration profiles along the channel width. They match well in the middle region of the channel but deviate at both sides as discuss above. Optimization results indicate that solution with flow rates q_1 = {26.1082, 9.394} nl min^{-1} and q_2 = {17.3975, 21.8716} nl min^{-1} should be respectively supplied to the sample and buffer reservoirs (inlets 1 and 2) to attain the prescribed profiles $c_s = 0.8 - 0.4\eta$ and $c_s = 0.4 - 0.2\eta$.

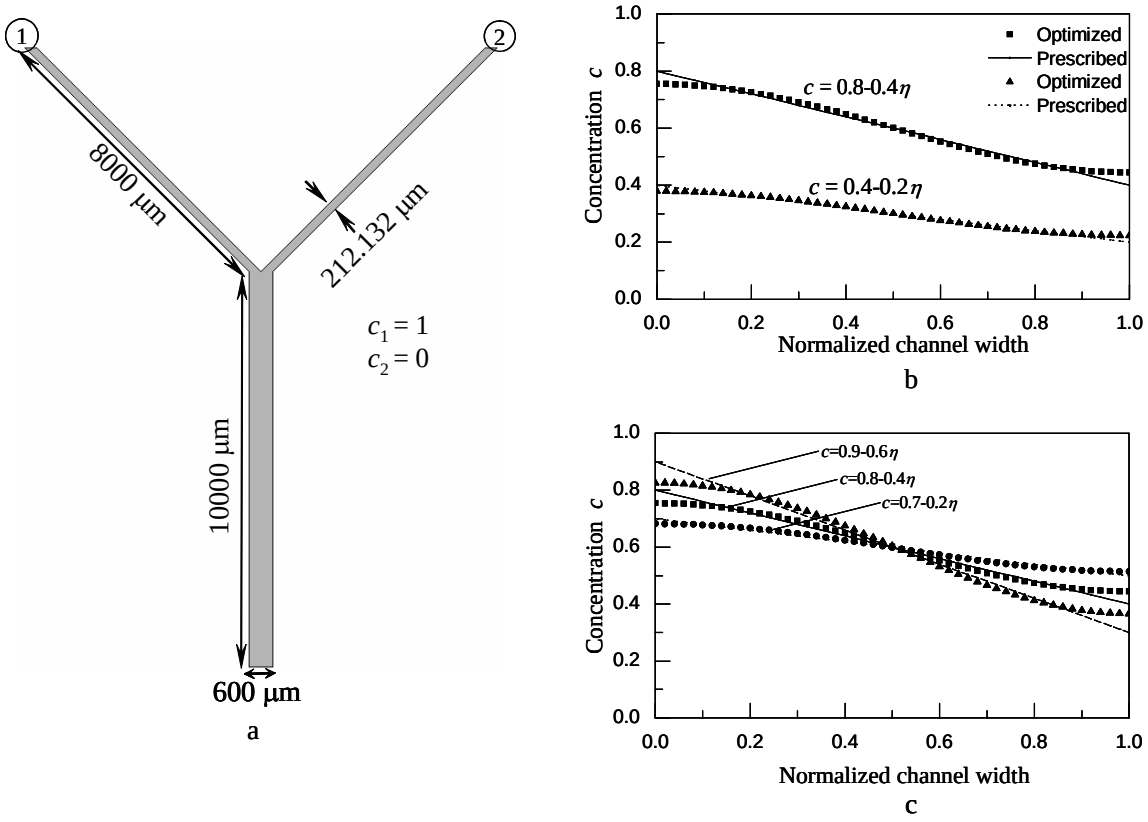

Figure 8-13. (a) The network topology and dimensions of a T-mixer. The flow rates of the solution through branch channels are selected as optimization variables. (b) Comparison of the prescribed (line) and optimized (symbol) concentration profiles along the channel width ($c = 0.8 - 0.4\eta$ and $c = 0.4 - 0.2\eta$) detected at the end of the mixing channel. Flow rates q_1 = {26.1082, 9.394} nl min^{-1} and q_2 = {17.3975, 21.8716} nl min^{-1} are needed. (c) Three different prescribed and optimized profiles ($c = 0.9 - 0.6\eta$, $c = 0.8 - 0.4\eta$ and $c = 0.7 - 0.2\eta$). Flow rates q_1 = {36.7214, 26.1082, 17.9104} nl min^{-1} and q_2 = {24.4793, 17.3975, 12.0247} nl min^{-1} are found to generate them respectively. These q_1 and q_2 combinations remain the same flow rate ratio of q_1/q_2=1.5.

However, the optimization can be improved. Based on mass balance, the average sample concentration c_{avg} in the main mixing channel is the flow-rate weighted "centroid" of the initial reservoir concentration values, that is, $c_{avg} = (c_1 q_1 + c_2 q_2) / (q_1 + q_2)$. For example, given c_1 = 1 and c_2 = 0, flow ratio of q_1 / q_2 = 1.5 and q_1 / q_2 = 0.43 have to be satisfied for $c = 0.8 - 0.4\eta$ with c_{avg}=0.6 and $c = 0.4 - 0.2\eta$ with c_{avg}=0.3. Therefore, a constraint can be imposed to the ratio of flow rates q_1 and q_2, so that either q_1 or q_2 can be chosen as the optimization variable. This greatly speeds the optimization process.

Subjected to this constraint, the absolute values of q_1 and q_2 determine the sample residence time in the mixing channel and hence the profile slope. Figure 8-13c illustrates three different prescribed and optimized profiles: $c = 0.9 - 0.6\eta$, $c = 0.8 - 0.4\eta$ and $c = 0.7 - 0.2\eta$, all having the same c_{avg} but different slopes. Therefore, solution with the same ratio of q_1/q_2 but different q_1 and q_2 values needs to be pumped into the network. At larger flow rates (e.g., q_1 = 36.7214 nl min^{-1} and q_2 = 24.4793 nl min^{-1}), sample spends less time within the channel for mixing, leading to a steeper gradient (B_2 = –0.6).

8.5.2 Bell-Shape Profile Generators

In this section, the process of designing a bell-shape profile generator will be described. A symmetric bell-shape profile along the channel width can be mathematically described as the difference between two Error functions,

$$c = \frac{Erf\left(B_1\left(\eta - B_2\right)\right) - Erf\left(B_1\left(\eta - \left(1 - B_2\right)\right)\right)}{2} \tag{8.9}$$

where B_1 and B_2 dictate the slope and position of the sigmoid sides of the bell shape profile (see Figure 8-14).

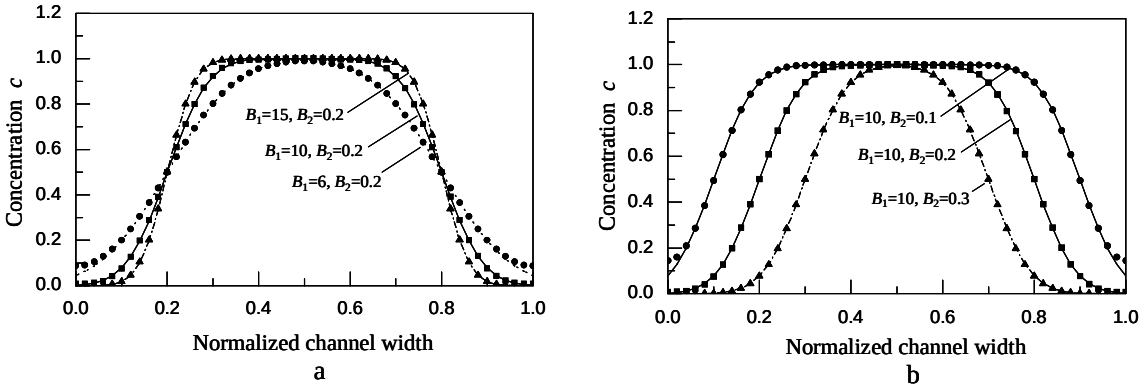

Figure 8-14. Comparison between prescribed (line) and optimized (symbol) bell-shape concentration profiles. (a) Different B_1 values lead to different side slopes of the bell-shape profile. Flow rates $q_1 = q_3 = \{175.202, 479.9, 1081.5\}$ nl min^{-1} and $q_2 = \{523.6, 1440, 3245.8\}$ nl min^{-1} yield $B_1 = \{6, 10, 15\}$. (b) Different B_2 values lead to different positions of the sigmoid sides of the bell-shape profile. Flow rates $q_1 = q_3 = \{253.4, 479.9, 721.2\}$ nl min^{-1} and $q_2 = \{1997, 1440, 962\}$ nl min^{-1} yield $B_2 = \{0.1, 0.2, 0.3\}$.

Based on previous knowledge in Figure 8-4, the cross-focusing mixer is selected. The sample and buffer flow rates through the middle and side branch channels (Figure 8-4a) are preferentially chosen as optimization variables. Other parameters, such as the channel sizes and initial sample concentrations are the same as those in Figure 8-4 and kept unchanged during optimizations. Figure 8-14 shows the comparison between the prescribed (line) and optimized (symbol) bell-shape concentration profiles and excellent agreement is found. Figure 8-14a depicts a family of bell-shape concentration profiles with different side slopes by adjusting B_1 values. Larger flow rates (e.g., $q_1 = q_3 = 1081.5$ and $q_2 = 3245.8$ nl min^{-1}) accelerate the sample migration through the main mixing channel, leading to less mixing and steeper side slopes (larger values of the B_1), namely a more drastic gradient change. Figure 8-14b illustrates a family of bell-shape profiles with different positions of the sigmoid sides due to disparate values of B_2. As B_2 increases, both sides translate towards the channel centerline, leading to the shrunk top-plateaus and area under the curves. This can be achieved by diminishing the ratio of q_2/q_1 (or q_2/q_3) to cut down sample quantity

flowing into the network. Further reducing B_2 can yield a Gaussian or a Dirac δ profile without plateaus.

8.5.3 Periodic Linear Profile Generators

In this section, the design will be extended to a periodic linear profile generator by taking advantage of mass balance. With N periodic constituent linear profiles aligning along the channel width and the ith contained in $(i-1)/N \le \eta \le i/N$ ($i = 1, 2...N$), the overall profile can be mathematically described by

$$c = B_{1,i} + B_2\eta \quad , \quad (i-1)/N \le \eta \le i/N \tag{8.10}$$

where $B_{1,i}$ is the interception of the ith constituent profile and B_2 is the slope common to all constituent profiles. In this specific design, three constituent linear profiles (N = 3) are considered and Eq. (8.10) can be rewritten as

$$c = \begin{cases} B_{1,1} + B_2\eta & , \quad 0 \le \eta < 1/3 \\ B_{1,2} + B_2\eta & , \quad 1/3 \le \eta < 2/3 \\ B_{1,3} + B_2\eta & , \quad 2/3 \le \eta \le 1 \end{cases} \tag{8.11}$$

Meanwhile, values of $B_{1,2}$ and $B_{1,3}$ should satisfy $B_{1,2} = B_{1,1} - B_2/3$ and $B_{1,3} = B_{1,1} - 2B_2/3$ to ensure identical peak values of all constituent profiles. Clearly the generator consisting of three T-mixing units is selected (Figure 8-9) and the initial sample concentrations in the reservoirs are chosen as the optimization variables, which have not been discussed in the previous examples. The other parameters including flow rates and channel sizes are given in Figure 8-9. As all T-mixing units have identical dimensions and buffer flow rates, constraints of $c_1 = c_3 = c_5$, $c_2 = c_4 = c_6$ and $c_{avg} = (c_1 + c_2)/2$ are imposed. Eventually, either c_1 or c_2 is selected as an independent optimization variable.

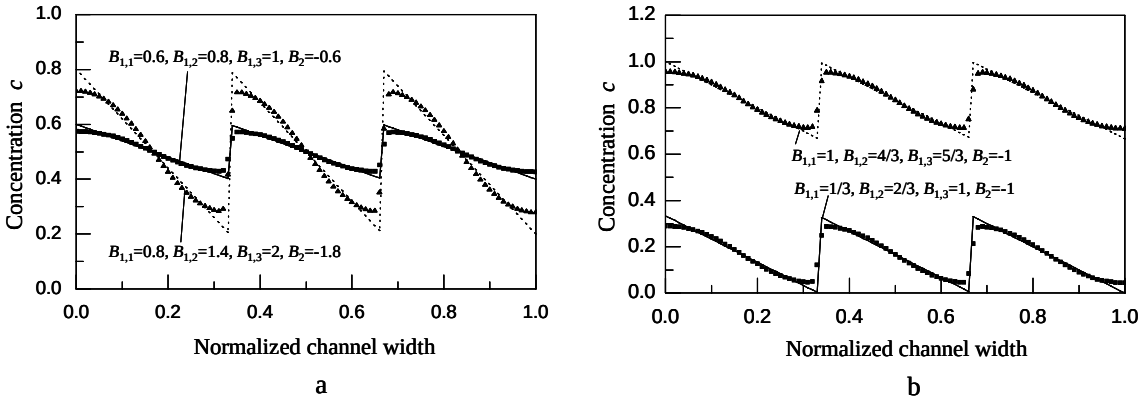

Figure 8-15. Comparison between prescribed (line) and optimized (symbol) periodic linear profiles. (a) Triple linear component profiles with different slopes and peak values but the same mean values. (b) Triple linear component profiles with different peak and average concentration values but the same slopes.

Figure 8-15 shows the comparison between the prescribed (line) and optimized (symbol) profiles from the Triple-T generator. Both agree well along the channel width except at the stream interfaces and channel walls. Specifically, Figure 8-15a shows two periodic linear profiles with different slopes (B_2) and peak values ($B_{1,1}$) but the same mean values by adjusting their reservoir sample concentrations. Sample concentrations at reservoirs are set to $c_1 = c_3 = c_5 = \{0.747, 0.583\}$, $c_2 = c_4 = c_6 = \{0.253, 0.417\}$ to obtain $B_{1,1} = \{0.8, 0.6\}$, $B_{1,2} = \{1.4, 0.8\}$, $B_{1,3} = \{2, 1\}$ and $B_2 = \{-1.8, -0.6\}$. A larger difference of the initial concentrations at the adjacent reservoirs (e.g., reservoirs 1 and 2) in a T-mixing unit causes a steeper linear output. Figure 8-15b depicts the periodic profiles with different mean and peak values but the same slopes. Correspondingly, Sample concentrations at reservoirs are set to $c_1 = c_3 = c_5 = \{0.3, 0.97\}$ and $c_2 = c_4 = c_6 = \{0.03, 0.03\}$ to attain $B_{1,1} = \{1/3, 1\}$, $B_{1,2} = \{2/3, 4/3\}$, $B_{1,3} = \{1, 5/3\}$ and $B_2 = \{-1, -1\}$.

8.6 Summary

A novel microfluidic device capable of generating temporally and spatially stable concentration profiles of complex shapes, along with its design methodology has been

presented. The underlying principle is to superimpose the constituent profiles (e.g., linear and bell-shape) arising from T- or cross-mixers side-by-side to achieve composite profiles (e.g., periodic and hybrid) along channel widths. To assist design of the proposed generators, the composable modeling and simulation approach has been exploited. Analytical and parameterized behavioral models for the elements (e.g., mixing channels and converging intersections) in pressure driven flow have been developed and integrated to achieve a system simulation. Simulation results exploring various generators (e.g., linear, bell-shape, periodic and hybrid) have been validated by the numerical FVM analysis. Hence, the accurate and fast models can be used for the generator design based on the iterative simulation. Design processes to achieve prescribed profiles (e.g., linear, bell-shape and periodic) by quantitatively modulating flow rates and initial sample concentrations at reservoirs have been demonstrated. The strategy that takes advantage of mass balance to reduce the optimization variable number and speed up the design has been discussed as well. Good agreement between the prescribed and optimized designs indicates that flow rates and reservoir sample concentrations are flexible and convenient means to adjust concentration gradients.

In contrast to previous approaches, the proposed generators are able to create complex and smooth concentration profiles by using very simple microfluidic network structure. Thereby, it enables the profile generation in even smaller scales with less fabrication effort and low possibility of clogging and leakage (lower pressure drop). The limitation of the proposed approach is its inefficiency to yield strictly linear profiles due to the mass insulation at channel walls.

Chapter 9 Summary and Future Work

This thesis introduces a behavioral modeling and schematic simulation methodology of electrokinetic biofluidic lab-on-a-chip systems. Key issues that have been discussed include schematic representation, behavioral modeling, numerical and experimental validation, modeling efficiency as well as model extensibility.

9.1 Summary

Behavioral modeling and schematic simulation of biofluidic LoC systems is based on its geometrical and functional decomposition. A complex design can be decomposed into a set of commonly used elements of simple geometries (e.g., turns and straight channels), each with an associated function (e.g. mixing or separation). Both electric and biofluidic pins are defined at element terminals to support communication between the elements and describe the local sample/species state. These pins are then linked by analog wiring buses to form a system-level schematic for simulation. Lumped models are analytically derived to capture the behavior of these elements and correlate the sample/species state at element terminals. The models are parameterized by design geometries, material properties and operational parameters (e.g., electric field). The behavioral models have been implemented in an analog HDL, Verilog-A. Schematics are composed in Cadence's virtuoso schematic editor and are simulated by Cadence Spectre. In contrast to previous studies, our efforts for system-level designs of LoCs demonstrate the following significant features and characteristics

(1). **Hierarchical design**. In contrast to previous studies, our method is based on a hierarchical LoC representation and emphasizes both element-level multi-physics modeling and system-level simulations. Therefore, LoC performance evaluation can be conducted at

various levels (element-subsystem-system), depending on the design needs. Element-level modeling allows for the analysis of element behavior and its response to changes of element parameters (e.g., studies on skew interaction in Section 4.4 and Joule heating mass transfer regimes in Section 5.3); while the system-level simulation captures overall effects of subsystem-level parameters (e.g., separator and mixer topologies and types; operational electric fields and injection schemes) and element-level parameters (e.g., length and width of mixing and separation channels) on system performance, as well as tradeoffs among them, enabling optimal system-level design. Hence, the hierarchical design of LoCs with large system complexity is supported by the approach developed in this thesis.

(2). **Model parameterization and reusability**. Unlike reduced order macromodels that need to be regenerated whenever the geometry and property are perturbed, the parameterization of geometry, material property and operation parameters enables model reusability. The system topology can be readily modified by updating the choice of the element model, the parameters in the element instance and the wiring connections, without impacting the embedded model contents. This effectively supports the decomposition of the system complexity that exists in integrated LoC devices.

(3). **Ability to consider complex sample transport**. In contrast to previous research that mainly focuses on bulk fluid flow in microchannels or takes advantage of the analogy between fluidic and sample transport, this thesis focuses on local non-ideal sample transport that often becomes the performance-limiting factor in a LoC design. Turn and Joule heating induced dispersion in electrophoretic separation chips is studied using the method of moments. The skew of the species band is represented by a set of the Fourier cosine series coefficients that capture the effect of band skew on separation performance in

complex chip geometries. Sample concentration profiles in laminar diffusion based-micromixers are also represented by a Fourier cosine series. Models that correlate the variation of the concentration profile between the element inlet and outlet are then developed. They accurately consider the overall effects of mixer topology, size and electric field on mixing performance as well as their tradeoffs. Therefore, the model can be used for the top-down design of LoC devices.

(4). **Fast speed**. Fast simulation speed is another important requirement for iterative system-level design. As all behavioral models in this thesis are analytically derived and in a closed form, they offer tremendous speedup over the numerical simulation, e.g., a maximum speed up of 400,000 × has been achieved over a FEM simulation for a hybrid electrophoresis microchip in Section 4.5.4.

(5). **Adequate accuracy**. All the modeling results in this thesis are validated through comparison to either full numerical simulation or reported experimental data. In most practical cases, our behavioral models show very good accuracy (generally less than 5 %) relative to numerical results. In certain cases, such as the ultra-high Peclet regime (e.g., DNA electrophoresis in sieving matrix in Section 4.5.2), the discrepancy can become larger (but is still ~ 10 %). This discrepancy can be attributed to the errors induced by modeling approximations or the numerical discretization of the convection-diffusion equation.

(6). **Format consistency and multi-physics modeling**. As discussed in Chapter 3, multi-physics modeling of electrokinetic LoCs can be generalized into a uniform format. The electric pins are present in all element models regardless of their functions, while the biofluidic pins calculated in terms of signal flow are specific to multi-physics within individual elements. This organization not only retains the format consistency among

different behavioral models in a library, but also allows for introducing new multi-physics models (e.g., the concentration gradient generator of pressure driven flow in Chapter 8).

In a summary, the approach investigated in this thesis meets the requirements for modeling and simulation of integrated biofluidic LoCs discussed in Chapter 1.

9.2 Future Work

In the future, several issues can be studied to extend and generalize the results obtained in this thesis.

During modeling of turn-induced dispersion, a discontinuous electric field is assumed at the interface between a turn and a straight channel. This treatment has led to considerable simplification by allowing the well-developed species velocity profile to be used to reformulate the convection-diffusion problem in straight channels and turns in such a way that analytical solutions are available. This simplification generally gives accurate results, which have been verified numerically and experimentally. However, appreciable errors could occur at the high-Peclet number regime, where convective effect becomes dominant. In this case the dispersion characteristics are significantly affected by inaccuracies in the velocity profile. As the transverse component of electrokinetic species velocity at junction regions can be analytically described and considered second order to the axial velocity, a simple perturbation method might be used to account for the extra dispersion induced at element interfaces.

For Joule heating induced dispersion modeling, channel walls are assumed to be at uniform temperature. This approximation considerably simplifies the formulation of the heat transfer problem in the model, and is accurate for substrates that are good thermal conductors or channels that have large aspect ratios. To improve the accuracy of the model

for general substrates and channel aspect ratios, where there may be significant temperature variations on channel walls, heat transfer in the substrate as well as in the buffer needs to be accounted for. This consideration will also provide a more accurate knowledge of average buffer temperature, allowing accurate evaluation of average material properties for use in the model. Such a heat transfer problem will generally no longer permit an analytical solution. However, it may still be possible to obtain closed-form correlations that are fitted to numerical solutions expressed in appropriate dimensionless parameters [207].

Chapter 6 focuses on electrokinetic passive micromixers, but the modeling approach can be extended to pressure driven flow. In Chapter 8, the EK mixing model is directly applied, with minor modifications, to pressure-driven concentration gradient generators. The stream-wise dispersion term is neglected in a simplified analysis of sample transport in mixing channels with relatively large width-to-depth ratios [171, 172]. Refs. [164, 205, 208] have pointed out that the effects of non-uniform buffer velocity profiles along the channel depth on sample mixing can be characterized by a stream-wise Taylor dispersion coefficient and tend to be more noticeable at high Peclet numbers. A more accurate model considering axial dispersion can be implemented in the future. In the case of pressure-driven mixers using channels of smaller width-to-depth ratios, no analytical solution exists to our knowledge. A combined approach of the analytical solution (based on the case of the flat channel) and using correction factors (obtained from numerical analysis) may be applied to predict the depth-averaged concentration profile. Neural network (NN) theory might be used to fit the numerical data to obtain the correction factor.

In Chapter 7, a simplified immunoassay reaction model assuming complete mixing and reaction has been proposed for the integrated LoC simulation, which does not capture the

reaction kinetics and requires sufficient channel lengths. The mixer model presented in this thesis is able to predict the intermediate mixing process and provides an accurate estimate to the channel length that achieves complete mixing. In the mixing-limiting case, where the reaction rate is faster than the diffusion-based mixing rate; a channel with complete mixing also ensures complete reaction. Therefore our reactor model based on mass balance and the decoupling of mixing and reaction process can be only applied to chip design with fast reactions ($\mathrm{Da}\cdot\mathrm{Pe}\left(w/L\right)\gg 1$ and Da is the Damkohler number). To address this issue, a reaction model that can handle simultaneous mixing and reaction is needed. This can be done in two ways: integrating a numerical scheme into the existing LoC modeling and simulation framework or using neural network theory to fit the dependence of the reaction yield on the dimensionless groups that incorporate the effects of reactor dimensions, material properties and kinetic constants. The latter seems more promising to synthesis and optimization that might involve hundreds and thousands of iterative evaluations.

Also for micro-reaction systems, lumped reaction models may be categorized and developed according to their specific applications (e.g., PCR, enzymatic and immunoassay reactions) rather than in a general form (such as A+B⇔C or A⇔B), as their mechanisms are distinctly different, leading to different dimensionless groups and modeling approaches (e.g., in the PCR reaction, temperature might be a parameter impacting the reaction yield).

For concentration generators, future work focuses on creating more varieties of gradients and improving the optimization algorithm. The proposed gradient generators in this thesis are not able to generate strictly linear profiles, which can be addressed by attaching three splitting channels at the end of the T-mixing channel. Thus, the bent sides of the concentration profile will be chopped off and the strictly linear portion at the middle

will remain for the analysis. In addition, the current optimization is essentially iterative simulation on all discretized nodes created by meshing the parameter space. Therefore, efficient optimization algorithm can be integrated to speed up the optimization process.

Reference

[1] D. Erickson and D. Q. Li, "Integrated microfluidic devices," *Analytica Chimica Acta*, vol. 507, pp. 11-26. 2004.

[2] K. K. Jain, "Biochips and microarrays: Technology and commercial potential," Informa Pharmaceuticals, Pharmaceutical Industry Report 2000.

[3] Multimedia Research Group Inc. and Fuji-Keizai, "The worldwide biochips & equipments market 2005 biochips business roadmap: Technology update, market, business trends and directions," 2005, pp. 176.

[4] B. H. Weigl, R. L. Bardell, and C. R. Cabrera, "Lab-on-a-chip for drug development," *Advanced Drug Delivery Reviews*, vol. 55, pp. 349-377. 2003.

[5] A. W. Chow, "Lab-on-a-chip: Opportunities for chemical engineering," *AICHE Journal*, vol. 48, pp. 1590-1595. 2002.

[6] D. J. Harrison, C. Skinner, S. B. Cheng, G. Ocvirk, S. Attiya, N. Bings, C. Wang, J. Li, P. Thibault, and W. Lee, "From micro-motors to micro-fluidics: The blossoming of micromachining technologies in chemistry, biochemistry and biology," *Proceedings of 10th International Conference on Solid-State Sensors and Actuators*, Sendai, Japan, pp. 12-15, June 7-10. 1999.

[7] P. M. S. John, T. Woudenberg, C. Connell, M. Deshpande, J. R. Gilbert, M. Garguilo, P. Paul, J. Molho, A. E. Herr, T. W. Kenny, and M. G. Mungal, "Metrology and simulation of chemical transport in microchannels," *Proceedings of the 8th IEEE Solid-State Sensor and Actuator Workshop*, Hilton Head Island, SC, U.S.A, pp. 106-111, June 7-11. 1998.

[8] P. Stout, H. Q. Yang, P. Dionne, A. Leonard, Z. Tan, A. Przekwas, and A. Krishnan, "CFD-ACE+MEMS: a CAD system for simulation and modeling of MEMS," *Proceedings of Design, Test, Integration and Packaging of MEMS and MOEMS (DTIP'99)*, Paris, France, pp. 328-339. 1999.

[9] S. Hardt and F. Schonfeld, "Laminar mixing in different interdigital micromixers: II. Numerical simulations," *AICHE Journal*, vol. 49, pp. 578-584. 2003.

[10] R. M. Magargle, J. F. Hoburg, and T. Mukherjee, "A simple description of turn-induced transverse field dispersion in microfluidic channels for system-level design," *Technical Proceedings of the 2003 Nanotechnology Conference and Trade Show*, San Francisco, CA, U.S.A, pp. 214-217, Feb. 23-26. 2003.

[11] G. F. Yao, "A computational model for simulation of electroosmotic flow in microsystem," *Technical Proceedings of the 2003 Nanotechnology Conference and Trade Show (NanoTech 2003)*, San Francisco, CA, pp. 218-221, February 23-27. 2003.

[12] M. Horner, "Computational analysis of on-line coupled ITP-CE," *Technical Proceedings of the 2005 NSTI Nanotechnology Conference and Trade Show (NanoTech 2005)*, Anaheim, CA, pp. 583-586. 2005.

[13] Y. Wang, Q. Lin, and T. Mukherjee, "A model for Joule heating-induced dispersion in microchip electrophoresis," *Lab on a Chip*, vol. 4, pp. 625-631. 2004.

[14] Comsol Inc. "Low-voltage electroosmotic micropump," *FEMLAB 3.0 Multiphysics Modeling Tutorial*. 2005.

[15] C. A. Emrich, H. J. Tian, I. L. Medintz, and R. A. Mathies, "Microfabricated 384-lane capillary array electrophoresis bioanalyzer for ultrahigh-throughput genetic analysis," *Analytical Chemistry*, vol. 74, pp. 5076-5083. 2002.
[16] N. H. Chiem and D. J. Harrison, "Microchip systems for immunoassay: an integrated immunoreactor with electrophoretic separation for serum theophylline determination," *Clinical Chemistry*, vol. 44, pp. 591-598. 1998.
[17] S. B. Cheng, C. D. Skinner, J. Taylor, S. Attiya, W. E. Lee, G. Picelli, and D. J. Harrison, "Development of a multichannel microfluidic analysis system employing affinity capillary electrophoresis for immunoassay," *Analytical Chemistry*, vol. 73, pp. 1472-1479. 2001.
[18] M. Schena, D. Shalon, R. W. Davis, and P. O. Brown, "Quantitative monitoring of gene-expression patterns with a complementary-DNA microarray," *Science*, vol. 270, pp. 467-470. 1995.
[19] M. Schena, D. Shalon, R. Heller, A. Chai, P. O. Brown, and R. W. Davis, "Parallel human genome analysis: Microarray-based expression monitoring of 1000 genes," *Proceedings of the National Academy of Sciences of the United States of America*, vol. 93, pp. 10614-10619. 1996.
[20] D. Shalon, S. J. Smith, and P. O. Brown, "A DNA microarray system for analyzing complex DNA samples using two-color fluorescent probe hybridization," *Genome Research*, vol. 6, pp. 639-645. 1996.
[21] P. O. Brown and D. Botstein, "Exploring the new world of the genome with DNA microarrays," *Nature Genetics*, vol. 21, pp. 33-37. 1999.
[22] M. J. Heller, "DNA microarray technology: Devices, systems, and applications," *Annual Review of Biomedical Engineering*, vol. 4, pp. 129-153. 2002.
[23] M. F. Templin, D. Stoll, J. M. Schwenk, O. Potz, S. Kramer, and T. O. Joos, "Protein microarrays: Promising tools for proteomic research," *Proteomics*, vol. 3, pp. 2155-2166. 2003.
[24] S. Bodovitz, T. Joos, and J. Bachmann, "Protein biochips: the quiet before the storm," *Drug Discovery Today*, vol. 10, pp. 283-287. 2005.
[25] H. A. Stone, A. D. Stroock, and A. Ajdari, "Engineering flows in small devices: Microfluidics toward a lab-on-a-chip," *Annual Review of Fluid Mechanics*, vol. 36, pp. 381-411. 2004.
[26] P. K. Wong, T. H. Wang, J. H. Deval, and C. M. Ho, "Electrokinetics in micro devices for biotechnology applications," *Ieee-Asme Transactions on Mechatronics*, vol. 9, pp. 366-376. 2004.
[27] A. A. Darhuber and S. M. Troian, "Principles of microfluidic actuation by modulation of surface stresses," *Annual Review of Fluid Mechanics*, vol. 37, pp. 425-455. 2005.
[28] B. S. Gallardo, V. K. Gupta, F. D. Eagerton, L. I. Jong, V. S. Craig, R. R. Shah, and N. L. Abbott, "Electrochemical principles for active control of liquids on submillimeter scales," *Science*, vol. 283, pp. 57-60. 1999.
[29] D. E. Kataoka and S. M. Troian, "Patterning liquid flow on the microscopic scale," *Nature*, vol. 402, pp. 794-797. 1999.
[30] M. K. Chaudhury and G. M. Whitesides, "How to make water run uphill," *Science*, vol. 256, pp. 1539-1541. 1992.

[31] S. Daniel and M. K. Chaudhury, "Rectified motion of liquid drops on gradient surfaces induced by vibration," *Langmuir*, vol. 18, pp. 3404-3407. 2002.
[32] M. Vallet, B. Berge, and L. Vovelle, "Electrowetting of water and aqueous solutions on poly(ethylene terephthalate) insulating films," *Polymer*, vol. 37, pp. 2465-2470. 1996.
[33] M. Vallet, M. Vallade, and B. Berge, "Limiting phenomena for the spreading of water on polymer films by electrowetting," *European Physical Journal B*, vol. 11, pp. 583-591. 1999.
[34] M. G. Pollack, R. B. Fair, and A. D. Shenderov, "Electrowetting-based actuation of liquid droplets for microfluidic applications," *Applied Physics Letters*, vol. 77, pp. 1725-1726. 2000.
[35] M. G. Pollack, A. D. Shenderov, and R. B. Fair, "Electrowetting-based actuation of droplets for integrated microfluidics," *Lab on a Chip*, vol. 2, pp. 96-101. 2002.
[36] S. K. Cho, H. J. Moon, and C. J. Kim, "Creating, transporting, cutting, and merging liquid droplets by electrowetting-based actuation for digital microfluidic circuits," *Journal of Microelectromechanical Systems*, vol. 12, pp. 70-80. 2003.
[37] T. S. Sammarco and M. A. Burns, "Thermocapillary pumping of discrete drops in microfabricated analysis devices," *Aiche Journal*, vol. 45, pp. 350-366. 1999.
[38] H. A. Pohl, "The motion and precipitation of suspensoids in divergent electric fields," *Journal of Applied Physics*, vol. 22, pp. 869-871. 1951.
[39] R. Pethig and G. H. Markx, "Applications of dielectrophoresis in biotechnology," *Trends in Biotechnology*, vol. 15, pp. 426-432. 1997.
[40] M. P. Hughes, "AC electrokinetics: applications for nanotechnology," *Nanotechnology*, vol. 11, pp. 124-132. 2000.
[41] S. K. Fan, C. Hashi, and C. J. Kim, "Manipulation of multiple droplets on N X M grid by cross-reference EWOD driving scheme and pressure-contact packaging," *Proceedings of IEEE Micro Electro Mechanical Systems Conference*, Kyoto, Japan, pp. 694-697, January 19-23. 2003.
[42] A. R. Wheeler, H. Moon, C. J. Kim, J. A. Loo, and R. L. Garrell, "Electrowetting-based microfluidics for analysis of peptides and proteins by matrix-assisted laser desorption/ionization mass spectrometry," *Analytical Chemistry*, vol. 76, pp. 4833-4838. 2004.
[43] V. Srinivasan, V. K. Pamula, and R. B. Fair, "Droplet-based microfluidic lab-on-a-chip for glucose detection," *Analytica Chimica Acta*, vol. 507, pp. 145-150. 2004.
[44] V. Srinivasan, V. K. Pamula, and R. B. Fair, "An integrated digital microfluidic lab-on-a-chip for clinical diagnostics on human physiological fluids," *Lab on a Chip*, vol. 4, pp. 310-315. 2004.
[45] J. Zeng and T. Korsmeyer, "Principles of droplet electrohydrodynamics for lab-on-a-chip," *Lab on a Chip*, vol. 4, pp. 265-277. 2004.
[46] W. M. Arnold and U. Zimmermann, "Electro-rotation-Development of a technique for dielectric measurements on individual cells and particles," *Journal of Electrostatics*, vol. 21, pp. 151-191. 1988.
[47] K. L. Chan, P. R. C. Gascoyne, F. F. Becker, and R. Pethig, "Electrorotation of liposomes: verification of dielectric multi-shell model for cells," *Biochimica Et Biophysica Acta-Lipids and Lipid Metabolism*, vol. 1349, pp. 182-196. 1997.

[48] R. Georgieva, B. Neu, V. M. Shilov, E. Knippel, A. Budde, R. Latza, E. Donath, H. Kiesewetter, and H. Baumler, "Low frequency electrorotation of fixed red blood cells," *Biophysical Journal*, vol. 74, pp. 2114-2120. 1998.
[49] J. Suehiro and R. Pethig, "The dielectrophoretic movement and positioning of a biological cell using a three-dimensional grid electrode system," *Journal of Physics D-Applied Physics*, vol. 31, pp. 3298-3305. 1998.
[50] S. W. Lee and Y. C. Tai, "A micro cell lysis device," *Sensors and Actuators a-Physical*, vol. 73, pp. 74-79. 1999.
[51] C. X. Xu, Y. Wang, M. Cao, and Z. H. Lu, "Dielectrophoresis of human red cells in microchips," *Electrophoresis*, vol. 20, pp. 1829-1831. 1999.
[52] U. Zimmermann, U. Friedrich, H. Mussauer, P. Gessner, K. Hamel, and V. Sukhoruhov, "Electromanipulation of mammalian cells: Fundamentals and application," *IEEE Transactions on Plasma Science*, vol. 28, pp. 72-82. 2000.
[53] G. Abou-Ali, K. V. I. S. Kaler, R. Paul, N. K. Bjorklund, and R. Gordon, "Electrorotation of axolotl embryos," *Bioelectromagnetics*, vol. 23, pp. 214-223. 2002.
[54] T. B. Jones, M. Gunji, M. Washizu, and M. J. Feldman, "Dielectrophoretic liquid actuation and nanodroplet formation," *Journal of Applied Physics*, vol. 89, pp. 1441-1448. 2001.
[55] A. van den Berg and T. S. J. Lammerink, "Micro total analysis systems: Microfluidic aspects, integration concept and applications," *Microsystem Technology in Chemistry and Life Science*, vol. 194, pp. 21-49. 1998.
[56] M. Gad-el-Hak, *The MEMS handbook*. Boca Raton, FL: CRC Press, 2002.
[57] D. J. Laser and J. G. Santiago, "A review of micropumps," *Journal of Micromechanics and Microengineering*, vol. 14, pp. R35-R64. 2004.
[58] G. M. Walker, M. S. Ozers, and D. J. Beebe, "Cell infection within a microfluidic device using virus gradients," *Sensors and Actuators B-Chemical*, vol. 98, pp. 347-355. 2004.
[59] J. S. Ko, H. C. Yoon, H. S. Yang, H. B. Pyo, K. H. Chung, S. J. Kim, and Y. T. Kim, "A polymer-based microfluidic device for immunosensing biochips," *Lab on a Chip*, vol. 3, pp. 106-113. 2003.
[60] S. Lai, S. N. Wang, J. Luo, L. J. Lee, S. T. Yang, and M. J. Madou, "Design of a compact disk-like microfluidic platform for enzyme-linked immunosorbent assay," *Analytical Chemistry*, vol. 76, pp. 1832-1837. 2004.
[61] D. C. Duffy, H. L. Gillis, J. Lin, N. F. Sheppard, and G. J. Kellogg, "Microfabricated centrifugal microfluidic systems: Characterization and multiple enzymatic assays," *Analytical Chemistry*, vol. 71, pp. 4669-4678. 1999.
[62] J. Lichtenberg, N. F. de Rooij, and E. Verpoorte, "Sample pretreatment on microfabricated devices," *Talanta*, vol. 56, pp. 233-266. 2002.
[63] P. Jandik, B. H. Weigl, N. Kessler, J. Cheng, C. J. Morris, T. Schulte, and N. Avdalovic, "Initial study of using a laminar fluid diffusion interface for sample preparation in high-performance liquid chromatography," *Journal of Chromatography A*, vol. 954, pp. 33-40. 2002.
[64] F. E. P. Mikkers, F. M. Everaerts, and T. P. E. M. Verheggen, "High-performance zone electrophoresis," *Journal of Chromatography*, vol. 169, pp. 11-20. 1979.

[65] D. S. Burgi and R. L. Chien, "Application of sample stacking to gravity injection in capillary electrophoresis," *Journal of Microcolumn Separations*, vol. 3, pp. 199-202. 1991.
[66] D. S. Burgi and R. L. Chien, "Optimization in sample stacking for high-performance capillary electrophoresis," *Analytical Chemistry*, vol. 63, pp. 2042-2047. 1991.
[67] R. L. Chien and D. S. Burgi, "On-column sample concentration using field amplification in CZE," *Analytical Chemistry*, vol. 64, pp. A489-A496. 1992.
[68] H. Yang and R. L. Chien, "Sample stacking in laboratory-on-a-chip devices," *Journal of Chromatography A*, vol. 924, pp. 155-163. 2001.
[69] J. Lichtenberg, E. Verpoorte, and N. F. de Rooij, "Sample preconcentration by field amplification stacking for microchip-based capillary electrophoresis," *Electrophoresis*, vol. 22, pp. 258-271. 2001.
[70] B. Jung, R. Bharadwaj, and J. G. Santiago, "Thousandfold signal increase using field-amplified sample stacking for on-chip electrophoresis," *Electrophoresis*, vol. 24, pp. 3476-3483. 2003.
[71] S. C. Jacobson, T. E. McKnight, and J. M. Ramsey, "Microfluidic devices for electrokinetically driven parallel and serial mixing," *Analytical Chemistry*, vol. 71, pp. 4455-4459. 1999.
[72] X. Y. Jiang, J. M. K. Ng, A. D. Stroock, S. K. W. Dertinger, and G. M. Whitesides, "A miniaturized, parallel, serially diluted immunoassay for analyzing multiple antigens," *Journal of the American Chemical Society*, vol. 125, pp. 5294-5295. 2003.
[73] N. L. Jeon, S. K. W. Dertinger, D. T. Chiu, I. S. Choi, A. D. Stroock, and G. M. Whitesides, "Generation of solution and surface gradients using microfluidic systems," *Langmuir*, vol. 16, pp. 8311-8316. 2000.
[74] S. K. W. Dertinger, D. T. Chiu, N. L. Jeon, and G. M. Whitesides, "Generation of gradients having complex shapes using microfluidic networks," *Analytical Chemistry*, vol. 73, pp. 1240-1246. 2001.
[75] N. L. Jeon, H. Baskaran, S. K. W. Dertinger, G. M. Whitesides, L. Van de Water, and M. Toner, "Neutrophil chemotaxis in linear and complex gradients of interleukin-8 formed in a microfabricated device," *Nature Biotechnology*, vol. 20, pp. 826-830. 2002.
[76] S. J. Wang, W. Saadi, F. Lin, C. M. C. Nguyen, and N. L. Jeon, "Differential effects of EGF gradient profiles on MDA-MB-231 breast cancer cell chemotaxis," *Experimental Cell Research*, vol. 300, pp. 180-189. 2004.
[77] V. Hessel, H. Lowe, and F. Schonfeld, "Micromixers - a review on passive and active mixing principles," *Chemical Engineering Science*, vol. 60, pp. 2479-2501. 2005.
[78] N. T. Nguyen and Z. G. Wu, "Micromixers - a review," *Journal of Micromechanics and Microengineering*, vol. 15, pp. R1-R16. 2005.
[79] P. A. Aurouz, D. Lossifidis, D. R. Reyes, and A. Manz, "Micro total analysis systems. 2. analytical standard operations and applications," *Analytical Chemistry*, vol. 74, pp. 2637-2652. 2002.
[80] D. R. Reyes, D. Lossifidis, P.-A. Auroux, and A. Manz, "Micro total analysis systems. 1. Introduction, theory, and technology," *Analytical Chemistry*, vol. 74, pp. 2623-2636. 2002.
[81] P. Watts and S. J. Haswell, "Microfluidic combinatorial chemistry," *Current Opinion in Chemical Biology*, vol. 7, pp. 380-387. 2003.

[82] A. Manz, N. Graber, and H. M. Widmer, "Miniaturized total chemical-analysis systems - A novel concept for chemical sensing," *Sensors and Actuators B-Chemical*, vol. 1, pp. 244-248. 1990.
[83] M. Krishnan, V. Namasivayam, R. S. Lin, R. Pal, and M. A. Burns, "Microfabricated reaction and separation systems," *Current Opinion in Biotechnology*, vol. 12, pp. 92-98. 2001.
[84] Y. N. Shi, P. C. Simpson, J. R. Scherer, D. Wexler, C. Skibola, M. T. Smith, and R. A. Mathies, "Radial capillary array electrophoresis microplate and scanner for high-performance nucleic acid analysis," *Analytical Chemistry*, vol. 71, pp. 5354-5361. 1999.
[85] C. S. Effenhauser, G. J. M. Bruin, A. Paulus, and M. Ehrat, "Integrated capillary electrophoresis on flexible silicone microdevices: Analysis of DNA restriction fragments and detection of single DNA molecules on microchips," *Analytical Chemistry*, vol. 69, pp. 3451-3457. 1997.
[86] S. C. Jacobson and J. M. Ramsey, "Integrated microdevice for DNA restriction fragment analysis," *Analytical Chemistry*, vol. 68, pp. 720-723. 1996.
[87] A. T. Woolley, K. Q. Lao, A. N. Glazer, and R. A. Mathies, "Capillary electrophoresis chips with integrated electrochemical detection," *Analytical Chemistry*, vol. 70, pp. 684-688. 1998.
[88] P. Ertl, C. A. Emrich, P. Singhal, and R. A. Mathies, "Capillary electrophoresis chips with a sheath-flow supported electrochemical detection system," *Analytical Chemistry*, vol. 76, pp. 3749-3755. 2004.
[89] L. L. Shultz-Lockyear, C. L. Colyer, Z. H. Fan, K. I. Roy, and D. J. Harrison, "Effects of injector geometry and sample matrix on injection and sample loading in integrated capillary electrophoresis devices," *Electrophoresis*, vol. 20, pp. 529-538. 1999.
[90] A. T. Woolley, D. Hadley, P. Landre, A. J. deMello, R. A. Mathies, and M. A. Northrup, "Functional integration of PCR amplification and capillary electrophoresis in a microfabricated DNA analysis device," *Analytical Chemistry*, vol. 68, pp. 4081-4086. 1996.
[91] L. C. Waters, S. C. Jacobson, N. Kroutchinina, J. Khandurina, R. S. Foote, and J. M. Ramsey, "Multiple sample PCR amplification and electrophoretic analysis on a microchip," *Analytical Chemistry*, vol. 70, pp. 5172-5176. 1998.
[92] L. C. Waters, S. C. Jacobson, N. Kroutchinina, J. Khandurina, R. S. Foote, and J. M. Ramsey, "Microchip device for cell lysis, multiplex PCR amplification, and electrophoretic sizing," *Analytical Chemistry*, vol. 70, pp. 158-162. 1998.
[93] W. C. Dunn, S. C. Jacobson, L. C. Waters, N. Kroutchinina, J. Khandurina, R. S. Foote, M. J. Justice, L. J. Stubbs, and J. M. Ramsey, "PCR amplification and analysis of simple sequence length polymorphisms in mouse DNA using a single microchip device," *Analytical Biochemistry*, vol. 277, pp. 157-160. 2000.
[94] R. C. Anderson, X. Su, G. J. Bogdan, and J. Fenton, "A miniature integrated device for automated multistep genetic assays," *Nucleic Acids Research*, vol. 28, pp. e60. 2000.
[95] J. Khandurina and A. Guttman, "Bioanalysis in microfluidic devices," *Journal of Chromatography A*, vol. 943, pp. 159-183. 2002.

[96] C. Wang, R. Oleschuk, F. Ouchen, J. J. Li, P. Thibault, and D. J. Harrison, "Integration of immobilized trypsin bead beds for protein digestion within a microfluidic chip incorporating capillary electrophoresis separations and an electrospray mass spectrometry interface," *Rapid Communications in Mass Spectrometry*, vol. 14, pp. 1377-1383. 2000.
[97] N. X. Xu, Y. H. Lin, S. A. Hofstadler, D. Matson, C. J. Call, and R. D. Smith, "A microfabricated dialysis device for sample cleanup in electrospray ionization mass spectrometry," *Analytical Chemistry*, vol. 70, pp. 3553-3556. 1998.
[98] Q. L. Mao and J. Pawliszyn, "Demonstration of isoelectric focusing on an etched quartz chip with UV absorption imaging detection," *Analyst*, vol. 124, pp. 637-641. 1999.
[99] O. Hofmann, D. P. Che, K. A. Cruickshank, and U. R. Muller, "Adaptation of capillary isoelectric focusing to microchannels on a glass chip," *Analytical Chemistry*, vol. 71, pp. 678-686. 1999.
[100] J. D. Xu, L. Locascio, M. Gaitan, and C. S. Lee, "Room-temperature imprinting method for plastic microchannel fabrication," *Analytical Chemistry*, vol. 72, pp. 1930-1933. 2000.
[101] J. S. Rossier, A. Schwarz, F. Reymond, R. Ferrigno, F. Bianchi, and H. H. Girault, "Microchannel networks for electrophoretic separations," *Electrophoresis*, vol. 20, pp. 727-731. 1999.
[102] J. Gao, J. D. Xu, L. E. Locascio, and C. S. Lee, "Integrated microfluidic system enabling protein digestion, peptide separation, and protein identification," *Analytical Chemistry*, vol. 73, pp. 2648-2655. 2001.
[103] S. Ekstrom, P. Onnerfjord, J. Nilsson, M. Bengtsson, T. Laurell, and G. Marko-Varga, "Integrated microanalytical technology enabling rapid and automated protein identification," *Analytical Chemistry*, vol. 72, pp. 286-293. 2000.
[104] L. B. Koutny, D. Schmalzing, T. A. Taylor, and M. Fuchs, "Microchip electrophoretic immunoassay for serum cortisol," *Analytical Chemistry*, vol. 68, pp. 18-22. 1996.
[105] N. Chiem and D. J. Harrison, "Microchip-based capillary electrophoresis for immunoassays: Analysis of monoclonal antibodies and theophylline," *Analytical Chemistry*, vol. 69, pp. 373-378. 1997.
[106] D. Schmalzing, L. B. Koutny, T. A. Taylor, W. Nashabeh, and M. Fuchs, "Immunoassay for thyroxine (T4) in serum using capillary electrophoresis and micromachined devices," *Journal of Chromatography B*, vol. 697, pp. 175-180. 1997.
[107] J. Wang, A. Ibanez, M. P. Chatrathi, and A. Escarpa, "Electrochemical enzyme immunoassays on microchip platforms," *Analytical Chemistry*, vol. 73, pp. 5323-5327. 2001.
[108] J. W. Choi, C. H. Ahn, S. Bhansali, and H. T. Henderson, "A new magnetic bead-based, filterless bio-separator with planar electromagnet surfaces for integrated bio-detection systems," *Sensors and Actuators B-Chemical*, vol. 68, pp. 34-39. 2000.
[109] K. Sato, M. Tokeshi, T. Odake, H. Kimura, T. Ooi, M. Nakao, and T. Kitamori, "Integration of an immunosorbent assay system: Analysis of secretory human immunoglobulin A on polystyrene beads in a microchip," *Analytical Chemistry*, vol. 72, pp. 1144-1147. 2000.

[110] K. Sato, M. Tokeshi, H. Kimura, and T. Kitamori, "Determination of carcinoembryonic antigen in human sera by integrated bead bed immunoasay in a microchip for cancer diagnosis," *Analytical Chemistry*, vol. 73, pp. 1213-1218. 2001.
[111] J. W. Choi, K. W. Oh, J. H. Thomas, W. R. Heineman, H. B. Halsall, J. H. Nevin, A. J. Helmicki, H. T. Henderson, and C. H. Ahn, "An integrated microfluidic biochemical detection system for protein analysis with magnetic bead-based sampling capabilities," *Lab on a Chip*, vol. 2, pp. 27-30. 2002.
[112] R. F. Probstein, *Physicochemical Hydrodynamics : An Introduction*, 2nd ed. New York: John Wiley & Sons, 2003.
[113] J. H. Masliyah, *Electrokinetic transport phenomena*. Edmonton, Alta.: Alberta Oil Sands Technology and Research Authority, 1994.
[114]D. F. Evans and H. Wennerstrom, *The Colloidal Domain : Where Physics, Chemistry, Biology, and Technology Meet*, 2nd edition ed: Wiley-VCH, 1999.
[115] R. J. Hunter, *Zeta potential in colloid science : principles and applications*. London: Academic Press, 1981.
[116] E. B. Cummings, S. K. Griffiths, R. H. Nilson, and P. H. Paul, "Conditions for similitude between the fluid velocity and electric field in electroosmotic flow," *Analytical Chemistry*, vol. 72, pp. 2526-2532. 2000.
[117] S. J. Haswell, "Development and operating characteristics of micro flow injection analysis systems based on electroosmotic flow - A review," *Analyst*, vol. 122, pp. R1-R10. 1997.
[118] S. C. Jacobson, R. Hergenroder, L. B. Koutny, R. J. Warmack, and J. M. Ramsey, "Effects of injection schemes and column geometry on the performance of microchip electrophoresis devices," *Analytical Chemistry*, vol. 66, pp. 1107-1113. 1994.
[119] S. Krishnamoorthy and M. G. Giridharan, "Analysis of sample injection and band-broadening in capillary electrophoresis microchips," *Technical Proceedings of the 2000 International Conference on Modeling and Simulation of Microsystems*, San Diego, CA, U.S.A, pp. 528-531, March 27-29. 2000.
[120] M. Turowski, Z. J. Chen, and A. Przekwas, "Automated generation of compact models for fluidic microsystems," *Analog Integrated Circuits and Signal Processing*, vol. 29, pp. 27-36. 2001.
[121] T. Q. Truong and N. T. Nguyen, "Simulation and optimization of tesla valves," *Technical Proceedings of the 2003 Nanotechnology Conference and Trade Show (NanoTech 2003)*, San Francisco, CA, pp. 178-181, February 23-27. 2003.
[122] Y. Wang, Q. Lin, and T. Mukherjee, "A model for laminar diffusion-based complex electrokinetic passive micromixers," *Lab on a chip*, vol. 5, pp. 877-887. 2005.
[123] Y. Wang, Q. Lin, and T. Mukherjee, "System-oriented dispersion models of general-shaped electrophoresis microchannels," *Lab on a Chip*, vol. 4, pp. 453-463. 2004.
[124] J. C. Harley, R. F. Day, J. R. Gilbert, M. Deshpande, J. M. Ramsey, and S. C. Jacobson, "System design of two dimensional microchip separation devices," *Technical Proceedings of the Fifth International Conference on Micro Total Analysis Systems (MicroTAS 2001)*, Monterey, CA, U.S.A, pp. 63-65, Oct. 2001.
[125] O. Mikulchenko, A. Rasmussen, and K. Mayaram, "A neural network based macromodel for microflow sensors," *Technical Proceedings of 2000 International Conference on Modeling and Simulation of Microsystems (MSM'00)*, San Diego, CA, pp. 540-543. 2000.

[126] R. Magargle, J. F. Hoburg, and T. Mukherjee, "Microfluidic injector models based on neural networks," *Technical Proceedings of the 2005 NSTI Nanotechnology Conference and Trade Show (Nanotech 2004)*, pp. 616-619. 2005.
[127] R. Qiao and N. R. Aluru, "A compact model for electroosmotic flows in microfluidic devices," *Journal of Micromechanics and Microengineering*, vol. 12, pp. 625-635. 2002.
[128] X. C. Xuan and D. Q. Li, "Analysis of electrokinetic flow in microfluidic networks," *Journal of Micromechanics and Microengineering*, vol. 14, pp. 290-298. 2004.
[129] http://www.coventor.com.
[130] B. Baidya, T. Mukherjee, and J. F. Hoburg, "Dispersion modeling in microfluidic channels for system-level optimization," *Technical Proceedings of the 2002 NSTI Nanotechnology Conference and Trade Show*, San Juan, PR, USA, pp. 182-185, April 22-25. 2002.
[131] T. H. Zhang, K. Chakrabarty, and R. B. Fair, "Behavioral modeling and performance evaluation of microelectrofluidics-based PCR systems using SystemC," *IEEE Transactions on Computer-Aided Design of Integrated Circuits and Systems*, vol. 23, pp. 843-858. 2004.
[132] A. N. Chatterjee and N. R. Aluru, "Combined circuit/device modeling and simulation of integrated microfluidic systems," *Journal of Microelectromechanical Systems*, vol. 14, pp. 81-95. 2005.
[133] H. Chang, *A top-down constraint-driven design methodology for analog integrated circuits*. Boston: Kluwer Academic, 1997.
[134] T. Mukherjee, G. K. Fedder, and R. D. S. Blanton, "Hierarchical design and test of integrated microsystems," *IEEE Design & Test of Computers*, vol. 16, pp. 18-27. 1999.
[135] C. T. Culbertson, S. C. Jacobson, and J. M. Ramsey, "Dispersion sources for compact geometries on microchips," *Analytical Chemistry*, vol. 70, pp. 3781-3789. 1998.
[136] A. Robbins and W. Miller, *Circuit analysis : Theory and practice*, 3rd ed. Australia ; Clifton Park, NY: Thomson/Delmar Learning, 2004.
[137] http://www.cadence.com.
[138] D. J. Harrison, A. Manz, Z. H. Fan, H. Ludi, and H. M. Widmer, "Capillary electrophoresis and sample injection systems integrated on a planar glass chip," *Analytical Chemistry*, vol. 64, pp. 1926-1932. 1992.
[139] A. Manz, D. J. Harrison, E. M. J. Verpoorte, J. C. Fettinger, A. Paulus, H. Ludi, and H. M. Widmer, "Planar chips technology for miniaturization and integration of separation techniques into monitoring systems - Capillary electrophoresis on a chip," *Journal of Chromatography*, vol. 593, pp. 253-258. 1992.
[140] C. S. Effenhauser, A. Paulus, A. Manz, and H. M. Widmer, "High-speed separation of antisense oligonucleotides on a micromachined capillary electrophoresis device," *Analytical Chemistry*, vol. 66, pp. 2949-2953. 1994.
[141] D. E. Raymond, A. Manz, and H. M. Widmer, "Continuous sample pretreatment using a free-flow electrophoresis device integrated onto a silicon chip," *Analytical Chemistry*, vol. 66, pp. 2858-2865. 1994.
[142] A. T. Woolley and R. A. Mathies, "Ultra-high-speed DNA-sequencing using capillary electrophoresis chips," *Analytical Chemistry*, vol. 67, pp. 3676-3680. 1995.

[143] S. C. Jacobson, R. Hergenroder, L. B. Koutny, and J. M. Ramsey, "High-speed separations on a microchip," *Analytical Chemistry*, vol. 66, pp. 1114-1118. 1994.
[144] C. T. Culbertson, S. C. Jacobson, and J. M. Ramsey, "Microchip devices for high-efficiency separations," *Analytical Chemistry*, vol. 72, pp. 5814-5819. 2000.
[145] B. M. Paegel, L. D. Hutt, P. C. Simpson, and R. A. Mathies, "Turn geometry for minimizing band broadening in microfabricated capillary electrophoresis channels," *Analytical Chemistry*, vol. 72, pp. 3030-3037. 2000.
[146] N. Gottschlich, S. C. Jacobson, C. T. Culbertson, and J. M. Ramsey, "Two-dimensional electrochromatography/capillary electrophoresis on a microchip," *Analytical Chemistry*, vol. 73, pp. 2669-2674. 2001.
[147] S. K. Griffiths and R. H. Nilson, "Band spreading in two-dimensional microchannel turns for electrokinetic species transport," *Analytical Chemistry*, vol. 72, pp. 5473-5482. 2000.
[148] J. I. Molho, A. E. Herr, B. P. Mosier, J. G. Santiago, T. W. Kenny, R. A. Brennen, G. B. Gordon, and B. Mohammadi, "Optimization of turn geometries for microchip electrophoresis," *Analytical Chemistry*, vol. 73, pp. 1350-1360. 2001.
[149] A. J. Pfeiffer, T. Mukherjee, and S. Hauan, "Computer-aided synthesis of microscale electrophoretic separation systems in confined areas," *Proceedings of 2003 ASME International Mechanical Engineering Congress and RD&D Expo (IMECE 2003)*, Washington D.C, Nov. 2003.
[150] R. Aris, "On the dispersion of a solute in a fluid flowing through a tube," *Proceedings of the Royal Society of London Series a-Mathematical and Physical Sciences*, vol. 235, pp. 67-77. 1956.
[151] J. I. Molho, "Electrokinetic Dispersion in Microfluidic Separation Systems," Ph.D. Thesis in *Department of Mechanical Engineering*: Stanford University, 2001.
[152] http://www.comsol.com.
[153] S. K. Griffiths and R. H. Nilson, "Design and analysis of folded channels for chip-based separations," *Analytical Chemistry*, vol. 74, pp. 2960-2967. 2002.
[154] J. C. Giddings, *Unified separation science*. New York: Wiley, 1991.
[155] S. C. Jacobson, C. T. Culbertson, J. E. Daler, and J. M. Ramsey, "Microchip structures for submillisecond electrophoresis," *Analytical Chemistry*, vol. 70, pp. 3476-3480. 1998.
[156] http://www.matlab.com.
[157] E. Grushka, R. M. Mccormick, and J. J. Kirkland, "Effect of temperature-gradients on the efficiency of capillary zone electrophoresis separations," *Analytical Chemistry*, vol. 61, pp. 241-246. 1989.
[158] G. Taylor, "Dispersion of soluble matter in solvent flowing slowly through a tube," *Proceedings of the Royal Society of London Series a-Mathematical and Physical Sciences*, vol. 219, pp. 186-203. 1953.
[159] G. Taylor, "Conditions under which dispersion of a solute in a stream of solvent can be used to measure molecular diffusion," *Proceedings of the Royal Society of London Series a-Mathematical and Physical Sciences*, vol. 225, pp. 473-477. 1954.
[160] J. H. Knox and I. H. Grant, "Miniaturization in pressure and electroendosmotically driven liquid-chromatography - Some theoretical considerations," *Chromatographia*, vol. 24, pp. 135-143. 1987.

[161] J. H. Knox, "Thermal effects and band spreading in capillary electro-separation," *Chromatographia*, vol. 26, pp. 329-337. 1988.
[162] A. Cifuentes and H. Poppe, "Rectangular capillary electrophoresis - Some theoretical considerations," *Chromatographia*, vol. 39, pp. 391-404. 1994.
[163] M. R. Doshi, P. M. Daiya, and W. N. Gill, "3 Dimensional laminar dispersion in open and closed rectangular conduits," *Chemical Engineering Science*, vol. 33, pp. 795-804. 1978.
[164] K. D. Dorfman and H. Brenner, "Comment on "Taylor dispersion of a solute in a microfluidic channel" [J. Appl. Phys. 89, 4667 (2001)]," *Journal of Applied Physics*, vol. 90, pp. 6553-6554. 2001.
[165] J. H. Knox and K. A. Mccormack, "Temperature effects in capillary electrophoresis .1. Internal capillary temperature and effect upon performance," *Chromatographia*, vol. 38, pp. 207-214. 1994.
[166] F. Foret, M. Deml, and P. Bocek, "Capillary zone electrophoresis - Quantitative study of the effects of some dispersive processes on the separation efficiency," *Journal of Chromatography*, vol. 452, pp. 601-613. 1988.
[167] Y. Wang, Q. Lin, and T. Mukherjee, "Universal Joule heating model in electrophoretic separation microchips," *Proceedings of 2002 Symposium on Micro Total Analysis Systems (MicroTAS '02)*, Nara, Japan, pp. 82-84. 2002.
[168] L. Bousse, C. Cohen, T. Nikiforov, A. Chow, A. R. Kopf-Sill, R. Dubrow, and J. W. Parce, "Electrokinetically controlled microfluidic analysis systems," *Annual Review of Biophysics and Biomolecular Structure*, vol. 29, pp. 155-181. 2000.
[169] S. C. Jacobson and J. M. Ramsey, "Electrokinetic focusing in microfabricated channel structures," *Analytical Chemistry*, vol. 69, pp. 3212-3217. 1997.
[170] J. B. Knight, A. Vishwanath, J. P. Brody, and R. H. Austin, "Hydrodynamic focusing on a silicon chip: Mixing nanoliters in microseconds," *Physical Review Letters*, vol. 80, pp. 3863-3866. 1998.
[171] M. Koch, D. Chatelain, A. G. R. Evans, and A. Brunnschweiler, "Two simple micromixers based on silicon," *Journal of Micromechanics and Microengineering*, vol. 8, pp. 123-126. 1998.
[172] P. Lob, K. S. Drese, V. Hessel, S. Hardt, C. Hofmann, H. Lowe, R. Schenk, F. Schonfeld, and B. Werner, "Steering of liquid mixing speed in interdigital micro mixers - from very fast to deliberately slow mixing," *Chemical Engineering & Technology*, vol. 27, pp. 340-345. 2004.
[173] L. M. Fu, R. J. Yang, C. H. Lin, and Y. S. Chien, "Novel microfluidic mixer utilizing electrokinetic driving forces under low switching frequency," *Electrophoresis*, vol. 26, pp. 1814-1824. 2005.
[174] L. M. Fu, R. J. Yang, G. B. Lee, and Y. J. Pan, "Multiple injection techniques for microfluidic sample handling," *Electrophoresis*, vol. 24, pp. 3026-3032. 2003.
[175] B. H. Weigl and P. Yager, "Microfluidics - Microfluidic diffusion-based separation and detection," *Science*, vol. 283, pp. 346-347. 1999.
[176] M. A. Holden, S. Kumar, E. T. Castellana, A. Beskok, and P. S. Cremer, "Generating fixed concentration arrays in a microfluidic device," *Sensors and Actuators B-Chemical*, vol. 92, pp. 199-207. 2003.
[177] N.-T. Nguyen and S. T. Wereley, *Fundamentals and applications of microfluidics*. Boston, MA: Artech House, 2002.

[178] T. T. Veenstra, T. S. J. Lammerink, M. C. Elwenspoek, and A. van den Berg, "Characterization method for a new diffusion mixer applicable in micro flow injection analysis systems," *Journal of Micromechanics and Microengineering*, vol. 9, pp. 199-202. 1999.
[179] J. Branebjerg, P. Gravesen, J. P. Krog, and C. R. Nielsen, "Fast mixing by lamination," *IEEE-MEMS'96*, San Diego, U.S.A, pp. 441-446, Feb. 11-15. 1996.
[180] F. Schonfeld, K. S. Drese, S. Hardt, V. Hessel, and C. Hofmann, "Optimized distributive micro-mixing by 'chaotic' multilamination," *Proceedings of Modeling and Simulation of Microsystems (MSM'04)*, Boston, MA, pp. 378-381. 2004.
[181] V. Hessel, S. Hardt, H. Lowe, and F. Schonfeld, "Laminar mixing in different interdigital micromixers: I. Experimental characterization," *Aiche Journal*, vol. 49, pp. 566-577. 2003.
[182] D. Gobby, P. Angeli, and A. Gavriilidis, "Mixing characteristics of T-type microfluidic mixers," *Journal of Micromechanics and Microengineering*, vol. 11, pp. 126-132. 2001.
[183] C. X. Qiu and D. J. Harrison, "Integrated self-calibration via electrokinetic solvent proportioning for microfluidic immunoassays," *Electrophoresis*, vol. 22, pp. 3949-3958. 2001.
[184] K. S. Drese, "Optimization of interdigital micromixers via analytical modeling - exemplified with the SuperFocus mixer," *Chemical Engineering Journal*, vol. 101, pp. 403-407. 2004.
[185] P. S. Dittrich, B. Muller, and P. Schwille, "Studying reaction kinetics by simultaneous FRET and cross-correlation analysis in a miniaturized continuous flow reactor," *Physical Chemistry Chemical Physics*, vol. 6, pp. 4416-4420. 2004.
[186] F. Schonfeld, V. Hessel, and C. Hofmann, "An optimised split-and-recombine micro-mixer with uniform 'chaotic' mixing," *Lab on a Chip*, vol. 4, pp. 65-69. 2004.
[187] M. S. Munson and P. Yager, "Simple quantitative optical method for monitoring the extent of mixing applied to a novel microfluidic mixer," *Analytica Chimica Acta*, vol. 507, pp. 63-71. 2004.
[188] X. He, "Electrokinetic control of microfluidic reaction-mixing systems," *AICHE Anaual Meeting*, Austin TX, pp. 430f, November 11. 2004.
[189] R. B. Bird, E. N. Lightfoot, and W. E. Stewart, *Transport phenomena*, 2nd ed. New York: J. Wiley, 2002.
[190] Y. Wang, R. M. Magargle, Q. Lin, J. F. Hoburg, and T. Mukherjee, "System-oriented modeling and simulation of biofluidic lab-on-a-Chip," *Proceedings of the 13th International Conference on Solid-State Sensors and Actuators*, Seoul, Korea, pp. 1280-1283, June 5-9, 2005. 2005.
[191] P. J. A. Kenis, R. F. Ismagilov, S. Takayama, G. M. Whitesides, S. L. Li, and H. S. White, "Fabrication inside microchannels using fluid flow," *Accounts of Chemical Research*, vol. 33, pp. 841-847. 2000.
[192] X. Y. Jiang, Q. B. Xu, S. K. W. Dertinger, A. D. Stroock, T. M. Fu, and G. M. Whitesides, "A general method for patterning gradients of biomolecules on surfaces using microfluidic networks," *Analytical Chemistry*, vol. 77, pp. 2338-2347. 2005.
[193] S. Boyden, "Chemotactic effect of mixtures of antibody and antigen on polymorphonuclear leucocytes," *Journal of Experimental Medicine*, vol. 115, pp. 453-&. 1962.

[194] O. D. Weiner, G. Servant, M. D. Welch, T. J. Mitchison, J. W. Sedat, and H. R. Bourne, "Spatial control of actin polymerization during neutrophil chemotaxis," *Nature Cell Biology*, vol. 1, pp. 75-81. 1999.
[195] P. C. Wilkinson and J. M. Lackie, "The influence of contact guidance on chemotaxis of human neutrophil leukocytes," *Experimental Cell Research*, vol. 145, pp. 255-264. 1983.
[196] D. Zicha, G. A. Dunn, and A. F. Brown, "A new direct-viewing chemotaxis chamber," *Journal of Cell Science*, vol. 99, pp. 769-775. 1991.
[197] S. H. Zigmond, "Ability of polymorphonuclear Leukocytes to orient in gradients of chemotactic factors," *Journal of Cell Biology*, vol. 75, pp. 606-616. 1977.
[198] C. Neumann and S. Cohen, "Morphogens and pattern formation," *Bioessays*, vol. 19, pp. 721-729. 1997.
[199] F. Lin, W. Saadi, S. W. Rhee, S. J. Wang, S. Mittal, and N. L. Jeon, "Generation of dynamic temporal and spatial concentration gradients using microfluidic devices," *Lab on a Chip*, vol. 4, pp. 164-167. 2004.
[200] G. M. Walker, J. Q. Sai, A. Richmond, M. Stremler, C. Y. Chung, and J. P. Wikswo, "Effects of flow and diffusion on chemotaxis studies in a microfabricated gradient generator," *Lab on a Chip*, vol. 5, pp. 611-618. 2005.
[201] M. S. Yang, J. Yang, C. W. Li, and J. L. Zhao, "Generation of concentration gradient by controlled flow distribution and diffusive mixing in a microfluidic chip," *Lab on a Chip*, vol. 2, pp. 158-163. 2002.
[202] M. S. Yang, C. W. Li, and J. Yang, "Cell docking and on-chip monitoring of cellular reactions with a controlled concentration gradient on a microfluidic device," *Analytical Chemistry*, vol. 74, pp. 3991-4001. 2002.
[203] F. M. White, *Viscous fluid flow*, 2nd ed. New York: McGraw-Hill, 1991.
[204] A. E. Kamholz, B. H. Weigl, B. A. Finlayson, and P. Yager, "Quantitative analysis of molecular interaction in a microfluidic channel: The T-sensor," *Analytical Chemistry*, vol. 71, pp. 5340-5347. 1999.
[205] D. A. Beard, "Taylor dispersion of a solute in a microfluidic channel," *Journal of Applied Physics*, vol. 89, pp. 4667-4669. 2001.
[206] C. P. Coelho, S. D. Desai, D. Freeman, and J. White, "A robust approach for estimating diffusion constants from concentration data in microchannel mixers," *Proceedings of 2005 NSTI Nanotechnology Conference and Trade Show (Nanotech 2004)*, Anaheim, CA, pp. 549-552. 2005.
[207] Q. Lin, F. Jiang, X. Wang, Z. Han, Y. C. Tai, J. Lew, and C. M. Ho, "MEMS thermal shear-stress sensors: Experiments, theory and modeling," *Technical Digest of 2000 Solid-State Sensor and Actuator Workshop (Hilton Head 2000)*, Hilton Head Island, SC, U.S.A, pp. 304-307. 2000.
[208] D. A. Beard, "Response to "Comment on 'Taylor dispersion of a solute in a microfluidic channel' [J. Appl. Phys. 90, 6553 (2001)]"," *Journal of Applied Physics*, vol. 90, pp. 6555-6556. 2001.

Publication List

No.	***Peer-Reviewed Journal Papers***
1	Y. Wang, Q. Lin and T. Mukherjee, System-oriented dispersion models of general-shaped electrophoresis microchannels, *Lab on a chip*, 4(5), pp. 453-463, 2004
2	Y. Wang, Q. Lin and T. Mukherjee, A model for Joule heating-induced dispersion in microchip electrophoresis, *Lab on a chip*, 4(6), pp. 625-631, 2004
3	Y. Wang, Q. Lin and T. Mukherjee, A model for laminar diffusion-based complex electrokinetic passive micromixers, *Lab on a chip*, 5(8), pp. 877-887, 2005
4	Y. Wang, Q. Lin and T. Mukherjee, Composable behavioral models and schematic-based simulation of electrokinetic lab-on-a-chips, *IEEE Transactions on computer-aided design of integrated circuits and systems* (in press), 2005
5	A.S. Bedekar, Y. Wang and S. Krishnamoorthy *et al.* System-level simulation of flow induced dispersion in lab-on-a-chip systems. *IEEE Transactions on computer-aided design of integrated circuits and systems* (in press), 2005

No.	***Peer-Reviewed Conferences Papers***
1	Y. Wang, R. Magargle, Q. Lin, J.F. Hoburg and T. Mukherjee, System-oriented modeling and simulation of biofluidic lab-on-a-chip, *Proceedings of the 13th International Conference on Solid-State Sensors and Actuators*, Vol. 2, pp. 1280-1283, Jun. 5-9, 2005, Seoul, Korea.
2	Y. Wang, Q. Lin and T. Mukherjee, System simulations of complex electrokinetic passive micromixers, Technical *Proceedings of the 2005 NSTI Nanotechnology Conference and Trade Show*, Vol. 1, pp. 579-582, May 8-12, 2005, Anaheim, CA
3	Y. Wang, Q. Lin and T. Mukherjee, Models for Joule heating dispersion in complex electrophoretic separation microchannels, *Proceedings of IMECE2004 ASME International Mechanical Engineering Congress & Exposition*, Vol.2, Paper No. IMECE2004-60970, Nov. 13-19, 2004, Anaheim, CA.
4	Y. Wang, Q. Lin and T. Mukherjee, Applications of behavioral modeling and simulation on lab-on-a-chip: micro-mixer and separation system, *Proceedings of the 2004 IEEE International Behavioral Modeling and Simulation Conference*, pp. 8-13, Oct 21-22, 2004, San Jose, CA.
5	Y. Wang, Q. Lin and T. Mukherjee, Analytical models for complex electrokinetic passive micromixers, *Proceedings of the Eighth International Conference on Miniaturized* Systems *for Chemistry and Life Sciences (MicroTAS 2004)*, Vol. 1, pp. 596-598, Sep. 26-30, 2004, Malmö, Sweden.
6	Y. Wang, Q. Lin and T. Mukherjee, Composable system simulation of dispersion in complex electrophoretic separation microchips, *Technical Proceedings of the 2004 NSTI Nanotechnology Conference and Trade Show*, Vol. 1, pp. 59-62, Mar. 7-11, 2004, Boston, MA
7	Y. Wang, Q. Lin and T. Mukherjee, Analytical dispersion models for efficient simulation of complex microchip electrophoresis systems, *Proceedings of the Seventh International Conference on Miniaturized Systems for Chemistry and Life Sciences (MicroTAS 2003)*, Vol. 1, pp. 135-138, Oct. 5-9, 2003, Squaw Valley, CA.
8	A. J. Pfeiffer, Y. Wang, Q. Lin, R. S. Magargle, J.F. Hoburg, T. Mukherjee and S. Hauan, Design and optimization of microchip based electrophoretic channel topologies, *Proceedings of the 2003 Annual Meeting of the American Institute of Chemical Engineers (AIChE 2003)*, pp. 24b, Nov. 16-21, 2003, San Francisco, CA.
9	Y. Wang, Q. Lin and T. Mukherjee, Universal Joule heating model in electrophoretic separation microchips, *Proceedings of the Sixth International Conference on Miniaturized Systems for Chemistry and Life Sciences (MicroTAS 2002)*, Vol. 1, pp. 82-84, Nov. 3-7, 2002, Nara, Japan.
10	Y. Wang, Q. Lin, J.F. Hoburg and T. Mukherjee, Modeling of Joule heating in electrophoretic separation microchips, *Technical Proceedings of the 2002 NSTI Nanotechnology Conference and Trade Show*, Vol. 1, pp. 80-83, Apr. 22-25, 2002, San Juan, Puerto Rico